═══════════════════ **TOKAMAKS** ═══════════════════

*I devote this paper and my very best wishes
to Prof. L.I. Rudakov—my "Teacher of Teacher"
in Plasma Physics
V. Parail*

Integrated Predictive Modeling of JET H-mode Plasma with Type-I and Type-III ELMs*

**V. Parail[1], G. Bateman[2], M. Becoulet[3], G. Corrigan[1], D. Heading[1], J. Hogan[4],
W. Houlberg[4], G. T. A. Huysmans[3], J. Kinsey[2], A. Korotkov[1], A. Kritz[2], A. Loarte[5],
J. Lonnroth[6], D. McDonald[1], P. Monier-Garbet[3], T. Onjun[2], G. Saibene[5],
R. Sartori[5], S. E. Sharapov[1], H. R. Wilson[1], and JET-EFDA contributors**

[1] *EURATOM/UKAEA Fusion Association, Culham Science Centre, Abingdon OX14 3DB, United Kingdom*
[2] *Lehigh University, 16 Memorial Drive East, Bethlehem, PA 18015, USA*
[3] *Association Euratom-CEA, Cadarache 13108 Saint Paul lez Durance, France*
[4] *Oak Ridge National Laboratory, P.O. Box 2009, MS 8071, USA*
[5] *EFDA CSU–Garching, D85748 Garching, Germany*
[6] *EURATOM-TEKES Association, Helsinki University of Technology, P.O. Box 2200, FIN–02015 HUT, Finland*
e-mail: vparail@jet.uk
Received October 10, 2002

Abstract—Edge plasma parameters influence plasma performance in many different ways (profile stiffness is probably one of the best known examples). In the ELMy H-mode plasma, a thin region with improved transport characteristics (the edge transport barrier) links the core and the scrape-off layer. There is a strong coupling between these three areas, so that even a modest variation of plasma parameters in one region can lead to a dramatic change in the overall plasma performance. A systematic MHD stability analysis and self-consistent integrated predictive modeling of a series of JET ELMy H-mode plasmas, including scans in gas fueling and triangularity, are presented. The main conclusion is that plasma performance indeed sensitively depends on the edge plasma parameters, which should be modeled in a self-consistent way. © 2003 MAIK "Nauka/Interperiodica".

1. INTRODUCTION

A self-consistent integrated predictive modeling of ELMy H-mode plasma should ideally include a simulation of the evolution of plasma parameters in the core, within the edge transport barrier (ETB), and in the scrape-off layer (SOL). Transport modeling should be complemented by the MHD stability analysis and a further simulation of edge-localized MHD instabilities (ELMs). The failure of dealing with one of the above-mentioned items seriously undermines the understanding of the underlying physical processes and can lead to a loss of predictability. The paper deals with several characteristic examples of the strong link between core transport, the ETB, and the SOL: the effect of strong gas puffing and magnetic configuration on the performance of type-I ELMy H-mode plasma. We also discuss the dynamics of the transition of the type-III ELMs to type-I ELMs, as well as the role of ballooning and kink/peeling mode stability in ELM dynamics.

2. BACKGROUND EXPERIMENTAL INFORMATION

We have selected four recent JET ELMy H-mode plasmas, which constitute a scan in gas puffing and triangularity. All of the discharges have very similar values of the plasma current $I_p \cong 2.5$ MA, the toroidal magnetic field $B_T \cong 2.6$ T, ellipticity $k \cong 1.7$, and the level of additional heating provided by Neutral Beam Injection (NBI): $P_{NBI} \cong 15$ MW. Two discharges belong to the triangularity scan (shot no. 53186 has $\delta = 0.3$ and shot no. 53298 has $\delta = 0.5$) and three shots (nos. 53298, 53299, and 52739) constitute the gas puffing scan (with $\Gamma = 0$ for shot no. 53298, $\Gamma \cong 4.5 \times 10^{22}$ s^{-1} for shot no. 53299 and $\Gamma \cong 6.0 \times 10^{22}$ s^{-1} for shot no. 52739). Figure 1 shows the time evolution of the energy content for these shots together with the D_α signal and energy confinement time normalized to the H-mode scaling (H98y). At least two conclusions can be drawn from this figure:

(1) Plasma with higher triangularity has a better performance (in terms of both plasma stored energy and

───────────────

*This article was submitted by the authors in English.
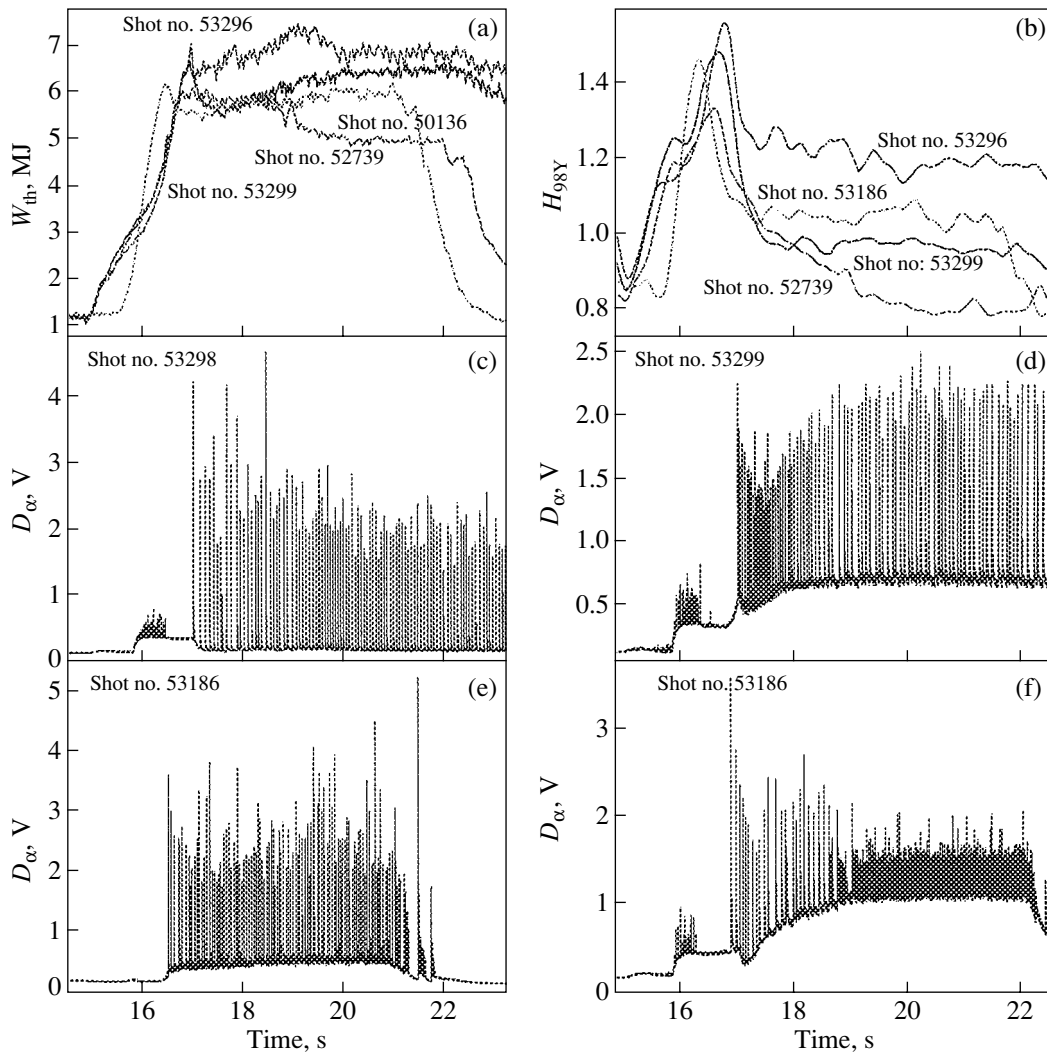
Fig. 1. The time evolution of (a) the energy content, (b) the energy confinement-time enhancement factor H98Y2, and (c–f) the D_α signals for JET shot nos. 53186, 53298, 53299, and 52739.

normalized confinement) than similar low-triangularity plasma;

(2) Strong gas puffing leads to a significant increase in the ELM frequency (followed by transition to the type-III ELMy H-mode in extreme cases). This leads to a noticeable degradation in the plasma performance. It is worth noting that an intermediate level of gas puffing can lead to a decrease of the ELM frequency and a transition to a mixed type I-II ELMy H-mode (see shot no. 53299) [1].

We will also discuss the possible cause of the sudden transition from type-I to type-III ELMs, which was observed in many experiments with a modest level of heating power [2], and try to associate the transition with a bifurcation in the edge MHD instability.

3. TRANSPORT MODELS, CODES, AND OTHER TOOLS USED IN INTEGRATED PREDICTIVE MODELING

As we discussed earlier, there is a strong link between the core transport and plasma parameters within the ETB and the SOL. To take this coupling into consideration, we use the COCONUT suite of JET transport codes, which consists of the 1.5D core transport code JETTO [3] coupled to the 2D edge transport code EDGE2D/NIMBUS [4]. JETTO explicitly takes the region of the edge transport barrier into account. It is assumed that anomalous transport is completely suppressed within the ETB, so that the only remaining transport is neoclassical [5]. The width of the ETB is considered an external parameter, which is calculated using recently developed models [6]. Perpendicular transport in the SOL is assumed to be neoclassical as well, with longitudinal transport being classical.
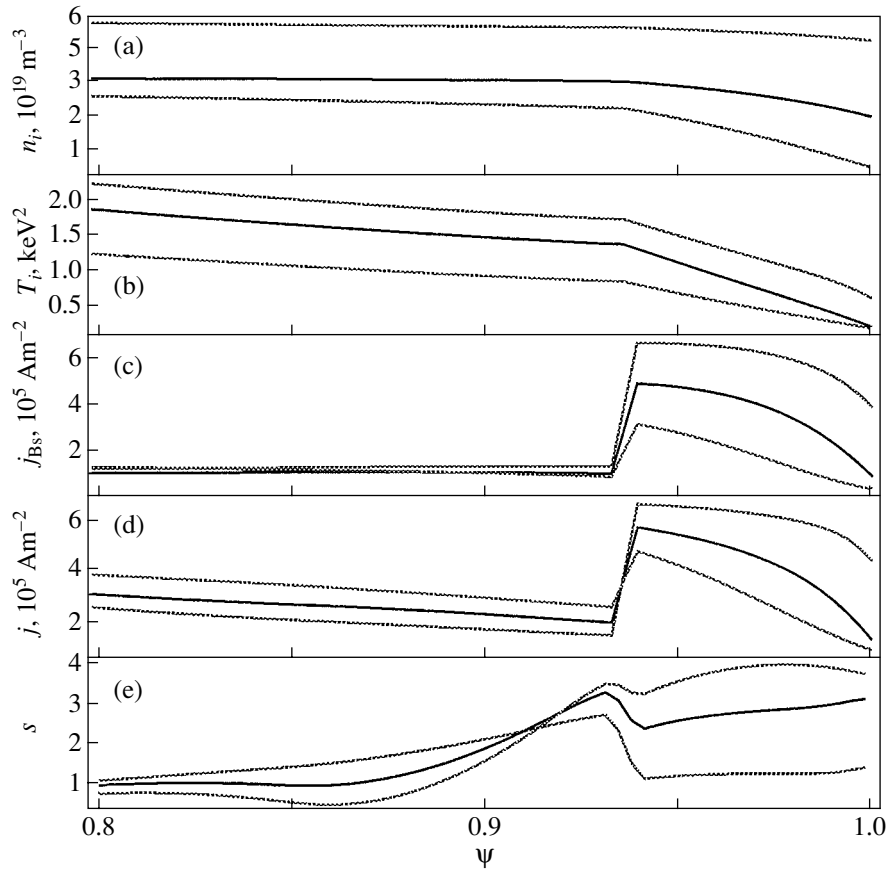
Fig. 2. Edge plasma profiles for a gas scan: (a) ion density, (b) ion temperature, (c) bootstrap current density, (d) total current density, and (e) magnetic shear.

JETTO has a fixed boundary solver of the Grad-Shafranov equation, which generates equilibrium that is consistent with the predicted pressure and current profiles in the core and ETB. JETTO is linked with the MHD stability code IDBALL, which generates ideal ballooning stability diagrams in s–α coordinates. Recently, JETTO has been linked with the much more sophisticated MHD stability code MISHKA [7], which includes the stability analysis of both finite-n ballooning and kink/peeling modes.

To simulate ELMs, JETTO uses simple analytical formulas, which evaluate ballooning and kink stability inside the separatrix: $\alpha \equiv -\dfrac{2\mu_0 q^2}{B_0^2 \varepsilon}\left(\dfrac{dp}{d\rho}\right) \leq \alpha_{crit}$ or $j_{ETB} <$ j_{crit}, where p is the plasma pressure and j is the current density within the ETB. The α_{crit} and j_{crit} parameters are variable numerical factors, which are checked against the results of the MHD stability codes IDBALL and MISHKA and adjusted accordingly. To simulate the ELM, JETTO temporarily increases the level of anomalous transport within the ETB as soon as the stability criterion is violated. Both the pressure gradient and the edge current drop as a result, so plasma returns to the pre-ELM state and the cycle repeats.

4. MODELING OF THE ELMY H-MODE WITH STRONG GAS PUFFING

As noted above, we have selected three JET shots (nos. 53298, 53299 and 52739) to study the role of gas puffing in type-I ELMy H-mode plasma performance. Three different levels of gas puffing have been used throughout the simulations: $\Gamma = 0$, 4×10^{22}, and 10^{23} s^{-1}. We use the COCONUT suite to simulate the time evolution of both core and SOL profiles between ELMs. Figure 2 shows some characteristic profiles for the three reference cases. The inspection of these profiles shows that gas puffing leads to an increase in the density in both the core and the SOL. However the increase in density near the separatrix is much stronger than that in the core. Since in the computations we try to keep the pressure gradient within the ETB roughly the same for all three runs, the lower density gradient in the case with strong gas puffing translates into a higher temperature gradient, which, in turn, results in a lower edge temperature. Both of these factors lead to a dramatic increase in the plasma collisionality for the case of strong gas puffing. Since the bootstrap current decreases with plasma collisionality, we conclude that strong gas puffing significantly reduces the edge current (see Fig. 2c). Given the essential role played by the
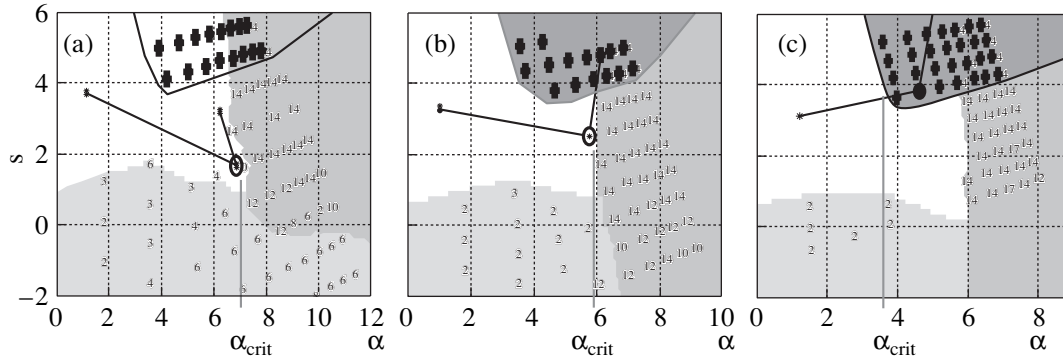
Fig. 3. MHD stability (ideal ballooning is represented by blue crosses; finite-n ballooning, the dark shaded area; and kink/peeling, the light shaded area) of the gas scan shots from Fig. 1: $\Gamma =$ (a) 0, (b) 4×10^{22}, and (c) 10^{23} s^{-1}. Three operational points are shown: just inside the ETB (at $\psi = 0.93$), on the top of the ETB (at $\psi = 0.93$) and a point at $\psi \approx 0.98$–0.99.

edge current in both kink and ballooning stability, we run the MISHKA code for all three cases. The result of this analysis is presented in Fig. 3 and allows us to draw the following conclusions:

(1) The discharge without gas puffing generates a strong bootstrap current within the ETB (Fig. 3a). This reduces the magnetic shear and allows access to a second ballooning stability region. The maximum stable pressure gradient corresponds to $\alpha_{crit} \approx 6$ and is limited by finite-n ballooning/peeling modes, with the radial localization approximately equal to the width of the ETB.

(2) A medium level of gas puffing reduces the bootstrap current only near the separatrix (for the normalised poloidal flux $\psi \geq 0.98$). This blocks the access to the second stability region and reduces the level of the critical pressure gradient to $\alpha_{crit} \approx 3.5$ for those magnetic surfaces outside $\psi \geq 0.98$ (see Fig. 3b). The rest of the ETB still has access to a second stability region with a high enough critical pressure gradient ($\alpha_{crit} \approx 6$).

(3) The highest level of gas puffing destroys the bootstrap current across the whole ETB. The entire edge barrier loses access to the second stability region, so the maximum achievable normalized pressure gradient drops to $\alpha_{crit} \approx 3.5$.

To find out how the ELM frequency depends on the level of α_{crit}, we first run JETTO for two cases: with zero gas puffing and with maximum gas puffing. The same assumptions about the amplitude and structure of ELM were used but we assume that $\alpha_{crit} \approx 6$ for the case without gas puffing and $\alpha_{crit} \approx 3.5$ for the case with very strong puffing ($\Gamma_{max} = 10^{23}$ s^{-1}). The result of this study is shown in Figs. 4a and 4b and allows us to conclude that qualitatively (both in terms of the ELM frequency and the change in confinement) the transition from the second to the first ballooning stability limit corresponds to a transition from type-I to type-III ELMs. It is worth noting that the first ballooning stability boundary can be controlled by the resistive rather than by the ideal ballooning mode in highly collisional plasma. This can

further reduce achievable level of the critical pressure gradient to below $\alpha_{crit} \approx 3.5$, which was used in our analysis. Other effects, such as differential plasma rotation or the diamagnetic effect, may affect the stability boundaries as well.

To simulate discharge with the medium level of gas puffing, we split the edge barrier into two parts: external (with $\psi \geq 0.98$ and $\alpha_{crit} \approx 3.5$) and internal (with $0.94 \leq \psi < 0.98$ and $\alpha_{crit} \approx 6$). The result of the modeling is shown in Fig. 4c and allows us to conclude that it qualitatively reproduces the experimentally observed mixed type I-II ELMy H-mode plasma in JET [1].

The next step of our analysis was to look at the dynamics of the evolution of the plasma parameters while approaching the MHD stability limit. To do it, we assume that the plasma parameters within the ETB are not limited by any edge MHD instabilities (peeling or ballooning). We just monitor the MHD stability of the plasma edge during such unrestricted evolution, fully suppressing any anomalous transport within the ETB. Figure 5 shows that the trajectory of the "top-of-the-barrier" operational point is in s–α space, starting from the L–H transition. One can observe that plasma heating leads to an increase in the plasma pressure gradient, which is accompanied by an increase in the edge current (both bootstrap and Ohmic) with a corresponding reduction in the magnetic shear. As a result, the top-of-the-barrier operational point moves in s–α space so that it crosses the first ideal ballooning stability limit before entering the second stability region. We should stress that this kind of evolution is quite typical; in fact, it is observed in all of the shots we have simulated so far.

Thus, if the ETB region crosses the ideal ballooning unstable area before entering the second stability region, then the question arises as to how the plasma can overcome this "primary" instability. Numerical modeling shows that one way to do it would be to avoid the unstable region by increasing the edge current without increasing the pressure gradient [8]. This method works indeed, but it requires a certain special current ramp-up technique only occasionally used in present-
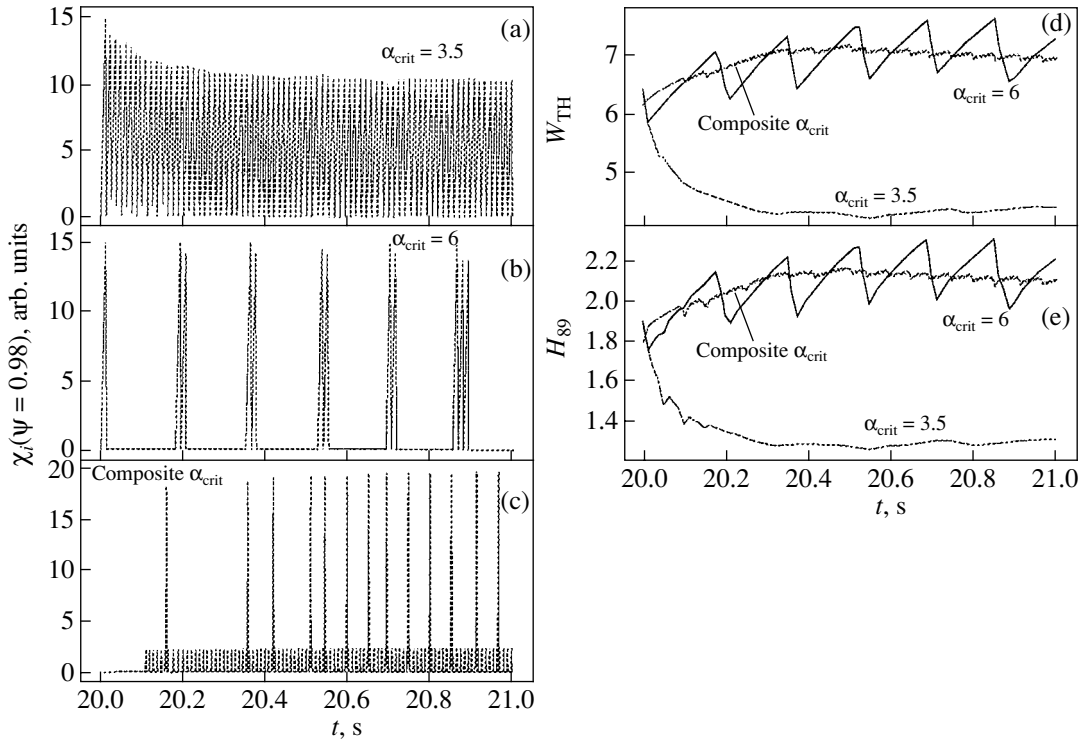
Fig. 4. Time evolution of the simulated ion thermal conductivity χ_i at $\psi \approx 0.99$ for (a) $\alpha_{crit} = 3.5$, (b) $\alpha_{crit} = 6$, and (c) a composite α_{crit}; (d) the thermal energy content and (e) confinement-time enhancement factor H89 for shot no. 53298.

day experiments. Another way would be to assume that the ideal ballooning instability (with $n \longrightarrow \infty$) generates relatively small, incremental transport. If this is the case, then the plasma can be pushed through the unstable region with the help of "extra" power. We leave the detailed discussion of this idea for future work and finish this paragraph with only one remark. It is known from experiments that the plasma edge passes through a chain of transformations while the heating power is increasing. First, the L–H transition occurs, followed by the type-III ELMy H-mode with the ELM frequency scaling inversely proportional to the heating power. The plasma jumps into an ELM-free H-mode state when more power is applied and finally enters into the type-I ELMy H-mode with the ELM frequency increasing with the power. Qualitatively, this chain of transitions is similar to what we found in our simulations: the plasma reaches the first ballooning stability limit after the establishment of the ETB (L–H transition) and stays there if the power is not high enough. This corresponds to a type-III ELMy H-mode plasma. With more power, the plasma enters the second stability region (ELM-free period), followed by the strong type-I ELMy H-mode, which is caused by finite ballooning and peeling instabilities.

5. TRIANGULARITY SCAN

It is known from experiments and MHD theory that the magnetic configuration influences the plasma per-

formances in many respects. In particular, a higher triangularity allows a better confinement (see Fig. 1) and a higher normalised density to be reached [9]. We select two recent JET shots that are identical in all other respects but have different triangularities: shot no. 53187 has $\delta = 0.3$ and shot no. 53298 has $\delta = 0.5$. We performed predictive modeling of these two shots with
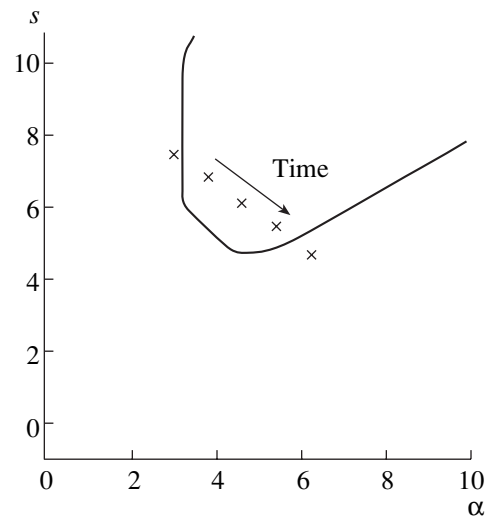
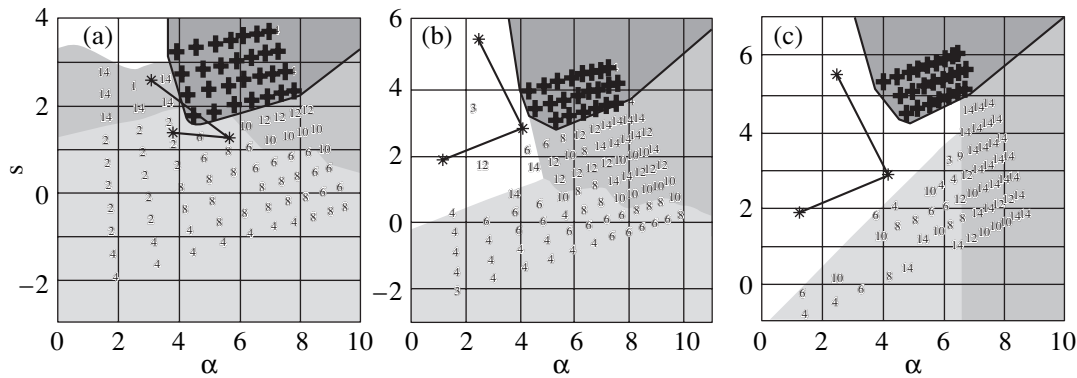**Fig. 5.** Time evolution of the operational point at $\psi = 0.94$ (top of the barrier) in s–α space.

Fig. 6. MHD stability of the triangularity scan δ = (a) 0.1, (b) 0.3, and (c) 0.5.

JETTO using the same models for the ETB width [6] and the same assumptions about the ballooning stability. The modeling confirmed that both low- and high-triangularity plasmas could enter the second stability after passing through the ballooning unstable region, with the characteristic width of the unstable region increasing with triangularity. Using the same assumption for α_{crit} leads to either underestimation of the high-triangularity plasma energy content or overestimation of the low-triangularity plasma (depending on the level of α_{crit}). To elucidate the situation with MHD stability we generated a range of magnetic configurations with the triangularity varying from $\delta = 0.1$ to $\delta = 0.5$ and performed a predictive modeling and full MHD stability analysis of three otherwise identical plasmas with $\delta = 0.1$, 0.3, and 0.5. Some results of the MHD analysis are shown in Fig. 6 and allow us to draw the following conclusions. The very low triangularity ($\delta = 0.1$) plasma has no access to a second stability region, mainly because of the low-n kink/peeling mode. The medium-triangularity plasma ($\delta = 0.3$) has some access to a second stability, but this access is very narrow in the s–α space and requires an accurate tailoring of the edge plasma parameters to enter into it. Increasing the triangularity above 0.3 widens the access to the second stability, although it only slightly increases the maximum level of α_{crit} (see [8]).

6. CONCLUSIONS

Self-consistent integrated modeling of a number of JET type-I and type-III ELMy H-mode discharges has been carried out using the COCONUT suite of JET transport codes coupled with the MHD stability codes IDBALL and MISHKA. It has been shown that, generally, JET plasmas with an ETB can have access to second ballooning stability, with the critical level of the normalized pressure gradient being controlled by the medium-n ballooning/peeling modes. Strong gas puffing reduces the edge current and brings the operational point back into the first ballooning stability region. This transition is accompanied by a dramatic increase in the

ELM frequency similar to the experimentally observed transition from type-I to type-III ELMs. A medium level of gas puffing leads to a mixed type I-II ELMy H-mode without the serious degradation of the plasma confinement. Modeling plasmas with different triangularity reveals that a higher triangularity results in better access to a second ballooning stability, which improves the plasma performance.

REFERENCES

1. G. Saibene, R. Sartori, A. Loarte, *et al.*, Plasma Phys. Controlled Fusion **44**, 1769 (2000).

2. R. Sartori, B. Balet, S. Clement, *et al.*, Plasma Phys. Controlled Fusion **40**, 757 (1998); R. Sartori, D. Bobra, G. D. Conway, *et al.*, in *Proceedings of the 26th EPS Conference on Controlled Fusion and Plasma Physics, Maastricht, 1999*, ECA **23J**, 197 (1999).

3. G. Cenacchi and F. Taroni, Rep. JET-IR(88)03 (JET Joint Undertaking, Abingdon, 1988).

4. R. Simonini, G. Corrigan, G. Radford, *et al.*, Contrib. Plasma Phys. **34**, 368 (1994).

5. V. Parail, G. Corrigan, D. Heading, *et al.*, in *Proceedings of the 27th EPS Conference on Controlled Fusion and Plasma Physics, Budapest, 2000*, ECA **24B**, 61 (2000).

6. T. Onjun, G. Bateman, A. H. Kritz, and G. Hammett, Phys. Plasmas **9**, 5018 (2002).

7. A. B. Mikhaĭlovskiĭ, G. T. A. Huysmans, W. O. K. Kerner, and S. E. Sharapov, Fiz. Plazmy **23**, 916 (1997) [Plasma Phys. Rep. **23**, 844 (1997)].

8. P. B. Snyder, H. R. Wilson, J. R. Ferron, *et al.*, Phys. Plasmas **9**, 2037 (2002).

9. G. Saibene, L. D. Horton, R. Sartori, *et al.*, Nucl. Fusion **39**, 1133 (1999).

<center>
**NONLINEAR
PHENOMENA**
</center>

The DNLS Equation and Parametric Decay Instability[1]

V. I. Shevchenko*, R. Z. Sagdeev**, V. L. Galinsky*, and M. V. Medvedev***

* University of California, San Diego, La Jolla, CA 92093–0407, USA
** University of Maryland, College Park, MD 20742–3280, USA
*** University of Kansas, Lawrence, KS 66045, USA
Received October 24, 2002

Abstract—A model that describes the interaction of nonlinear Alfvén packets propagating in opposite directions parallel to the ambient magnetic field is constructed. This model incorporates both (i) the parametric interaction of harmonics propagating in the same direction, which can be responsible for the transportation of the wave energy to the short-wavelength region of the spectrum, and (ii) the parametric interaction of Alfvén waves propagating in opposite directions, which can be responsible for the excitation of backward-propagating waves by the parametric decaylike instability of the forward-propagating fluctuations. © *2003 MAIK "Nauka/Inter-periodica".*

1. INTRODUCTION

Historically, parametric interactions of Alfvén waves that involve ion acoustic-like modes have been studied in two different contexts.

On the one hand, it has been well known for a long time, that finite-amplitude Alfvén waves in plasma are unstable with respect to the excitation of a backward-propagating daughter Alfvén wave and a forward-propagating ionacoustic wave (parametric decay instability) [1]. Parametric interactions of Alfvén waves involving ion-acoustic modes have been investigated in detail by many authors [2–13].

In another context, the parametric coupling of Alfvén waves propagating in the same direction, which developed through ponderomotively driven density fluctuations, was also a subject of intensive studies. The processes of the steepening of the wave profile and the transportation of the wave energy to the small-scale part of the spectrum due to this coupling are described by the so-called derivative nonlinear Schroedinger (DNLS) equation, which was first derived by Rogister [14] using kinetic theory and subsequently by several authors [15–21] in the hydrodynamic approximation. A shortcoming of the DNLS equation-based approach is that this equation doesn't describe the nonlinear interaction of waves propagating in opposite directions, such as the decay-type interaction.

From our point of view, a separation of these two processes is not warranted as both parametric interactions work on the same order of the wave amplitude. The goal of this paper is to develop a model that includes both types of parametric interaction of Alfvén waves and to study the parametric interaction of Alfvén packets propagating in opposite directions parallel to the ambient magnetic field.

---

[1] This article was submitted by the authors in English.

2. EQUATIONS OF THE MODEL AND SOLUTION

Let us consider two Alfvén wave packets propagating in opposite directions along the magnetic field

$$B(z, t) = B^+ + B^-, \tag{1}$$
$$B^\pm = B_x(z \pm v_A t, \tau) + i B_y(z \pm v_A t, \tau).$$

Here, $v_A = B_0^2/4\pi n_0 m$ is the Alfvén velocity, B_0 is the ambient magnetic field, n_0 is the density of the plasma, m is the proton mass, and τ is the slow time arising due to the nonlinearity of the waves.

The ion-acoustic-like motions of plasma are excited because of the nonlinearity of the Alfvén waves; the equations for density δn and velocity v perturbations in these motions can be written in the following form:

$$\frac{\partial v}{\partial t} + c_S^2 \frac{1}{n_0} \frac{\partial \delta n}{\partial z} = -\frac{1}{8\pi n_0 m} \frac{\partial}{\partial z} |B|^2, \tag{2}$$

$$\frac{\partial \delta n}{\partial t} + n_0 \frac{\partial v}{\partial z} = 0, \tag{3}$$

where $c_S = \sqrt{T/m}$ is the ion-acoustic velocity and T is the sum of the electron and ion temperatures $T = T_e + T_p$.

Taking into account Eq. (1), the nonlinear term in (2) has the form

$$|B(z, t)|^2 = |B^+|^2 + |B^-|^2 + (B^+ B^{-*} + B^{+*} B^-). \tag{4}$$

In accordance with the structure of drive force, the solution of Eqs. (2) and (3) can be written as

$$\delta n = \delta n^+ + \delta n^- + \delta n^{\text{par}}(z, t), \tag{5}$$

$$v = v^+ + v^- + v^{\text{par}}(z, t). \tag{6}$$

Here, δn^+, v^+, as well as δn^-, v^-, can easily be found from (2) and (3):

$$\delta n^{\pm} = n_0 \frac{1}{2(1-\beta)} \frac{\left|B^{\pm}\right|^2}{B_0^2}, \quad v^{\pm} = \mp v_A \frac{\delta n^{\pm}}{n_0}, \quad (7)$$

where $\beta = c_S^2/v_A^2$.

The last terms in δn and v arise as a result of the parametric interaction of Alfvén waves propagating in opposite directions.

We consider here the decaylike parametric interaction of oppositely propagating wave packets in a small-β plasma ($\beta = c_S^2/v_A^2 \ll 1$). As one can see from Eqs. (2) and (3), the frequency of driven ion-acoustic-like perturbations of the density and velocity δn^{par} and δv^{par} is on the order of the ion-acoustic frequency or is defined by the nonlinearity of the Alfvén waves. Thus, for $\beta \ll 1$, the problem under consideration is the interaction of high-frequency waves (Alfvén waves) with slow plasma motions (ion-acoustic-like oscillations) with $\omega \ll k v_A$, where ω is a characteristic frequency of low-frequency motions of plasma and k is the wave number. This interaction includes the decay process, as well as the modulation instability of Alfvén waves that was revealed by Vedenov and Rudakov [22] for Langmuir waves. As a result, the system of equations describing the parametric interaction of wave packets propagating in opposite directions has the following form:

$$\frac{\partial B^+}{\partial \tau} + i \frac{v_A^2}{2\omega_c} \frac{\partial^2 B^+}{\partial z^2} - \frac{v_A}{4B_0^2} \frac{\partial}{\partial z}(\left|B^+\right|^2 B^+)$$
$$= -\frac{v_A}{2} \frac{\delta n^{\mathrm{par}}}{n_0} \frac{\partial B^-}{\partial z}, \quad (8)$$

$$\frac{\partial B^-}{\partial \tau} + i \frac{v_A^2}{2\omega_c} \frac{\partial^2 B^-}{\partial z^2} + \frac{v_A}{4B_0^2} \frac{\partial}{\partial z}(\left|B^-\right|^2 B^-)$$
$$= \frac{v_A}{2} \frac{\delta n^{\mathrm{par}}}{n_0} \frac{\partial B^+}{\partial z}, \quad (9)$$

$$\frac{\partial^2 \delta n^{\mathrm{par}}}{\partial \tau^2} - c_S^2 \frac{\partial^2 \delta n^{\mathrm{par}}}{\partial z^2} = \frac{1}{8\pi m} \frac{\partial^2}{\partial z^2}(B^+ B^{-*} + B^- B^{+*}), (10)$$

where ω_c is the proton gyro frequency.

It is easy to show that Eqs. (8)–(10) have an integral of motion that has the form

$$\frac{1}{4\pi v_A} \int \{\left|B^-\right|^2 - \left|B^+\right|^2\} dz + m \int v \delta n dz = \text{const}, \quad (11)$$

This integral is just the conservation of the momentum in the system that consists of two Alfvén wave packets and low-frequency motions of plasma.

We represent the solution of (8)–(10) as

$$B^+ = \frac{1}{\sqrt{L}} \sum B_k^+(\tau) e^{i\lambda_k(z + v_A t)},$$

$$B^- = \frac{1}{\sqrt{L}} \sum B_k^-(\tau) e^{i\lambda_k(z - v_A t)}, \quad (12)$$

$$\delta n_{\mathrm{par}} = \frac{1}{\sqrt{L}} \sum \delta n_k(\tau) e^{i\lambda_k z},$$

where $\lambda_n = 2\pi n/L$, n is an integer number, and L is the length of the system.

It is easy to see from Eqs. (8)–(10) that the parametric interaction of Alfvén wave packets involves sets of three harmonics B_k^+, B_{-k}^-, and δn_{2k}. Assuming that the B_k^+ harmonic has a finite amplitude and considering B_{-k}^- and δn_{2k} as small perturbations, we obtain a dispersion relation for three-harmonic interaction that describes the parametric excitation of a backward-propagating Alfvén wave and an ionacoustic-like perturbation,

$$(\omega^2 - 4k^2 c_S^2)(\omega - k^2 v_A^2/2\omega_c) = k^3 v_A \frac{1}{L} \frac{\left|B_k^+\right|^2}{4\pi n_0 m}, \quad (13)$$

which is identical to the dispersion relation of the parametric decaylike instability [23].

The solution of nonlinear equations (8)–(10) was obtained numerically. We introduced dimensionless variables

$$B^{\pm} = \frac{B^{\pm}}{B_0}, \quad \delta n^{\mathrm{par}} = \frac{\delta n^{\mathrm{par}}}{n_0}, \quad z = \frac{z}{\bar{z}},$$
$$\tau = \frac{\tau}{\bar{\tau}}, \quad B_k = \frac{B_k}{B_0 \sqrt{\bar{z}}}, \quad (14)$$

where $\bar{\tau} = 144/\omega_c$, $\bar{z} = 36c/\omega_p$, and ω_p is the proton plasma frequency, and chose the length of the box $L = 1130c/\omega_p$.

First, we studied the nonlinear evolution of the decaylike parametric interaction of the three harmonics. Results of the solution of the nonlinear equations in this case, which are similar to the standard dynamics of decay instability [1], are presented in Figs. 1 and 2, where the nonlinear evolution of B_k^+ and B_{-k}^-, as well as the growth rate of the B_{-k}^- harmonic, are shown.

In the general case of parametrically interacting wave packets, we solved Eqs. (8)–(10) by the spectral method using the predictor-,-corrector scheme; the nonlinear terms were calculated with the help of fast Fourier transform. Periodic boundary conditions were set at $z = 0$ and $z = l$ (where $l = L/\bar{z}$), and 2048 harmonics and spatial points $-1024 < n < 1024$ were assumed in (11).
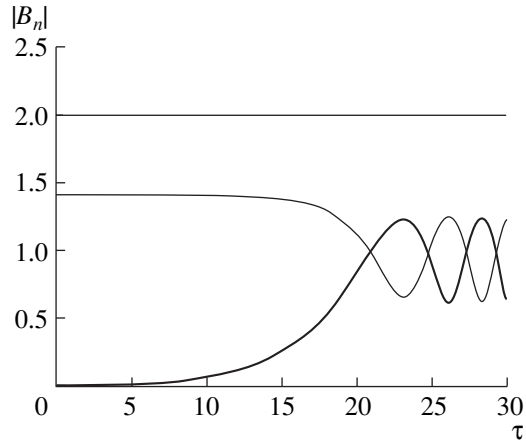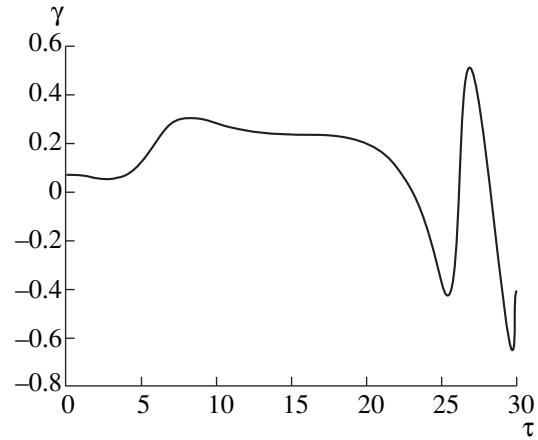
Fig. 1. Nonlinear dynamics of decay-type interaction of the three harmonics in a plasma with $\beta = 0.01$. The thin and thick curves are the amplitudes of the pump harmonic B_1^+ and the daughter harmonic B_{-1}^-, respectively, and the thin horizontal line is an integral of equations.

Fig. 2. The growth rate of the parametric instability $\gamma = \dfrac{dB_{-1}^-/d\tau}{B_{-1}^-}$.

We consider a low-β plasma where the forward-propagating wave packet B_{avg}^- has a large average wave amplitude B^-, while backward-propagating fluctuations have zero amplitudes, and there are slow motions of the plasma with small average density perturbations δn_{avg}. The spectrum of the forward waves was chosen as having a power law $\left|B_k^-\right|^2 \sim |k|^{-\alpha}$ up to $|k| = k_m$ and exponentially decreasing for larger $|k|$. The initial spectrum of the acoustic-like motions was set in a similar way.

Parametric decay interaction leads to the excitation of backward-propagating Alfvén fluctuations. The dynamics of the wave energy density in both wave packets for $\beta = 0.01$, $B_{\mathrm{avg}}^- = 0.25$, $\alpha = 1.5$, $m = 16$, and $\delta n_{\mathrm{avg}} = 10^{-2}$ is shown in Fig. 3, where the thick curve is for forward-propagating waves and the thin one is for backward-propagating ones. The wave profiles for the B^--packet are shown in Figs. 4a–4c for dimensionless times $\tau =$ (a) 0, (b) 1, and (c) 60. One can see from Fig. 4b that a DNLS-type nonlinearity (the third term in the left-hand side of (8)–(9)) leads to the steepening of the wave profile and the generation of typical whistler-like packets. The wave profile for a long time ($\tau = 60$, Fig. 4c) significantly differs from the initial one. The spectral characteristics of the forward-propagating wave packet at times $\tau = 0$ (thin line) and $\tau = 60$ (thick line) that are shown in Fig. 5 demonstrate the creation of higher harmonics due to the nonlinear coupling of Alfvén waves moving in the same direction. The wave profile of the wave packet propagating in opposite direction at time $\tau = 60$ is shown in Fig. 4d, and its spectrum is shown in Fig. 6.

3. DISCUSSION

In this study, we formulated the model that describe both (i) the steepening of Alfvén wave profile that leads to the wave transportation to the short-wavelength region of spectrum and (ii) the excitation of backward-propagating waves due to a decaylike instability. Results of this investigation may be related to some problems of solar-wind physics.

It is a conventional point of view that outward-propagating waves are excited by impulsive reconnection events that release the free energy of closed magnetic loops in to the chromosphere [24]. Because the outward-propagating Alfvén waves are exact solutions of MHD equations, in an incompressible MHD no spec-
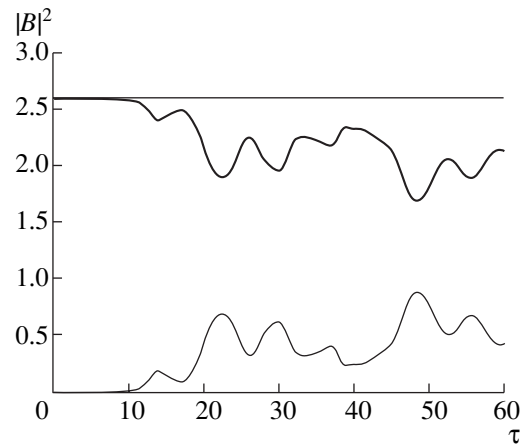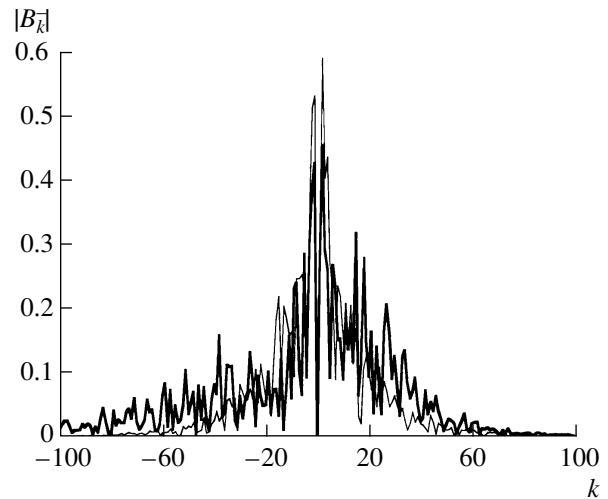

Fig. 3. The nonlinear dynamics of the wave energy density in forward- (thick curve) and backward-propagating (thin curve) wave packets. The horizontal line is an integral of Eqs. (8)–(10).
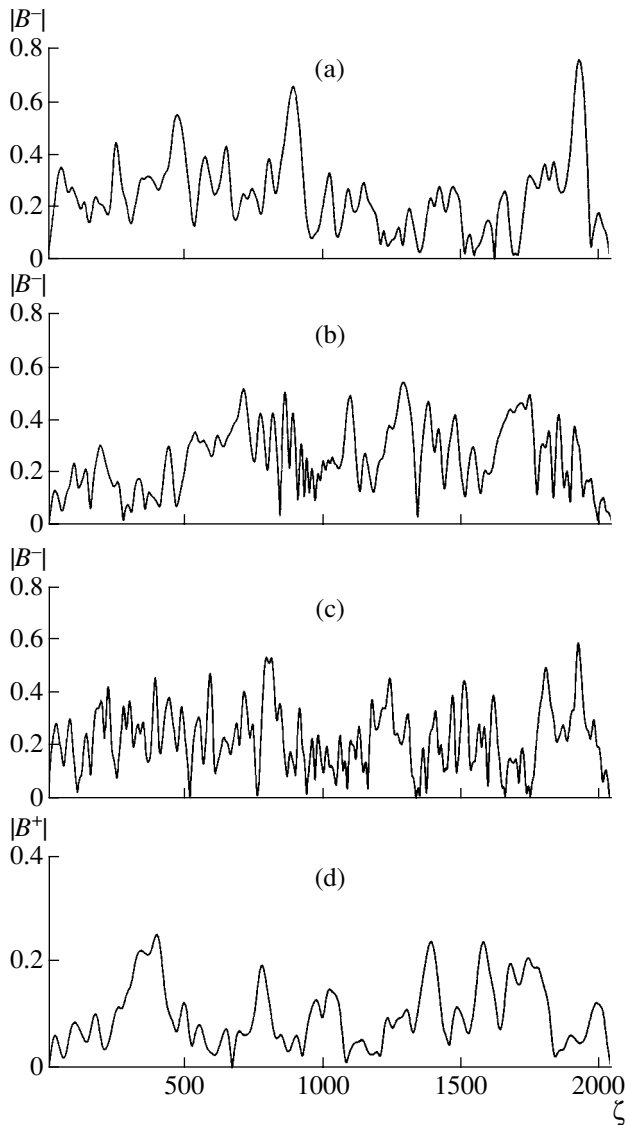
Fig. 4. The wave profiles B^- of forward-propagating fluctuations at times τ = (a) 0, (b) 1, and (c) 60. Panel (d) shows the wave profile B^+ of the backward-propagating Alfvén fluctuations that were generated due to the parametric instability of the B^- packet.

Fig. 5. The spectra of the forward-propagating wave packet at times $\tau = 0$ (thin curve) and $\tau = 60$ (thick curve). The excitation of higher harmonics takes place due to the nonlinear coupling of harmonics in the B^- packet.
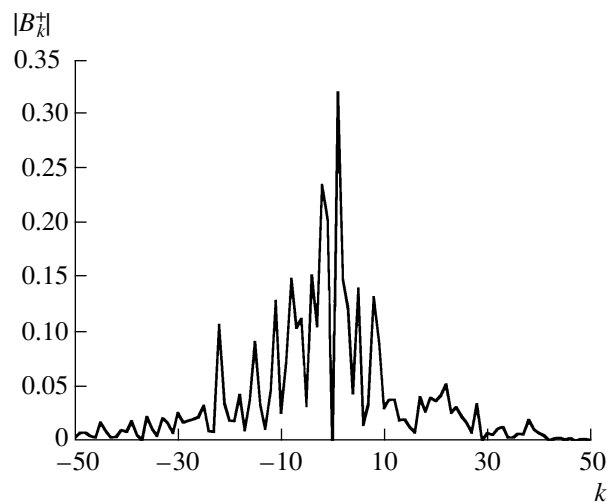
Fig. 6. The spectrum of the backward-propagating Alfvén fluctuations that were created due to a decaylike parametric interaction at time $\tau = 60$.

tral evolution should occur, so the existence of inward-propagating Alfvén waves is crucial for incompressible MHD turbulence models of the solar wind (see [25, 26]). At the same time, the nature of inward-propagating Alfvénic turbulence is still not well understood. Analysis of observational data [27, 28] brought additional evidence of the existence of inward-propagating Alfvénic fluctuations and suggested an interdependence of the inward- and outward-propagating waves.

Because the WKB theory fails to predict the presence of any inward-propagating fluctuations in the expanding solar wind, the so-called mixing mechanism of the generation of inward-propagating waves was proposed [29, 30] (see also reviews [25, 26] and references therein). The mixing mechanism is a leading order non-WKB effect associated with reflection from density gradients; it disappears in a WKB approximation.

Another scenario is connected with the velocity shear between fast and slow solar-wind streams. The velocity-shear instability leads to the generation of both outward- and inward-propagating large-scale Alfvén waves (see [25] and references therein).

Our model describes a possible generation mechanism of inward-propagating Alfvén waves by outward-propagating fluctuations that works even in homoge-

neous conditions. Taking into account the solar-wind parameters, it is needed to construct the similar model for isothermal ($T_e \approx T_p$) plasma, when parametric decay interaction is just the induced scattering of waves on plasma particles. We plan to conduct this study in the future.

ACKNOWLEDGMENTS

REFERENCES

1. R. Z. Sagdeev and A. A. Galeev, *Nonlinear Plasma Theory*, Ed. by T. O'Neil and D. Book (Benjamin, New York, 1969), p. 8.

2. J. V. Hollweg, J. Geophys. Res. **76**, 5155 (1971).

3. J. V. Hollweg, J. Geophys. Res. **99**, 23431 (1994).

4. R. H. Cohen and R. L. Dewar, J. Geophys. Res. **79**, 4174 (1974).

5. C. N. Lashmore-Davies, Phys. Fluids **19**, 587 (1976).

6. J. A. Ionson and R. S. B. Ong, Plasma Phys. **18**, 809 (1976).

7. M. L. Goldstein, Astrophys. J. **219**, 700 (1978).

8. N. F. Derby, Jr., Astrophys. J. **224**, 1013 (1978).

9. J. Sakai and B. U. O. Sonnerup, J. Geophys. Res. **88**, 9069 (1983).

10. H. K. Wong and M. L. Goldstein, J. Geophys. Res. **91**, 5617 (1986).

11. T. Terasawa, M. Hoshino, J. Sakai, and T. Hada, J. Geophys. Res. **91**, 4171 (1986).

12. V. Jayanti and J. Hollweg, J. Geophys. Res. **98**, 19049 (1993).

13. F. Malara and M. Velli, Phys. Plasmas **3**, 4427 (1996).

14. A. Rogister, Phys. Fluids **14**, 2733 (1971).

15. R. H. Cohen and R. M. Kulsrud, Phys. Fluids **17**, 2215 (1974).

16. E. Mjolhus, J. Plasma Phys. **16**, 321 (1976).

17. K. Mio, T. Ogino, K. Minami, and S. Takeda, J. Phys. Soc. Jpn. **41**, 265 (1976).

18. S. R. Spangler and J. P. Sheerin, J. Plasma Phys. **27**, 193 (1982).

19. P. K. Shukla and L. Stenflo, Phys. Rev. A **30**, 2110 (1984).

20. S. Ghosh and K. Papadopoulos, Phys. Fluids **30**, 1371 (1987).

21. C. F. Kennel, B. Buti, T. Hada, and R. Pellat, Phys. Fluids **31**, 1949 (1988).

22. A. A. Vedenov and L. I. Rudakov, Dokl. Akad. Nauk SSSR **159**, 767 (1964) [Sov. Phys. Dokl. **9**, 1073 (1964)].

23. A. A. Galeev and R. Z. Sagdeev, in *Reviews of Plasma Physics*, Ed. by M. A. Leontovich (Gosatomizdat, Moscow, 1973; Consultants Bureau, New York, 1979), Vol. 7.

24. W. I. Axford and J. F. McKenzie, *Cosmic Winds and the Heliosphere*, Ed. by J. R. Jokipii, C. P. Sonett, and M. S. Giampapa (Arizona Univ., Tuscon, 1977), p. 243.

25. M. L. Goldstein, D. A. Roberts, and W. H. Matthaeus, Annu. Rev. Astron. Astrophys. **33**, 283 (1995).

26. C.-Y. Tu and E. Marsch, Space Sci. Rev. **73**, 1 (1995).

27. R. Grippin, A. Mangeney, and E. Marsch, J. Geophys. Res. **95**, 8197 (1990).

28. R. Bruno, B. Bavassano, E. Pietropaolo, V. Carbone, and H. Rosenbauer, J. Geophys. Res. **102**, 14687 (1997).

29. M. Heinemann and S. Olbert, J. Geophys. Res. **85**, 1311 (1980).

30. Y. Zhou and W. H. Matthaeus, J. Geophys. Res. **95**, 10291 (1990).

NONLINEAR PHENOMENA

Excitation of Inertial Alfvén Waves Via Modulational Interaction with Lower Hybrid Waves[1]

V. D. Shapiro*, D. Üçer*, and K. B. Quest**

* Physics Department, University of California, San Diego, La Jolla, CA 92037, USA
e-mail: vshapiro@physics.ucsd.edu, ducer@physics.ucsd.edu
** ECE Department, University of California, San Diego, La Jolla, CA 92037, USA
e-mail: quest@ece.ucsd.edu
Received October 24, 2002

Abstract—The concept of modulational instability, which results from the coupling of waves modes of very different time and space scales, was introduced to plasma physics through an elegant paper by Vedenov and Rudakov in 1964 [1]. Our paper is devoted to the theory of modulational instability resulting from the interaction of lower hybrid waves and slow density perturbations associated with inertial Alfvén waves. The nonlinear set of equations describing the modulational coupling of these two types of waves is constructed. The lower hybrid wave trajectories are analyzed within predefined density structures and it is shown that these waves can be trapped in the vicinity of the density extremum. The density modulations, originally being associated with inertial Alfvén waves, deepen due to the trapping of lower hybrid waves; this leads to modulational instability. A dispersion relation describing the modulational instability is constructed and analyzed. The threshold intensity of the lower hybrid waves for the onset of instability is obtained and it is shown that instability can serve as an efficient mechanism for the excitation of inertial Alfvén waves in the auroral ionosphere. © 2003 MAIK "Nauka/Interperiodica".

1. INTRODUCTION

Lower hybrid waves (LHWs) play a significant role in many areas of space physics. These waves are usually excited by a modified two-stream instability. This type of instability is driven by the relative motion of the different plasma components at an angle to the magnetic field and plays a key role in many space-physics problems. These problems include the following: counterstreaming ions in the flow of the solar wind reflected from Earth's bowshock [2]; mixed plasma populations, such as solar wind and planetary ions at the boundaries of the ionospheres of the nonmagnetic planets Mars and Venus [3]; and mass loading of the solar wind with newly born cometary photoions in the problem of solar wind/cometary interaction [4]. The important feature of the LHWs is their ability to couple light fast electrons and slow heavy ions in the resonant wave–particle interaction (e.g., [5, 6]). This is because the frequency of the lower hybrid waves is between the electron and ion gyrofrequencies. Electrons are strongly magnetized in these waves. They mainly have uniform motion along the magnetic-field lines. If the velocity of the uniform motion of electrons coincides with the parallel phase velocity of the wave, an electron stays in phase resonance with the wave for a longer time. The electron then acquires energy from the wave or gives energy to it. This is the so-called Landau wave-particle resonance

$$\omega = k_\parallel v_\parallel, \qquad (1)$$

where ω is the wave frequency and $k_\parallel$ and $v_\parallel$ are field-aligned components of wave vector and electron velocity.

At the same time, ions do not feel the presence of the magnetic field, because the frequency of their Larmor rotation is much less than the wave frequency. LHWs have wave vectors almost perpendicular to the field lines ($k_\perp \gg k_\parallel$), and they can be considered almost electrostatic ($\mathbf{E} \sim -\nabla\varphi$). As a result of this, unmagnetized ions oscillate across the magnetic-field lines under the action of the main component of the transverse electric field, and therefore the wave–particle resonance condition for ions has the form:

$$\omega = \mathbf{k}_\perp \cdot \mathbf{v}_\perp. \qquad (2)$$

By comparing resonance conditions (1) and (2), and taking into account that $k_\perp \gg k_\parallel$, it is easy to see that the lower hybrid waves can be in simultaneous phase resonance with both slow unmagnetized ions and fast magnetized electrons. The energy is transferred from one plasma component to the other. In many cases, the free-energy source is the heavy ion component, e.g., the protons of solar wind interacting with comets or the reflected protons at the Earth's bowshock. On the other hand, in the auroral ionosphere, the energy source for the excitation of LHWs is the energetic precipitated electrons. In this case, the absorption of LHWs results in an efficient ion energization across the magnetic field, which is called the transverse acceleration of ions

---

[1] This article was submitted by the authors in English.

(TAI). This mechanism is responsible for the injection of heavy ions of ionospheric origin into the Earth's magnetosphere (e.g., energetic O$^+$ ions) [7].

One of the significant outcomes of rocket and satellite observations made in the auroral atmosphere is the detection of localized density depletions filled with electrostatic waves in the lower hybrid frequency range [8–10]. These structures are called spikelets, lower hybrid cavities, and lower hybrid solitary structures (LHSSs) by different authors. We are going to adopt the acronym LHSSs in this paper. It is also argued that the ion acceleration events (TAIs) are closely associated with these localized wave events (LHSSs) [11]. This idea makes understanding the mechanisms behind the formation of these structures even more appealing.

One of the mechanisms, which has been considered responsible for the formation of LHSSs, is the modulational interaction of lower hybrid waves with slow background density perturbations associated with ion-acoustic waves. The physics of this mechanism is similar to the instability resulting from the modulational interaction of short-wavelength and high-frequency plasma waves and smooth and slow density perturbations, which was proposed by Vedenov and Rudakov [1]. This type of instability has been investigated in detail and widely accepted in theoretical plasma physics [12]. The modulational interaction is initiated by the ponderomotive forces created by finite-amplitude high-frequency waves in plasma. These forces result in plasma modulation with a very low frequency. The density holes associated with the modulation act as potential wells, which are effective in trapping the high-frequency mode. The trapped modes are enhanced, which results in a further deepening of the density holes by the ponderomotive force, leading to the modulational instability.

This phenomenon is quite interesting because it demonstrates the fact that the interaction of different wave modes with very different time and space scales can lead to formation of localized structures in plasma. However, for some technical reasons, modulational interaction had not been directly observed in laboratory plasma. This is why the auroral observations, which, in our point of view, can be evidence for the modulational interaction between LHWs and low-frequency density modulations, are very important.

The modulational interaction of LHWs with slow background density fluctuations associated with ion-acoustic waves is considered in a number of references (see, e.g., [13, 14]). As explained above, this interaction leads to the creation of field-aligned structures that are strongly localized in the direction perpendicular to the ambient magnetic field (LHSS). It is also shown that the evolution of modulational instability leads to the compression of cavities. At this stage, which is called the collapse, the LH wave energy cascades to smaller and smaller scales. Finally, at the final stage of collapse, the scales are small enough for wave–particle reso-

Typical ionospheric parameters at altitudes ~1700 km

Ambient magnetic field, B_0	0.3 G
Electron temperature, T_e	3000 K
Ion temperature, T_i	2400 K
Average plasma density, n_0	10^3 cm^{-3}
Mass ratio, m_i/m_e	2000
Alfvén speed, v_A	1.9×10^9 cm/s
Electron cyclotron frequency, ω_{ce}	4.8×10^6 rad/s
Electron plasma frequency, ω_{pe}	1.7×10^6 rad/s
Ion plasma frequency, ω_{pi}	3.8×10^4 rad/s
Lower hybrid frequency, ω_{lh}	3.6×10^4 rad/s
Lower-hybrid dispersion length, R	19 cm
Electron skin depth, c/ω_{pe}	180 m
$\beta = 8\pi n_0 T/B_0^2$	2×10^{-7}

nance and the wave energy is dissipated, resulting in the energization of ions (TAI).

However, such an interpretation of LHSSs is not widely accepted and has been criticized in some papers. Among them, it is necessary to mention the paper by Pecseli *et al.* [15]. This paper includes a detailed statistical analysis of the properties of the observed structures. In this paper, it is stated that the space and time scales of collapse are not compatible with the observations. In the analysis presented in Pecseli *et al.*, which is based on Freja satellite observations, the transverse scales for the LHSSs change in the interval 40–80 m.

A rough estimation to the transverse scales of the cavities can be made for the model of modulational interaction by balancing the nonlinear term with the dispersion term in the governing equations [14]. This type of approach yields typical size of the order of

$$L_\perp = R\left[\frac{16\pi n_0 R m_e \omega_{ce}^2}{|E_0|^2 m_i \omega_{pe}^2}\right]^{1/2}, \qquad (3)$$

where n_0 is the plasma density; T is the sum of the electron and ion temperatures; $|E_0|^2$ is the square of the LH electric field inside the structure; m_i and m_e are the ion and electron masses; ω_{ce} is the electron cyclotron frequency, ω_{pe} is the electron plasma frequency; and finally, R is the typical scale determining the spatial dispersion of the LH frequency:

$$R^2 = \frac{T_i}{m_i \omega_{lh}^2} + \frac{2}{3}\frac{T_e}{m_e \omega_{ce}^2(1+s)},$$

where $s = \omega_{pe}^2/\omega_{ce}^2$.

The typical parameters of the auroral ionosphere that have been used in estimations made in the paper are presented in the table.

$E(r)$
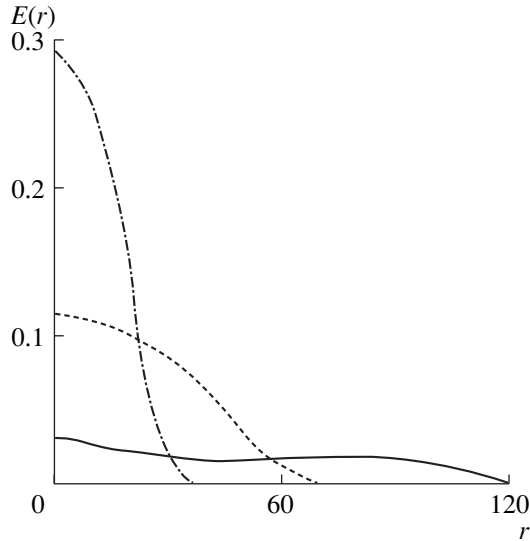
Fig. 1. Evolution of the radial dependence of electric-field amplitude during collapse. Result of the simulations presented in [14]. Dimensionless units are explained in the text.

For the value of $E_0 \sim 50$ mV/m, $L_\perp$ can be estimated as ~ 2 m, which clearly contradicts the observations. However, the numerical simulations presented in paper [14] show that the transverse cavity sizes are much wider than the estimated $L_\perp$. The result of these numerical calculations that is presented in Fig. 1 is directly taken from reference [14]. It can be seen that the transverse cavity size is $r^* \sim 120$ when the electric field in the center of cavity is $E^*(r) \sim 0.1$ in dimensionless units.

The correct dimensionless units for the electric field and distance used in this paper are

$$E^* = E/\sqrt{16\pi n_0 T \frac{m_e \omega_{pe}^2}{m_i \omega_{ce}^2}} \sim \frac{E}{(1 \text{ V/m})}$$

$$\text{and} \quad r^* = \frac{r}{\kappa R} \sim \frac{r}{(0.3 \text{ m})}.$$

The numerical factor $\kappa \sim 1.5$ and $R \sim 0.2$ m. Therefore, the simulations show that for $E_0 = 100$ mV/m, the size of the cavity is ~ 35 m. For a weaker electric field, a wider structure is expected, and these values are in good agreement with the observations.

Another contradiction with the theory, emphasized in Pecseli *et al.* [15], is related to the typical time scale of the evolution of the cavity collapse. The observations show that the structure of the cavities is not deformed during one passage of the satellite, which takes ~ 10 ms. This is why the collapse time should be larger then 10 ms, as discussed in [15]. A characteristic time scale for the formation of cavities similar to (3) can be obtained from the governing equations by balancing the

nonlinear term with the time dependence [14]. This estimations yields

$$t \sim \omega_{lh}^{-1} \frac{m_e}{m_i} \frac{\omega_{ce}^2}{\omega_{pe}^2} \frac{16\pi n_0 T}{|E_0|^2} \sim 1.5 \text{ ms} \quad (4)$$

for the parameters of the table; the electric field at the center of the cavity is taken to be $E_0 = 50$ mV/m. Again it is argued in Pecseli *et al.* that this time is too short for the theory of modulational instability be acceptable. However, the numerical solutions described in Shapiro *et al.* [14] show that the cavity preliminarily needs some time before going into collapse. As a result of this, a typical time of collapse is up to the order of $\sim 700\kappa^2 \omega_{lh}^{-1} \sim 50$ ms (obtained from simulations in [14]). This value is also in reasonable agreement with the observations.

The beam-plasma [5] or fan [16] instabilities due to the fluxes of the precipitated electrons act as permanent sources of excitation of lower hybrid waves in the auroral ionosphere. When such a constant source for the lower hybrid waves is present in the system, the following scenario, which has been discussed in [17], is quite plausible: When the energy of LHWs reaches a certain level, modulational instability evolves and leads to the formation of LHSSs. The formation of these structures is followed by their compression (collapse). The collapse is terminated by dissipation of the LHWs and ion energization (TAI). After one collapse run is completed, the "empty" density structures relax with the speed of sound. During this relaxation, they capture a new portion of waves, and a new collapse run starts. In this scenario, a quasi-stationary set of LHSSs is formed due to the balance between the permanent inflow of energy of LHWs in large scales by the excitation due to fluxes of precipitated electrons and the absorption of the energy in short scales by particle energization.

One characteristic of the observations, which was underlined in [18], is that the cavities are randomly distributed in space. One-dimensional numerical simulations of the modulational instability of a similar problem of Langmuir waves (e.g., [19]) show that the later stages of the instability result in the random distribution of cavities. Therefore, the random distribution of cavities does not contradict the modulational interaction theory. This point was also mentioned in [20]. It is also mentioned in paper [18] that the largest value of the electric field on the satellite path always falls within the region where cavities are observed. This agrees with the idea of the self-consistent creation of LHSSs by waves. The authors conclude from these observations that some nonlinear process is involved. This conclusion is also confirmed by other observations, described by [20], that "deeper cavities tend to have larger electric fields (statistically)."

These conclusions are in contradiction with the alternative explanation for the creation of LHSSs,

which assumes that the density structures acting as traps for LHWs are not created self-consistently via the ponderomotive force of the LHWs but are preexisting in space (see, e.g., [11, 15, 18, 21, 22]). Such a scenario avoids the answers to the questions for what the mechanism is that is responsible for the creation of these density structures and why do they have the field-aligned geometry of the LH ponderomotive force. It is stated in [23] that the longitudinal dimensions of LHSSs are of the order of several kilometers, while their transverse sizes are of the order of hundreds of meters. The typical wave number for LHWs is $k_\perp/k_\parallel \sim \sqrt{m_i/m_e} \sim 50$; this suggests if the density depletions are created by the LH ponderomotive force, the density depletions will be strongly elongated along the field lines with $l_\parallel/l_\perp \sim 50$, which is consistent with observations.

As every density depletion can result in the trapping of lower hybrid waves and, at the same time, observed wave pressures are sufficient for the creation of LHSSs by ponderomotive forces and modulational instability, it is possible that both investigated mechanisms play a competitive role in the formation of LHSSs, which would explain the controversy between some of the observations.

In conclusion, we would like to emphasize the fact that the observational data does not provide any satisfactory evidence to neglect the possibility of the formation of LH solitary structures due to the modulational instability, which is why we think it is worthwhile investigate the related mechanisms further.

There are two types of density modulations observed in the auroral ionosphere. The first type is density modulations produced by low frequency oscillations similar to the ion-acoustic mode; this mode is electrostatic and has been investigated in detail in the references mentioned above. The second type can be identified at observations of Freja satellite.[2] Examination of the Freja data shows that there is evidence of the correlation between the localizations of strong lower hybrid wave activity and the very low frequency magnetic-field oscillations. Figure 1 demonstrates this correlation. The plots are taken from the 1650 Freja orbit, on February 8, 1993 (the summary plots are taken from the referenced websites). The first two panels of Fig. 2a show the electric field measured by two probes of the electric-field instrument F1. The third panel is the standard deviation of the fluctuations of the electric field. The fourth panel is the F4 wave-instrument data; it shows the electric-field spectral density. We can see a strong localization of the electric-field fluctuations with a large amplitude ($\geq$50 mV/m) and frequency (>2 kHz). This frequency is close to the lower hybrid frequency ($f_{lh} \sim 2.5$–6 kHz) in the region. Figure 2b is the data from the magnetometer F2[3] for the same orbit. It is the spectral analysis of the perpendicular magnetic-field

fluctuations. Note that the magnetic-field fluctuations in the frequency range ~10 Hz correlate with the enhanced lower hybrid activity at $UT \simeq 05{:}59$.

The observed deflection of the transverse components of the magnetic field is typical for Alfvén waves. It is reasonable to identify them as short-wavelength kinetic (inertial) Alfvén waves (IAW), since only this type of Alfvén wave is compressional and forms density fluctuations that are able to trap LHWs. At the same time, these perturbations are not the usual type of Alfvén eigenmode: it is a driven collective mode excited by the ponderomotive force created by the fast LHWs. We shall call it the inertial Alfvén mode (IAM). It is important to note that the phase velocity of these driven modes could be different from the Alfvén velocity v_A and therefore the ratio of E/B would also be different from v_A/c.

Since in the low-β plasma of the auroral ionosphere, the phase velocities of these two low-frequency modes (inertial Alfvén and ion acoustic) are very different, we can analyze their interaction with LHWs independently. This paper is only dedicated to the theory of modulational interaction between IAMs and LHWs.

2. VECTOR VERSUS SCALAR NONLINEARITY AS A MECHANISM FOR MODULATIONAL COUPLING

Below, we shall describe how density structures can trap the LHWs. The density structures have much lower typical frequencies than LHWs. Therefore we can assume that wave evolution develops on the background of the quasi-stationary density profile. Electrons are magnetized in the lower hybrid oscillations, as the wave frequency $\omega \ll \omega_{ce}$, where ω_{ce} is the electron gyrofrequency. If the ambient magnetic field is assumed to be in the z direction, the velocity of the electron motion across the magnetic field can be written as

$$\mathbf{v}_{e\perp} = -\frac{c}{B_0}(\nabla\varphi \times \hat{\mathbf{z}}) - i\frac{\omega}{\omega_{ce}}\frac{c}{B_0}\nabla_\perp\varphi. \qquad (5)$$

Here, φ is the electric potential of the wave. LHWs are considered to be almost electrostatic. The first term on the r.h.s is the usual $\mathbf{E} \times \mathbf{B}$ drift. The second term is a small ($\sim\omega/\omega_{ce}$) correction determining the polarization drift due to the time variation in the electric field.

The perturbation of electron density in the lower hybrid wave is determined by the continuity relation
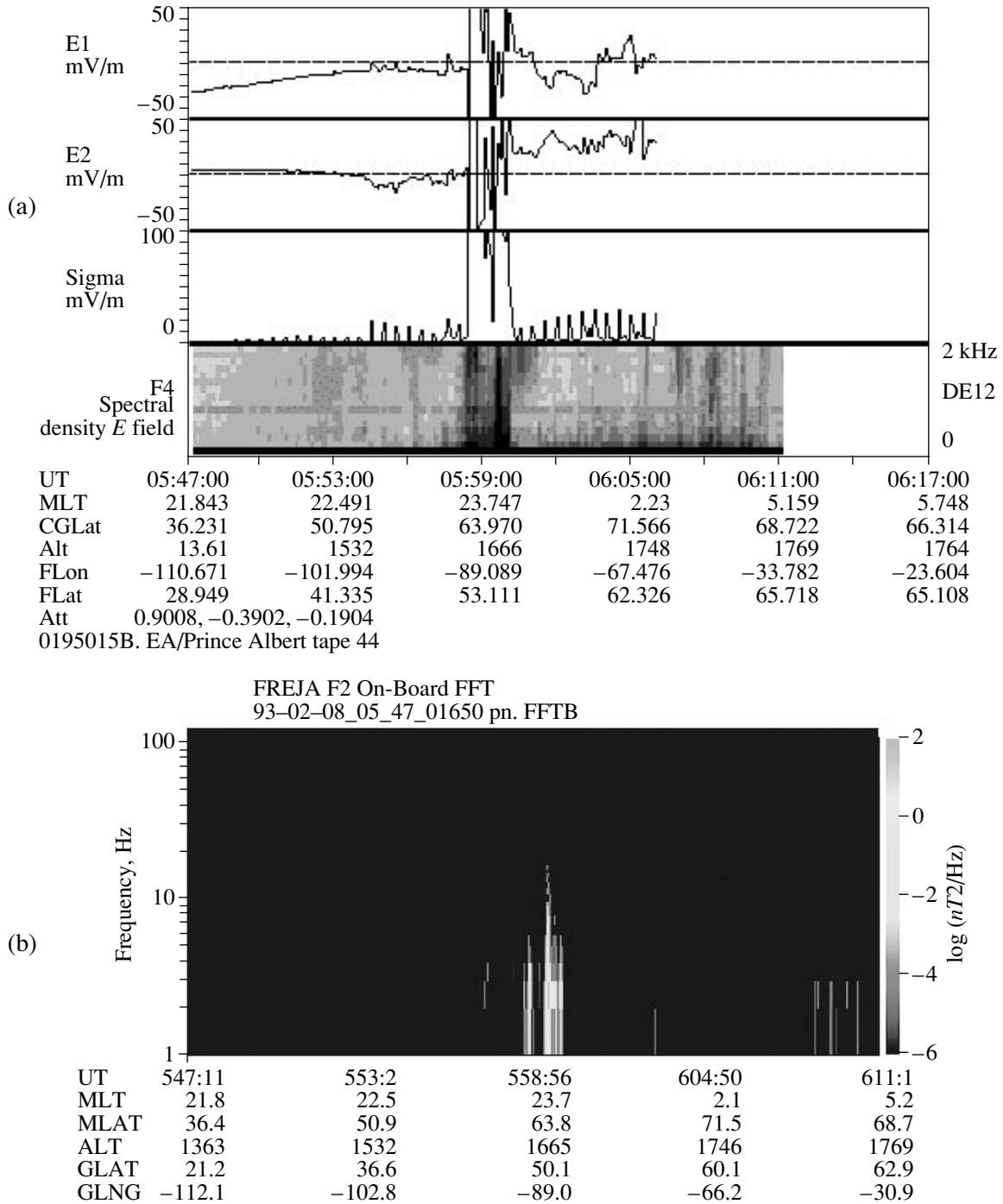
$$n_e' = \frac{1}{i\omega}[(n_0 + \delta n)\nabla \cdot \mathbf{v}_e + \mathbf{v}_e \cdot \nabla\delta n]. \qquad (6)$$

Here, $n = n_0 + \delta n(\mathbf{r})$ is the quasi-stationary density profile of the background across which the wave is propagating. Since the first term in the electron velocity (5) is the $\mathbf{E} \times \mathbf{B}$ drift and it corresponds to an incompressible flow ($\nabla \cdot \mathbf{v} = 0$), density perturbations can occur only if the wave is propagating in an inhomogeneous density

Fig. 2. Freja satellite data from orbit 1650, on February 8, 1993: (a) the localization of electric field fluctuations with frequencies >2 kHz; (b) the magnetic field fluctuation with low frequency (~10 Hz) in correlation with localizations of electric field around *UT* ≃ 05:59.

background (the second term in the r.h.s of Eq. (6)). On the other hand, the last term in Eq. (5) is the compressible part of electron motion ($\nabla \cdot \mathbf{v} \neq 0$), which contributes to the first term in the r.h.s of Eq. (6). Finally, the density perturbation takes the following form:

$$n_e' = -\frac{c}{i\omega B_0}\left[\frac{i\omega}{\omega_{ce}}(n_0 + \delta n)\nabla_\perp^2 \varphi + (\nabla\varphi \times \hat{\mathbf{z}}) \cdot \nabla\delta n\right]. \quad (7)$$

The first nonlinear term in Eq. (7) is smaller by a factor ω/ω_{ce}. Therefore, last term can be dominant even if the

scale of the density inhomogeneity exceeds the lower hybrid wavelength.

Ions are unmagnetized in the lower hybrid oscillations because their gyrofrequency is much lower than the wave frequency, and the Lorentz force in the equations of motion is not important. Their velocity and density can be written as

$$\mathbf{v}_i = \frac{e}{im_i\omega}\nabla\varphi, \tag{8}$$

$$n_i' = -\frac{e(n_0 + \delta n)}{m_i\omega^2}\nabla^2\varphi. \tag{9}$$

We will consider the WKB-type lower hybrid wave propagating in the inhomogeneous density background such that $\varphi \sim \exp[i(\int \mathbf{k}\cdot\mathbf{r} - \omega t)]$. By combining Poisson's equation and Eqs. (6) and (9) for the electron and ion densities, the following relation is derived for the LHW frequency:

$$\omega = \omega_{lh}\left[1 + \frac{3}{2}k^2R^2 + \frac{\delta n}{2n_0(1+s)}\right.$$
$$\left. - \frac{\omega_{lh}}{\omega_{ce}}\frac{m_i}{m_e}\frac{1}{2k^2}(\mathbf{k}\times\nabla\delta n/n_0)_z\right], \tag{10}$$

where $\omega_{lh} = \omega_{pi}/\sqrt{1+s}$ is the lower hybrid frequency, and $s = \omega_{pe}^2/\omega_{ce}^2$. The dispersive correction to the lower hybrid frequency is taken from reference [14]. There are two corrections to the lower hybrid frequency originating from the density modulation $\delta n/n_0$. The first one is of the scalar type ($\propto \delta n$), and has a transparent meaning: the frequency of a wave that is trapped inside the density well decreases in comparison with the frequency of a freely moving wave quantum. The second correction is of the vector type. It vanishes when the wave propagates parallel to the direction of the density gradient. The second correction is larger than the scalar-type correction by a factor of $\omega_{ce}/\omega_{lh} \sim 100$. Therefore, we consider the effect of vector nonlinearity as the dominant nonlinearity effect in the following analysis. Taking the periodicity in the azimuthal direction into account, the wave potential for LHWs can be written as

$$\varphi = \varphi(r)e^{i\mu\theta}, \tag{11}$$

where μ is an integer. For such geometry, the nonlinear and dispersive corrections to the frequency of LHWs can be rewritten as the following:

$$\delta\omega = \omega - \omega_{lh} = \omega_{lh}\left[\frac{3}{2}k^2R^2 + \frac{\omega_{lh}}{\omega_{ce}}\frac{m_i}{m_e}\frac{1}{2k^2}\frac{\mu}{r}\frac{d}{dr}\frac{\delta n}{n_0}\right]. \tag{12}$$

The rocket observations [24] show that there is a phase shift, which was measured by two antennas positioned at two different polar angles around the axis along the ambient magnetic field. The sign of the phase shift indi-

cates the direction of rotation of the wave mode. If this phase shift corresponds to right-hand polarization ($\mu > 0$), the frequency of the signal inside the density depletion ($d\delta n/dr > 0$) is above ω_{lh}, and if the phase shift corresponds to $\mu < 0$, then the wave frequency $\omega < \omega_{lh}$. In the calculations, we took into account that the dispersion term is much smaller than the nonlinear term for relevant parameters, and therefore the nonlinear term determines the sign of $\delta\omega$. Consequently, it is possible to observe both right-handed waves above the lower hybrid frequency and left-handed waves below the lower hybrid frequency inside density depletions. This is consistent with observations [24–26].

Hamiltonian equations of motion for wave quanta can be used to demonstrate how the trapping by the density structures occurs:

$$\frac{d\mathbf{k}}{dt} = -\nabla\omega, \quad \frac{d\mathbf{r}}{dt} = \frac{\partial\omega}{\partial\mathbf{k}}. \tag{13}$$

Let us consider the density structure to be a Gaussian function that is consistent with the observations [20]:

$$\delta n = n_m\exp[-r^2/a^2],$$

where n_m is the value at the density extremum and a is the width of the Gaussian. When we substitute the predicted profile for the density, the dimensionless expression for frequency (10) takes the form

$$\bar{\omega} = 1 + \frac{1}{2}\alpha\bar{k}^2 - \beta\frac{n_m}{n_0}\frac{\mu}{\bar{k}^2}e^{-\bar{r}^2}, \tag{14}$$

where the dimensionless parameters are introduced as the following:

$$\bar{\omega} = \omega/\omega_{lh}, \quad \bar{k} = ka, \quad \bar{r} = r/a,$$

$$\beta = \frac{\omega_{lh}}{\omega_{ce}}\frac{m_i}{m_e}, \quad \alpha = 3\frac{R^2}{a^2}.$$

The following equations can be obtained from the LHW dispersion relation for the predicted Gaussian density structure (the bars are omitted for simplicity):

$$\dot{r} = \alpha k_r + 2k_r\beta\frac{\mu}{k^4}\frac{n_m}{n_0}e^{-r^2}, \tag{15}$$

$$\dot{k_r} = \alpha\frac{\mu^2}{r^3} - 2\beta\frac{\mu r}{k^4}\frac{n_m}{n_0}e^{-r^2}\left[k_r^2 + \frac{\mu}{r^2}\left(1 - \frac{1}{r^2}\right)\right]. \tag{16}$$

These equations determine the trajectory of the wave packet that is localized in r and has a periodic profile in the azimuthal direction. Theoretically, LHWs can not exist below ω_{lh} without the existence of density depletions, as can be seen from Eq. (12). Therefore, for $\omega < \omega_{lh}$, only trapped modes are possible with $\mu < 0$ (clockwise rotation). These modes decay out of the cavity. For $\omega > \omega_{lh}$, the modes that exist within the density cavity can also exist outside. Therefore, we expect the
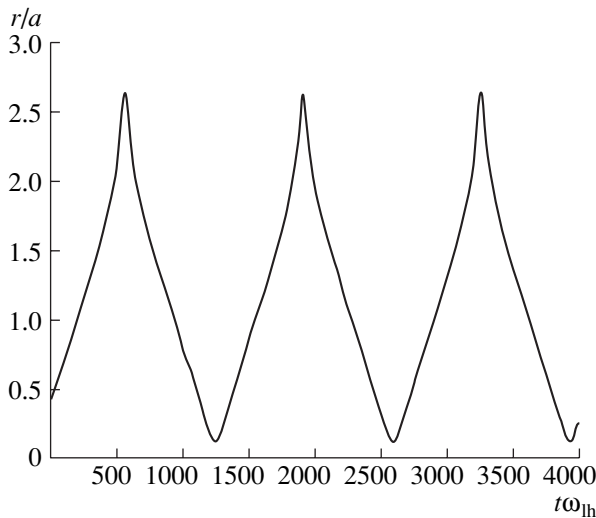
Fig. 3. Radial trajectory of the wave quantum with $\mu = -1$ inside a density depletion.

LHWs with $\omega > \omega_{lh}$ to pass through the depletions. However, solving the equations of motion for r and k_r, we find that in sufficiently deep depletions, bounded trajectories exist for modes having frequencies both above and below ω_{lh} depending on the initial condition. Figure 3 shows the oscillations in the radial position of the wave quantum in time for $\mu = -1$ and $n_m/n_0 = -5\%$; the initial position of wave quantum is at $r(0)/a = 0.4$. The wave quantum is trapped for $\mu < 0$, as expected. If we solve the equations of motion for $\mu > 0$ for the same initial conditions and density structure, we obtain an unbounded trajectory, corresponding to a monotonic change of the radial position. However for a slightly deeper density well, the wave quantum with $\mu > 0$ is also trapped.

In the theory of modulational instability, the density structures that trap the LHWs are created by the Reynold's stresses exerted on the background plasma by the LHWs. The main driver is the longitudinal component of the lower hybrid Reynold's stress:

$$(F_{\text{wave}})_z = -m_e \langle (\mathbf{v}_e \cdot \nabla) v_{ez} \rangle, \qquad (17)$$

where the brackets denote averaging over the fast time dependence. After taking the average, the remaining terms will be as follows:

$$F_{\text{wave}} = -\frac{\partial P_{\text{wave}}}{\partial z} = -\frac{m_e}{4}(\mathbf{v}_e^* \cdot \nabla v_{ez} + \mathbf{v}_e \cdot \nabla v_{ez}^*). \ (18)$$

In the case of scalar nonlinearity, the last term in expression (5), which is the velocity component along the wave electric field, is important. The electron velocity in the magnetic-field direction can be written as

$$v_{ez} = -\frac{e}{im_e\omega_{lh}}\frac{\partial \varphi}{\partial z}, \qquad (19)$$

which yields the wave pressure acting on plasma electrons as

$$P_{\text{wave}} = \frac{e^2}{4m_e\omega_{ce}^2}|\nabla\varphi|^2. \qquad (20)$$

In the case of vector nonlinearity, the first term on the r.h.s of Eq. (5) is important. This term corresponds to $\mathbf{E} \times \mathbf{B}$ drift of electrons. Here, the expression for the longitudinal component of the lower hybrid Reynold's stress will be

$$F_{\text{wave}} = -\frac{\partial P_{\text{wave}}}{\partial z} = m_e \langle (\mathbf{v}_{\mathbf{E}\times\mathbf{B}}) \cdot \nabla v_{ez} \rangle, \qquad (21)$$

which gives the wave pressure acting on plasma electrons

$$P_{\text{wave}} = -\frac{1}{16\pi i n_0}\frac{\omega_{pe}^2}{\omega_{lh}\omega_{ce}}(\nabla\varphi^* \times \nabla\varphi)_z. \qquad (22)$$

By comparing Eqs. (20) and (22), it is easy to see that the wave pressure arising from the scalar-type nonlinearity is smaller by a factor of $\omega_{lh}/\omega_{ce} \sim 10^{-2}$. This result shows that the modulational coupling between LHWs and the low frequency density perturbations is much stronger in the case of vector nonlinearity. This was first demonstrated in [27].

Taking into account the periodicity in the azimuthal direction (11), expression (22) can be written as

$$P_{\text{wave}} = -\frac{1}{16\pi n_0}\frac{\omega_{pe}^2}{\omega_{lh}\omega_{ce}}\frac{\mu}{r}\frac{d}{dr}|\varphi(r)|^2. \qquad (23)$$

Analyzing this equation, we assume that the wave potential is maximum in the center of the localization. As it was observed by Bonnell *et al.* [24], most LHSSs show enhancement in the wave power at frequencies above the lower hybrid cut-off one. This corresponds to right-handed wave rotation and positive wave pressure, which lead to density depletions. This is the indication that the ponderomotive forces created by the LHWs act in the desired direction; this can lead to the formation of LHSSs with density depletion at the center. In the opposite case, when the enhancement of the wave power occurs at the frequencies below the lower hybrid cut-off, the negative wave pressure leads to the formation of density humps.

3. SYSTEM OF EQUATIONS FOR MODULATIONAL INTERACTION

We now consider only the vector nonlinearity that couples LHWs with the extremely low frequency density fluctuations. The equation for the lower hybrid electric potential $\varphi(t, \mathbf{r})$ that develops in a background of very slow density perturbations, was obtained in [6]. The quickly oscillating phase and slowly varying enve-

lope amplitude of the lower hybrid potential can be separated as

$$\varphi(t, \mathbf{r}) = \frac{1}{2}\varphi(t, \mathbf{r})\exp(-i\omega_{lh}t) + \text{c.c.}, \qquad (24)$$

$$\mathbf{E} = -\nabla\varphi, \qquad (25)$$

and the equation for envelope amplitude can be written as

$$-\frac{2i}{\omega_{lh}}\frac{\partial}{\partial t}\nabla_\perp^2\varphi - 3R^2\nabla_\perp^4\varphi + \frac{m_i}{m_e}\frac{\partial^2\varphi}{\partial z^2} + \frac{\omega_{pe}^2}{c^2}\varphi$$
$$= -\frac{\omega_{lh}}{in_0\omega_{ce}}\frac{m_i}{m_e}(\nabla\varphi \times \nabla\delta n)_z. \qquad (26)$$

Here, we used the vector-type nonlinear correction to the wave frequency, as it was obtained in Eq. (10). The last three terms on the l.h.s of Eq. (26) determine different corrections to the lower hybrid frequency: due to the thermal particle motion; due to the deviation from a strictly transverse wave propagation; and, finally, due to the electromagnetic correction. The term on the r.h.s. describes the nonlinear coupling between the LHWs with the slow density perturbations.

As mentioned earlier in the introduction, there are two types of low-frequency oscillations that can drive this density modulation: the ion-acoustic waves or the inertial Alfvén modes (IAMs). In this paper, we assume that the density modulations are only due to the IAMs. Because of the large difference between the phase velocity of the IAMs and the ion-acoustic waves $v_A/\sqrt{T_e/m_i} \sim 1/\sqrt{\beta} \sim 10^3$ for typical ionospheric conditions, their interaction with the LHWs can be considered separately.

The IAM is created from an oblique shear Alfvén wave with $k_\perp \gg k_\parallel$. The frequency of the wave is such that $\omega \ll \omega_{ci} \ll \omega_{ce}$; hence, the electrons and ions are both magnetized. In the consideration of an ionospheric plasma with $\beta \ll m_e/m_i$, the finite electron inertia in the longitudinal direction leads to the following frequency dispersion:

$$\omega = \frac{k_\parallel v_A}{\sqrt{1 + k_\perp^2 c^2/\omega_{pe}^2}}. \qquad (27)$$

The magnetic field in the z direction remains constant, while the transverse components of the magnetic field can be expressed through the mode vector potential as

$$B_x = \frac{\partial A}{\partial y}, \quad B_y = -\frac{\partial A}{\partial x}. \qquad (28)$$

The electric field associated with the wave is

$$E_x = -\frac{\partial\psi}{\partial x}, \quad E_y = -\frac{\partial\psi}{\partial y}, \quad E_z = -\frac{\partial\psi}{\partial z} - \frac{1}{c}\frac{\partial A}{\partial t}. \quad (29)$$

The equations governing the effect of LHWs on IAMs are obtained considering the IAMs as quasi-neutral.

The ion density perturbations will arise from compressible ion motion following the transverse electric field. The electron density perturbations are mainly due to the electron motion along the magnetic field:

$$\frac{\partial\delta n_i}{\partial t} - n_0\frac{c^2 m_i}{eB_0^2}\frac{\partial}{\partial t}\nabla_\perp^2\psi = 0, \qquad (30)$$

$$\frac{\partial\delta n_e}{\partial t} + n_0\frac{\partial v_{ez}}{\partial z} = 0. \qquad (31)$$

We use the longitudinal component of Ampère's law to derive the field dependence of the longitudinal electron motion. With the help of Eq. (28), we obtain the following relation:

$$\nabla_\perp^2 A = \frac{4\pi e n_0}{c}v_{ez}. \qquad (32)$$

Since the IAMs are quasi-neutral, $\delta n_e = \delta n_i = \delta n$, combining Eqs. (30), (31), and (32), we express the relationship between scalar and vector potentials in IAMs as

$$\frac{\partial\psi}{\partial t} = -\frac{v_A^2}{c}\frac{\partial A_z}{\partial z}. \qquad (33)$$

Thus, the density perturbations in IAMs can be rewritten as

$$\frac{\partial}{\partial t}\frac{\delta n}{n_0} = -\frac{c}{4\pi e n_0}\frac{\partial}{\partial z}\nabla_\perp^2 A. \qquad (34)$$

As noted previously, the electron motion along the ambient magnetic field $\mathbf{B}_0$ is affected by the Reynold's stresses. When the high-frequency waves that create the Reynold's stress are LHWs, the wave pressure is not isotropic, as seen in Eq. (17). Instead, the longitudinal component of the Reynold's stress results in a field-aligned shear flow described by

$$\frac{\partial v_{ez}}{\partial t} = -\frac{e}{m_e}E_z - \langle\mathbf{v}_{\mathbf{E}\times\mathbf{B}} \cdot \nabla v_{ez}\rangle. \qquad (35)$$

Differentiating this equation with respect to y and combining it with Eq. (32), the relationship for the longitudinal component of the electric field is

$$\frac{\partial E_z}{\partial y} = -\frac{c}{\omega_{pe}^2}\nabla_\perp^2\frac{\partial B_x}{\partial t} - \frac{m_e}{e}\frac{\partial}{\partial y}\langle\mathbf{v}_{\mathbf{E}\times\mathbf{B}} \cdot \nabla v_{ez}\rangle. \qquad (36)$$

We can then obtain a relation for E_y via the transverse component of Ampère's law:

$$\frac{\partial B_x}{\partial z} = -\frac{4\pi e}{c}\langle n_e' v_{ey}\rangle + \frac{4\pi n_0 m_i c}{B_0^2}\frac{\partial E_y}{\partial t}, \qquad (37)$$

where the first term on the r.h.s is a nonlinear electron current forced on the plasma by lower hybrid oscilla-

tions. Induction law in the x direction will relate the y and z components of the electric field such that

$$\frac{\partial E_z}{\partial y} - \frac{\partial E_y}{\partial z} = -\frac{1}{c}\frac{\partial B_x}{\partial t}. \tag{38}$$

Differentiating this equation once with respect to time and using Eqs. (36) and (37) yields the final nonlinear equation

$$\frac{\partial^2}{\partial t^2}\left(1 - \frac{c^2}{\omega_{pe}^2}\nabla_\perp^2\right)B_x - v_A^2\frac{\partial^2 B_x}{\partial z^2}$$

$$= \omega_{ci}B_0\frac{\partial}{\partial z}\left\langle\frac{n_e'}{n_0}v_{ey}\right\rangle + \frac{m_e c}{e}\frac{\partial^2}{\partial t\partial y}\langle\mathbf{v}_{\mathbf{E}\times\mathbf{B}}\cdot\nabla v_{ez}\rangle. \tag{39}$$

The nonlinear current is evaluated in terms of the LH electron density fluctuations and transverse electron velocity:

$$n_e' = -n_0\frac{m_e c^2}{eB_0^2}\nabla_\perp^2\varphi, \quad v_{ye} = \frac{c}{B_0}\frac{\partial\varphi}{\partial x}. \tag{40}$$

The Reynold's stress was already obtained in Eqs. (21) and (22). Substituting these and (40) into the r.h.s of equation (39), we obtain

$$\text{r.h.s} = \frac{c^2}{4B_0}\frac{\partial}{\partial z}\left[-\frac{m_e}{m_i}\left(\frac{\partial\varphi^*}{\partial x}\nabla_\perp^2\varphi + \text{c.c.}\right)\right.$$

$$\left. + \frac{i}{\omega_{lh}}\frac{\partial^2}{\partial t\partial y}(\nabla\varphi^*\times\nabla\varphi)\right]. \tag{41}$$

Comparing the two nonlinear terms of Eq. (41), we note that the first term describing the nonlinear current is small with respect to the second term, which describes the Reynold's stresses by the factor $m_e\omega_{lh}/m_i\omega_A$, where ω_A is the frequency of the Alfvén mode. Neglecting the first term in Eq. (41), we can rewrite Eq. (39) in terms of the vector potential as

$$\frac{\partial^2}{\partial t^2}\left(1 - \frac{c^2}{\omega_{pe}^2}\nabla_\perp^2\right)A - v_A^2\frac{\partial^2 A}{\partial z^2}$$

$$= \frac{ic^2}{4\omega_{lh}B_0}\frac{\partial^2}{\partial t\partial z}(\nabla\varphi^*\times\nabla\varphi). \tag{42}$$

4. LINEAR THEORY OF THE MODULATIONAL INSTABILITY

In this section, we shall analyze the modulational instability arising from the modulational interaction of the LHWs with the quasi-neutral density perturbations in IAMs. This interaction leads to the modulation of the

amplitude of the LHWs by two satellite waves, which we will label red ($\omega_0 - \omega$) and blue ($\omega_0 + \omega$), where ω_0 is the frequency of the pump wave. The wave potential can be represented as

$$\varphi = \{\varphi_0 + \Sigma_\pm\varphi_\pm\exp[\pm i(\mathbf{k}\cdot\mathbf{r} - \omega t)]\}$$

$$\times \exp\left[i\left(\mathbf{k}_0\cdot\mathbf{r} - \frac{3}{2}\omega_{lh}k_0^2 R^2 t\right)\right]. \tag{43}$$

For simplicity, we neglect the electromagnetic correction to the lower hybrid frequency and assume that the pump wave is propagating across the magnetic field ($k_{0z} = 0$).

Wave pressure created by the modulation of the amplitude of the LHWs results in a density perturbation

$$\delta n(t, \mathbf{r}) = \frac{1}{2}\delta n\exp[i(\mathbf{k}\cdot\mathbf{r} - \omega t)] + \text{c.c.} \tag{44}$$

A very important feature of the modulational interaction of the LHWs with the low-frequency density fluctuations is that it is driven by a strong vector nonlinearity. When the wave vectors of pump and satellite waves are parallel ($\mathbf{k} \parallel \mathbf{k}_0$), the vector nonlinearity vanishes. Then, the modulational interaction is driven by a much weaker scalar nonlinearity, similar to the case of the modulational interaction of Langmuir waves. For the scalar nonlinearity, we know that the threshold of the wave energy for the onset of instability is comparable to the plasma thermal energy ($|E|^2 \sim nT$) [12]. In typical ionospheric conditions, the wave energy is much less than the thermal energy, so this condition cannot be satisfied. However, if the vector nonlinearity is taken into account, the condition for the instability is modified. For instance, for a previously studied case of ion-acoustic waves, the threshold of the wave energy was evaluated as $|E|^2 \sim (m_e/m_i)nT$, where the factor $m_e/m_i \sim 5\times 10^{-4}$ in an auroral ionosphere (one $\sqrt{m_e/m_i}$ is due to the nonlinear frequency shift arising from the density modulations (Eq. (10)), while the other factor $\sqrt{m_e/m_i}$ is due to the wave pressure creating these density modulations (Eq. (22)). If the wave vectors are parallel and the vector nonlinearity vanishes, any infinitely small deviation from the parallel case will grow exponentially with a growth rate larger by a factor of $\sqrt{m_i/m_e}$ than the case of scalar nonlinearity. The evolution of this fast modulational instability will destroy the alignment of $\mathbf{k}_0$ and $\mathbf{k}$. Therefore, we conclude that the vector nonlinearity is dominant for the modulational interaction of the LHWs with the slow background density fluctuations.
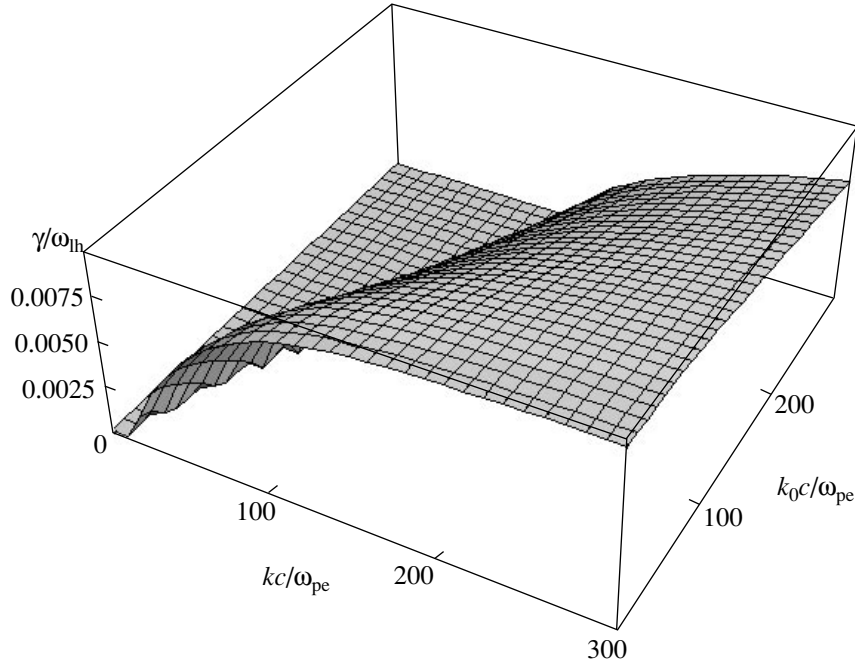
Fig. 4. Growth rate of the modulational instability as a function of the pump wave number k_0 and the excited wave number k.

The dispersion equation for the resulting instability of IAMs can be written as follows:

$$\omega^2\left(1 + \frac{k_\perp^2 c^2}{\omega_{pe}^2}\right) = k_\parallel^2 v_A^2\left(1 - \frac{k_\perp^2 c^2}{\omega_{pe}^2}P_A\frac{(\mathbf{k}_\perp \times \mathbf{k}_0)^2}{k^2 k_0^2}\right.$$

$$\left. \times\left[\frac{k^2}{(\mathbf{k}_\perp + \mathbf{k}_0)^2}\frac{\omega_{lh}}{\Delta_+ - \omega} + \frac{k^2}{(\mathbf{k}_\perp - \mathbf{k}_0)^2}\frac{\omega_{lh}}{\Delta_- + \omega}\right]\right), \tag{45}$$

where the frequency mismatches between the satellites and the pump LHWs and the dimensionless pump amplitude are

$$\Delta_\pm = \omega_{lh}\frac{m_i}{m_e}\frac{k_\parallel^2}{(\mathbf{k}_0 \pm \mathbf{k}_\perp)^2} + \frac{3}{2}\omega_{lh}R^2[(\mathbf{k}_0 \pm \mathbf{k}_\perp)^2 - k_0^2], \tag{46}$$

$$P_A = \frac{k_0^2|\varphi_0|^2}{4B_0^2}\frac{\omega_{pe}^2}{\omega_{ce}^2}\frac{m_i^2}{m_e^2}. \tag{47}$$

For the case when the amplitude of the pump wave is small, this dispersion relation describes the parametric decay of the pump LHWs into red satellite and inertial Alfvén waves. With the growth of the pump amplitude, this decay evolves into the modulational instability with a growth rate comparable to the eigenfrequency of the Alfvén wave. In this case, the inertial Alfvén wave is transformed into a driven IAM. If we assume for simplicity that the pump wave has very short wavelength ($k \ll k_0$), the expression for the mismatches is reduced to

$$\Delta_\pm = \Delta = \frac{k_\parallel^2}{k_0^2}\frac{m_i}{m_e}\omega_{lh} + 3\omega_{lh}R^2 k_0 k_\perp \sin^2\alpha. \tag{48}$$

Then, the dispersion equation simplifies to the following biquadratic equation that is easy to solve analytically:

$$(\omega^2 - \omega_A^2)(\omega^2 - \Delta^2) = 2P_A\omega_A^2\omega_{lh}\Delta\frac{k_\perp^2}{k_0^2}\frac{k_\perp^2 c^2}{\omega_{pe}^2}\sin^2\alpha, \tag{49}$$

where α is the angle between the vectors $\mathbf{k}_\perp$ and $\mathbf{k}_0$.

A strong aperiodic ($\mathrm{Re}\,\omega = 0$) modulational instability follows from this equation if the pump amplitude of the LHWs is sufficiently large, such that:

$$P_A > \frac{\Delta}{2\omega_{lh}}\frac{k_0^2}{k_\perp^2}\frac{\omega_{pe}^2}{k_\perp^2 c^2 \sin^2\alpha}.$$

In a more general case, the solution of dispersion equation (45) can be obtained only numerically. For the numerical solution, it is convenient to rewrite this dispersion equation in the dimensionless form:

$$\bar{\omega}^2(1 + \bar{k}_\perp^2)$$

$$= \bar{k}_\parallel^2\eta\left(1 - P_A\bar{k}_\perp^4\sin^2\alpha\left[\frac{1}{\bar{k}_{\perp+}^2(\delta_+ - \bar{\omega})} + \frac{1}{\bar{k}_{\perp-}^2(\delta_- + \bar{\omega})}\right]\right), \tag{50}$$

where the dimensionless parameters are introduced in the following way:

$$\delta_\pm = \frac{m_i}{m_e} \frac{\bar{k}_\parallel^2}{\bar{k}_0^2 + \bar{k}_\perp^2 \pm 2\bar{k}_0\bar{k}_\perp\cos\alpha} \quad (51)$$
$$+ 3\chi^2(\bar{k}_\perp^2 \pm 2\bar{k}_0\bar{k}_\perp\cos\alpha),$$

$$\bar{\omega} = \frac{\omega}{\omega_{lh}}, \quad \bar{k} = \frac{kc}{\omega_{pe}}, \quad \eta = \frac{v_A}{c}\frac{\omega_{pe}}{\omega_{lh}} = \sqrt{(1+s)/s},$$
$$\chi = \frac{R\omega_{pe}}{c}. \quad (52)$$

The numerical solution to Eq. (50) for $P_A = 10^{-5}$ and the ionospheric parameters given in the table is presented in Fig. 4. This corresponds to a pump wave amplitude of $E_0 \sim 80$ mV/m and $k_\parallel/k_\perp \sim 10^{-3}$. Note that, for large k, the growth rate approaches a constant value. This constant value can be obtained from Eq. (45) by taking the limit $k \longrightarrow \infty$:

$$\gamma^2 = \frac{m_i}{m_e}\frac{c^2}{R^2}\frac{|E_0|^2}{3B_0^2}\frac{\bar{k}_\parallel^2}{\bar{k}_\perp^2}\sin^2\alpha. \quad (53)$$

The threshold for the onset of instability, which is obtained numerically, is equal to $P_A \sim 2 \times 10^{-6}$. For the typical ionospheric parameters given in the table, this corresponds to a pump wave amplitude $E_0 \sim 35$ mV/m. This value is consistent with amplitudes of the LHWs observed in the ionosphere.

In conclusion, we have demonstrated that the lower hybrid wave activity observed in the active regions of the ionosphere is subject to modulational interaction with extremely low frequency density perturbations. These density perturbations could be of two types: associated with either electrostatic ion-acoustic modes or electromagnetic modes similar to inertial Alfvén waves. The nonlinearity that drives the interaction is vector-type nonlinearity. In the case of vector nonlinearity, the value of the wave power for the onset of modulational instability is sufficiently low and agrees with observations. The LHWs are trapped in the density structures resulting from the modulational interaction; these waves exert Reynold's stresses on background plasma and deepen the wells, which leads to a modulational instability.

REFERENCES

1. A. A. Vedenov and L. I. Rudakov, Dokl. Akad. Nauk SSSR **159**, 767 (1964) [Sov. Phys. Dokl. **9**, 1073 (1964)].

2. M. M. Hoppe, C. T. Russell, T. E. Easman, and L. A. Frank, J. Geophys. Res. **87**, 643 (1982).

3. Z. Dobe, K. B. Quest, V. D. Shapiro, *et al.*, Phys. Rev. Lett. **83**, 260 (1999).

4. K. Szëgo, R. Z. Sagdeev, V. D. Shapiro, and V. I. Shevchenko, Geophys. Res. Lett. **13**, 85 (1986).

5. T. Chang and B. Coppi, Geophys. Res. Lett. **8**, 1253 (1981).

6. V. D. Shapiro and V. I. Shevchenko, in *Basic Plasma Physics*, Ed. by A. A. Galeev and R. N. Sudan (North Holland, Amsterdam, 1984), Vol. 2, p. 123.

7. R. D. Sharp, R. G. Johnson, and E. G. Shelley, J. Geophys. Res. **82**, 3324 (1977).

8. J. LaBelle, P. M. Kintner, A. W. Yau, and B. A. Whalen, J. Geophys. Res. **91**, 7113 (1986).

9. P. M. Kintner, J. Vago, S. Chesney, *et al.*, Phys. Rev. Lett. **68**, 2448 (1992).

10. A. I. Eriksson, B. Holback, P. O. Dovner, *et al.*, Geophys. Res. Lett. **21**, 1843 (1994).

11. K. A. Lynch, R. L. Arnoldy, P. M. Kintner, *et al.*, J. Geophys. Res. **104** (A12), 28515 (1999).

12. R. Z. Sagdeev, Rev. Mod. Phys. **51**, 1 (1979).

13. S. L. Musher and B. I. Sturman, Pis'ma Zh. Éksp. Teor. Fiz. **22**, 537 (1975) [JETP Lett. **22**, 265 (1975)].

14. V. D. Shapiro, V. I. Shevchenko, G. I. Soloviev, *et al.*, Phys. Fluids B **5**, 3148 (1993).

15. H. L. Pécseli, K. Iranpour, and Ø. Holter, J. Geophys. Res. **101**, 5299 (1996).

16. Y. A. Omelchenko, V. D. Shapiro, V. I. Shevchenko, *et al.*, J. Geophys. Res. **99**, 5965 (1994).

17. V. D. Shapiro, G. I. Soloviev, J. M. Dawson, and R. Bingham, Phys. Plasmas **2**, 516 (1995).

18. S. H. Kjus, H. L. Pécseli, B. Lybekk, *et al.*, J. Geophys. Res. **103**, 26633 (1998).

19. L. M. Degtyarev, R. Z. Sagdeev, V. D. Shapiro, and V. I. Shevchenko, Fiz. Plazmy **2**, 438 (1976) [Sov. J. Plasma Phys. **2**, 240 (1976)].

20. S. H. Høymork, H. L. Pécseli, B. Lybekk, *et al.*, J. Geophys. Res. **105**, 18519 (2000).

21. C. E. Seyler, J. Geophys. Res. **99** (A10), 19513 (1994).

22. P. W. Schuck, C. E. Seyler, J. L. Pinçon, *et al.*, J. Geophys. Res. **103** (A4), 6935 (1998).

23. J. L. Vago, P. M. Kintner, S. W. Chesney, *et al.*, J. Geophys. Res. **97**, 16935 (1992).

24. J. W. Bonnell, P. W. Schuck, J. L. Pinçon *et al.*, Phys. Rev. Lett. **80**, 5734 (1998).

25. L. L. Pinçon, P. M. Kintner, P. W. Schuck, and C. E. Seyler, J. Geophys. Res. **102** (A8), 17283 (1997).

26. K. L. McAdams, J. LaBelle, P. W. Schuck, and P. M. Kintner, Geophys. Res. Lett. **25**, 3091 (1998).

27. M. Porkolab, Phys. Fluids **17**, 1432 (1974).

On the Efficiency of ELF/VLF Generation Using HF Heating of the Auroral Electrojet[1]

K. Papadopoulos[1, 2], T. Wallace[1], M. McCarrick[1], G. M. Milikh[1, 2], and X. Yang[1]

[1] Advanced Power Technologies Inc., Washington, DC, USA
[2] University of Maryland, College Park, MD, USA
Received October 24, 2002

Abstract—Using experimental measurements and theoretical analysis, it is shown that the HF/ELF conversion efficiency is controlled by the timescale for electron temperature saturation. This is a function of the ERP and frequency of the heater and the ionospheric electron density profile. For the current HAARP parameters, this corresponds to frequencies between 2 and 4 kHz. Efficiency optimization techniques as applied to the projected upgrading of the HAARP heater to its design power of 3.6 MW are discussed. © 2003 MAIK "Nauka/Interperiodica".

1. INTRODUCTION

A fundamental plasma physics concept among the main pioneering by Leonid Rudakov was the concept of electron magnetohydrodynamics (EMHD) [1]. The work presented here is a classic example of EMHD application in the Earth's ionosphere, in general, and in the electrojet, in particular.

Electron Hall currents driven by ionospheric electric fields in the D-region of the high latitude zone are responsible for a most fascinating plasma property: the potential to act as a frequency transformer that converts HF power injected from a high power HF transmitter into the ionosphere into coherent lower frequency VLF/ELF/ULF waves. The conversion principle relies on modulating the electrojet currents in the ionospheric D and E regions by using amplitude-modulated HF heating. The low-frequency fields subsequently couple to the earth–ionosphere wave guide, while a fraction of their power leaks towards the magnetosphere. Despite several years of theoretical [2–10] and experimental [11–16] work, many scientific and technical issues remain unresolved. Understanding the physics underlying their generation is important in increasing the HF to ELF/VLF conversion efficiency and utilizing this technique for ionospheric diagnostics. A puzzling feature of the experiments has been the variation of the conversion efficiency with frequency and the unusually large relative amplitude of the harmonics. Figure 1 shows the frequency dependence of the average field amplitude normalized to the amplitude at 2 kHz measured near the HAARP site. These data are typical of many other measurements and consistent with the data reported using the EISCAT heater [12]. The most important features seen in Fig. 1 and from previous data are the following:

(1) An enhanced efficiency relative to the neighboring frequencies at 2 kHz and its harmonics.

(2) If we ignore the enhanced regions, the maximum efficiency is in the frequency range between 2 and 4 kHz. The efficiency is proportional to the frequency f between 2 kHz and 500 Hz. There is a weak increase in the efficiency between 500 and 100 Hz. The efficiency is proportional to $1/f$ between 4 and 10 kHz.

(3) Harmonics with significant relative amplitudes up to ten or larger are present. The amplitudes of the harmonics are much higher than expected from the Fourier analysis of the HF heating waveforms.

Although the various sets of data have been collected under different heating parameters and iono-
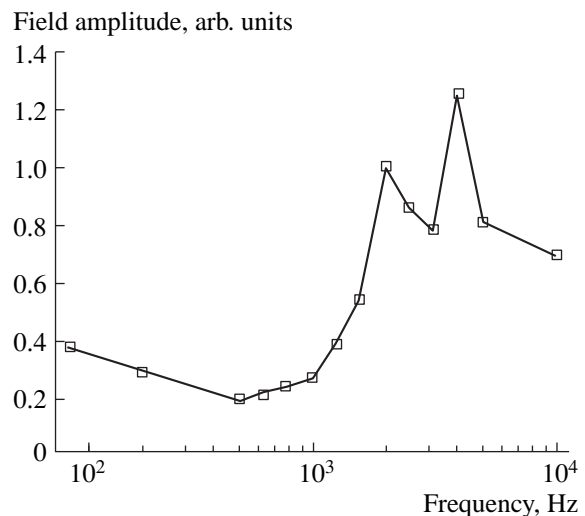
Fig. 1. The average field amplitude measured near the HAARP site versus the ELF/VLF frequency. The amplitude is normalized.
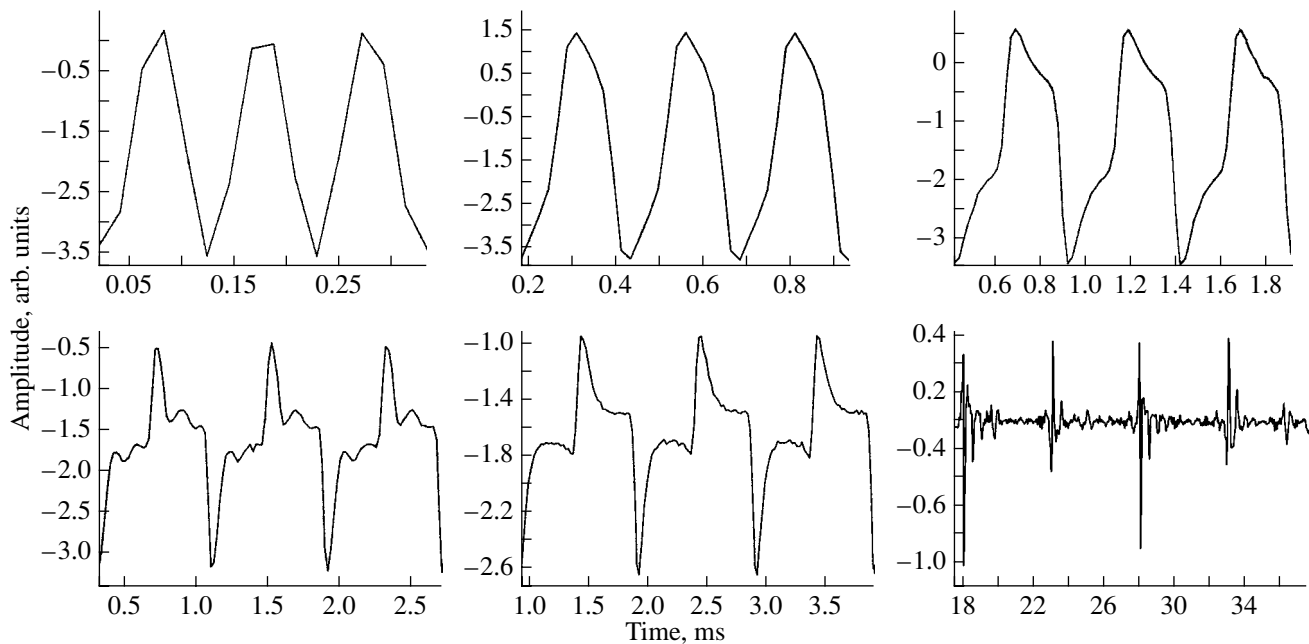
Fig. 2. Temporally resolved waveforms for the N–S components of the magnetic field recorded on March 4, 2001.

spheric conditions, the features described above are very consistent.

As discussed previously [2, 6, 7] and in the absence of propagation effects, the conversion efficiency depends on the value of the ambient electric field in the modified region and the spatiotemporal behavior of the modified conductivity in response to the HF heating pulse. Since the first factor, which basically controls the maximum value of the modified current, is beyond our control, our investigation focused on understanding the physics of the second factor. We present below the first temporally resolved ELF/VLF waveforms measured during modulated ionospheric heating. The results are compared with theoretical models and their implications are discussed.

2. EXPERIMENTAL RESULTS

The data presented below were obtained using the HAARP heater in Gakona, Alaska, during two campaigns. The first involved 48 hours of operation during the period September 17–30, 2000; and the second, 68 hours of operation during the period March 4–14, 2001. In all the results presented here, the heater operated at 3.3 MHz in the X-mode with power 960 kW and ERP 73 dBW. Since we are interested in near-field effects, the ELF/VLF data were recorded at a diagnostic trailer site located 12 km away from the heater. The magnetic fields were measured with EMI BF–6 sensors oriented along the magnetic N–S and E–W directions. The sensor output was digitized at a 24-bit resolution with a 48 kHz sampling frequency, giving temporal resolution of 20 μs in the measured ELF/VLF waveform.

They were generated using square-wave HF amplitude modulation between 100 Hz and 10 kHz.

Figure 2 shows temporally resolved waveforms for the dominant magnetic field component (N–S) for the frequencies recorded on March 4 between 05.32 UT and 06:00 UT. Two things are apparent. First, the peak value of amplitude is minimum at 10 kHz. The peak value increases at lower frequencies and reaches a saturation value at a frequency of 4 kHz. Second, the waveforms in the VLF range have significant power in the fundamental frequency. However they deteriorate significantly at the ELF range (1 kHz or lower). Note that in this frequency region the waveform is composed of a spike with duration of 0.125 ms at the beginning of each cycle, followed by a plateau of approximately one-third of the peak amplitude for the remaining pulse. As a result, at low frequencies, the HF-to-ELF conversion is low for most of the cycle. Furthermore, a Fourier analysis of the waveforms is consistent with the presence of harmonics with anomalously high amplitudes.

An additional feature revealed by these data is the presence of weaker peaks with a form similar to the driven waveform with a delay time of approximately 0.5 ms. The last feature was previously reported in [11, 17] and correctly interpreted as echoes generated by the reflection of the original pulse from the ionosphere. Rietveld *et al.* [11] have used these features to determine the ionospheric reflection height and the reflection coefficient and access the heating and cooling times in the D region. The data show the appearance of a plateau in the magnetic field with amplitude approximately 0.3 of the maximum, similar to the plateau
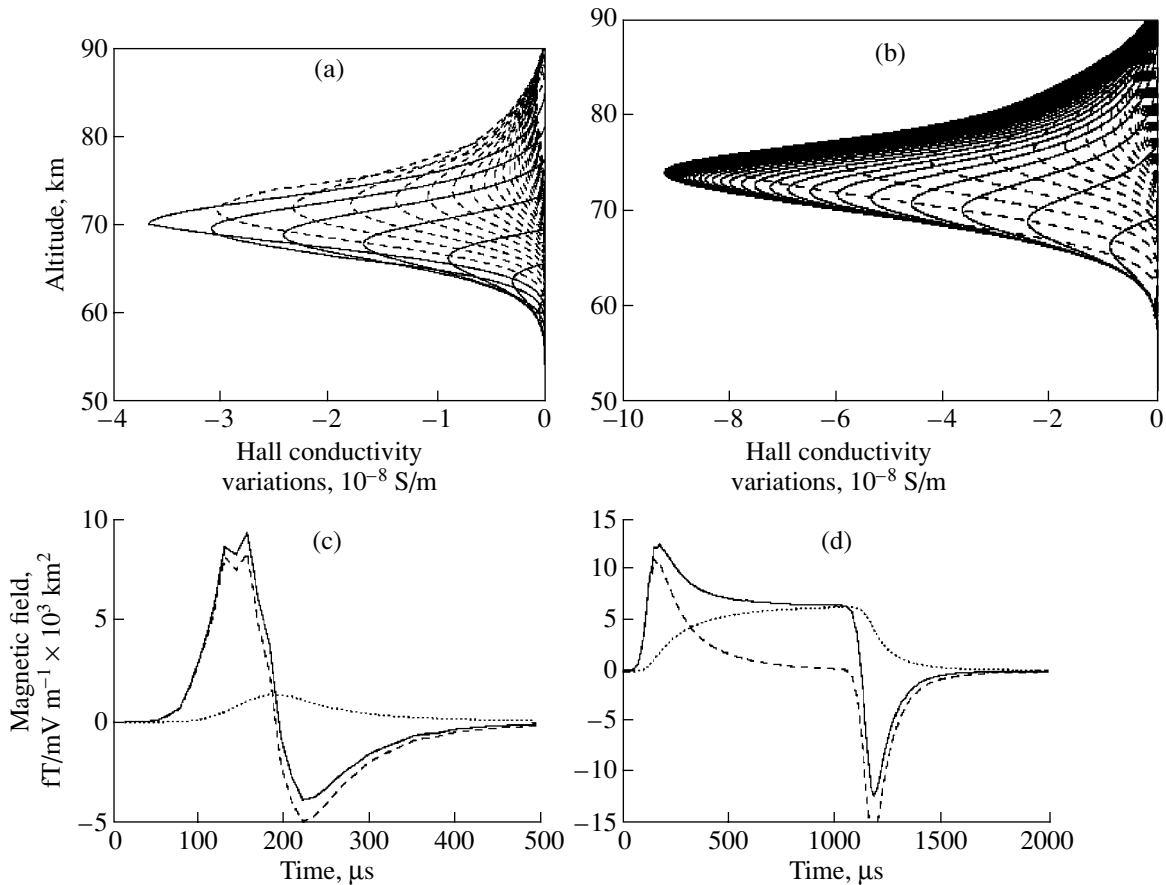
Fig. 3. Variations of the Hall conductivity caused by HF pulses with durations of (a) 50 and (b) 100 μs. Here the solid and broken lines show conductivities produced at the time of HF heating and after the pulse termination, respectively. Plots (c) and (d) reveal the associated temporal evolution of the magnetic field on the ground computed per 1 mV/m of the ambient electric field and per 1000 km^2 of the HF heated area.

shown in Fig. 2 for the ELF range of frequencies. The echoes feature is superimposed on the plateau for pulses longer than 0.5 ms. Referring to Fig. 2 in [17], we note that the plateau region is either lost in the noise or filtered by a low-pass filter. The rest of their waveform is similar to ours.

The ionospheric diagnostics was provided by a digital ionosonde, a magnetometer, and a 30-MHz riometer. During the testing period, the HAARP fluxgate magnetometer showed a moderate 50 gammas predominantly westward magnetic field and a corresponding southward electrojet current. The 30-MHz riometer absorption was about 0.5 dB, corresponding to a nighttime ionospheric profile.

3. THEORETICAL MODELING

The physics underlying these observations can be understood by referring to theoretical modeling. There are two steps in the computation. The first is to find the spatial-temporal profile of the current $\mathbf{j}(\mathbf{r}, t)$ induced by the heater. The second is to compute the near field at the observation site, which we take as the origin of the

coordinate system, using a retarded potential method described by the following set of equations:
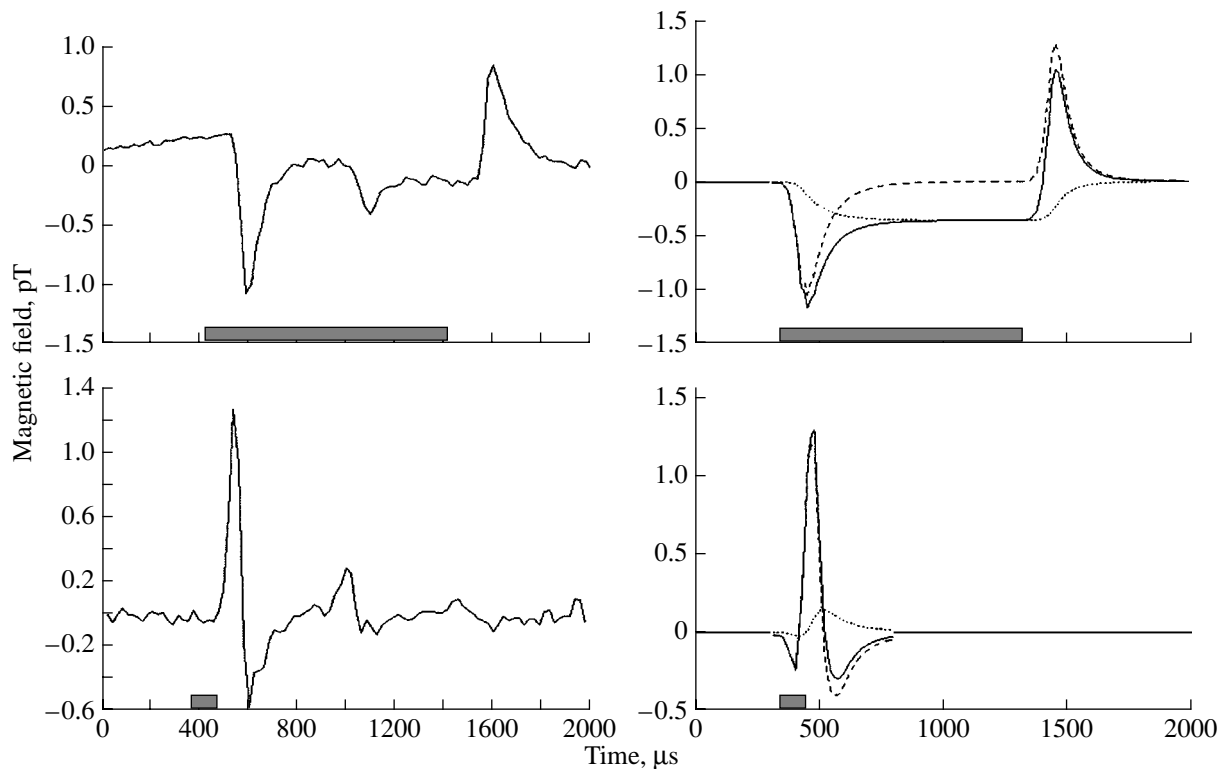
$$\mathbf{A}(0, t) = \int \frac{\mathbf{j}(r, t - r/c)}{4\pi\varepsilon_0 c^2 r} d\mathbf{r} \qquad (1)$$

$$\mathbf{B}(\mathbf{r}, t) = \nabla \times \mathbf{A}(\mathbf{r}, t). \qquad (2)$$

From these equations and assuming the ambient electric field E_0 in the x direction, the magnetic fields at the observation point per unit area and per unit electric field are given by

$$B_x(0, t)/SE_0 k$$
$$= \int \left[\frac{\Delta\sigma_H(z, t - z/c)}{z^2} + \frac{\Delta\dot{\sigma}_H(z, t - z/c)}{cz} \right] dz \qquad (3)$$

$$B_y(0, t)/SE_0 k$$
$$= \int \left[\frac{\Delta\sigma_P(z, t - z/c)}{z^2} + \frac{\Delta\dot{\sigma}_P(z, t - z/c)}{cz} \right] dz, \qquad (4)$$

Fig. 4. Experimental results (left column) along with the theoretical predictions (right column) for pulses with durations 1000 μs (on the top) and 50 μs (on the bottom).

where $\sigma_{H,P}$ are the Hall and Pedersen conductivities, S is the HF heated area, $k = 1/4\pi\varepsilon_0 c^2$, ε_0 is permittivity of free space, and $\Delta\dot{\sigma}_{P,H}$ represents derivative with respect to the retarded time. Note that the first term in the square brackets in Eqs. (3) and (4) describes the magnetic field due to the ionospheric current induced by the HF heating, while the second term is due to the time derivative of the current.

The spatial-temporal profile of the conductivity can be found by using 1D HF heating code, such as the one described in APTI, Technical Report 5007, 1991. The inputs to this code are the electron density profile as a function of altitude and the effective radiated power (ERP), frequency, polarization, and modulation format of the heater. A number of ionospheric profiles similar to the ones discussed in [18] are used depending on the value the riometer absorption. In the code, the effects of changing electron temperatures and the ionospheric absorption characteristics are calculated in a self-consistent manner. The output of the code is shown in Fig. 3, for a profile consistent with the experimental times shown in Fig. 2. They were computed for ERP = 73 dBW with a 12.5 μs time step. Figures 3a and 3b reveal the modified Hall conductivity as a function of time for pulse lengths of 0.05 ms and 1.0 ms, while Figs. 3c and 3d display the associated temporal evolution of the magnetic field on the ground. As shown in Figs. 3c and 3d the total field, represented by the con-

tinuous line, is composed of two contributions corresponding to the two terms in Eq. (3) and (4). Furthermore, the dotted line indicates the input from the ionospheric current, as discussed above after Eq. (4), while the slashed line exhibits the input from its derivative. It clearly explains the behavior observed in Fig. 3.

For times shorter than 0.125 ms, the second term—the time derivative of the induced ionospheric current—dominates, while at later times this term approaches zero and the dominant contribution is due to the current itself. Furthermore the HF-to-ELF/VLF conversion efficiency is by about 10 dB higher in the first 0.125 ms than the rest of the cycle. This is connected with the saturation of the electron temperature and the conductivity that is dependent only on the intensity of the heating wave at the absorption altitude.

To compare quantitatively the experimental results of Fig. 4 with the theoretical predictions, we took the area $S = 1300$ km², consistent with the HAARP antenna gain at 3.3 MHz. Since we could not measure the ambient electric field, we normalized the theoretical value of the magnetic-field peak achieved after 0.125 ms of heating to the experimentally observed value. In understanding Fig. 4, we have to note that the second spike in the experimental data, which appears approximately 1 ms after the main spike, represents the ionospheric reflection of the signal. This effect is not included in the current model.

As Fig. 4 shows, the theoretical and experimental waveforms are in good agreement. Similar agreement was found for the other pulse lengths, as well as for the rest of the experimental times. We should remark that the results of Fig. 4 imply a value of the ambient electric field of about 30 mV/m.

4. CONCLUSIONS

Temporally resolved ELF/VLF waveforms obtained during recent experiments at HAARP show that the efficiency of ELF/VLF generation by the ionospheric HF heating peaks at 2–4 kHz. In order to interpret the experimental results, a new model of ELF/VLF generation by pulsed ionospheric HF heating is presented. This model consists of two elements. The first is the 1D numerical code that computes the electron heating along with the modifications of the conductivity tensor in the ionosphere. The output of this code is fed into a model that computes the magnetic field in the near zone of the virtual ionospheric antenna caused by the HF heating. The magnetic field computed by the model is checked against observations made at the HAARP site. The overall agreement is very good, which implies that our model includes the essential physics and can be used to guide further studies and heater design.

Studies of waveforms show that the saturated heating is the cause of the inefficiency of the ELF production. In order to increase the HF-to-ELF/VLF conversion efficiency, we are planning to apply such techniques as painting, frequency chirping, or fast sweeping.

ACKNOWLEDGMENTS

REFERENCES

1. A. V. Gordeev, A. S. Kingsep, and L. I. Rudakov, Phys. Rep. **253** (5), 1 (1994).
2. R. Barr and P. Stubbe, Radio Sci. **19**, 1111 (1984).
3. H. G. James, J. Atmos. Terr. Phys. **47**, 1129 (1985).
4. V. K. Tripathi, C. L. Chang, and K. Papadopoulos, Radio Sci. **17**, 1321 (1982).
5. V. M. Sorokin and A. K. Yashenko, Radiophys. Quantum Electron. **35**, 247 (1990).
6. K. Papadopoulos, A. S. Sharma, and C. L. Chang, Comm. Plasma Phys. Control. Fusion **13**, 1 (1989).
7. K. Papadopoulos, C. L. Chang, P. Vitello, and A. Drobot, Radio Sci. **25**, 1311 (1990).
8. G. M. Milikh, K. Papadopoulos, M. McCarrick, and J. Preston, Radiophys. Quantum Electron. **42**, 728 (1999).
9. H. B. Zhou, K. Papadopoulos, A. S. Sharma, and C. L. Chang, Phys. Plasmas **3**, 1484 (1996).
10. H. L. Rowland, J. Geophys. Res. **104**, 4319 (1999).
11. M. T. Rietveld, H. Kopka, and P. Stubbe, J. Atmos. Terr. Phys. **48**, 311 (1986).
12. M. T. Rietveld, P. Stubbe, and H. Kopka, Radio Sci. **24**, 270 (1989).
13. A. J. Ferraro, H. S. Lee, T. W. Collins, *et al.*, IEEE Trans. Antennas Propag. **37**, 802 (1989).
14. M. McCarrick, D. D. Sentman, A. Y. Wong, *et al.*, Radio Sci. **25**, 1291 (1990).
15. R. Barr and P. Stubbe, Geophys. Res. Lett. **18**, 1035 (1991).
16. L. F. Mironenko, V. O. Rapoport, S. N. Mityakov, and D. S. Kotik, Radiophys. Quantum Electron. **41**, 196 (1998).
17. M. T. Rietveld and P. Stubbe, Radio Sci. **22**, 1084 (1987).
18. M. T. Rietveld, H.-P. Mauelshagen, P. Stubbe, *et al.*, J. Geophys. Res. **92**, 8707 (1987).

A Hall Dynamo Effect Driven by Two-Fluid Tearing Instability[1]

V. V. Mirnov, C. C. Hegna, and S. C. Prager

University of Wisconsin, Madison, WI 53706, USA

Received October 24, 2002

Abstract—A quasi-linear prediction of the two-fluid dynamo effect is analyzed with the use of tearing eigenfunctions obtained for force-free equilibrium. In the range of parameters of practical interest, the basic shear Alfvén mode is decoupled from fast compressional Alfvén and slow magneto-acoustic modes. Kinetic Alfvén modification of the shear Alfvén wave drives an instability with a growth rate $\propto \delta^{1/3} \rho_s^{2/3}$, where δ is the electron skin depth and ρ_s is the ion-sound gyroradius. A net dynamo effect parallel to the magnetic field is calculated at $\rho_s \gg \delta$ for large values of the stability factor $\Delta' \rho_s^{1/3} \delta^{2/3} \gg 1$. The dynamo effect caused by the $\mathbf{j} \times \mathbf{B}$ Hall term dominates the contribution from the $\mathbf{v} \times \mathbf{B}$ term (the alpha effect) by a factor $\propto (\rho_s/\delta)^2$ in the narrow electron layer, while in the broader ion layer these contributions are comparable. The results are compared with the case of a strong guiding field where $\rho_s \ll \delta$ and the tearing instability is described by resistive MHD. © *2003 MAIK "Nauka/Interperiodica".*

1. INTRODUCTION

The spontaneous generation of a magnetic field (the dynamo effect) in laboratory and astrophysical plasmas has been extensively studied through single-fluid magnetohydrodynamics (MHD). In the MHD dynamo, sometimes known as the alpha effect, large-scale magnetic fields are driven by correlations between the smaller scale spatial fluctuations in the velocity and magnetic field of the plasma. In laboratory plasmas, the tearing instabilities that induce magnetic reconnection generate the fluctuations. The tearing-mode dynamo effect driven by the $\mathbf{v} \times \mathbf{B}$ term in Ohm's law has been investigated by quasi-linear theory [1], nonlinear computation [2], and experiment [3]. However, at high temperatures, single-fluid MHD treatment becomes questionable for various laboratory and astrophysical situations. This is especially important for tearing modes where the spatial structure of eigenfunctions near the resonant surface (in the linear tearing layer) is determined by the electron skin depth, which is normally much shorter than the ion gyroradius or c/ω_{pi}.

The smallness of the electron skin depth compared to the ion scales leads to the decoupling of electrons from ions in the vicinity of the reconnection layer, the speeding up of the instability, and the broadening of the tearing layer. An extreme limiting case of the ion–electron decoupling is described by electron magnetohydrodynamics (EMHD), when ion motion is completely ignored. Fundamental EMHD theory was developed and a large variety of applications were investigated in pioneering works by L.I. Rudakov and coauthors (see, for example, review paper [4]). In particular, they analyzed tearing instability and magnetic reconnection within the scope of EMHD equations in the cold plasma limit, $\beta = 0$, and large c/ω_{pi}. In the following presentation, we extend the ideas of L.I. Rudakov and his colleagues for the case of hot plasmas, where ion–electron decoupling is caused by large ion gyroradii. We extend our analysis to quasi-linear theory and present calculations of the quadratic Hall and alpha dynamo terms in generalized Ohm's law that are driven by two-fluid tearing instabilities.

2. STATEMENT OF THE PROBLEM

Two-fluid effects, considered below, affect dynamos in two ways: by altering the MHD $\mathbf{v} \times \mathbf{B}$ dynamo and by introducing new dynamo mechanisms. The new effects are evident in the generalized Ohm's law,

$$\mathbf{E} + \frac{1}{c}\mathbf{v} \times \mathbf{B} = \frac{1}{nec}\mathbf{j} \times \mathbf{B} - \frac{\nabla p_e}{ne} - \frac{m_e}{e}\frac{d\mathbf{v}_e}{dt} + \eta \mathbf{j}, \quad (1)$$

where the first three terms on the right-hand side (the Hall term, the electron pressure gradient, and electron inertia) are absent in MHD. The dynamo effect caused by a gradient in the mean electron pressure has been considered theoretically [5] and experimentally [6]. Two-fluid treatment of the fluid Reynolds stress has also been evaluated [7]. We consider here that the mean electron pressure is constant. It is known (see, for example, [8–10]) that, in this case, two-fluid treatment accurately describes dynamics on disparate electron and ion scale lengths. At a uniform mean electron pressure, fluctuations contribute to the parallel component of the mean field Ohm's law as follows:

$$\mathcal{E}_\parallel = \langle \mathbf{E} \rangle_\parallel - \eta \langle \mathbf{j} \rangle_\parallel$$
$$= -\frac{1}{c}\langle \mathbf{v}^{(1)} \times \mathbf{B}^{(1)} \rangle_\parallel + \frac{1}{en^{(0)}c}\langle \mathbf{j}^{(1)} \times \mathbf{B}^{(1)} \rangle_\parallel, \quad (2)$$

---

[1] This article was submitted by the authors in English.

where $\langle \dots \rangle$ denotes the average over the fluctuation spatial scale, the parallel components are defined with respect to $\mathbf{B}^{(0)}$, and the superscripts (0) and (1) indicate mean quantities and linear fluctuations, respectively. The right-hand side of Eq. (2) contains two dynamo terms: the alpha effect driven by plasma velocity and a Hall dynamo that arises from current density fluctuations. All other quadratic terms driven by density and electron pressure perturbations vanish after the flux surface averaging.

In this paper, we use the two-fluid quasi-linear theory to evaluate the right-hand side of Eq. (2). We calculate the linear eigenfunctions for a two-fluid tearing instability, from which we form the dynamo terms. We find that the Hall dynamo driven by the second term in the right-hand side of Eq. (2) is the dominant dynamo effect, being more than the order of magnitude larger than the first term corresponding to the alpha effect. This strong enhancement takes place in a narrow electron skin layer. We also find that the alpha effect is broadened in its spatial width to the order of an ion-sound gyroradius, $\rho_s = c_s/\omega_{Bi}$, $\omega_{Bi} = eB^{(0)}/m_i c$, where the ion-sound speed $c_s^2 = (\gamma_e T_e + \gamma_i T_i)/m_i$, with $\gamma_{i,e} = 5/3$ in the adiabatic case and $\gamma_{i,e} = 1$ in the isothermal case. At this larger scale ρ_s, the Hall dynamo is diminished and is comparable to the alpha dynamo term. The last one is broadened in its spatial width to the order of the external scale L, which is determined by the spatial distribution of the mean magnetic field. Thus, our quasi-linear calculations predict that the Hall dynamo effect in two-fluid theory is locally much larger than the contribution from the $\mathbf{v} \times \mathbf{B}$ dynamo term. The effect results from the decoupling of electrons from ions in the vicinity of the reconnection layer.

The Hall dynamo is important for many high-temperature astrophysical [11] and laboratory plasmas (in particular, in reversed-field pinches where the nonlinear action of tearing instability is to flatten the equilibrium current profile to the Taylor state of minimum energy [12]). The possible importance of the Hall dynamo was inferred in experiments [3], where measurements of the left-hand side of Eq. (2) were not equal to the measured $\langle \mathbf{v}^{(1)} \times \mathbf{B}^{(1)} \rangle_\parallel$ term in the right-hand side of this equation.

3. BASIC EQUATIONS AND EIGENFUNCTIONS

An analytic theory is developed for a plasma slab geometry in a force-free equilibrium. Uniform density, temperature, and pressure profiles are assumed for electrons and ions. The equilibrium magnetic field consists of a small shearing component that is created by an equilibrium current sheet of thickness L and a large guiding field. It is known that the dynamo effect can be related to both collisional and collisionless processes [13]. The effects of electron inertia and plasma resistivity are included in the combined electron skin depth $\delta^2 = d_e^2 + \delta_R^2$, which consists of collisionless $d_e = c/\omega_{pe}$

and resistive $\delta_R^2 = c^2\eta/4\pi\gamma$ parts and accounts for terms that break the frozen flux theorem, where γ is the growth rate of purely growing modes.

Linear two-fluid tearing equations are formulated for a hot plasma with $c_s \gg \gamma L$. In this approximation, the compressional Alfven mode is decoupled and the two-fluid tearing instability is driven by shear-Alfven (SA) and magneto-acoustic (MA) modes modified by the Hall term. We consider the range $m_e/m_i \ll \beta \ll (\delta/d_i)^{1/2} \geq$ $(m_e/m_i)^{1/4} \sim 15\%$, with $\beta = 8\pi p/B_z^{(0)^2}$ and $d_i = c/\omega_{pi}$, where the coupling with the MA wave, as well as the effect of the diffusion of the magnetic perturbations parallel to the guiding field, can be ignored. In this situation, the decoupling of electrons from ions leads to a mode dispersion typical for kinetic Alfven waves with $\omega \propto k^2$. In two-fluid theory, this dependence results from the joint effect of the Hall term and the plasma compressibility, $\nabla \cdot \mathbf{v} \neq 0$. The growth rate scales as $\gamma \sim \delta^{1/3}\rho_s^{2/3}$ [8] in the large Δ' limit ($\Delta'\delta^{2/3}\rho_s^{1/3} \geq 1$), where the stability factor Δ' is defined by formula (6).

An orthogonal reference frame is used with x oriented in the radial direction, and y and z along the sheared $B_y^{(0)}(x)$ and guiding $B_z^{(0)}(x)$ components of the unperturbed magnetic field. All perturbations are x dependent and proportional to $\exp i(ky - \omega t)$, while $\partial/\partial z = 0$. A sheet pinch equilibrium profile $B_y^{(0)}(x) = B_y^{(\infty)}\tanh x/L$ is specified for calculations for which $x = 0$ is the position of the resonance surface determined by the condition $\mathbf{k} \cdot \mathbf{B}^{(0)}(x) = kB_y^{(0)}(x) = 0$. We define the growth rate $\gamma = -i\omega$, and dimensionless variables $v = iv_x/v_a$, $v_a = B_y^{(\infty)}/(4\pi\rho^{(0)})^{1/2}$, $B_{x,z} \longrightarrow B_{x,z}/B_y^{(\infty)}$, $\tau_A = L/v_a$, $x \longrightarrow x/L$, $d_{e,i} \longrightarrow c/(\omega_{pe,i}L)$, $k \longrightarrow kL$, $B_y^{(0)}(x) \longrightarrow \tanh x$. The electron skin depth $\delta = d_e(1 + 1/d_e^2 S\gamma\tau_A)^{1/2}$ is γ-dependent, where the Lunquist number $S = \tau_R/\tau_A = 4\pi L^2/\tau_A c^2\eta$. Using smallness $\delta \ll \rho_s$ we derive a dispersion relation in terms of $\delta(\gamma)$ that can be then solved explicitly for γ.

In a contrast to single-fluid MHD, the perturbations of the guiding magnetic field $B_z^{(1)}$ are important in the two-fluid case. They are described by the z component of the Faraday induction equation. In this equation, $\nabla \cdot \mathbf{v}$ is multiplied by the large factor $B_z^{(0)}$; thus, the use of the incompressible approximation $\nabla \cdot \mathbf{v} = 0$ in this equation is not correct at $\beta \ll 1$ [14]. Equation (3) for $B_z^{(1)}$ is obtained by expressing $\nabla \cdot \mathbf{v} \propto 1/B_z^{(0)}$ from the Faraday equation and substituting it into the equation of equilibration of total (magnetic + thermal) pressure, where variations of the thermal pressure are treated as either adiabatic or isothermal. In the plasma momentum equation, small terms proportional to $\nabla \cdot \mathbf{v} \propto 1/B_z^{(0)}$ can be neglected. Hence, we derive the vorticity

equation (4). The parallel component of the generalized Ohm's law is given by Eq. (5). Using the smallness of $\epsilon = B_y^{(\infty)}/B_z^{(0)} \ll 1$, linearized equations for perturbations are (superscript (1) is omitted)

$$B_z = \frac{\beta d_i}{\gamma \tau_A}\left(B_y^{(0)}(x)\nabla^2 B_x - \frac{d^2 B_y^{(0)}}{dx^2}B_x\right), \tag{3}$$

$$\frac{\gamma \tau_A}{k}\nabla^2 v = \left(\frac{d^2 B_y^{(0)}}{dx^2}B_x - B_y^{(0)}(x)\nabla^2 B_x\right), \tag{4}$$

$$\frac{\gamma \tau_A}{k}(B_x - \delta^2 \nabla^2 B_x) = (v + d_i k B_z)B_y^{(0)}(x). \tag{5}$$

System (3)–(5) coincides with the equations derived in [15] from the four-field model [16] and in [17] from two-fluid theory. At small $\beta \ll m_e/m_i$, equation (3) and the B_z term in Eq. (5) can be ignored, yielding single-fluid MHD equations. At larger β, when $\rho_s \gg \delta$, the perturbations of B_z dominate on scales smaller than ρ_s, which decouples electron and ion flows in the (x, y) plane and allows a high growth rate. Solving Eqs. (3)–(5), we will apply the boundary layer method based on the asymptotic matching of the tearing inner and ideal outer solutions with the use of the stability factor

$$\Delta' = \left(\frac{1}{B_x}\frac{dB_x}{dx}\right)_{+0} - \left(\frac{1}{B_x}\frac{dB_x}{dx}\right)_{-0}, \tag{6}$$

where $\Delta' > 0$ indicates instability. The ideal equation in the outer zone follows from Eqs. (3) and (4) as $\gamma \longrightarrow 0$:

$$B_y^{(0)}(x)\nabla^2 B_x - \frac{d^2 B_y^{(0)}}{dx^2}B_x = 0. \tag{7}$$

The sheet pinch profile solution of Eq. (7), which is even function of x and satisfies the decaying boundary conditions at infinity, has a discontinuity of dB_x/dx at $x = 0$,

$$B_x = -C_1 \sin ky \exp(-k|x|)\left(1 + \frac{\tanh|x|}{k}\right), \tag{8}$$

with $\Delta'(k) = 2/k - 2k$. At $x \ll 1$ $B_x(x)$ takes the form

$$B_x(x, y) = -(C_1 + C_2|x|)\sin ky, \tag{9}$$

which is used to match tearing inner solutions with (8), where $\Delta'(k) = 2C_2/C_1 > 0$ is a function of k. We consider the limiting case $\Delta' \longrightarrow \infty$ and set $C_1 = 0$, keeping $C_2 > 0$ as an arbitrary constant that defines the amplitudes of the eigenfunctions.

Assuming tearing parity, we introduce even function $B(x) > 0$ by $B_x = -B(x)\sin ky$ and write $v_x(x, y) = V(x)\cos ky$ and $B_z(x, y) = -B_z(x)\sin ky$, where we deduce from Eqs. (3) and (4) that $V(x)$ and $B_z(x)$ are odd functions of x. Using $\nabla \cdot \mathbf{v} = 0$, $\nabla \cdot \mathbf{B} = 0$, $\nabla \cdot \mathbf{j} = 0$, and $j_x = (ikc/4\pi)B_z$ gives the following for v_y, B_y and $j_{x,y}$: $v_y(x, y) = -(1/k)\sin ky\, dV/dx$, $B_y(x, y) = -(1/k)\cos ky\, dB/dx$, $j_y(x, y) =$

$(c/4\pi)\sin ky\, dB_z/dx$, $j_x(x, y) = -(ck/4\pi)\cos ky\, B_z(x)$. Taking a projection of $-(1/c)\mathbf{v} \times \mathbf{B}$ and $(1/n^{(0)}ec)\mathbf{j} \times \mathbf{B}$ on $\mathbf{B}^{(0)}/B^{(0)}$ in accordance with Eq. (2) and averaging over y yields

$$\mathscr{E}_{\parallel}^{(v)}/\mathscr{E}_0 = \frac{d}{dx}(VB), \quad \mathscr{E}_{\parallel}^{(j)}/\mathscr{E}_0 = kd_i\frac{d}{dx}(B_z B), \tag{10}$$

where $\mathscr{E}_0 = B_y^{(\infty)^2}/(2ck\sqrt{4\pi n^{(0)}m_i})$ and we put $B_z^{(0)}(x)/B^{(0)} \simeq 1$ at $\epsilon \ll 1$. Equations (10) show that the three dimensionless functions B_z, B, and V determine the dynamo effects in two-fluid theory.

Single-fluid MHD ($\rho_s \ll \delta$) contains at large $\Delta'\delta \geq 1$ one scale δ, which separates tearing inner and ideal outer solutions. In two-fluid theory ($\rho_s \gg \delta$), there are two inner layers and an ideal outer layer specified as follows: (a) an inner diffusive layer $|x| \ll x_\rho = \rho_s\Gamma \ll 1$, $\Gamma = \gamma \tau_A/k\rho_s$, where electron diffusivity is important, electrons and ions are decoupled, and the Hall dynamo term dominates while the contribution from the $\mathbf{v} \times \mathbf{B}$ term can be ignored; (b) an ideal two-fluid inner layer $x_\delta = \Gamma\delta \ll |x| \ll 1$, where electron diffusivity plays no role and the electron and ion flows are decoupled; and (c) an ideal outer layer $x_\rho \ll |x|$ described by Eq. (7), where electrons and ions are coupled within the scope of ideal MHD.

From (3) and (7), it follows that in the outer layer $B_z \longrightarrow 0$; while from Eqs. (4), (5), and (9) the functions asymptotically become $V(x) \longrightarrow \rho_s\Gamma C_2$, $u(x) = dV/dx \longrightarrow 0$. This determines the matching conditions for the two-fluid inner and outer solutions of Eqs. (3)–(5), simplified at $x \ll 1$:

$$B - \left(\delta^2 + \frac{x^2}{\Gamma^2}\right)\frac{d^2 B}{dx^2} = \frac{x}{\rho_s\Gamma}V, \tag{11}$$

$$\rho_s\Gamma\frac{d^2 V}{dx^2} = -x\frac{d^2 B}{dx^2}. \tag{12}$$

Integrating (12) over x yields

$$\rho_s\Gamma u(x) = -x^2\frac{d}{dx}\frac{B}{x}, \tag{13}$$

with zero constant of integration at $\Delta' \longrightarrow \infty$ ($\Delta'\delta^{2/3}\rho_s^{1/3} \geq 1$). In the two overlapping zones (a) and (b), the inner equations can be further simplified. In zone (a), one can ignore the V-dependent term in (11), yielding an even solution for $B(x)$ in terms of the hypergeometrical function

$$B^{(a)}(x)$$
$$= B(0)_2F_1[-1/4 - Q/4, -1/4 + Q/4, 1/2, -(x/\Gamma\delta)^2], \tag{14}$$

where $Q = \sqrt{1 + 4\Gamma^2}$. In zone (b), the term proportional to δ^2 in Eq. (11) can be dropped, yielding a solution for $u(x)$ decaying at $x/\rho_s \gg 1$:

$$u^{(b)}(x) = C_u\left(\frac{x}{2\rho_s}\right)^{1/2} K_{Q/2}\left(\frac{x}{\rho_s}\right), \qquad (15)$$

where $K_{Q/2}(x/\rho_s)$ is the modified Bessel function. Differentiating Eq. (14) in accordance with Eq. (13) gives the asymptotic expansion for $u^{(a)}$ at $x \gg x_\delta$. Matching this expansion with the expansion of (15) at $x \ll \rho_s$ yields Γ and a relationship between C_u and $B(0)$. This matching technique is applicable in two-fluid case $\delta/\rho_s \ll 1$, when the interval $x_\delta \ll x \ll x_\rho$ exists, where both solutions (14) and (15) are overlapped. In this case, automatically, $\Gamma \ll 1$, $Q \longrightarrow 1$, and the above expressions are simplified as follows:

$$\Gamma = \left(\frac{2\delta}{\pi\rho_s}\right)^{1/3}, \quad B(0) = \frac{\sqrt{\pi}}{2}\rho_s\Gamma C_u. \qquad (16)$$

$$u^{(b)}(x) \longrightarrow \frac{\sqrt{\pi}}{2}C_u\exp(-x/\rho_s). \qquad (17)$$

Expression (17) represents a good approximation for $u(x)$ not only in zone (b) but in a whole range of x, except for a small corrections in zone (a) near $x = 0$ where $du^{(a)}/dx(0) = 0$. In particular, expression (17) gives good accuracy upon integration, determining $V(x)$:

$$V(x) = \int_0^x u(x')dx' = \frac{\sqrt{\pi}\rho_s}{2}C_u[1 - \exp(-x/\rho_s)]. \quad (18)$$

Matching (18) with its asymptotic value in the outer layer, $V(x) \longrightarrow \rho_s\Gamma C_2$, yields C_u and $B(0)$

$$C_u = \frac{2}{\sqrt{\pi}}\Gamma C_2, \quad B(0) = \rho_s\Gamma^2 C_2. \qquad (19)$$

Integrating Eq. (13) from infinity to x using (20) gives a good analytical approximation for $B(x)$ except in a small vicinity near $x = 0$ where $dB^{(a)}/dx(0) = 0$:
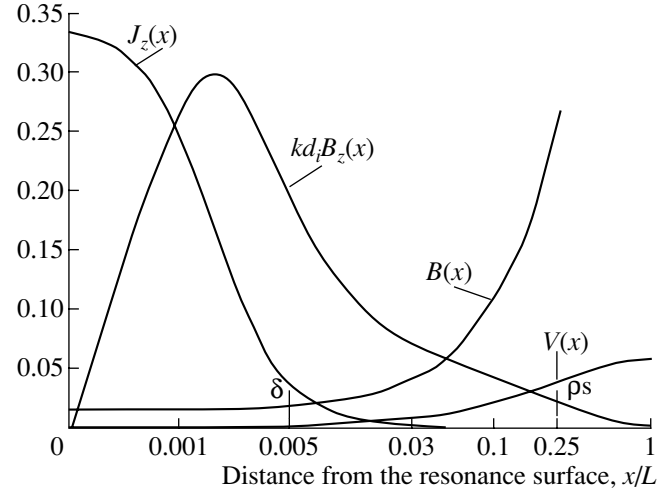
$$B(x)/C_2 = x\left(1 + \Gamma^2 \int_{x/\rho_s}^{\infty} \frac{dx'\exp(-x')}{x'^2}\right). \qquad (20)$$

The exact eigenfunctions are illustrated in Fig. 1.

4. TWO-FLUID DYNAMO

As $V(x)$ grows slowly with x, the main contribution to V, B, and $\mathscr{E}_\parallel^{(v)}$ comes from $x \simeq \rho_s$. In a contrast to

Two-fluid tearing eigenfunctions

Fig. 1. Even $B(x)$, $J_z(x)$ (current density) and odd $V(x)$, $kd_iB_z(x)$ eigenfunctions at $\delta = 0.005$, $\rho_s = 0.25$, and $C_2 = 1$. Peaks of $J_z(x)$, $B_z(x)$ are localized on short scale x_δ, while $V(x)$ is broadened to a scale ρ_s. The intersection of the curves $kd_iB_z(x)$ and $V(x)$ at $x \simeq \rho_s\ln 2$ separates the area $x \ll \rho_s$ where $v_e \gg v_i$ and the area $x \gg \rho_s$ where $v_e \simeq v_i$.

this, due to the sharp peak of $B_z(x)$ in zone (a), the product B_zB contributes to $\mathscr{E}_\parallel^{(j)}$ mainly in this zone,

$$(B_zB)^{(a)} = C_2^2F(\mu)\frac{\beta d_i\rho_s\Gamma^4}{k\delta}, \qquad (21)$$

where $F(\mu) = \mu_2F_1^2[-1/4 - Q/4, -1/4 + Q/4, 1/2, -\mu^2]/(1 + \mu^2)$, $\mu = x/(\Gamma\delta)$. In zone (b), this function is

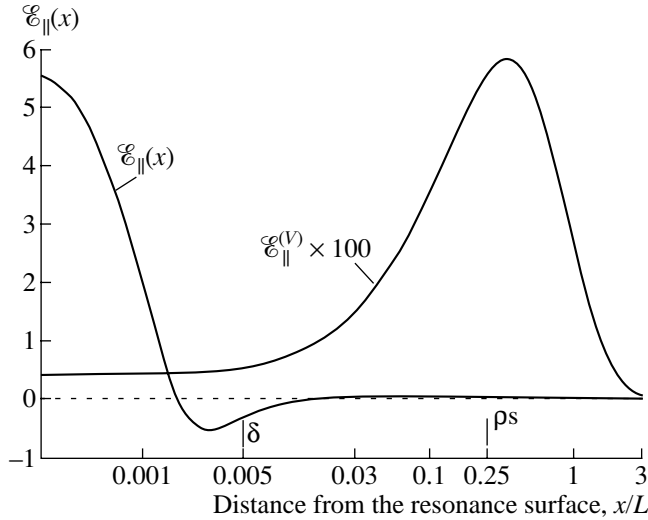$$(B_zB)^{(b)} = C_2^2H(\xi)\frac{\beta d_i\Gamma}{k}, \qquad (22)$$

where $H(\xi)$ is a product of $\exp(-\xi)$ and (20) expressed in terms of $\xi = x/\rho_s$. Since the products B_zB depend on the dimensionless variables μ and ξ, their derivatives can be estimated as $(d/dx)^{(a)} \sim (\Gamma\delta)^{-1}$, $(d/dx)^{(b)} \sim \rho_s^{-1}$, yielding estimates for $\mathscr{E}_\parallel^{(j)}$ (in units of $C_2^2\mathscr{E}_0$)

$$\mathscr{E}_{\parallel a}^{(j)} \simeq \frac{\rho_s^3\Gamma^3}{\delta^2} \simeq \frac{\rho_s^2}{\delta}, \quad \mathscr{E}_{\parallel b}^{(j)} \simeq \rho_s\Gamma \simeq \rho_s^{2/3}\delta^{1/3}, \qquad (23)$$

while estimates for $\mathscr{E}_\parallel^{(v)}$ in the same units are

$$\mathscr{E}_{\parallel a}^{(v)} \simeq \rho_s\Gamma^3 \simeq \delta, \quad \mathscr{E}_{\parallel b}^{(v)} \simeq \rho_s\Gamma \simeq \rho_s^{2/3}\delta^{1/3}. \qquad (24)$$

Tearing-induced dynamo effect ε(x)

Fig. 2. Total dynamo effect $\mathscr{E}_\parallel(x) = \mathscr{E}_\parallel^{(v)} + \mathscr{E}_\parallel^{(j)}$ and the contribution $\mathscr{E}_\parallel^{(v)}(x)$ from the $\mathbf{v} \times \mathbf{B}$ term (10^2-fold) in the two-fluid case at $\delta = 0.005$ and $\rho_s = 0.25$ (all functions are even functions of x and normalized to $C_2^2 \mathscr{E}_0$).

For comparison, in resistive MHD theory ($\rho_s \ll \delta$) the dynamo effect is driven by the $\mathscr{E}_\parallel^{(v)}$ term, which is determined by the *VB* product

$$VB = C_2^2 \delta^2 \left(\frac{2}{\pi}\right)^{3/2} \left(\int_0^\nu \exp(-x'^2) dx'\right)$$

$$\times \left(\exp(-\nu^2) + 2\nu \int_0^\nu \exp(-x'^2) dx'\right), \qquad (25)$$

$$\nu = \frac{x}{\sqrt{2}\delta}, \quad |x| \ll 1,$$

where functions *V* and *B* are exact solutions to Eqs. (11) and (12) without the Hall term x^2/Γ^2 in Eq. (11) (for $\Delta'\delta \gg 1$). Approximating $d/dx \sim \delta^{-1}$ yields an estimate for $\mathscr{E}_\parallel^{(mhd)}$:

$$\mathscr{E}_\parallel^{(mhd)} \simeq \delta. \qquad (26)$$

Note that two-fluid estimates (23) and (24) and single-fluid one (26) are well matched at $\rho_s \sim \delta$. Exact numerical results for functions (10) are illustrated in Fig. 2 and confirm the analytic estimates.

5. CONCLUSIONS

In summary, we have derived quasi-linear predictions of the dynamo effect using a two-fluid theory model of tearing-mode instabilities. For sufficiently high plasma temperatures, the two-fluid theory indicates the appearance of two spatial scales in the tearing layer; an inner electron layer where the ion motion is negligible; and a broader layer, where ion flow plays a role. With increasing the value of ρ_s, the Hall dynamo $(1/en^{(0)}c)\langle \mathbf{j}^{(1)} \times \mathbf{B}^{(1)} \rangle_\parallel$ dominates the contribution from the MHD dynamo $(1/c)\langle \mathbf{v}^{(1)} \times \mathbf{B}^{(1)} \rangle$ by a factor $\propto (\rho_s/\delta)^2$ in the narrow electron layer $|x| \leq \delta^{4/3}\rho_s^{-1/3}$. In the broader ion layer, the Hall and MHD contributions to the dynamo are comparable.

This indicates that two-fluid effects are required to accurately describe dynamo processes in high-temperature plasmas. In particular, above conclusions are important for the measurements and treatments of dynamo in reversed field pinch experiments. As an example, we refer to the Madison Symmetric Torus (MST) experiments. Due to the relatively high plasma temperature and low guiding magnetic field, the ion-sound gyroradius is large at the resonant reversal surface, $\rho_s \simeq 2.5$ cm, while the electron skin depth is small in here, $\delta \simeq 0.5$ cm. In this situation, the amplitude of the Hall dynamo is about 25 times greater than the usual $\mathbf{v} \times \mathbf{B}$ term. This is important for nonlinear current flattening and relaxation to the Taylor's state of minimum energy.

REFERENCES

1. A. Bhattacharjee and E. Hameiri, Phys. Rev. Lett. **57**, 206 (1986).
2. S. Ortolani and D. Schnack, *Magnetohydrodynamics of Plasma Relaxation* (World Scientific, Singapore, 1993).
3. P. W. Fontana, D. J. Den Hartog, G. Fiksel, and S. C. Prager, Phys. Rev. Lett. **85**, 566 (2000).
4. A. V. Gordeev, A. S. Kingsep, and L. I. Rudakov, Phys. Rep. **243**, 215 (1994).
5. G. C. Lee, P. H. Diamond, and Z. C. An, Phys. Fluids B **1**, 99 (1989).
6. H. Ji, S. C. Prager, A. F. Almagri, *et al.*, Phys. Plasmas **3**, 1935 (1996).
7. C. C. Hegna, Phys. Plasmas **5**, 2257 (1998).
8. F. Porcelli, Phys. Rev. Lett. **66**, 425 (1991).
9. T. J. Schep, F. Pegoraro, and B. N. Kuvshinov, Phys. Plasmas **1**, 2843 (1994).
10. B. N. Kuvshinov and B. N. Mikhaĭlovskiĭ, Fiz. Plazmy **22**, 582 (1996) [Plasma Phys. Rep. **22**, 529 (1996)].
11. P. D. Mininni, D. O. Gomez, and S. M. Mahajan, Astrophys. J. Lett. **567**, L81 (2002).
12. J. B. Taylor, Phys. Rev. Lett. **33**, 134 (1974).
13. R. G. Kleva, Phys. Rev. Lett. **73**, 1509 (1994).
14. D. Biskamp, E. Schwarz, and J. F. Drake, Phys. Plasmas **4**, 1002 (1997).
15. A. Y. Aydemir, Phys. Fluids B **3**, 3025 (1991).
16. R. D. Hazeltine, C. T. Hsu, and P. J. Morrison, Phys. Fluids **30**, 3204 (1987).
17. L. Zakharov and B. Rogers, Phys. Fluids B **4**, 3285 (1992).

Review of Experimental Studies of the Dynamics of Light Liners at the Russian Research Centre Kurchatov Institute

Yu. G. Kalinin

Russian Research Centre Kurchatov Institute, pl. Kurchatova 1, Moscow, 123182 Russia
Received November 21, 2002

Abstract—The results of experimental studies on the implosion of liners by megaampere currents that were carried out in the Department of Relativistic Beams of the Russian Research Centre Kurchatov Institute are reviewed. The main line of research was to study the possibility of realizing the liner–converter (or liner–target) scheme proposed by L.I. Rudakov. © *2003 MAIK "Nauka/Interperiodica"*.

1. INTRODUCTION

The low efficiency with which electric energy is converted into soft X-ray (SXR) emission by electron drivers and problems related to power sharpening stimulated the search for alternative methods of producing high-power X-ray pulses with the help of high-current generators. In the late 1970s, studies aimed at examining the possibility of employing for these purposes light cylindrical shells (in particular, liners accelerated by the magnetic field pressure produced by megaampere current pulses with characteristic times on the order of 100 ns) were begun in the Department of Relativistic Beams of the Russian Research Centre Kurchatov Institute, as well as in other laboratories [1–5].

Unlike ablative acceleration, whose efficiency is no higher than 10%, the magnetic acceleration of a liner matched to an external electric circuit can provide a 70% conversion of the electrical energy of the generator forming line into the kinetic energy of the shell. Then, this kinetic energy can be converted either into the electron temperature by adiabatically compressing the liner material or into X radiation by a collision at the axis. The latter scheme was successfully implemented in a number of experiments on the generation of SXR emission (see, e.g., [6, 7]). Note that the physical processes underlying this scheme appeared to be not so primitive as they seemed previously and still remain incompletely understood.

Another scheme that was investigated for several years in the Department of Relativistic Beams is the liner–target (or liner–converter) scheme proposed by L.I. Rudakov [8]. This scheme is based on the following concept:

(i) During implosion, a significant fraction of the kinetic energy of the liner, which is initially a hollow plasma cylinder with a relatively low internal plasma density, is converted into the thermal energy of the central plasma, while the temperature of the liner "wall" remains not very high.

(ii) A magnetic field provides the thermal insulation of the hot central plasma from the liner wall, and the stored plasma energy is transferred via electron heat conduction along the liner axis to a converter and is emitted as X rays.

The separation of the functions of the energy storage unit and the emitter between the central liner plasma and the converter, respectively, makes it possible to vary the energy of the generated X-ray photons by changing the converter material (from several hundreds of electronvolts for Pb and W to several tens of kiloelectronvolts for Kr and Mo).

The separation of functions provides two significant advantages of the scheme under consideration:

(i) the possibility of efficiently heating a low-Z (H or He) plasma to high electron temperatures because of the low radiation losses, which are many times lower than those typical of high-Z plasmas, and

(ii) the efficient emission of K lines of the converter material due to the fast transport of high-energy electrons toward the converter.

In spite of its multistage design, this scheme can provide the more efficient generation of moderately hard X-ray emission (10–30 keV) in comparison with the collisional scheme [9, 10].

The power sharpening and the spatial concentration of energy, which allow one to produce an intense X-ray source on the converter, are based on the fact that the plasma thermal conductivity is proportional to $T_e^{3.5}$. As a result, the energy flow sharply increases at the time of the maximum liner compression, when the electron temperature reaches its maximum value. Such a strong nonlinearity, however, complicates the implementation of this scheme in relatively small devices, because the emission intensity from the converter rapidly increases with the current and reaches a substantial value at currents higher than 10 MA. For this reason, our efforts were focused on experimentally studying the following aspects of this scheme:
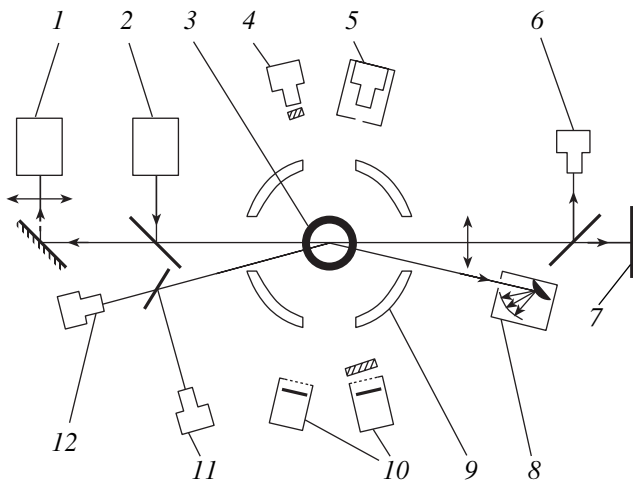
Fig. 1. General layout of the liner-implosion experiments: (*1*) streak camera, (*2*) laser system, (*3*) liner, (*4*) integral pinhole camera, (*5*) open X-ray image tubes, (*6*, *11*, *12*) optical frame image tubes, (*7*) system for recording laser shadowgraphs, (*8*) X-ray spectrograph, (*9*) return-current electrodes, and (*10*) X-ray diodes.

(i) the instability of the implosion of light liners and the possibility of achieving stable implosion,

(ii) the increase in the efficiency of energy transfer from ions to electrons during magnetic compression, and

(iii) the realization of the entire process at relatively low energies and a comparison of its characteristics with the results of numerical simulations.

2. EXPERIMENTAL FACILITIES AND DIAGNOSTIC TECHNIQUES

Experiments were carried out in the Module A-5 [11] and S-300 [12] high-current generators with water lines. In experiments conducted in the Module A-5 device ($U = 2$ MV, $I \sim 0.8$ MA, $\tau \sim 140$ ns) with an output resistance of $\rho = 2.2$ Ω, a pulse transformer with water transmission lines was used [13]. The double forming line of the Module A-5 generator serves as a primary line of the pulse transformer. Forty-eight secondary coaxial transmission lines, each having a wave impedance of 2 Ω, were placed into a common water-filled vessel. The transformation ratio of the pulse transformer was $K = 6$, and the output impedance was 0.04 Ω.

The pulse-transformer power is supplied to the liner unit through a three-dimensional energy concentrator (EC) [14] consisting of 16 nonuniform three-strip magnetically-insulated transmission lines (MITLs). The 150-kV voltage from the secondary lines of the pulse transformer is applied to the MITL electrodes. The lines join in the central unit of the EC, where the liner is placed. At a total EC inductance of 3–4 nH, the current through the liner attains 2.2 MA.

The S-300 device is an eight-module high-current generator with the output parameters $U = 1.3$ MV and $P = 10$ TW and the current pulse full width at half-maximum (FWHM) $\tau = 45$ ns. Its output forming system consists of 16 planar water forming lines, each having a wave impedance of 4.8 Ω and an equivalent electric length of 30 ns. These lines are charged in 180 ns to a voltage of 3.2 MV by means of 16 uncontrolled seven-channel water gaps and, then, are switched to the transmission water lines. A specific feature of the forming system is that the gaps are positioned in the middle of each forming line, which results in a twofold reduction in both the electric length of the forming system and the output resistance (to 0.15 Ω). The voltage pulse is introduced in the vacuum chamber through 16 triple planar water transmission lines. The liner unit is supplied with power through a three-dimensional low-inductance vacuum capacitor with magnetic self-insulation. The total inductance of the transmission circuit is no higher than 10 nH.

When the generator capacitors were charged to the half-maximum voltage (the so-called "cruising regime"), the current in the short-circuiting regime attained 4.2 MA and the current through the liner attained 3.6 MA, the rise time being 50–70 ns.

In magnetic implosion experiments, different types of liners were used: plastic liners with and without a gas shell, hollow cylindrical gas puffs with different aspect ratios, and the combinations of plastic liners with gas puffs. The liner parameters varied in the following ranges: the initial diameter was 2–5 cm, the length was 0.5–1 cm, and the mass was 40–300 µg.

In the experiments, the currents and voltages were measured at different points of the system. The measurements were performed with a wide set of diagnostics:

(i) visible-light electron-optical imaging of an imploded liner in the frame and streak-camera regimes,

(ii) SXR and XUV electron-optical imaging with the use of open X-ray image tubes with MCP photocathodes at an exposure time of 2–5 ns,

(iii) vacuum X-ray diodes with metal cathodes and different filters and X-ray pin-diodes,

(iv) different versions of laser probing, and

(v) X-ray spectrographs with planar and convex crystals.

Some of the specific features of the diagnostics used will be described when presenting the relevant experimental results.

A typical schematic of the experiment is shown in Fig. 1.

3. STUDIES OF THE PLASMA SHELL STABILITY DURING MAGNETIC IMPLOSION

A key problem related to the efficiency of the liner–target scheme, as well as other schemes employing

light liners as power sharpeners in devices intended for inertial confinement fusion (ICF) research, is the problem of the stability of the liner implosion. In this section, we present the results of systematic studies of the stability of liner implosion that were carried out in the Module A-5 and S-300 devices.

3.1. Implosion of Composite Plastic Gas-Shell Liners

The inhomogeneities of the density of the current flowing through the shell substantially increase the possibility of the onset of various large-scale instabilities. For this reason, the problem of the formation of a homogeneous current shell is of great importance.

One of the methods providing the current homogeneity is the use of composite plastic gas-shell liners. Such a liner consists of two coaxial cylindrical nitrocellulose shells with a thickness of 200 to 2000 nm. The gas between the shells is at a pressure of several torr, which is close to the minimum of the Paschen curve [15]. The liner mass can be varied by varying the shell thickness within the above range. The presence of a gas between the shells at a pressure close to the minimum of the Paschen curve substantially decreases the breakdown voltage. As a result, the number of current channels located on the inner side of the outer shell increases substantially (an image of breakdown recorded with the help of laser shadowgraphy is presented in Fig 2.). This ensures the azimuthal homogeneity of the initial electric breakdown and, accordingly, a homogeneous distribution of the current along the liner perimeter [16].

In experiments, the degree of the current homogeneity was qualitatively assessed from visible-light electron-optical images of the imploded liner. The degree of homogeneity of the initial electric breakdown of a plastic liner was compared in the case when the gas density near the liner surface was 10^{16} cm^{-3} and in the case of the breakdown of a plastic liner in vacuum. In the former case, an azimuthally homogeneous annular plasma column was formed, whereas in the latter case, well-defined surface-breakdown channels were observed. This effect was also clearly seen in streak images. In the case of the breakdown of a plastic liner in vacuum, well-defined luminous channels were formed, which remained visible at least up to the time $t = 150$ ns after the beginning of the current pulse. When breakdown occurred in the presence of a gas, the plasma glow was rather uniform.

In view of this fact, it was expected that the implosion of a liner with a well-formed current shell would be fairly stable. Indeed, the implosion of relatively heavy liners (with masses larger than 200 μg) turned out to be stable. The time dependence of the radius of the glowing plasma (see Fig. 3) and the instant of maximum compression, which were determined by processing streak images, agree with the one-dimensional model of the liner motion. For liners with a mass of
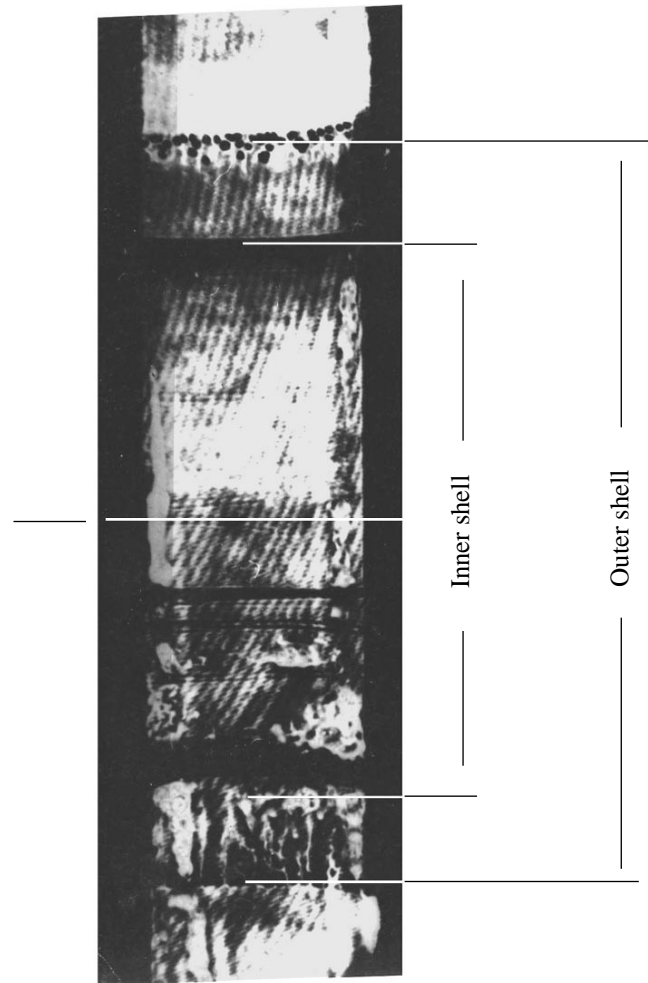
Fig. 2. Shadow photograph of the breakdown of a double-shell liner in the Module A-5 device ($\lambda = 5320$ Å; the diameters of the outer and inner shells are 2.8 and 2.0 cm, respectively; the gas pressure is 6 torr). Plasma formations are seen on the inner surface of the outer liner shell.

220 μg and height of 8 mm, the maximum radial velocity attains 2×10^7 cm/s and the implosion time (counted from the beginning of the current pulse) amounts to 180 ± 20 ns. The compression ratio R_0/r, which is determined from the frame shadow photographs and streak images, reaches 10. It follows from the laser shadow photographs [16] that no more than a few percent of the total mass of the liner material remain outside the opaque boundary of the compressed liner. From these photographs, it is also seen that, at densities $n > 10^{19}$ cm^{-3}, the surface of the compressed liner is not exactly cylindrical. This may be attributed to both the nonuniform compression of the liner material and the development of MHD instability.

At the instant of maximum compression, XUV and SXR pulses are generated with a FWHM duration of nearly 10 ns (Fig. 3) and power of up to 3×10^{11} W. XUV and SXR plasma images recorded at the instant of
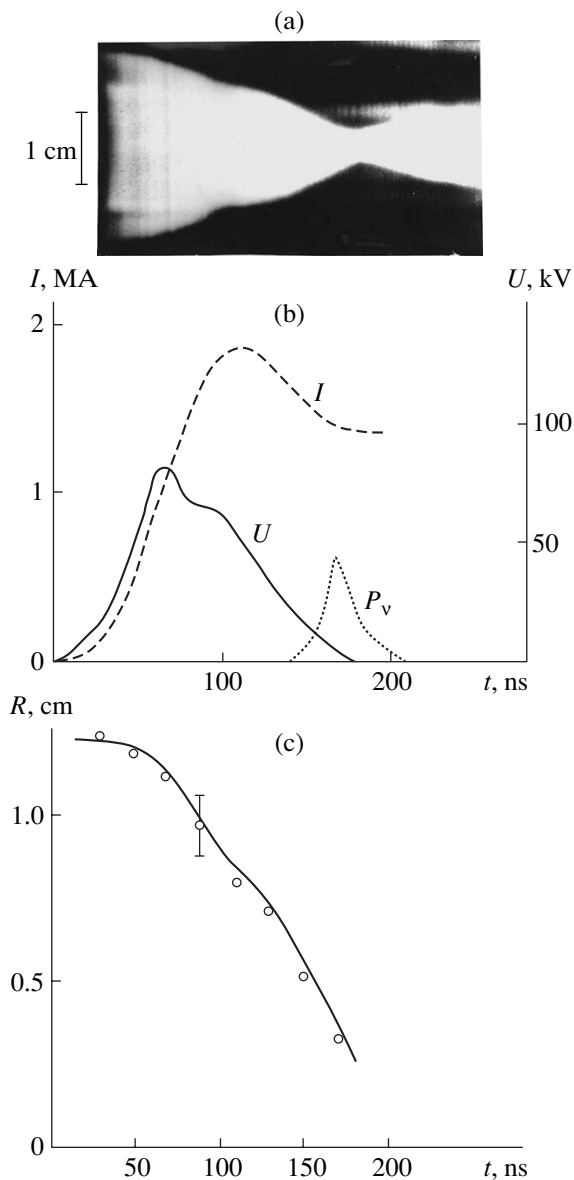
Fig. 3. Implosion of a double-shell liner with a mass of 220 mg in the Module A-5 device: (a) a visible-light streak image, (b) the electric parameters (the current I and the voltage U at the central unit) and the intensity of SXR emission P_ν, and (c) a comparison of the calculated (solid line) and experimental (circles) time dependences of the liner radius.

maximum compression show that, in a photon energy range higher than 10 eV, the radiation is emitted from a cylindrical plasma column 1.5–2 mm in diameter.

It might seem that the implosion of a two-shell liner of the same design, but with a smaller mass, would be similar to the implosion of a heavier liner. This would be promising for achieving higher final velocities. However, for liners with masses smaller than 200 µg, there is a discrepancy between the calculated results and the measured time dependences of the liner radius deduced from the plasma glow radius:

(i) for most of implosion process, the implosion velocity is almost constant and is smaller than the calculated one;

(ii) the measured implosion time is substantially longer than the calculated one;

(iii) several tens of nanoseconds before the collapse of the bulk plasma, a luminous precursor appears on the axis; and

(iv) XUV and SXR pulses arise well before (50–100 ns) the instant of maximum compression.

All this indicates that the liner stability is determined by not only the process of the current-shell formation but also other factors.

3.2. Implosion of Gas Puffs

The use of a light liner as a power sharpener in devices intended for ICF research requires the compact acceleration of the entire liner material. However, such an acceleration can be hampered by the onset of instability, in particular, the Rayleigh–Taylor instability. It is well known that, because of the onset of this instability, shells with a low aspect ratio ($R_0/\Delta R < 10$) are more stable during magnetic implosion in comparison with thin shells ($R_0/\Delta R > 10$). Consequently, it might be expected that the implosion of a hollow gas jet would be more stable in comparison with the implosion of a thin plastic shell. For this reason, a large series of experiments on the magnetic implosion of gas puffs was performed in the Module A5-01 and C-300 devices [17–20]. The main goals in these studies were the following:

(i) to clarify the nature of the instability developing during the liner implosion and

(ii) to find conditions for the most stable implosion.

The experiments on magnetic implosion were performed with hollow cylindrical gas jets. Such jets were produced by supersonic annular nozzles with Mach numbers of 3–5 in combination with high-speed pulsed (electromagnetic or explosive) valves. The initial density of the working gas (N_2, He, D_2, SF_6, Ar, Ne, and their mixtures) were varied over a wide range by varying the delay time of the high-voltage pulse with respect to the instant of gas puffing.

A characteristic feature of the implosion of highly radiative gas puffs ($Z > 2$), as well as plastic shells, is a discrepancy between the experimental and calculated time dependences of the liner radius at small masses (≤ 200 µg) of the accelerated shells. The measured implosion time exceeds the calculated time, and the measured final velocity and the corresponding kinetic energy are lower than the those calculated from the electrotechnical parameters. It is also important that the liner boundary moves with a nearly constant velocity. As in the case with a plastic liner, several tens of nanoseconds before the collapse of the bulk mass of the liner, a luminous precursor appears on the axis. XUV
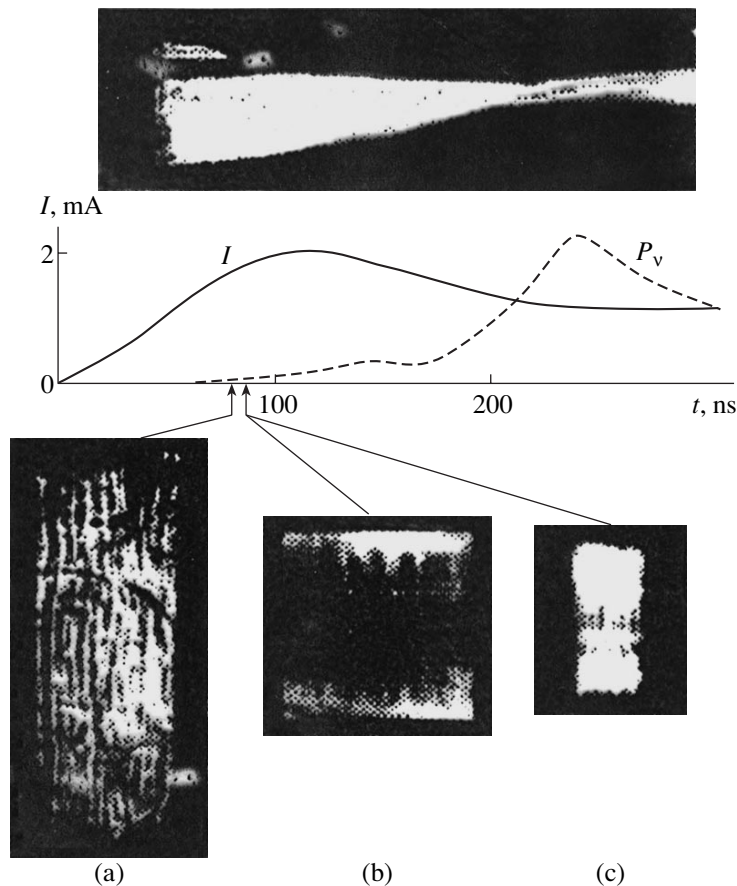
Fig. 4. Implosion of a gas (N$_2$) puff. A streak image (on the top), a shadow photograph (a), and frame SXR (b) and visible-light (c) images corresponding to the times marked on the current oscillogram.

and SXR pulses arise well before (50–100 ns) the instant of maximum compression (Fig. 4).

Such time behavior of the liner can be explained by the penetration of the current, magnetic field, and rare plasma inside the liner through discontinuities in the current shell. The current cannot flow through the discontinuous shell; as a result, the shell moves by inertia.

The fact that the instability develops in the early stage of implosion was confirmed by visible-light and SXR electron-optical images, as well as by laser shadow photographs. It can be seen in XUV and SXR images that, starting from 80–130 ns, a longitudinal modulation in the form of strata appears in the brightness of the plasma column (Fig. 4). The characteristic modulation period is in the range 0.8–2.0 mm and depends on the mass and chemical composition of the liner. Along with the strata, a luminous precursor appears on the axis. This radiation corresponds to XUV and SXR ($h\nu \leq 100$ eV) photons. Then, the irregularities of the outer boundary increase, but the characteristic spatial modulation period changes insignificantly. We note that the strata on the laser shadow photographs correspond to the strata on the electron-optical images recorded in the frame regime. Their orientation coincides with the direction the magnetic field B_φ. The best

proof of this circumstance is the fact that the strata are tilted at an angle to the axis when a longitudinal magnetic field is applied (see below).

By the time perturbations appear on the liner boundary and the strata appear in the streak images and laser shadow photographs, the shell boundary has been displaced to a distance that is much shorter than the initial thickness of the gas jet. It might seem that, in this case, there is no sense in talking about the onset of the Rayleigh–Tailor instability. However, the process of the current-shell formation turns out to be more complicated. A particular role in the study of this process is played by laser probing. For this reason, we will describe this technique and results obtained with it in more detail.

In these experiments, we employed frame laser probing and simultaneously obtained shadow and schlieren photographs of the plasma using the second harmonic of a YAG : Nd laser ($\lambda = 5320$ Å, see Fig. 5). The laser pulse duration was 7 ns, and the laser energy at the second harmonic was 20 mJ.

The recording system had an aperture of 0.25, which was the maximum possible value under our conditions. In this case, the electron-density gradient that gives shading due to the refraction in the shadow channel
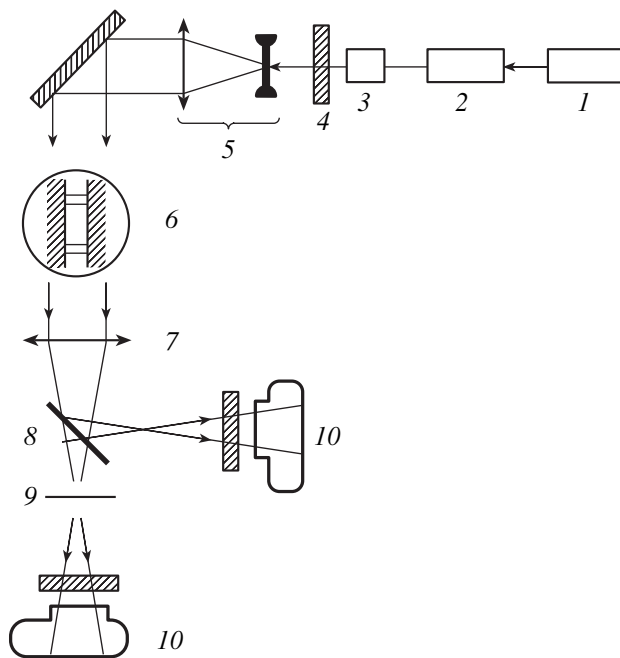
Fig. 5. Arrangement of simultaneous schlieren and shadow photography: (*1*) oscillator, (*2*) amplifier, (*3*) nonlinear crystal (lithium niobate), (*4*) SZS-22 filter, (*5*) telescope, (*6*) liner, (*7*) receiving lens, (*8*) beam splitter, (*9*) schlieren fiber, and (*10*) photographic camera with filters.

must satisfy the condition $|\nabla N_e| \geq 2 \times 10^{21}$ cm^{-4}, which follows directly from the formula $|\nabla N_e| = \dfrac{\Omega}{4.46 \times 10^{-14} \lambda^2 l}$ [21], where Ω is the objective-lens aperture and l is the laser path in the plasma. For our experiments, this corresponds to an electron density of $\sim 2 \times 10^{20}$ cm^{-3}. For a nitrogen gas puff at $T_e \sim 10$ eV, this corresponds to a line-averaged ion density of $\sim (5–7) \times 10^{19}$ cm^{-3}.

In the schlieren channel, a fiber was placed at the lens focus so that it was parallel to the liner axis. In such a way, we could visualize the density gradients perpendicular to the axis; in particular, we could resolve the shell boundaries.

Figure 6 shows the results of the laser probing of a liner 80 ns after the beginning of the current pulse. It can be seen from the schlieren photograph that, by the probing time, the outer liner boundary has been displaced by 3–4 mm and the total number of ions involved in the acceleration process is no more than 5×10^{18} (i.e., no more than one-half of the total shell mass). In the shadow photograph, one can see narrow (~ 0.01 cm) transparent regions (strata) oriented transverse to the liner axis. The strata are spaced by ~ 0.1 cm, and the radiation attenuation in the shadow region is ~ 5.[1] The appearance of a shadow at so small a mass

---

[1] A similar picture was observed in [22], but the authors restricted the interpretation to the brief comment that they observed sausage instability.
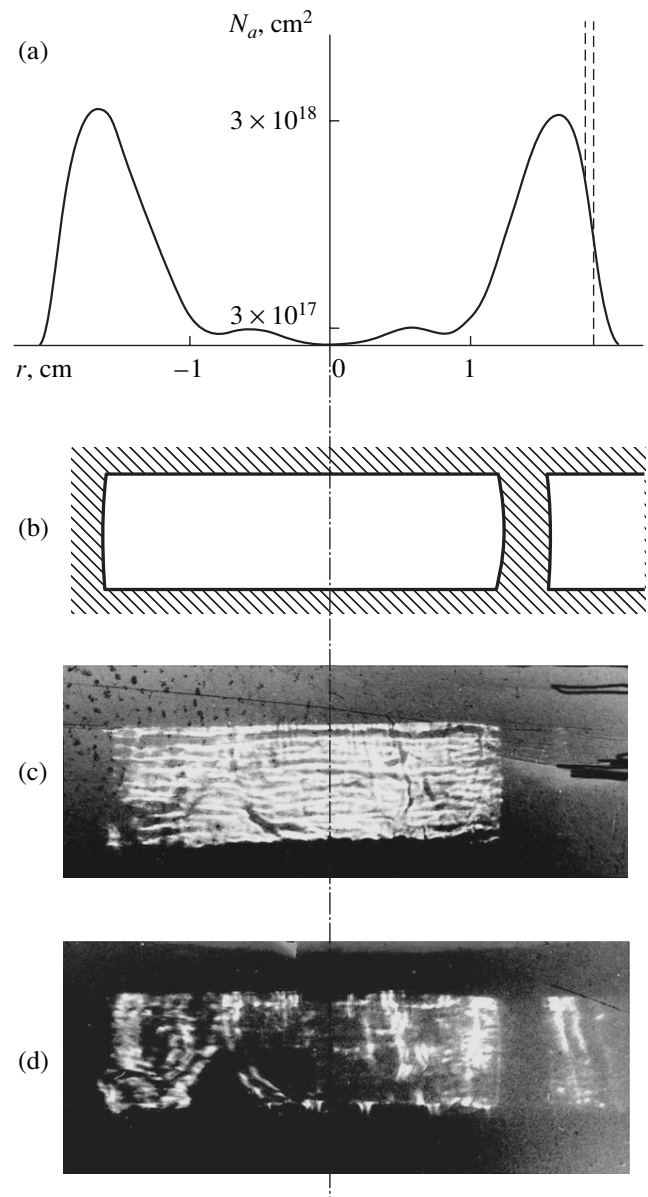
Fig. 6. Results of the laser probing of a gas (N$_2$) puff: (a) the initial gas-density distribution (solid curve) and the model distribution of ions at the liner boundary (dashed line) that is required to provide laser absorption ($N_i > 5 \times 10^{19}$ cm^{-3}); (b) the return-current electrode with a diagnostic window; and (c) a shadow and (d) a schlieren photograph of the liner 80 ms after the beginning of the current pulse (the schlieren fiber is parallel to the liner axis).

involved in the acceleration process indicates that a thin shell is formed. According to the formula $N_i = 7.5\nu(\varepsilon T_e^{3/2}/Z^3 g)^{1/2}$, where ν is the probing frequency, ε is the absorption coefficient, and g is the Gaunt factor (see [23] for details), in order to ensure inverse bremsstrahlung, the shell thickness must be no more than 2×10^{-2} cm at an ion density of no higher than 5×10^{19} cm^{-3}.

At this density and $T_e = 10$ eV, which approximately corresponds to the equilibrium between radiative losses and Ohmic heating, the equality $B^2/8\pi = (n_i + n_e)T$ holds in the shell. The above shell thickness is much smaller than the skin depth $\delta_{sk} = (c^2\tau/4\pi\sigma)^{1/2}$, which is equal to 0.1 cm under our conditions.

We note that the shadow regions visualize the high-density shell; however, no inferences about the current flowing through the shell can be made from these data. The density distribution in the shell is similar to that in the snow plow model (see Fig. 6) with a compression ratio higher than 20.

Seemingly, the best fit to the experimental results is provided by the liner model proposed by Chukbar [24]. In this model, a thin hot current shell is surrounded by a dense shell comprising almost the entire mass of the imploding liner. One of the consequences of this model is that, due to strongly nonuniform heating, the electric field is not skinned, whereas the magnetic field is skinned and concentrated in the current shell. This is because, in the inner cold layers, the conductivity σ and, consequently, the current almost vanish. As a result, the electric field can cause breakdowns along the inner surface of the dense shell, thus giving rise to precursors.

We note that the implosion of such a thin liner can be accompanied by the onset of the Rayleigh–Tailor instability. However, there are good reasons to believe that the liner instabilities are of different nature. Numerous experiments allow one to conclude that these instabilities possess properties that cannot be described in terms of the Rayleigh–Taylor instability [20]:

(i) At the same total mass, the imploding gas puffs made of materials with a lower atomic weight are generally more stable than those made of materials with a higher atomic weight. The implosion of heavier shells is more stable than that of light shells. In particular, at currents of 2.5–3.0 MA, "heavy" liners with a linear mass density of 400–500 μg/cm turn out to be stable.

(ii) Instability develops even in the implosion phases in which the liner moves with a constant velocity. Instability is also observed in the early stage of implosion when the shell just begins to move (e.g., when the shell is displaced by less than one-tenth of its initial radius).

(iii) The characteristic thickness of a dense shell is 2×10^{-2} cm $\sim c/\omega_{pi}$. Under these conditions, the MHD approach is certainly inapplicable.

On the other hand, the above experimental observations do not contradict the Hall instability, whose theory was developed in [20, 25, 26]. This instability results in the deep longitudinal modulation of the shell thickness, which, in turn, stimulates longitudinal plasma flows and, finally, can result in the breaking of the current shell. Perturbations caused by the Hall instability can also serve as a seed for the subsequent onset of the Rayleigh–Taylor instability.

Thus, although the type of the observed instability is hardly possible to unambiguously identify in the "crude" experiment (whose physical picture can also be additionally distorted by many side effects[2]), all the experimental evidence allows us to conclude that the Hall instability plays a dominant role under our experimental conditions.

4. EXPERIMENTAL MODELING OF THE LINER–TARGET SCHEME

In this section, we present the results of the experimental modeling of the liner–target scheme. The experiments were carried out in the Module A-5 device [28, 29] with a relatively low longitudinal magnetic field. The use of a low magnetic field was motivated by two reasons:

(i) the necessity of decreasing the electron heat transport across the hot plasma column to the dense cold imploding shell, and

(ii) the aim of increasing the stability of the imploding liner.

From the general considerations, it follows that the stability of an imploding shell should increase with increasing shell thickness. This can be achieved, e.g., by freezing the longitudinal (axial) magnetic field in the shell [30, 31]. Moreover, due to the different radial distributions of the B_φ and B_Z components, the magnetic field lines at different radii are inclined to the axis at different angles (i.e., the magnetic field is sheared), which also increases the stability of the system. We note, however, that the magnetic shear plays an important role only when the axial magnetic field component is comparable with the azimuthal one. Below, it will be shown that, in our experiments, this condition is satisfied even at a relatively low longitudinal magnetic field because of the specific structure of gas puffs.

In the experiments carried out in the Module A-5 device, a supersonic ($M = 4$–6) cylindrical hollow gas jet was used as a liner. The working gas was deuterium or helium with 2% diagnostic addition of Ne. The jet was formed with the help of a high-speed pulsed valve (with an operating time of ~100 μs) that had a supersonic annular nozzle. The nozzle exit served as a negative electrode of the discharge gap. The anode was either an annular grid electrode or a wire array in the form of a spoke wheel. The liner length was 1 cm, and the outer and inner nozzle diameters varied in the ranges 2–4 cm and 1.0–2.6 cm, respectively. The mass per unit length varied from 50 to 100 μg/cm. The amplitude of the current flowing through the liner was 2.5 MA, and the current rise time was 100 ns.

The 15-kG longitudinal quasi-steady magnetic field in the liner acceleration region was produced by a coil

---

[2] One of the effects of this sort may be the initial small-scale gas density inhomogeneity that was revealed in our experiments with the help of Rayleigh scattering [27].
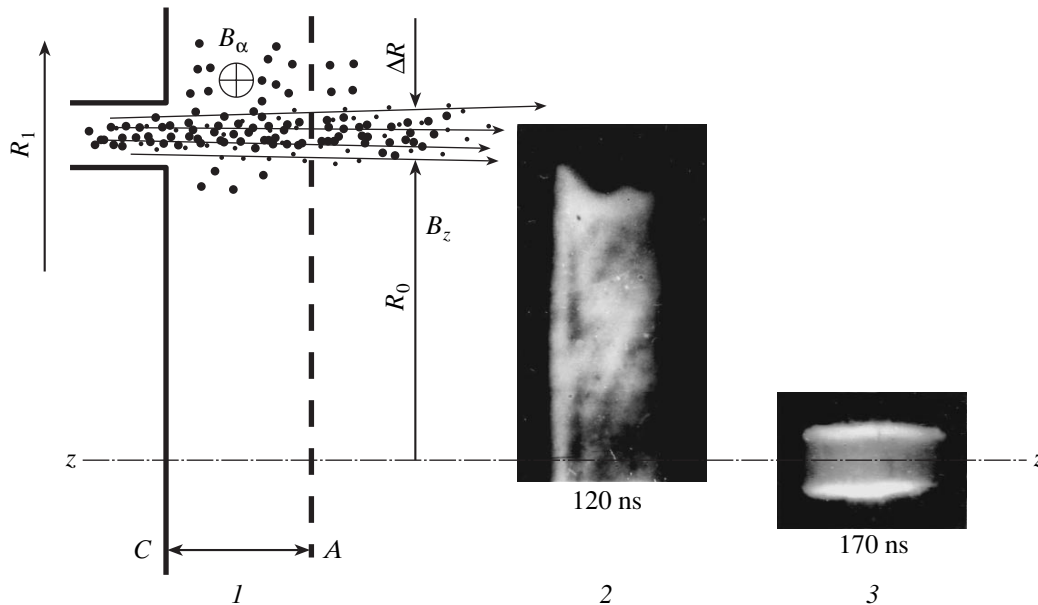
Fig. 7. Liner implosion in the presence of a longitudinal magnetic field: (*1*) a schematic of the experiment, (*2*) an SXR image of the liner at the instant of maximum current (strata tilted at an angle of ~45° to the axis are seen; applying a reversed longitudinal magnetic field changes the tilt angle by 90°), and (*3*) an SXR image of the liner at the instant of maximum compression.

that was fed by a current pulse with a duration of 20 ms. A schematic of the experiment is shown in Fig. 7.

The time evolution of the plasma was studied with the help of a standard set of diagnostics. In order to simultaneously observe X-ray images of the liner in different spectral ranges and increase the dynamic range of the X-ray camera, the liner image on the cathode of each framing X-ray image tube was formed with the help of two pinhole cameras that had different apertures and filters. Streak-camera laser shadowgraphy was also used. Let us consider this technique in more detail.

Frame laser probing is commonly used to diagnose the time evolution of a dense plasma. This technique was also used by us in experiments on liner implosion (see [18]). Probing in the frame regime gives two-dimensional images, which, however, provide information only at some instants of implosion, whereas it is desirable to obtain information about the entire implosion process.

The main difficulty in the implementation of streak-camera laser shadowgraphy is the generation of a smooth laser pulse with a duration of several hundred nanoseconds. To this end, we created an original and simple generator consisting of two identical YAG : Nd lasers that operated in a free-running mode. The pumping intensity was much higher than the lasing-action threshold; as a result, the number of intensity oscillations arising due to the spiking character of the emission ($\tau = 250$ ns) were reduced to 4–5. The two beams with mutually orthogonal polarization were aligned by a Glan prism and, then, led into a telescope, forming a probing beam (Fig. 8). There were no more than two to three intensity oscillations with a period of 300–400 ns in such a beam, which is acceptable for streak imaging.

The receiving part of this diagnostics (Fig. 8) consisted of two lenses producing a reduced image of the object on the slit of an FER-6 streak camera, which was synchronized with the experimental device. The lasers started 20–40 μs before the beginning of the liner current because, in this time interval, the pulsations of laser radiation were minimal. To decrease the influence of refraction, the receiving part was designed so as to ensure a viewing angle as large as possible. For the given design of the output unit, this angle attained 0.2 rad, which allowed us to interpret the appearance of a shadow as the influence of inverse bremsstrahlung in a plasma with $N_e \sim (6–8) \times 10^{19}$ cm^{-3} at $T_e \sim 50$ eV.

Experiments have shown that the initial longitudinal magnetic field with $B_{z0} \geq 5$ kG (which is much lower than the azimuthal magnetic field $B_\varphi \sim 200$ kG at the liner surface in the initial stage of implosion) significantly affects the character of the liner acceleration. In this case, the liner implosion is symmetric (Fig. 9a) and the acceleration process is stable and reproducible. Figure 9b shows the experimental time dependence $R(t)$ of the liner radius obtained by processing streak images and the time dependence calculated by the formula that was derived by the snow plow model with allowance for the longitudinal magnetic field:

$$m'\frac{d^2R(t)}{dt^2} = -\frac{1}{c^2}\frac{I^2(t)}{R(t)} + \frac{B_{z0}^2 R(t)}{4}[R_0^4/R^4(t)],$$
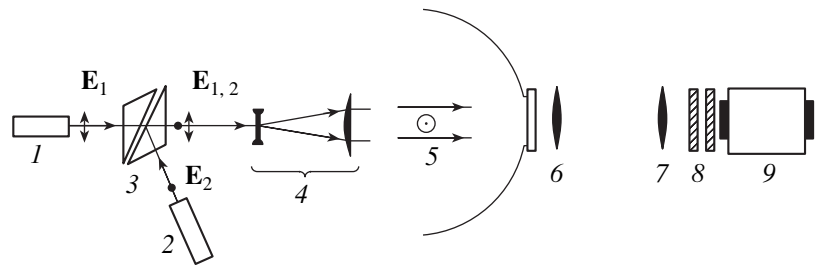
Fig. 8. Layout of streak-camera laser shadowgraphy (the streak-camera slit lies in the plane of the figure): (*1*, *2*) YAG : Nd lasers producing radiation with mutually orthogonal polarization, (*3*) Glan prism, (*4*) telescope, (*5*) liner, (*6*, *7*) receiving lenses, (*8*) filters, and (*9*) streak camera.
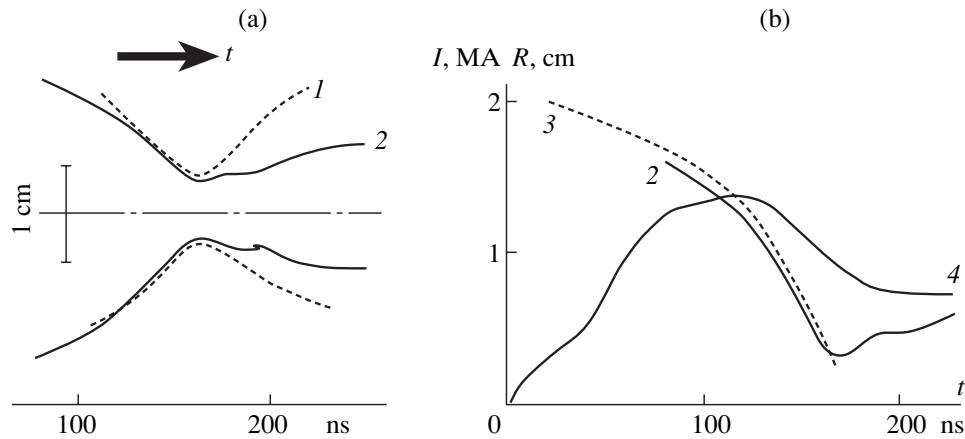
Fig. 9. Implosion of a deuterium gas puff in a magnetic field: (a) the dynamics of implosion by the data of (*1*) laser shadowgraphy and (*2*) self-radiation measurements, and (b) the measured (*2*) and calculated (*3*) time evolution of the liner radius for the current waveform given by curve *4*.

where m' is the liner mass per unit length, R_0 is the initial liner radius, and B_{z0} is the initial longitudinal magnetic field. It can be seen from Fig. 9b that the time dependence $R(t)$ calculated by formula (1) for the experimental values of the liner current agrees well with the measured values of the shell radius for deuterium jets with a mass of 50–75 μg.

By the end of implosion, the liner velocity attained 3×10^7 cm/s and the compression ratio was $R_0/R_{min} > 8$. The minimum radius of the emitting plasma, which was determined from laser-shadow streak images and self-radiation streak images in the visible spectrum, amounted to 2–3 mm (Figs. 7, 9).

At the instant of maximum compression, an elastic reflection of the shell occurs, which is observed most clearly in the laser-shadow streak images. This effect is quite expectable when the energy loss is smaller than the kinetic energy of the liner, which is the case under our experimental conditions. The difference between the self-radiation and laser-shadow streak images can be attributed to the onset of instability in the stage of plasma expansion. In the course of expansion, most of the plasma mass passes through the magnetic field by moving apart the field lines. In doing so, the plasma

cools and ceases to glow, but continues to absorb laser radiation. The remaining low-density plasma with a relatively high temperature and the pressure $nT \leq B_\varphi^2 /8\pi$ is confined by the magnetic field for a rather long time and glows brightly.

The radiation emitted from the internal plasma region and recorded in streak images is weakly absorbed by the cold shell (which produces a shadow in laser-shadow streak images) because the wavelength of the emitted radiation differs from the laser wavelength. We note that self-radiation streak images were obtained by using a light filter with a transmission maximum in the wavelength range 4000–4200 Å, which is a factor of 2.5 shorter than the laser wavelength. This results in a sixfold decrease in the absorption coefficient.

As was mentioned above, a fairly homogeneous implosion can be achieved when an axial magnetic field with an induction of 5–10 kG (which is smaller than $0.1 B_\varphi$ at the maximum current) is applied to the liner. This is because, in the course of the liner formation, the axial magnetic flux that is frozen in the low-density plasma at the periphery of the jet (the gas corona) is gathered and pressed by the current-carrying shell
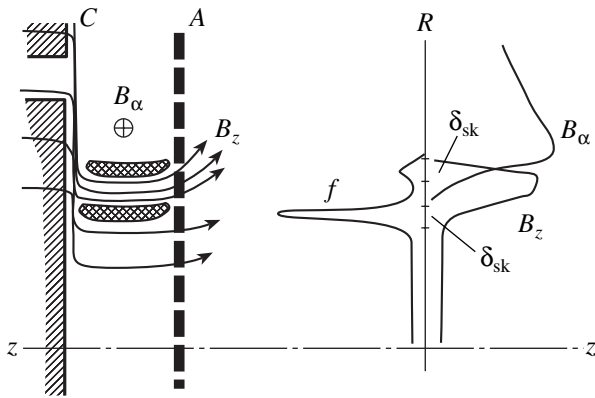
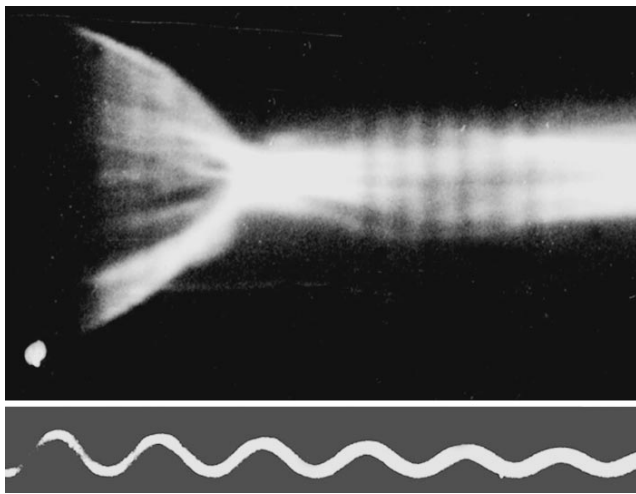**Fig. 10.** Model density and magnetic field distributions.

Fig. 11. Streak image of the implosion of a deuterium gas puff (on the bottom, the calibration curve with a frequency of 20 MHz is shown). The liner starts glowing 50–60 ns before the beginning of the current pulse; at this instant, the shell velocity is ~1.2×10^7 cm/s.

toward the plasma shell that is formed from the gas jet. As a result, a plasma layer with the frozen-in axial field $B_z = B_\varphi$ is formed (Fig. 10). The layer thickness $\pi[R_1^2 - (R_0 + R)^2]B_{z0}/2\pi(R_0 + R)B_\varphi$ (where R_1 is the radius of the return-current electrode) is comparable with the skin depth $\delta_{sk} = (c^2\tau/4\pi\sigma)^{1/2}$. For $R_1 = 4$ cm, $R_0 + R = 1.7$ cm, and $B_{z0} = 10^4$ G, we find that the plasma layer is 2 mm thick. The conclusion that the jet has a corona is confirmed by the experimental results. First, as is seen in streak images, the emission at the initial radius does not appear immediately after the beginning of the current pulse, but with a time delay of $t_0 = 50$–70 ns. Second, the boundary of the emitting region starts moving with a finite (rather than zero) velocity (Fig. 11).

These features of the jet glow can be attributed to the presence of a corona that comprises 3–10% of the jet mass and whose radius exceeds the jet radius by a factor of 2–2.5. The jet starts glowing brightly at time t_0, when the shock wave that is formed in the corona enters the liner, which immediately begins to implode with the velocity $B_\varphi(t_0)/(4\pi\rho)^{1/2} = 1$–$2 \times 10^7$ cm/s.

Figure 10 qualitatively shows the radial profiles of the magnetic fields B_z and B_φ and the density ρ that were found by Rudakov [29]. The bulk of the shell mass is concentrated in a layer (with the thickness δ_{sk}) that is located on the inner side of the shell. This mass is accelerated by the pressure of the field B_z, which is counterbalanced on the outer side by the skinned field B_φ.

The shell thickness was estimated experimentally with the help of laser shadowgraphy. Taking into account the data on inverse bremsstrahlung for a deuterium liner with a 2% addition of Ne and a mass of ~50 μg, we can estimate the thickness of the wall of the plasma cylinder that contains the bulk of the liner material. In the initial stage of implosion, this thickness is no larger than 0.2 mm, and it is no larger than 2 mm in the final stage.

According to theoretical predictions, a thin current-carrying shell accelerated by the pressure of the field B_φ is unstable [25, 26, 28]. The skin layer on the outer surface of the liner is unstable against the modulation of its thickness with a period of $2\pi\omega_{Be}\tau_{ei}\delta_{sk}$. The arising strata are oriented along the total magnetic field in the middle part of the skin layer. This field is a superposition of the longitudinal field B_z and the azimuthal field B_φ. In the liner images produced by X rays with photon energies $h\nu > 100$ eV, we observed modulation in which the strata were oriented at an angle of 30°–60° to the liner axis, i.e., in the direction of the total magnetic field (Fig. 7, 2). The interval between the strata was 1–2 mm. When the direction of the external magnetic field B_z was reversed, the direction of the strata changed by 90°. Therefore, the appearance of oblique strata is experimental evidence of the instability of the current-carrying shell. However, as follows from qualitative considerations, the field B_φ cannot break the plasma with the frozen-in field B_z and, hence, the current cannot penetrate into the shell.

It can be seen from Fig. 7 that the tubular structure of the shell is retained at a tenfold compression of the jet ($R_0/r_{min} = 10$). The shell radius is ≈1 mm, and the shell thickness is ≈0.4 mm. The ratio δ/r between the thickness and radius of the compressed shell is 0.2–0.4. The transverse size of the high-temperature internal plasma that is observed in images produced by X rays with photon energies $h\nu > 900$ eV is 0.1–0.15 cm.

From the experimental results listed above, it follows that a plasma shell is formed in a longitudinal magnetic field and that the shell acceleration toward the axis is stable.
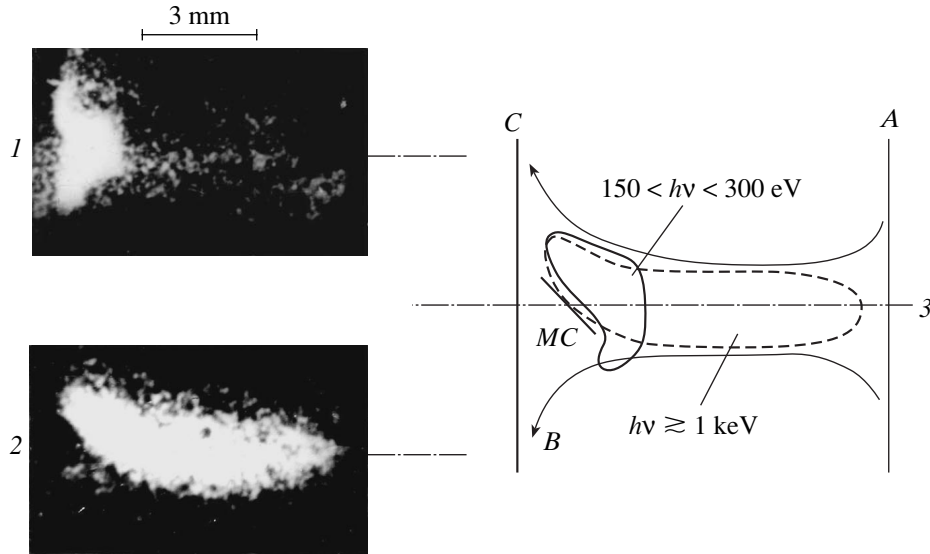
Fig. 12. SXR images of the liner plasma in two different spectral ranges, (*1*) $150 < h\nu < 300$ eV and (*2*) $h\nu \geq 1$ keV, at the instant of maximum compression in the presence of a longitudinal magnetic field and (*3*) a schematic of the imploded liner: (*C*) cathode, (*A*) anode, (*B*) magnetic field lines, and (*MC*) mica converter.

The shell thickness can be estimated from the following considerations. After the shell moving with velocity *V* is stopped by the counterpressure of the compressed axial magnetic flux $\pi R_0^2 B_{z0}$, the shell is heated. The shell temperature can be determined from the energy conservation law and the equality of the pressures (the radiative and ionization losses are relatively small):

$$\frac{H_z^2}{8\pi}\pi r^2 + 3n_i T_{sh} 2\pi \delta r = \frac{Mv^2}{2} 2\pi \delta n_i r.$$

From this equation, we find the shell temperature,

$$T_{sh} = \frac{Mv^2}{2} \frac{\delta}{r + 3\delta}.$$

For a thermal velocity of the shell of 2.5×10^7 cm/s ($Mv^2/2 = 625$ eV) and a temperature below 70–80 eV, the relative shell thickness is $\delta/r \leq 0.2$. Assuming that the shell is decelerated by the counterpressure of the field B_z, we find that the minimum shell radius is 1 mm at $B_z = 10^4$ G, which coincides with the experimental value. Accordingly, the shell thickness is 0.2 mm.

The success in realizing the stable compression of a gas shell in a longitudinal magnetic field allowed us to qualitatively model the heat-conduction scheme of an X-ray source. As a converter, we used a thin mica plate placed near the cathode at an angle of ~45° to the axis. The main diagnostics in this experiment was electron-optical imaging in two SXR spectral ranges: (i) $h\nu = 150$–300 eV and (ii) $h\nu > 1$ keV. Each X-ray image tube was equipped with a pinhole camera with two holes of different diameter, which were covered with different filters.

The results of this experiment are shown in Fig. 12, which presents the images of the plasma shell and the plasma generated by the converter. The images with an exposure of 3 ns were made in the above spectral ranges at the instant of maximum compression. The figure also shows the relative positions of the shell and the mica plate.

In the images, we can clearly see the heated plasma column and a burst of SXR emission generated in the converter and the surrounding low-temperature plasma. It is important that no SXR bursts were observed 10 ns before or after the instant of maximum compression. This clearly demonstrates the realization of the heat-conduction scheme of the conversion of the magnetic field energy into SXR emission.

Later, in joint experiments in the Ambiorix device (France), the possibility of stabilizing the implosion process by a longitudinal magnetic field was confirmed and the generation of SXR emission from the converter located at the end of the device was detected [32, 33]. It should be noted that the experimental values of the plasma parameters and converter emission are in fair agreement with the results of numerical simulations by Russian [34] and French [35, 36] codes.

Thus, the experiments carried out in the Module A-5 and Ambiorix devices clearly demonstrated the stabilization effect of the longitudinal magnetic field and the feasibility of the liner–target scheme, which allows one to produce an intense SXR source due to the heat transfer from the high-temperature liner plasma to the end of the plasma column.
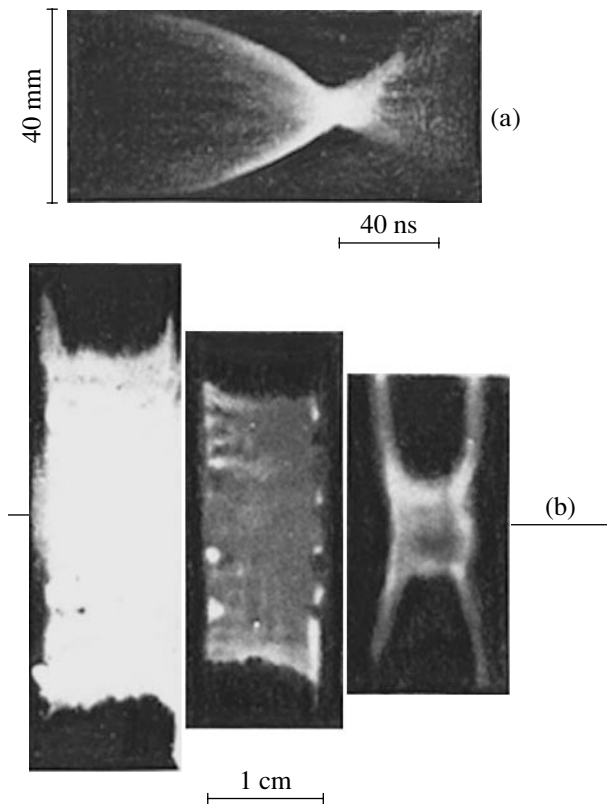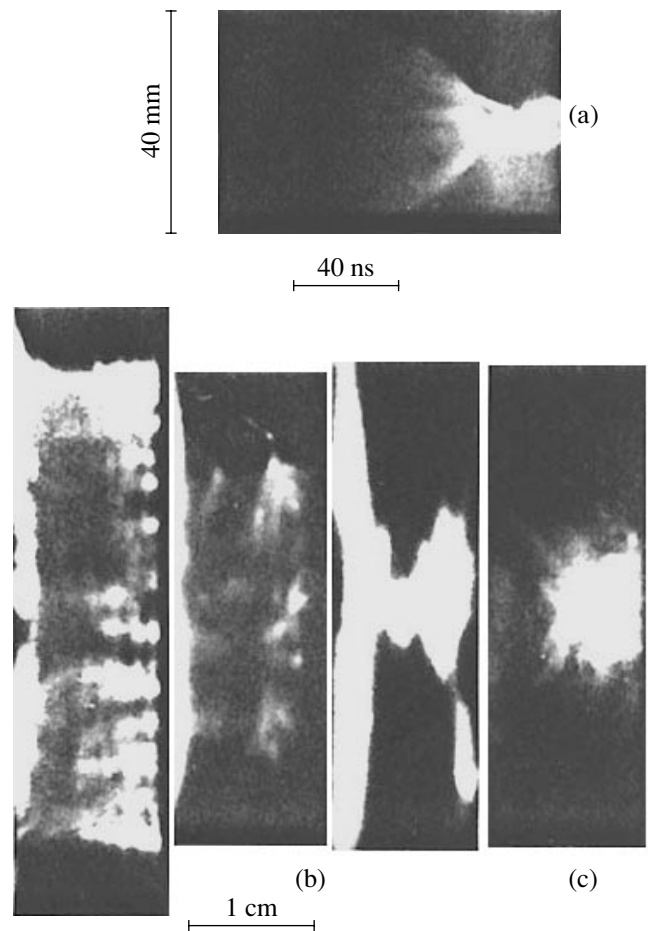
Fig. 13. Visible-light electron-optical images of an imploding helium gas puff in the (a) streak-camera and (b) frame regimes.

Fig. 14. (a, b) Visible-light and (c) SXR electron-optical images of an imploded argon gas puff in the (a) streak-camera and (b, c) frame regimes.

It should be emphasized, however, that this effect is nonlinear in terms of input energy; moreover, there is a threshold input energy. Hence, it can be said with assurance that the results agree with the theoretical model only qualitatively. Nevertheless, comparison of the experimental and computational results allows us to conclude that the basic concept of [8] is correct.

5. STUDIES OF THE FORMATION AND DYNAMICS OF HIGH-CURRENT HETEROGENEOUS Z-PINCHES

Remember that a specific feature of the liner–converter scheme is the separation of the functions of the energy storage unit and the emitter. The electrons of the low-radiative (hydrogen) plasma, which are heated up to 10 keV during the magnetic implosion, transfer their energy by conduction to the highly radiative converter located at the end of the plasma column. Theory and numerical simulations [9, 10] show that the efficiency of such a scheme is higher than that of the conventional scheme.

The implementation of this scheme requires stable implosion. In the previous section, it was shown that applying an axial magnetic field is an efficient method for suppressing instabilities. However, at large high-current devices, such a stabilization would require

magnetic fields of no lower than 100 kG, which is hardly possible in actual experiments. Therefore, an important problem is to search for other methods for stabilizing magnetic implosion.

Theory and numerical simulations [20, 26] show that, for the currents used in our experiments (~3 MA), the Hall instability is less pronounced in thick shells of low-Z gas puffs (H_2, He). For this reason, we carried out experiments on the implosion of a helium jet produced by an annular nozzle with the Mach number $M = 5$ and an outer and inner diameter of 4 and 1 cm, respectively. These experiments turned out to be successful [37].

Operating conditions were found under which a liner formed from a thick hollow helium jet is stable in the initial stage of implosion. The perturbations of the liner surface, which were recorded in visible light as strata, did not grow in the course of implosion. Moreover, both the absolute magnitude and the relative value $\Delta R/R(t)$ of these perturbations decreased. We believe that this effect is a manifestation of the two-dimensional Hall dynamics of the low-density coronal plasma. The Hall effects manifest themselves over

scale lengths of about c/ω_{pi}. A decrease in this parameter during implosion leads to a decrease in the modulation of the shell diameter. This results in the stable implosion of a thick helium liner up to $R_{in}/R_{fin} = 8–10$, the final velocity being $\sim 5 \times 10^7$ cm/s. The streak images of the implosion of a helium liner are presented in Fig. 13. For comparison, Fig. 14 demonstrates similar images of the unstable implosion of an argon gas puff formed by the same nozzle. Besides the absence of perturbations, the experimental evidence of stable implosion is the symmetric shape of the imploded shell and good reproducibility of the $R(t)$ dependences.

We note that, as early as in 1963, B.B. Kadomtsev showed that a continuous Z-pinch in which the pressure does not decrease too rapidly toward the periphery is stable against hydrodynamic perturbations [38].

However, the implementation of the heat-conduction scheme with a nearly continuous Z-pinch is hampered because of the contradictory requirements for the parameters of the liner plasma. In fact, the energy in the imploding plasma is initially concentrated in the kinetic energy of the moving shell. During the collision at the axis, this energy is converted into the thermal energy of the ions. Then, the ion thermal energy is transferred in Coulomb collisions to the electrons, which finally transport it to the converter. Estimates show that, in a low-Z (H, He) plasma, the slowest process that limits the efficiency of the entire scheme is the energy transfer from ions to electrons.

The electron heating can be intensified by increasing the ion charge. However, this leads to a decrease in the thermal conductivity; as a result, the heat flux can be insufficient for transferring the required amount of the plasma energy to the converter during the phase of maximum liner compression. Furthermore, the magnetic implosion of a Z-pinch or liner with a relatively large ion charge number is accompanied by the formation of a thin shell, which is unstable (see above). Moreover, in this case, the energy losses related to the emission in the SXR and XUV spectral regions increase.

These contradictions can be avoided by creating complex Z-pinches in which the region with the efficient electron-to-ion energy exchange is spatially separated from the region with the high electron thermal conductivity [39].

One of the possible realizations of this approach is the creation of a moderate-Z plasma by evaporating thin fibers with an appropriate chemical composition that are oriented parallel to the axis and form a cylindrical surface with a radius that is several times smaller than the initial radius of the gas puff (Fig. 15). The fibers will be evaporated under the action of the front of a heat wave generated by a shock wave in a light-gas cylinder under the action of a magnetic piston. Preliminary estimates show that, for a fiber thickness of 1–3 μm, the plasma produced expands 1–2 mm in a time of $\sim$10 ns. Hence, by locating thin fibers compactly, it is possible to produce a continuous cylindrical plasma with the
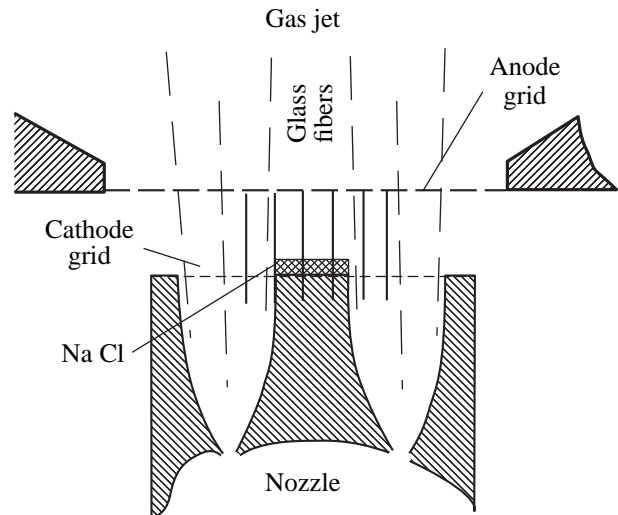

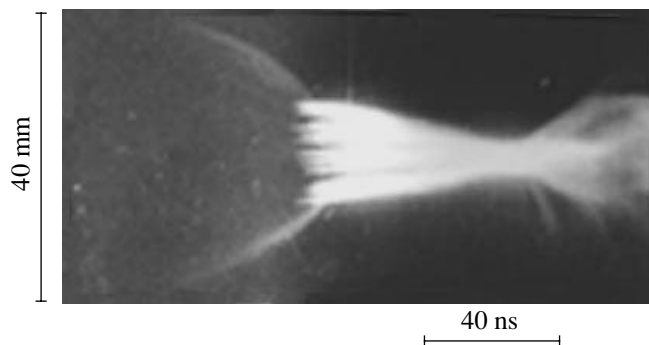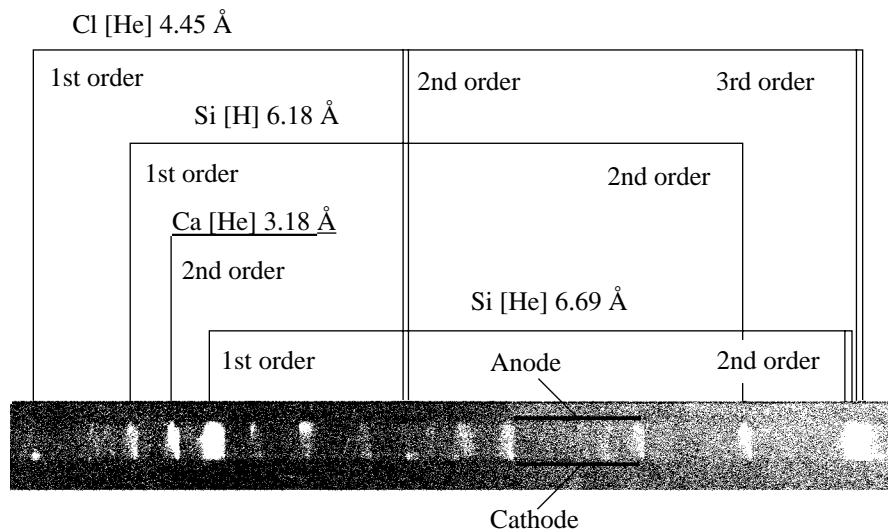**Fig. 15.** Schematic of the diode gap in experiments on the implosion of heterogeneous Z-pinches.

Fig. 16. Streak image of the implosion of a heterogeneous pinch.

required Z value. It should be emphasized that this method of creating a plasma from fibers is not accompanied by current instabilities or the mixing of gases during the formation of a heterogeneous jet.

We carried out experiments on creating heterogeneous pinches in the C-300 device [40]. A plasma with a moderate Z value was produced by evaporating thin glass fibers in a shock wave propagating through a helium plasma during the liner implosion. Initially, the fibers were arranged around the axis at a radius equal to one-third of the liner radius. With the help of laser probing and streak imaging (a streak image of the implosion of a helium liner with fibers is presented in Fig. 16), it is shown that the expansion of fibers and the formation of a plasma occur well before the boundary of the liner (current shell) reaches the fibers. The laser shadow photographs shows that the spatial nonuniformity of the fiber plasma expansion is much less than in the case

Cl [He] 4.45 Å

| 1st order | | 2nd order | 3rd order |

Si [H] 6.18 Å

1st order

Ca [He] 3.18 Å

2nd order

2nd order

Si [He] 6.69 Å

1st order

Anode

2nd order

Cathode

Fig. 17. X-ray spectrum of an imploding heterogeneous Z-pinch. The resonant line of the helium-like chlorine ion in the first, second, and third orders is emitted from a bright spot on the cathode.

when the plasma is produced by a current flowing through the fibers. This can be regarded as indirect proof that the fibers are evaporated under the action of a shock wave at the front of the magnetic piston.

The influence of high-Z impurities on the electron heating and thermal conductivity was investigated by recording the spectral lines of helium-like ions of chlorine (these ions were produced from NaCl deposited on the cathode end of the liner gap). We used an X-ray spectrograph with a convex mica crystal, which provided two-dimensional spatial resolution [41].

Figure 17 shows a typical X-ray spectrum, in which one can distinguish the lines of hydrogen- and helium-like ions of the glass elements (Al, Si, Ca, etc.) with excitation energies of up to 4 keV. The electron temperature, which was determined from the intensity ratios of these lines, is higher than 600 eV. In the spectrum, one can also see the resonant line of helium-like chlorine, which is emitted from a bright cathode spot with a radius of no more than 3 mm. In the absence of glass fibers, the intensity of this line is several times lower, which testifies that the thermal conductivity increases in the presence of impurities.

Therefore, the studies performed show that the liner–converter scheme with the use of a heterogeneous Z-pinch is promising for creating a high-power pulsed X-ray source.

6. CONCLUSIONS

(i) During the implosion of highly radiative gas-puffs, a thin high-density plasma shell is formed. The shell thickness is one order of magnitude smaller than the skin depth, whereas the density is more than one order of magnitude higher than the initial density.

(ii) Hall instability plays a dominant role in the liner implosion. This instability is most dangerous for low-density high-Z liners. This instability can be stabilized by increasing the initial thickness of the shell prepared of low-radiative gases (H_2, He) (in the limiting case, this corresponds to the magnetic implosion of a continuous Z-pinch) or applying an external longitudinal magnetic field.

(iii) The feasibility of the liner–converter scheme, in which the heat conduction mechanism is used to convert the magnetic energy into X rays, has been demonstrated experimentally. The experimental data agree well with the results of numerical simulations.

(iv) It is shown that the presence of local moderate-Z impurities in a helium Z-pinch increases the energy flux toward the liner end.

REFERENCES

1. S. G. Alikhanov, L. I. Rudakov, V. P. Smirnov, and I. R. Yampol'skiĭ, Pis'ma Zh. Tekh. Fiz. **5**, 1395 (1979) [Sov. Tech. Phys. Lett. **5**, 587 (1979)].

2. A. Fisher, J. Shiloh, and N. Rostoker, Phys. Rev. Lett. **40**, 515 (1978).

3. W. Clark, M. Gersten, T. Pearlman, *et al.*, J. Appl. Phys. **53**, 4099 (1982).

4. V. N. Mokhov, V. K. Chernyshev, V. B. Yakubov, *et al.*, Dokl. Akad. Nauk SSSR **247**, 83 (1979) [Sov. Phys. Dokl. **24**, 557 (1979)].

5. R. B. Baksht, I. M. Datsko, N. F. Kovsharov, *et al.*, Pis'ma Zh. Tekh. Fiz. **9**, 1192 (1983) [Sov. Tech. Phys. Lett. **9**, 512 (1983)].

6. E. V. Grabovskiĭ, S. V. Zakharov, V. P. Smirnov, *et al.*, Preprint No. 4587/6 (Kurchatov Inst. of Atomic Energy, Moscow, 1988).

7. R. B. Spielman, C. Deeney, G. A. Chandler, *et al.*, in *Proceedings of the 4th International Conference on Dense Z-Pinches, Vancouver, 1997*, p. 101.

8. L. I. Rudakov, RF Patent No. 1223766 M. C1. 3 G21B1/100, 33, No. 3730677/22, Publ. 210484.

9. L. I. Rudakov, N. A. Starostin, I. I. Yakunin, *et al.*, Pis'ma Zh. Éksp. Teor. Fiz. **65**, 502 (1997) [JETP Lett. **65**, 522 (1997)].

10. L. I. Rudakov, N. A. Starostin, I. I. Yakunin, *et al.*, in *Proceedings of the 4th International Conference on Dense Z-Pinches, Vancouver, 1997*, p. 187.

11. V. P. Bol'shakov, E. P. Velikhov, V. A. Glukhikh, *et al.*, At. Énerg. **53** (1), 14 (1982).

12. Yu. L. Bakshaev, A. V. Bartov, P. I. Blinov, *et al.*, in *Proceedings of the 18th Symposium on Plasma Physics and Technology, Prague, 1997*, p. 45.

13. V. V. Bulan, E. V. Grabovskiĭ, V. A. Kalenskiĭ, *et al.*, Prib. Tekh. Éksp., No. 5, 94 (1985).

14. E. I. Baranchikov, A. V. Gordeev, V. V. Zazhivikhin, *et al.*, Zh. Éksp. Teor. Fiz. **75**, 2101 (1978).

15. Yu. I. Shestakov and S. A. Dan'ko, USSR Inventor's Certificate No. 1134022, 1983.

16. S. L. Bogolyubskiĭ, E. M. Gordeev, S. A. Dan'ko, *et al.*, Pis'ma Zh. Tekh. Fiz. **11**, 1271 (1985) [Sov. Tech. Phys. Lett. **11**, 525 (1985)].

17. S. L. Bogolyubsky, E. M. Gordeev, S. A. Dan'ko, *et al.*, in *Proceedings of the 6th International Conference on High-Power Beams, Kobe, 1986*, p. 451.

18. S. L. Bogolyubskiĭ, A. G. Volkovich, E. M. Gordeev, *et al.*, Pis'ma Zh. Tekh. Fiz. **13**, 901 (1987) [Sov. Tech. Phys. Lett. **13**, 375 (1987)].

19. S. L. Bogolyubsky, E. M. Gordeev, Yu. G. Kalinin, *et al.*, in *Proceedings of the 7th International Conference on High-Power Beams, Karlsruhe, 1988*, p. 1255.

20. A. S. Chernenko, Yu. L. Bakshaev, A. V. Bartov, *et al.*, in *Proceedings of the 11th International Conference on High-Power Beams, Prague, 1996*, Vol. 1, p. 154.

21. E. P. Kruglyakov, Diagn. Plazmy, No. 3, 97 (1973).

22. W. Clark, M. Gersten, T. Pearlman, *et al.*, in *Proceedings of the 5th International Conference on High-Power Beams, San-Francisco, 1983*, p. 236.

23. Yu. G. Kalinin, E. V. Kravchenko, A. V. Korel'skiĭ, and A. Yu. Shashkov, Fiz. Plazmy **28**, 858 (2002) [Plasma Phys. Rep. **28**, 790 (2002)].

24. K. V. Chukbar, Fiz. Plazmy **19**, 1487 (1993) [Plasma Phys. Rep. **19**, 783 (1993)].

25. L. I. Rudakov, in *Proceedings of the 2nd International Conference on Dense Z-Pinches, Laguna Beach, 1989*, p. 290.

26. L. I. Rudakov and A. A. Sevastianov, in *Proceedings of the 11th International Conference on High-Power Beams, Prague, 1996*, Vol. 2, p. 776.

27. Yu. G. Kalinin and A. Yu. Shashkov, Fiz. Plazmy **23**, 1027 (1997) [Plasma Phys. Rep. **23**, 949 (1997)].

28. L. I. Rudakov, S. L. Bogolyubsky, E. M. Gordeev, *et al.*, in *Proceedings of the 17th European Conference on Control Fusion and Plasma Heating, Amsterdam, 1990*, Vol. 2, p. 609.

29. L. I. Rudakov, K. A. Baigarin, Yu. G. Kalinin, *et al.*, Phys. Fluids B **3**, 2414 (1991).

30. F. S. Felber, F. J. Wessel, N. C. Wild, *et al.*, Laser Part. Beams **5**, 699 (1987).

31. R. B. Baksht, A. L. Velikovich, B. A. Kablambaev, *et al.*, Zh. Tekh. Fiz. **57**, 242 (1987) [Sov. Phys. Tech. Phys. **32**, 145 (1987)].

32. A.-M. Gasque, P. Grua, Ph. Romary, *et al.*, in *Proceedings of the 11th International Conference on High-Power Beams, Prague, 1996*, Vol. 1, p. 550.

33. A. Gask, P. Gryua, F. Romari, *et al.*, Fiz. Plazmy **24**, 726 (1998) [Plasma Phys. Rep. **24**, 672 (1998)].

34. V. A. Gasilov, S. F. Grigor'ev, A. Yu. Krukovskiĭ, *et al.*, Preprint No. 4777/6 (Kurchatov Inst. of Atomic Energy, Moscow, 1989).

35. R. W. Lee, B. L. Whitten, and R. E. Stout, J. Quant. Spectrosc. Radiat. Transf. **32**, 91 (1984).

36. O. Peyrusse, Phys. Fluids B **4**, 2007 (1992).

37. Yu. L. Bakshaev, A. V. Barton, P. I. Blinov, *et al.*, in *Proceedings of the 4th International Conference on Dense Z-Pinches, Vancouver, 1997*, p. 149.

38. B. B. Kadomtsev, in *Reviews of Plasma Physics*, Ed. by M. A. Leontovich (Atomizdat, Moscow, 1963; Consultants Bureau, New York, 1966), Vol. 2.

39. L. I. Rudakov, in *Proceedings of the 4th International Conference on Dense Z-Pinches, Vancouver, 1997*, p. 183.

40. Yu. L. Bakshaev, A. V. Bartov, P. I. Blinov, *et al.*, in *Proceedings of the 12th International Conference on High-Power Beams, Haifa, 1998*, Vol. 1, p. 244.

41. S. A. Dan'ko, in *Proceedings of the 12th International Conference on High-Power Beams, Haifa, 1998*, Vol. 1, p. 459.

Translated by N.F. Larionova

<div align="center">

**PLASMA
DYNAMICS**

</div>

In Honour of the 70th Birthday of Dr. Leonid Rudakov

Energy Transfer to a Wire from a Surrounding Joule-Heated Corona[1]

M. G. Haines

Blackett Laboratory, Imperial College, London SW7 2BW, England
Received December 26, 2002

Abstract—This paper considers the early behavior of the current-carrying coronal plasma formed around the relatively colder liquid–vapor core of a wire. This has applications to both a wire array before global effects dominate and a single wire. An analytic, theoretical model is developed where the Joule heating in the coronal plasma is thermally conducted to the cold core. The balance of both energy and pressure are assumed, and it is further assumed that the Hall parameter is much less than one throughout the domain. This last assumption will be violated near the outside radius of the corona where runaway conditions and lower hybrid turbulence can also occur. The nonlinear second-order differential equation for the normalized temperature variation with a normalized radius has only one free dimensionless parameter, which is the ratio of the applied axial electric field to the mean radial temperature gradient (in electronvolts/m). The inverse of this ratio scales essentially as $T^2/\sqrt{n}$, thus showing that both a low Hall parameter and a low magnetic Reynolds' number can occur when the mean free path is less than the collisionless skin depth, a criterion for the onset of current or heat-flow driven electrothermal instabilities. © 2003 MAIK "Nauka/Interperiodica".

1. INTRODUCTION

The wire array, dense Z-pinch has demonstrated that it is an efficient and reproducible source of intense X-rays with a rise time of 4 to 5 ns and a peak power of nearly 300 TW [1]. Through a series of smaller scale experiments [2, 3], it has been shown through X-radiography that the wires melt and the core expands in a mixed liquid–vapor phase [2]. This is followed by the breakdown of the vapor around the core to form a coronal plasma, which with single wires can go unstable to the $m = 0$ MHD instability [4–6] with a wavelength that increases with time; this is consistent with the increasing radius of the coronal plasma suggested by computer simulations [7] and analytic theory [8]. However, in an array of parallel wires arranged in a circle, it is found that the coronal plasma is diverted by the global $\mathbf{J} \times \mathbf{B}$ force toward the axis to form a precursor plasma [9, 10]. Furthermore, there is evidence that the entire current flows close to the wire cores, which remain stationary until 80% of the implosion time. Thus, it would appear that the magnetic Reynolds' number is less than one, allowing the coronal plasma to slip through the magnetic field associated with the current-carrying region close to each wire [8].

The coronal plasma surrounds the relatively cold liquid–vapor cores of each wire, and in a three-dimensional analytic model [8], it was assumed that the cores received heat by flux-limited heat flow from the Joule-heated coronal plasma in each necked region. The purpose of this paper is to consider more formally the problem of a Joule-heated corona conducting heat radially inwards towards the core. It will be shown that, to be consistent with a magnetic Reynolds' number or a Lundqvist number less than one for a $\beta = 1$ (the magnetic pressure balancing the plasma pressure) model, the Hall parameter $\omega\tau$ for the electrons should also be much less than one in much of the domain. Here, ω is the electron cyclotron angular frequency and τ is the electron–ion collision time.

2. THE THEORETICAL MODEL

We consider a steady-state equilibrium in which the electromagnetic energy transferred per unit volume per unit time, $\mathbf{J} \cdot \mathbf{E}$, is balanced by the divergence of the electron heat flux $\mathbf{q}$. In cylindrical polars with axial and azimuthal symmetry, this becomes

$$\sigma_0 T^{\frac{3}{2}} E_z^2 = J_z E_z = -\frac{1}{r}\frac{d}{dr}\left(\kappa_0 T^{\frac{5}{2}}\frac{dT}{dr}\right), \qquad (1)$$

where the electrical and thermal conductivities σ and κ are functions of electron temperature T:

$$\sigma = \sigma_0 T^{\frac{3}{2}}, \qquad (2)$$

$$\kappa = \kappa_0 T^{\frac{5}{2}}, \qquad (3)$$

---

[1] This article was submitted by the author in English.

where σ_0 and κ_0, though containing the classical $\ln\Lambda$ term, are assumed to be constant. Because of the assumption of steady state, $\nabla \times \mathbf{E} = 0$ is zero, resulting in E_z being spatially uniform. Therefore, only this equation needs to be solved to obtain $T(r)$.

The boundary conditions are Neumann at the outer radius of the corona, r_2, and Dirichlet at the interface with the liquid–vapor core at radius r, with a known temperature T_1. To be more specific, dT/dr is zero (no heat flow) at $r = r_2$ and T is equal to T_1 at $r = r_1$.

The differential equation is second-order and non-linear but has no singular points in the domain $r_1 < r < r_2$. It will be solved numerically, but since the gradient is known only at $r = r_2$, it seemed useful to define the dimensionless parameters as follows, $x = r/r_2$, $y = T/T_2$, $v = dy/dx$, and $A = \sqrt{(2\sigma_0/\kappa_0)}\, E_z r_2/T_2$. Equation (1) then becomes

$$\frac{1}{2}A^2 = -\frac{y}{x}\frac{dy}{dx} - \frac{5}{2}\left(\frac{dy}{dx}\right)^2 - y\frac{d^2y}{dx^2}. \tag{4}$$

In terms of Braginskii's transport coefficients [11], which are given more accurately by Epperlein and Haines [12], the parameter A can be written in terms of the dimensionless parameters α^c and κ^c, which are functions of ion charge Z, as

$$A = \sqrt{\left(\frac{2}{\alpha^c\kappa^c}\right)}\frac{E_z r_2}{T_2}, \tag{5}$$

where the temperature T_2 (at $r = r_2$) is now in electron-volts.

The boundary conditions are such that at $x = 1$, we have $y = 1$ and $dy/dx = 0$. It follows that it is straightforward to integrate Eq. (4) numerically for a given value of A by solving the two first-order equations

$$\frac{dy}{dx} = v, \tag{6}$$

$$\frac{dv}{dx} = -\frac{A^2}{2y} - \frac{v}{x} - \frac{5v^2}{2y}. \tag{7}$$

But first, we note an interesting feature of (4); namely, that the left hand side is positive definite, and since we expect dy/dx to be positive in the domain (due to the heat flowing radially inward), the first two terms on the right-hand side are always negative, forcing d^2y/dx^2 to always be negative. Indeed, at $x = 1$ the last term is the only nonzero term on the right-hand side, and if it is always dominant, an analytic first interpretation can be found by multiplying the equation by $2y^{-2}\,dy/dx$ to give

$$A^2\frac{1}{y}\frac{dy}{dx} \approx -\frac{d}{dx}\left[\left(\frac{dy}{dx}\right)^2\right], \tag{8}$$

which integrates to give

$$v = \frac{dy}{dx} = A\ln^{\frac{1}{2}}\left(\frac{1}{y}\right). \tag{9}$$

3. OTHER PLASMA PARAMETERS

Once the temperature is found, the current density J_z is given simply by

$$J_z(x) = \sigma_0 T^{\frac{3}{2}}(x)E_z. \tag{10}$$

From this, the accumulated current $I(x)$,

$$I(x) = \int_{r_1}^{r} 2\pi J_z r\, dr, \tag{11}$$

can be found assuming that the core carries negligible current. This becomes

$$I(x) = 2\pi r_2^2 \sigma_0 T_2^{\frac{3}{2}} E_z \int_{x_1}^{x} y^{\frac{3}{2}} x\, dx, \tag{12}$$

and so allows the magnetic field $B_\vartheta(x)$ to be found from

$$B_\vartheta(x) = \mu_0 \sigma_0 E_z T_2^{\frac{3}{2}} r_2 \frac{1}{x}\int_{x_1}^{x} y^{\frac{3}{2}} x\, dx. \tag{13}$$

In turn, this permits the plasma pressure p to be found, assuming a momentum balance

$$J_z B_\vartheta = \mu_0 \sigma_0^2 E_z^2 T_2^3 r_2 \frac{y^{\frac{3}{2}}}{x}\int_{x_1}^{x} y^{\frac{3}{2}} x\, dx, \tag{14}$$

$$J_z B_\vartheta = -\frac{dp}{dr}. \tag{15}$$

If the boundary condition is that $p = 0$ at $x = 1$ ($r = r_2$), Eq. (15) can be interpreted to give

$$p = p_1 - \mu_0 \sigma_0^2 E_z^2 T_2^3 r_2^2 \int_{x_1}^{x}\left[\frac{y^{\frac{3}{2}}}{x}\int_{x_1}^{x} y^{\frac{3}{2}} x\, dx\right]dx \tag{16}$$

and, hence,

$$p = \mu_0 \sigma_0^2 E_z^2 T_2^3 r_2^2 \int_{x}^{1}\left[\frac{y^{\frac{3}{2}}}{x}\int_{x_1}^{x} y^{\frac{3}{2}} x\, dx\right]dx. \tag{17}$$

Similarly, the electron number density $n(x)$ can be found from

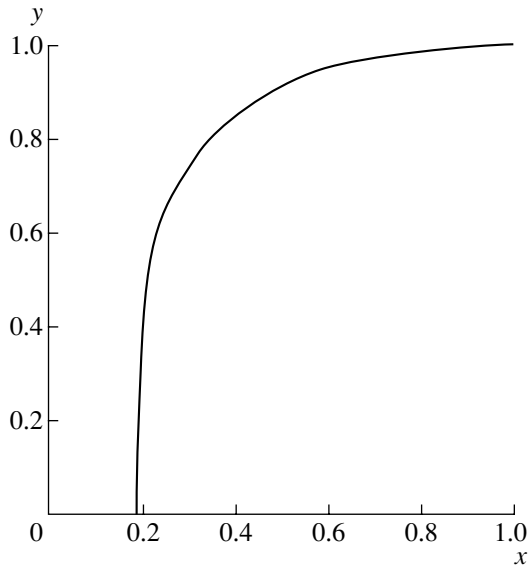$$n_e = \frac{p}{k_B T_e}\left(1 + \frac{T_i}{ZT_e}\right)^{-1} \tag{18}$$

Fig. 1. $y(x)$ for $A = 1$.

$$\Rightarrow n_e = \frac{\mu_0}{k_B}\alpha^2 E_z^2 T_2^2 r_2^2\left(1 + \frac{T_i}{ZT_e}\right)^{-1}\frac{1}{y}$$

$$\times\left\{\int_x^1\left[\frac{y^{\frac{3}{2}}}{x}\int_{x_1}^x y^{\frac{3}{2}}xdx\right]dx\right\}. \tag{19}$$

An parameter important for determining the validity of this theory is the Hall parameter $\omega\tau$, which can be written in terms of the dimensionless parameter A and the integrals leading to its x dependence as follows:

$$\omega\tau = \frac{1}{A}\left(1 + \frac{T_i}{ZT_e}\right)\frac{y^{\frac{5}{2}}}{x}\int_{x_1}^x y^{\frac{3}{2}}xdx/\int_x^1\left[\frac{y^{\frac{3}{2}}}{x}\int_{x_1}^x y^{\frac{3}{2}}xdx\right]dx, \tag{20}$$

which is valid provided $\omega\tau < 1$. The full implications of this condition will be discussed later.

4. SOLUTION FOR $A = 1$

The method of solution proceeds as follows. A stepwise finite-difference numerical integration of Eqs. (6) and (7) is undertaken backwards in x from $x = 1$, where $y = 1$ and $v = 0$. This is stopped at some $x = x_1$ where y tends to zero or a value appropriate for the cold-core interface. Then, knowing $y(x)$, a forward integration is carried out to find $I(x)$, $B_\vartheta(x)$, J_zB_ϑ, and the last term in Eq. (16) from Eqs. (12)–(14). At $x = 1$, this last integral

represents p_1^*, the dimensionless pressure at $x = x_1$, where

$$p_1^* = \int_{x_1}^1\left[\frac{y^{\frac{3}{2}}}{x}\int_{x_1}^x y^{\frac{3}{2}}xdx\right]dx, \tag{21}$$

$$p_1 = \mu_0\sigma_0^2 E_z^2 T_2^3 r_2^2 p_1^*. \tag{22}$$

In Figs. 1–4, $T/T_2 = y(x)$, $B_\vartheta^*(x)$, $(J_zB_\vartheta)^*$, and p^*, all dimensionless, are plotted where

$$B_\vartheta^* = \frac{1}{x}\int_{x_1}^x y^{\frac{3}{2}}xdx, \tag{23}$$

$$(J_zB_\vartheta)^* = y^{\frac{3}{2}}B_\vartheta^*, \tag{24}$$

$$p^* = \int_x^1\left[\frac{y^{\frac{3}{2}}}{x}\int_{x_1}^x y^{\frac{3}{2}}xdx\right]dx. \tag{25}$$

We note that the position of the inner boundary to the coronal plasma is at $x \approx 0.185$ while $p_1^* = p^*(x = x_1) \approx 0.171$.

It is interesting to compare the relative magnitude of the three terms in Eq. (7) that contribute to dv/dx as a function of x. We find that, for $0.6 < x < 1$, the dominant term is $A^2/2y$, which represents the source of heat, the Joule heating. For the case when $A = 1$, this is overtaken by the v/x term representing the effect of cylindrical curvature. However, below $x < 0.35$, the term $5v^2/2y$ dominates, representing the nonlinear effects of the $T^{5/2}$ dependence of the thermal conductivity. It is interesting to note that the assumption of $\omega\tau < 1$ is well satisfied in this region.

5. SOLUTIONS FOR OTHER VALUES OF A

For A less than 1, it is found that x_1 approaches closer to the axis. For example, for $A = \sqrt{0.1}$, we find $x_1 \simeq 4.6 \times 10^{-6}$, while for $A = 0.1$, we find that there is a tendency for $v \longrightarrow \infty$ as $x \longrightarrow 0$ at finite y. Numerically, we went as far as $x \sim 10^{-24}$, $v \sim 4 \times 10^{21}$ with $y \simeq 0.83$, way beyond the physical viability of the model taking into account the onset of the flux-limited heat flow. Essentially, $xy^{5/2}v$ is constant here; the solution consistent with a negligible source term. With this low value of the source term, the values of v were small ($v \ll 1$) in most of the domain ($0.01 < x < 1$) and y only fell from 1 to 0.995. Under these conditions of $A < 1$, $\omega\tau$ approaches $2x/[A(1 - x^2)]$, which equals 1 at $x = \sqrt{(1 + A^{-2})} - A^{-1}$, and is therefore greater than 1 over most of the domain, thus invalidating the model.
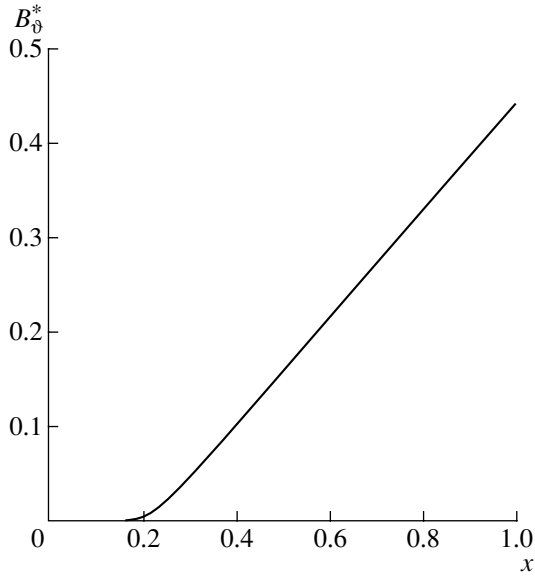
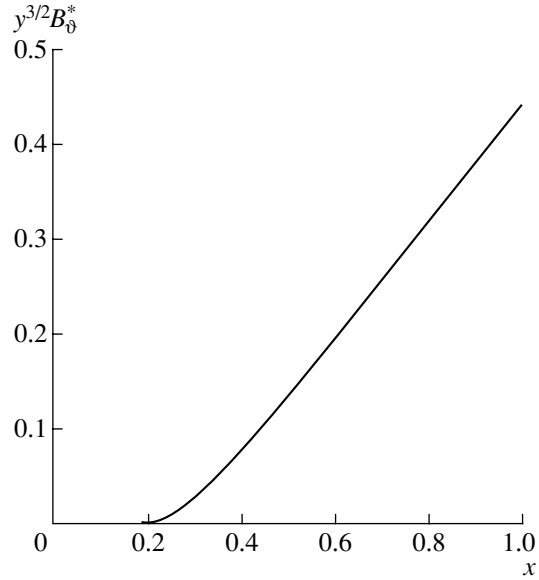**Fig. 2.** $B_{\vartheta}^*(x)$ for $A = 1$.

Fig. 3. $y^{3/2} B_{\vartheta}^*(x)$ for $A = 1$.

On the other hand, for A larger than 1, where we have considered the cases $A^2 = 10, 100$, and 10^4, we find that y tends to zero at x_1 equal to 0.67, 0.89, and 0.989, respectively; i.e., the coronal plasma becomes relatively thinner as A is increased. The outer half of the domain between x_1 and 1 has $\omega\tau > 1$, again invalidating the model. However, the region $x_1 < x < 0.5(1 + x_1)$ satisfies the model, and as x_1 is approached, the source term $A^2/2y$ is overtaken by $5/2\, v^2/y$ while the curvature effects are small.

For $A > 1$, therefore, we can divide the region into two parts: an outer region where the source term approximately balances the dv/dx term, with the first integration given by Eq. (9) and an inner region, given by $y^{5/2}v$, which is constant. At the boundary of the two regions, we assume that the terms $A^2/2y$ and $5/2\, v^2/y$ in Eq. (7) are equal in magnitude, the former dominating in the outer region and the latter in the inner region. Putting $x = x_b$, $y = y_b$, and $v = v_b$ at the boundary of these two regions, the above equality becomes

$$v_b = A/\sqrt{5} \qquad (26)$$

and, using Eq. (9),

$$v_b = A \ln^{1/2}(1/y_b). \qquad (27)$$

It follows that there is an explicit expression for y_b given by

$$y_b = \exp(-0.2) = 0.819. \qquad (28)$$

To find x_b, we can integrate Eq. (9) to give the approximate solution for the outer region,

$$A(1 - x) = \int_{y}^{1} \frac{dy}{\ln^{1/2}\left(\frac{1}{y}\right)} = \frac{\sqrt{\pi}}{2}\text{erf}\left[\ln^{1/2}\left(\frac{1}{y}\right)\right]. \qquad (29)$$

The integral can be taken using the substitution

$$u^2 = -\ln(1 - z) = -\ln y, \qquad (30)$$

giving

$$u\,du = \frac{dz}{1 - z} = e^{u^2}dz \qquad (31)$$

and

$$\int_{y}^{1}\frac{dy}{\ln^{\frac{1}{2}}y} = \int_{0}^{u}e^{-u^2}du = \sqrt{\frac{\pi}{2}}\text{erf}\,u. \qquad (32)$$

Inserting the value of y_b given by Eq. (28) into Eq. (29) gives

$$x_b \approx 1 - \frac{0.419}{A}. \qquad (33)$$

The appropriate solution for the inner region is

$$y^{\frac{5}{2}}v = y_b^{\frac{5}{2}}v_b = \frac{A}{e^{\frac{1}{2}}\sqrt{5}}, \qquad (34)$$

p^*

0.18

0.16

0.14

0.12

0.10

0.08

0.06

0.04

0.02

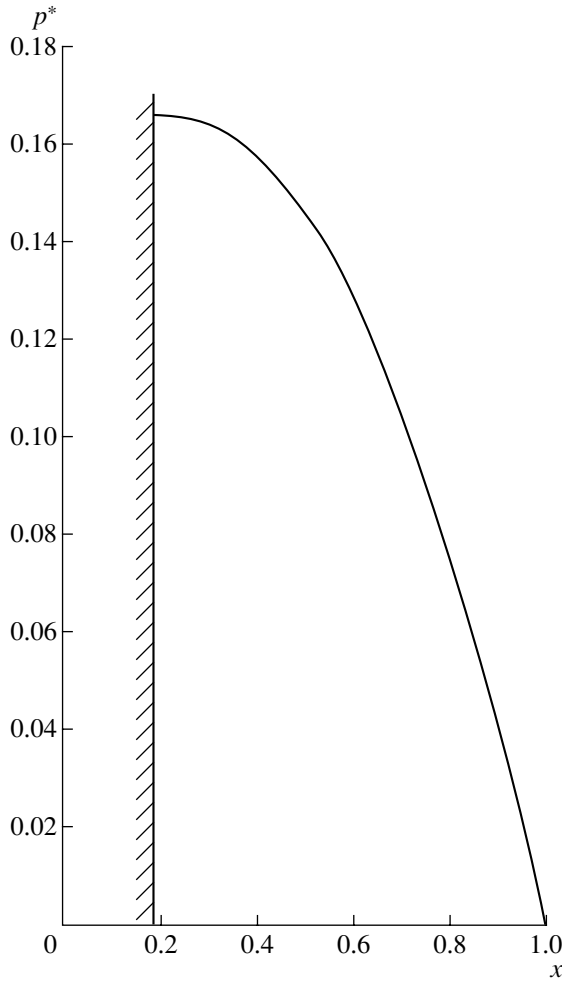0   0.2   0.4   0.6   0.8   1.0

x

Fig. 4. $p^*(x)$ for $A = 1$.

the integral of which, satisfying the boundary condition at $x = x_b$, $y = y_b$, is

$$\frac{2}{7}y^{\frac{7}{2}} = -\frac{A}{e^{\frac{1}{2}}\sqrt{5}}(1-x) + \frac{2}{7}\left(\frac{1}{5}\right)^{\frac{7}{4}} + \frac{0.419}{e^{y_2}\sqrt{5}}. \quad (35)$$

In the limit of $y \longrightarrow 0$, $x \longrightarrow x_1$, this gives a value of 0.482 for $A(1 - x_1)$, which differs significantly from the numerical value of 1.123 for $A \approx 100$.

To help resolve this, it turns out that, neglecting only the v/x curvature term in Eq. (7), it is possible to integrate Eqs. (7) and (8) one time analytically without splitting the region into two, giving

$$v = \frac{A}{\sqrt{5}}\left[\frac{1}{y^5} - 1\right]^{\frac{1}{2}}. \quad (36)$$

(This was found by successive integration of Eq. (7) using the first approximation given by Eq. (9) for the first substitution into $5/2\,v^2$; however, the resulting

Eq. (36), can be confirmed by direct substitution.) A second analytic integration of Eq. (36) would appear difficult since the domain includes $y = 1$. Writing $u^2 = y^{-5}$, the second integration is

$$\frac{A}{\sqrt{5}}(1-x) = \frac{2}{5}\int_0^u \frac{du}{(u^2+1)^{\frac{6}{5}}}, \quad (37)$$

$$\frac{2}{5}\int_0^u \frac{du}{(u^2+1)^{6/5}} < \frac{2}{5}\int_0^u \frac{du}{u^2+1} = \frac{2}{5}\tan^{-1}\sqrt{\left(\frac{1}{y^5}-1\right)}. \quad (38)$$

The inequality (38) leads to $A(1 - x_1) < \pi/\sqrt{5} = 1.405$. A lower bound to $A(1 - x_1)$ can be found by considering $(u^2 + 1)^{3/2}$ in the denominator of the integrand, leading to $A(1 - x_1) > 0.894$. The numerical value 1.123 lies between these two bounds.

6. INCLUSIONS OF THE HALL PARAMETER

The problem so far has been analytically tractable largely because of the neglect of the Hall parameter $\omega\tau$, which can be calculated from Eq. (20). Its dependence on $1/A$ is, however, misleading, since the effective range of integration from x_1 to 1 in the other terms, allowing for $A(1 - x_1) \simeq 1.123$, is dependent on A. In our calculations with $T_i = 0$ for $A = 1$, $\sqrt{10}$, 10, and 100, we find that $\omega\tau \geq 1$ at $x = 0.53$, 0.84, 0.95, and 0.996, respectively, compared to the values of $x_1 = 0.185$, 0.67, 0.89, and 0.989 quoted earlier. Thus, half the regime has $\omega\tau > 1$, though $\omega\tau > 10$ only close to the plasma boundary at $x = 0.91$, 0.97, 0.99, and 0.999 respectively.

The main effect of a finite $\omega\tau$ effects the reduction of the thermal conductivity by a term of the order of $(1 + \omega^2\tau^2)^{-1}$, though we should for consistency also include the Ettingshausen and Nernst effects (13). As a result, Eq. (1) is replaced by

$$\frac{n_e^2}{\alpha_1}E_z^2$$

$$= -\frac{1}{r}\frac{d}{dr}\left[r\left(k_1 - \frac{T_e n_e^2 \beta_\wedge^2}{\alpha_1}\right)\frac{dT}{dr}\right] - \frac{eT}{r}\frac{d}{dr}\left[\frac{r\beta_\wedge n_e^2 E_z}{\alpha_1}\right], \quad (39)$$

where we use the notation of Braginski (11) and the results of Epperlein and Haines (12). For large $\omega\tau$, Eq. (39) becomes

$$T^{\frac{3}{2}}E_z^2 = -\frac{1}{r}\frac{d}{dr}\left[\frac{rT^{\frac{1}{2}}}{\omega^2\tau^2}(k_1\alpha_1 - \beta_1^2)\frac{dT}{dr}\right]$$

$$-\frac{T_e}{r}\frac{d}{dr}\left[\frac{r\beta_1 T^{\frac{3}{2}}}{\omega\tau}\right]. \quad (40)$$

If $\omega\tau$ were a constant value $\geqslant 1$, the main effect would be effectively equivalent to increasing the value of A by $\omega\tau$ in this region, thus steepening the temperature gradients and reducing the thickness of the coronal plasma. This is necessary in order to provide the heat flux that is unaffected by the magnetic field close to the inner boundary. However, we have neglected the radiation transport, which in the diffusive limit will have a T^3 dependent coefficient, thus providing a term similar to the $T^{5/2}$ thermal conductivity and tending to compensate for any $\omega\tau$ reduction in κ.

7. FREE-STREAMING LIMIT

Even though the mean free path λ, which varies as T^2/n, decreases substantially as x decreases to x_1, the ratio of λ to the characteristic gradient scale length $T(\nabla T)^{-1}$ increases, and could reach the limit of validity of linear transport theory. The usual criterion for this is to consider the ratio f of the heat flow to the free streaming limit, $5/2nT(T/m)^{1/2}$. This is given in terms of dimensionless parameters by

$$f = y^2 \frac{dy}{dx} \frac{2}{5A^2 R_m} \sqrt{\frac{Zm_e}{m_i}}, \tag{41}$$

where the magnetic Reynolds' number is defined by

$$R_m = \mu_0 \sigma c_s r_2, \tag{42}$$

with

$$c_s^2 = \frac{ZT_e}{m_i}. \tag{43}$$

Recalling that experimentally [9, 10] and in a simplified 3-D model [8] the current and associated magnetic field essentially remain in the coronal plasma of the wire array despite an inward flow of the precursor plasma, it follows that $R_m \leq 1$ as was shown earlier [8]. Taking $R_m = 0.1$ and $A = 1$, it follows that, close to $x = x_1$, f typically has a value ≤ 0.1 as employed in [8]. Lower values of f pertain to larger values of A. Care must always be exercised to ascertain whether a full Fokker-Plank treatment is required here.

8. RUNAWAY ELECTRONS AND ANOMALOUS TRANSPORT

The critical electric field, E_D, commonly called the Dreicer electric field, above which electrons will run away, is given by

$$E_D = \frac{en_e k_B^{\frac{1}{2}}}{\sigma_0 m_e^{\frac{1}{2}} T_e}. \tag{44}$$

Clearly, the applied electric field E_z will exceed this as $r \longrightarrow r_2$, where n_e and p tend to zero. However, here the electrons are magnetized ($\omega\tau > 1$) and electrons will not run away. Indeed, the more energetic electrons in this region will tend to have an E/B drift inwards (the Ettingshausen heat flow in the direction of $\mathbf{J} \times \mathbf{B}$).

The ratio

$$\frac{E_D}{E_z} \simeq R_m A \sqrt{\frac{m_i}{Zm_e}} y P_1^* \left[1 - \left(\frac{x - x_1}{1 - x_1} \right)^2 \right], \tag{45}$$

i.e.,

$$\frac{E_D}{E_z} = R_m A \sqrt{\frac{m_i}{Zm_e}} y p_1^* g(x), \tag{46}$$

where a parabolic pressure profile (see Fig. 4) is assumed to be a reasonable approximation. For $R_m = 0.1$, $y = 1$, and $A p_1^*$ having values of 0.166, 0.110, 0.044, and 0.0049 for $A = 1$, $\sqrt{10}$, 10, and 100, respectively, we find that $E_z = E_D$ for g equal to 0.63, 0.98, 2.50, and 22.2. However, $g \leq 1$, which means that for $A = 10$ and 100 the electric field exceeds the Dreicer value for runaway production.

Before this happens, however, the drift velocity v_d of the electrons will trigger microscopic turbulence. Indeed, the ratio of v_d to the electron thermal speed is just the inverse of Eq. (45); i.e.,

$$v_d \sqrt{\frac{m_e}{k_B T_e}} = \frac{E_z}{E_D}. \tag{47}$$

Lower hybrid turbulence will be triggered when v_d exceeds a lower value of the ion sound speed c_s. Both the electrical and thermal conductivities will be reduced in Eq. (1). It is beyond the scope of this paper to address this problem.

9. DISCUSSION

We have considered the problem of a cylindrically symmetric coronal plasma carrying an axial current and surrounding a cold wire, which acts as a heat sink for the Joule-heated plasma. By assuming that the Hall parameter is small, the nonlinear second-order equation is tractable and leads to profiles of the temperature, magnetic field, and pressure in terms of a single dimensionless parameter A. This parameter is the ratio of the applied axial electric field multiplied by the coronal radius and divided by the electron temperature. Taking the inverse of A, we find that it orders as follows:

$$\frac{1}{A} \sim \frac{T_2}{E_z r_2} \sim \frac{\sigma_0 T^{\frac{5}{2}}}{J_z r_2} \sim \frac{\sigma_0 \mu_0 T^{\frac{5}{2}}}{B_\vartheta} \sim \frac{\sigma_0 \mu_0^{\frac{1}{2}} T^2}{k_B^{\frac{1}{2}} n^{\frac{1}{2}}}. \tag{48}$$

This is the ratio of the mean free path to the collisionless skin depth. A value of less than one is a necessary

condition for the onset of the heat flow-driven electro-thermal instability [14], which may account for the instability structure seen in laser probing measurements [3].

If the scale-length r_2 in Eq. (42) is ~100 mean free paths (to account for flux-limited heat-flow), it follows also that R_m scales as A^{-2}, thus accounting for the lack of convection of the magnetic flux in the precursor flow for $A > 1$.

The outer half of the coronal plasma is, however, found to have a Hall parameter greater than 1, necessitating a modification of the model, though radiation transport may mollify this effect. It is appropriate in the context of the dedication of this paper that the Hall parameter cannot be ignored. The free-streaming limit of the heat flow is approached in the inner region close to the cold boundary. Throughout the domain, the condition for the onset of electrostatic microinstabilities and associated anomalous transport, together with runaway electrons, requires further investigation.

ACKNOWLEDGMENTS

REFERENCES

1. C. Deeney, M. R. Douglas, R. B. Spielman, *et al.*, Phys. Rev. Lett. **81**, 4883 (1998).
2. D. Kalantar and D. Hammer, Phys. Rev. Lett. **71**, 3806 (1993).
3. S. V. Lebedev, F. N. Beg, S. N. Bland, *et al.*, Rev. Sci. Instrum. **72**, 671 (2001).
4. F. N. Beg, A. E. Dangor, P. Lee, *et al.*, Plasma Phys. Controlled Fusion **39**, 1 (1997).
5. M. D. Kruskal and M. Schwarzchild, Proc. R. Soc. London, Ser. A **223**, 348 (1954).
6. M. Coppins, Plasma Phys. Controlled Fusion **30**, 201 (1988).
7. J. P. Chittenden, R. Aliaga Rossel, S. V. Lebedev, *et al.*, Phys. Plasmas **4**, 4309 (1997).
8. M. G. Haines, IEEE Trans. Plasma Sci. **30**, 588 (2002).
9. I. K. Aĭvazov, V. D. Vikharev, G. S. Volkov, *et al.*, Fiz. Plazmy **14**, 197 (1988) [Sov. J. Plasma Phys. **14**, 110 (1988)].
10. S. V. Lebedev, F. N. Beg, S. N. Bland, *et al.*, Phys. Rev. Lett. **85**, 98 (2000).
11. S. I. Braginskiĭ, in *Reviews of Plasma Physics*, Ed. by M. A. Leontovich (Gosatomizdat, Moscow, 1963; Consultants Bureau, New York, 1965), Vol. 1.
12. E. M. Epperlein and M. G. Haines, Phys. Fluids **29**, 1029 (1986).
13. J. P. Chittenden and M. G. Haines, J. Phys. D **26**, 1048 (1993).
14. M. G. Haines, Phys. Rev. Lett. **47**, 917 (1981).

Electron Response in Laser-Irradiated Microclusters[1]

B. N. Breizman and A. V. Arefiev

Institute for Fusion Studies, University of Texas, Austin, Texas 78712, USA
Received October 16, 2002; in final form, December 12, 2002

Abstract—It is shown that a two-component electron distribution can emerge in a cluster under an intense laser pulse. The bulk of the internal electrons adjusts adiabatically to the laser field, whereas a smaller electron population at the cluster edge can undergo stochastic heating. A self-consistent equilibrium has been found for the confined electrons. © *2003 MAIK "Nauka/Interperiodica".*

1. INTRODUCTION

This work has been motivated by recent desktop laser fusion experiments, in which fusion reactions were produced by the irradiation of deuterium microclusters with a very short and intense laser beam [1–3]. From the outset it was recognized that the observed phenomenon is associated with the ion acceleration that takes place during the explosion of the cluster. There are two conceivable scenarios for such an explosion: an electrical one (Coulomb explosion) and a thermal one [4, 5]. The electrical scenario implies that the laser field quickly pulls the electrons out of the cluster, and the ions are then accelerated by the electric field of their space charge. The thermal scenario emphasizes the electron heating that leads to cluster expansion due to a high electron pressure. Although both scenarios involve the space-charge electric field as an accelerating force for the ions, the essential difference between the two is that the thermal scenario preserves quasi-neutrality, whereas the electrical scenario does not.

The picture of the electrical explosion is particularly simple when the laser field is strong enough to extract all of the electrons from the cluster. It is apparently more challenging to describe the case when the extraction is incomplete. This particular problem is the main topic of our paper.

In what follows, we will first formulate our basic assumptions that link the experimental situation to a properly idealized physics model. The key point here is the qualitative distinction between the confined and the extracted electrons, which is reflected in the separate treatment of these two groups. Next, we construct a simple analytical solution for an electrical explosion of an initially uniform spherical cluster. This solution is presented in Section 2. In Section 3, we develop a numerical procedure for calculating the space-charge electric field, together with the electron density distribution inside the cluster, for an arbitrary axially symmetric cluster. This procedure is designed to facilitate simulations of the ion dynamics by eliminating the

electron time-scales from the problem. However, the actual modeling of the ion motion goes beyond the scope of this paper. Finally, Section 4 deals with electron reflection from the cluster boundary, which causes phase mixing and gives rise to stochastic electron heating.

We will limit our consideration to the case in which the cluster radius (R) is much smaller than the laser wavelength (λ). This implies that the electric field of the laser beam can be treated as a spatially uniform, albeit time-dependent, external field. This external field oscillates at a laser frequency ω that is typically smaller than the electron plasma frequency ω_{pe} at a solid-state density of the cluster. For the sake of simplicity, we will henceforth assume that $\omega \ll \omega_{pe}$, which will allow us to treat the confined electrons adiabatically. As for the extracted electrons, we assume that they quickly move far away from the cluster and, therefore, do not contribute to the local space-charge density (the corresponding applicability condition is given by Eq. (14) below). The cluster will thus become positively charged, which happens so quickly that the ions hardly have time to move anywhere. We thus formulate the problem of finding an equilibrium configuration of the confined electrons in the self-consistent field that is a superposition of the external electric field and the space-charge field. This problem needs to be solved for a given spatial distribution of ions. Clearly, the total electric field and the space-charge density should vanish in the region occupied by the confined electrons provided that these electrons remain cold (this is indeed the case as long as one can neglect binary collisions). In other words, the confined electrons behave as a perfectly conducting fluid. What we need to find, when we look for equilibrium, is the boundary of that fluid.

In order to demonstrate the relevance of our model to the cluster experiments, we will relate the applicability conditions to the specific parameters described in [2]. In that particular experiment, a short pulse laser with a 35 fs pulse-width and a wavelength of 820 nm was employed at a peak intensity of $I = 2 \times 10^{16}$ W/cm². The typical deuterium cluster radius was about $R \approx 2.5$ nm

---
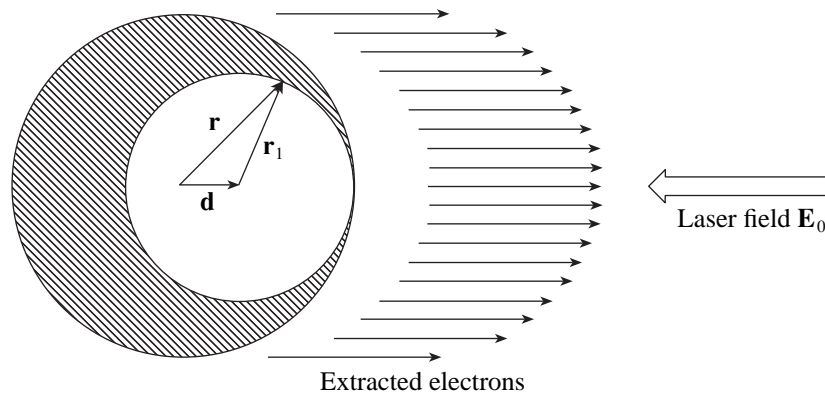
Fig. 1. Electron confined in a uniform spherical cluster in the presence of a laser field. The outer circle marks the edge of the ion background. The inner circle marks the boundary of the confined electron population. The shaded area represents the uncompensated ion space charge. The inner circle stays at the edge of the cluster when the electric field $\mathbf{E}_0$ increases monotonically in time. It detaches from the edge and shifts inward when $\mathbf{E}_0$ decreases after reaching its maximum.

and the deuterium cluster density was about $n \approx 4.5 \times 10^{22}$ cm^{-3}. For these parameters, the cluster radius is indeed much smaller than the laser wavelength ($R/\lambda \approx 3 \times 10^{-3}$) and the laser frequency is smaller than the electron plasma frequency ($\omega/\omega_{pe} \approx 0.2$). For the specified intensity, there is a core of cold electrons inside the cluster, because all of electrons can only be extracted at intensities above $I = 6 \times 10^{16}$ W/cm^2 (assuming a uniform cluster). Moreover, the extracted electrons do not contribute to the local space-charge density, since the corresponding applicability condition given by Eq. (14) is satisfied: $eE_0/(m_e\omega^2 R) \approx 5$, where E_0 is the laser field amplitude. The characteristic ion response time is roughly $1/\omega_{pi} \approx 10$ fs. This indicates that the ions do have time to expand during the entire laser pulse. However, short time intervals of the order of few laser periods can still be described under the assumption of immobile ions.

2. UNIFORM SPHERICAL CLUSTER

It is interesting that the electron equilibrium can be found analytically for a spherical cluster with a uniform ion density n_i. In order to do this, we note that the electric field created by the ion background alone is given by

$$\mathbf{E} = \frac{4\pi n_i|e|}{3}\mathbf{r} \qquad (1)$$

for $r \leq R$, where the radius $\mathbf{r}$ is measured from the cluster center as shown in Fig. 1. Similarly, a uniformly charged spherical volume of electrons (with the opposite charge density $-|e|n_i$) creates the field

$$\mathbf{E} = -\frac{4\pi n_i|e|}{3}\mathbf{r}_1, \qquad (2)$$

inside the volume, where the radius $\mathbf{r}_1$ is measured from the center of the electron sphere. If we superim-

pose the electron and the ion spheres, then the total space-charge field in the region where the two volumes overlap will be

$$\mathbf{E} = \frac{4\pi n_i|e|}{3}\mathbf{r} - \frac{4\pi n_i|e|}{3}\mathbf{r}_1 = \frac{4\pi n_i|e|}{3}\mathbf{d}, \qquad (3)$$

where $\mathbf{d}$ is the distance between the centers. It is noteworthy that this field is uniform, which allows us to choose the displacement $\mathbf{d}$ in such a way that $\mathbf{E}$ cancels the external electric field $\mathbf{E}_0$ satisfying the requirement that the total electric field vanishes in the region occupied by the confined electrons. We then obtain the following expression for $\mathbf{d}$:

$$\mathbf{d} = -\frac{3}{4\pi n_i|e|}\mathbf{E}_0. \qquad (4)$$

For this solution to be consistent, the entire electron sphere needs to be located inside the ion sphere (see Fig. 1). It may seem that, having found the displacement $\mathbf{d}$, we still have the freedom to choose the radius of the electron sphere anywhere between zero and $R - d$. However, this freedom is deceptive. The radius of the electron sphere (R_e) in our problem is actually determined by the time history of the external electric field. First, it is clear that R_e should be equal to $R - d$ if the external electric field grows monotonically from zero. Indeed, the condition $R_e = R - d$ ensures that the potential well for the electrons has a small leak at the pole of the cluster where the electron sphere touches the ion sphere. The need for such a leak is obviously due to the fact that the cluster is initially neutral and that any monotonic increase in d in this case requires a monotonic decrease in R_e. The situation changes when the external electric field passes through its maximum. If the field goes down, then the electron sphere just shifts closer to the center of the ion sphere with R_e being constant, i.e., without a leak. Furthermore, if the next cycle of the laser field has a larger amplitude, then there will

be a further reduction in R_e when the displacement d brings the electron sphere to the surface of the ion sphere.

Note that the motion of the electron sphere is caused by a small residual electric field inside the core. The value of this field is roughly $(\omega^2/\omega_{pe}^2)E_0$, since the acceleration of the core can be estimated as $\omega^2 d$. The condition $\omega \ll \omega_{pe}$ ensures that the residual field is much smaller than the laser field, which is consistent with our assumption that the electric field vanishes inside the electron sphere.

If the laser pulse is short enough so that the ions do not have time to expand during the pulse, then the value of R_e at the end of the laser pulse is

$$R_e = R - \frac{3}{4\pi n_i |e|}|\mathbf{E}_0|_{\max}, \tag{5}$$

where $|\mathbf{E}_0|_{\max}$ is the maximum value of the laser electric field during the pulse. It is also apparent that the electron and ion spheres remain concentric after the pulse; i.e., the cluster consists of a neutral core surrounded by a positive ion shell. The shell will then expand radially outwards on the ion time-scale, whereas the core will remain at rest. This expansion is described by the following equation of motion:

$$m_i \frac{d^2 r}{dt^2} = \frac{4\pi n_i e^2 [r_0^3 - (R-d)^3]}{3}\frac{1}{r^2}, \tag{6}$$

where m_i is the ion mass and r_0 is the initial position of the ion in the shell ($R \geq r_0 \geq R - d$). This equation has a straightforward energy integral that relates the ion kinetic energy after the expansion to the initial position r_0:

$$\frac{m_i V_\infty^2}{2} = \frac{4\pi n_i e^2 [r_0^3 - (R-d)^3]}{3 r_0}. \tag{7}$$

3. ARBITRARY CLUSTERS

The analytical solution presented above suggests a numerical procedure that allows us to quickly find an equilibrium configuration of the confined electrons for an arbitrarily shaped cluster. Instead of solving the actual electron equation of motion, which would involve many particles and require a very small time step, we use electron boundary dynamics as described below.

We introduce a boundary of the electron population, and we evolve this boundary assuming that its instantaneous velocity at any point is proportional to the local value of the electric field. We take the initial electron boundary at the edge of the cluster, so that the cluster is initially neutral, and we freeze the values of the external field $\mathbf{E}_0$ and the ion space-charge density while we evolve the electron boundary. If any time step takes a

part of the electron boundary outside the ion population, we simply eliminate the protrusion by forcing the appropriate segment of the electron boundary to the cluster edge. We also take the total charge density to be zero everywhere inside the electron boundary, which means that we calculate the instantaneous electric field as a sum of the external field and the electrostatic field created by the exterior ions (those that are outside the electron boundary). We have implemented this algorithm in a code that allows us to find the electron equilibrium for an arbitrary axisymmetric ion density profile. For a uniform spherical cluster, the code shows the rapid convergence to the analytical solution described above. An example of a calculation for a nonuniform spherical cluster is shown in Fig. 2. Note that the equilibrium configuration of the electron core is not spherical in this case.

The equilibrium solutions described above imply that the confined electrons remain cold. However, oscillations of the electron core in the laser field lead to some electron heating due to electron–ion friction. The corresponding heating rate can be estimated as

$$\frac{d\varepsilon}{dt} \approx \nu_{ei}(\varepsilon)\frac{m_e v_{\mathrm{core}}^2}{2}, \tag{8}$$

where

$$v_{\mathrm{core}} \approx \omega d \approx \frac{|e E_0|}{m_e \omega_{pe}^2} \tag{9}$$

is the characteristic velocity of the core, ε is the electron energy, and $\nu_{ei}(\varepsilon)$ is the electron–ion collision frequency. Taking into account that $\nu_{ei}(\varepsilon)$ scales as $\varepsilon^{-3/2}$, we find that the electron energy increases with time as

$$\varepsilon(t) \approx t^{2/5}\nu_{ei}^{2/5}(\varepsilon_*)\left(\frac{\omega}{\omega_{pe}}\right)^{4/5}\varepsilon_*, \tag{10}$$

where

$$\varepsilon_* = \frac{m_e}{2}\left(\frac{e E_0}{m_e \omega_{pe}}\right)^2. \tag{11}$$

The electron heating broadens the sharp boundary of the core, which affects the cold-core equilibrium significantly when the Debye length, estimated as $\lambda_D \approx \sqrt{\varepsilon/m_e \omega_{pe}^2}$, becomes comparable to d. It follows from Eq. (10) that the characteristic time τ_H of the boundary broadening is given by

$$\tau_H \approx \frac{1}{\nu_{ei}(\varepsilon_*)}\frac{\omega_{pe}^2}{\omega^2}, \tag{12}$$

which means that this time can be relatively long when $\omega \ll \omega_{pe}$. If the laser pulse is shorter than τ_H, then the role of the collisional heating is negligible.

Cluster cross section
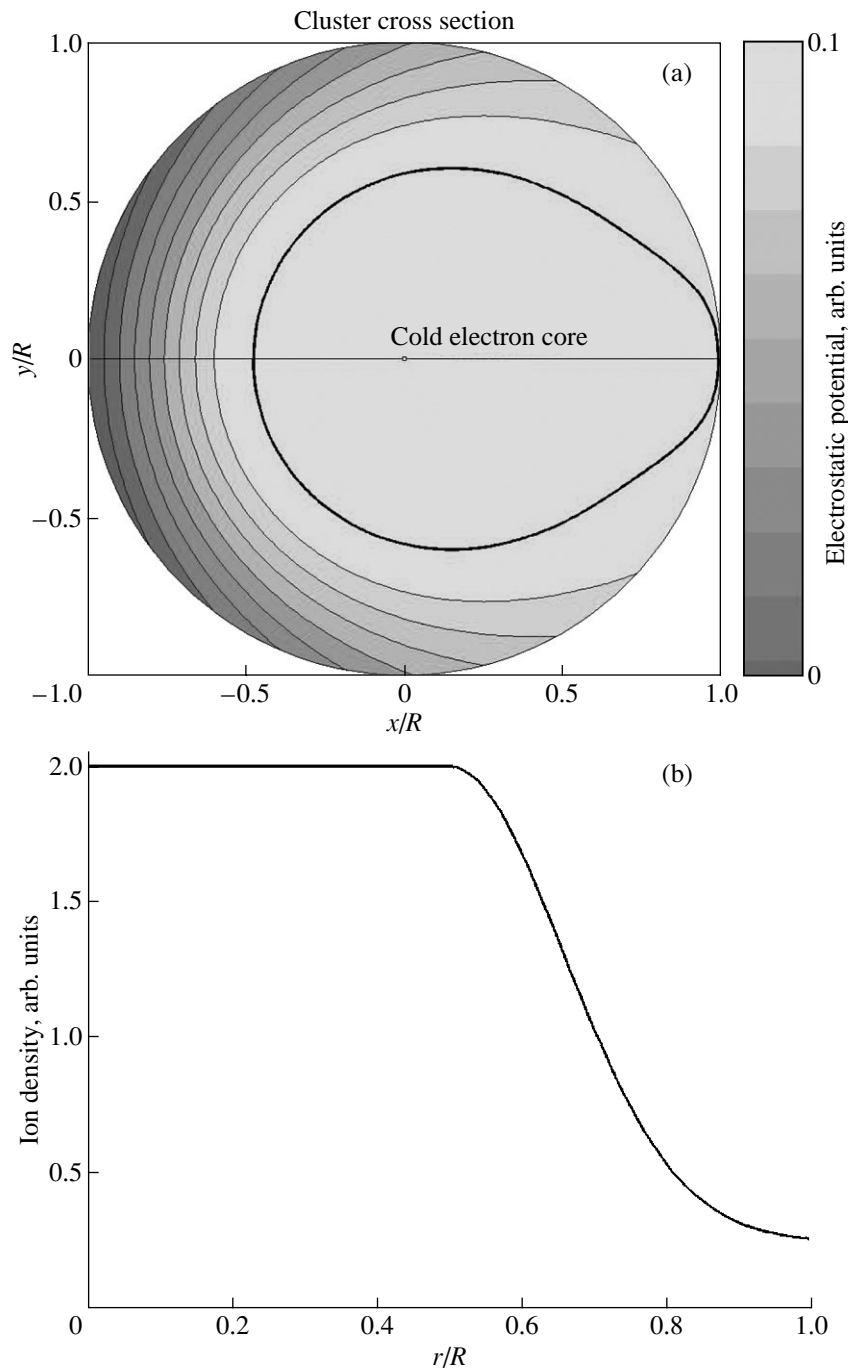
Fig. 2. Equilibrium of the cold electron core in a spherical cluster with nonuniform ion density: (a) the cluster cross section with a contour plot and grey-scale coding for the electrostatic potential and (b) the profile of the ion density. The thick inner line in plot (a) marks the electron core boundary.

4. EXTRACTED ELECTRONS

Once an electron leaves the cluster, it accelerates in the laser field until its kinetic energy reaches roughly $\frac{m_e}{2}\left(\frac{eE_0}{m_e\omega}\right)^2$ (assuming that the electron is nonrelativistic). The corresponding radial excursion of such an electron is on the order of $eE_0/m_e\omega^2$. Under the condi-

tion $\omega \ll \omega_{pe}$, the excursion is much larger than the thickness of the ion shell

$$|\mathbf{d}| = \frac{3|\mathbf{E}_0|_{max}}{4\pi n_i|e|}, \tag{13}$$

and therefore the extracted electrons contribute very little to the space-charge density in the shell. However, the condition $\omega \ll \omega_{pe}$ alone may not be sufficient for

neglecting the extracted electrons. In order to completely neglect these electrons, one needs the electron excursion to exceed the cluster radius (not just the shell thickness); i.e.,

$$\frac{eE_0}{m_e\omega^2} \gg R. \qquad (14)$$

This inequality presents an applicability condition for the equilibrium solutions described in Sections 2 and 3. Equation (14) implies that, once extracted, an electron typically does not return to the cluster. It also means that the characteristic energy of an extracted electron, $\frac{m_e}{2}\left(\frac{eE_0}{m_e\omega}\right)^2$, is larger than the final energy of an accelerated ion from the shell (see Eq. (7)). The expanding ion shell of the cluster never reaches quasi-neutrality under condition (14).

The situation is qualitatively different in the opposite limiting case,

$$\frac{eE_0}{m_e\omega^2} \ll R, \qquad (15)$$

in which most of the edge electrons that cross the ion boundary remain trapped by the ion space charge and oscillate through the cluster. As the fast electrons from the narrow edge layer expand, they spread over the entire cluster volume. They therefore contribute to the electron density inside the cold core, causing the core to expand. This expansion allows some cold electrons to come close enough to the edge to be extracted by the laser field during its next period. We therefore conclude that each period of the laser pulse should convert a small portion of the cold electrons into warm electrons. Since $d \ll R$, the converted fraction (per period) is roughly

$$\frac{|\mathbf{d}|}{R} = \frac{3|\mathbf{E}_0|}{4\pi n_i|e|R}, \qquad (16)$$

with the typical electron energy from the initial kick being $\frac{m_e}{2}\left(\frac{eE_0}{m_e\omega}\right)^2$. This is essentially the effect of the vacuum heating [6–8]. However, the vacuum heating in a small cluster has an additional aspect compared to that described in [6–8]. In the cluster case, the laser field can stochastically heat the earlier generations of extracted electrons as these electrons return to the cluster edge in their oscillatory motion in the ion potential well [9]. The bounce period in the well can be estimated as R/v, where v is the electron velocity. Each bounce oscillation adds roughly $\frac{m_e}{2}\left(\frac{eE_0}{m_e\omega}\right)^2$ to the electron energy, so that the rate of energy increase is

$$\frac{d}{dt}\frac{m_e v^2}{2} = \frac{v}{R}\frac{m_e}{2}\left(\frac{eE_0}{m_e\omega}\right)^2, \qquad (17)$$

and the resulting electron energy scales as

$$\frac{m_e v^2}{2} = m_e\left(\frac{\tau}{R}\right)^2\left(\frac{eE_0}{m_e\omega}\right)^4, \qquad (18)$$

where τ is the laser pulse duration (unless the heated electrons escape before the end of the pulse). It should be emphasized that this process of consecutive extraction and heating only applies to the electrons that cross the cluster edge. The electrons that are permanently confined inside the cluster remain relatively cold, as they adiabatically adjust to the laser field. There is, therefore, a mechanism for creating a two-component electron distribution if condition (15) is satisfied.

If the laser pulse is short enough, then a core of cold electrons will always remain in the cluster, and the corresponding number of core ions will not be involved in the cluster expansion. The ion shell will expand after the pulse under the hot electron pressure, and this will continue until the hot electrons cool down adiabatically. The final energy per single-charged ion will be roughly equal to the average energy of a heated electron.

REFERENCES

1. T. Ditmire, T. Donnelly, A. M. Rubenchik, *et al.*, Phys. Rev. A **53**, 3379 (1996).
2. T. Ditmire, J. Zweiback, V. P. Yanovsky, *et al.*, Nature (London) **398**, 489 (1999).
3. J. Zweiback, R. A. Smith, T. E. Cowan, *et al.*, Phys. Rev. Lett. **84**, 2634 (2000).
4. Y. Kishimoto, T. Masaki, and T. Tajima, Phys. Plasmas **9**, 589 (2002).
5. V. P. Krainov and M. B. Smirnov, Phys. Rep. **370**, 237 (2002).
6. F. Brunel, Phys. Rev. Lett. **59**, 52 (1987).
7. F. Brunel, Phys. Fluids **31**, 2714 (1988).
8. M. K. Grimes, A. R. Rundquist, Y.-S. Lee, and M. C. Downer, Phys. Rev. Lett. **82**, 4010 (1999).
9. T. D. Donnelly, M. Rust, I. Weiner, *et al.*, J. Phys. B **34**, L313 (2001).

Theory of the Anomalous Resistivity of a Randomly Inhomogeneous Plasma

A. S. Kingsep

Russian Research Centre Kurchatov Institute, pl. Kurchatova 1, Moscow, 123182 Russia

Received October 16, 2002; in final form, January 24, 2003

Abstract—The effect of random density inhomogeneities on the anomalous plasma resistivity caused by a current-driven ion acoustic instability is considered. It is shown that, under certain conditions, dissipation due to the plasma inhomogeneity can be more efficient than that due to nonlinear effects. The scenario under consideration can occur in the low-density corona of a high-density Z-pinch. © 2003 MAIK "Nauka/Interperiodica".

1. INTRODUCTION

Some effects associated with fluctuations of the plasma density in a fast Z-pinch were studied in a paper written by L.I. Rudakov in collaboration with the author [1], in which it was shown that such fluctuations, frequently occurring in nature, can strongly affect the corona dynamics through the combined action of the convective transport of a magnetic field (current) [2] and magnetic reconnection processes. Thus, the pinch dynamics can be modified by electron magnetohydrodynamic (EMHD) effects. The coefficient of the effective nonlinear magnetic-field diffusion was found to be equivalent to the Bohm transport coefficients. Formally, the expression for the plasma conductivity that follows from the expression for the magnetic-field diffusion coefficient was also derived from the model of anomalous resistivity developed by Sasorov [3].

In the EMHD theory [2], self-consistent electron flows are insensitive to both the dissipation mechanism and the dissipation coefficients, and even the resistivity of a plasmoid with the parameters in the applicability range of the EMHD theory,

$$c_S, v_A \ll j/ne \ll v_{Te}, v_{Ae} \qquad (1)$$

is a universal quantity. This makes it possible not to focus on the fact that conditions (1) determine, among other things, the plasma range in which anomalous resistivity may be important. In particular, under the condition

$$\omega_{pe} \gg \omega_{Be} \Leftrightarrow B^2 \ll nmc^2, \qquad (2)$$

the dominant mechanism for the anomalous resistivity should be the current-driven ion acoustic instability. For Z-pinches, condition (2) is satisfied by a large margin; in the EMHD theory, however, the dissipation mechanism, as was said, is unimportant.

On the other hand, the electron flow can be self-consistent and, accordingly, the resistivity can be universal

only under certain conditions on the plasma geometry. Specifically, according to [2], the transverse dimension of the electron flow can be represented as

$$\delta \sim \frac{ec}{\sigma B (\partial n^{-1}/\partial x)} \sim \frac{r}{\omega_{Be} \tau_{ei}}, \qquad (3)$$

where r is the characteristic spatial scale of the problem and the other notation is standard. In the case of the anomalous ion acoustic resistivity, which can be estimated, e.g., by the Sagdeev formula

$$\sigma_{\text{eff}} \approx \frac{\omega_{pe}}{4\pi} \frac{ne v_{Te}}{j}, \qquad (4)$$

the estimate that can be obtained for the transverse dimension of the electron flow is independent of the current and magnetic field:

$$\delta^2 \approx \frac{mc^2 r}{e\sqrt{4\pi nT}}. \qquad (5)$$

Hence, when the thickness of the current-carrying shell of the Z-pinch is small in comparison with the spatial scale determined by formula (5), self-consistent electron flows cannot form; i.e., the "tongues" of the field (current loops) that were considered in [1] cannot arise and the current in the Z-pinch corona will flow along the axis in a purely resistive regime.

2. FEATURES OF THE ANOMALOUS RESISTIVITY OF AN INHOMOGENEOUS PLASMA

It is appropriate to utilize the Sagdeev formula (4), which is valid for sufficiently strong electric fields, $E > \frac{m}{M}\sqrt{4\pi nT_e}$, in order to obtain estimates, e.g., for systems with high-current Z-pinches, i.e., for cases in which the plasma current is conditioned by an external circuit and, consequently, the critical quasilinear

regime [4] is practically impossible. Essentially, formula (4) derives from the analysis of a balance between the linear excitation of ion acoustic waves by the plasma current and the nonlinear stimulated scattering of these waves by ions. However, when the amplitude of the plasma density fluctuations is sufficiently large, the plasma resistivity can be determined not by this balance but by the plasma inhomogeneity, in accordance with the Hamiltonian equations of motion of the wave packet,

$$\frac{d\mathbf{r}}{dt} = \frac{\partial\omega}{\partial\mathbf{k}}, \quad \frac{d\mathbf{k}}{dt} = -\frac{\partial\omega}{\partial\mathbf{r}}. \tag{6}$$

It is well known that the problem of the plasma resistivity is a momentum-transfer problem. The electrons accelerated by an electric field acquire momentum and transfer it to the ions. The classical transfer mechanism is associated with collisions, while in the case of anomalous resistivity the transfer mechanism operates through an intermediate cause, whose role is played by noises, or, equivalently, a gas of quasi-particles. Formula (4) implies that momentum is transferred to the ions in the process of stimulated scattering. On the other hand, the electrons can transfer their momentum to the entire plasma and, thereby, to the ion component. This transfer mechanism is described by the second of Eqs. (6).

So, let us consider an object that was frequently encountered in numerical experiments [5]: a Z-pinch with a dense core and a low-density current-carrying corona in which the plasma density is randomly nonuniform. We assume that the characteristic spatial scale on which the plasma density fluctuates satisfies the inequality

$$v_A/a \ll \omega_{pi}, \tag{7}$$

where $v_A = B/\sqrt{4\pi nMA}$. This inequality, which can also be written as

$$a \gg B/4\pi ne \sim I/4\pi nerc;$$

allows us to exclude from consideration the effect of a rapid density redistribution and, accordingly, to assume that the plasma density is steady-state on ion acoustic time scales. Thus, even for $I \sim 20$ MA, we have $a \gg 4 \times 10^{-2}$ cm at $r \sim 2$ cm.

The dispersion relation for ion acoustic waves, $\omega_S(k) = kc_S/\sqrt{1 + (kr_{De})^2} = \omega_{pi}/\sqrt{1 + (kr_{De})^{-2}}$, and Eqs. (6) for an ion acoustic plasmon in an inhomogeneous plasma yield the relationships

$$k^{-2} + r_{De}^2 = \text{inv}, \quad \frac{dn}{dx} > 0 \Rightarrow k \longrightarrow k_{\min} = \omega/c_S,$$
$$n \longrightarrow 0 \Rightarrow k \longrightarrow \infty. \tag{8}$$

Hence, in contrast to a Langmuir plasmon, an ion acoustic plasmon is not subject to the effect of reflection; however, it can disappear due to the Landau damp-

ing by the ions when it moves in the direction in which the plasma density decreases. In order to describe the spectrum of incoherent ion acoustic waves (which is typical of kinetic instabilities), it is convenient to introduce the distribution function of the quasi-particles

$$N_\mathbf{k} = W_\mathbf{k}/\omega_\mathbf{k}. \tag{9}$$

In order to describe quasi-particles, we can use, instead of Eqs. (6), the Liouville equation for which Eqs. (6) are the equations of characteristics:

$$\frac{\partial N_\mathbf{k}}{\partial t} + \frac{\partial\omega}{\partial\mathbf{k}}\boldsymbol{\nabla}N_\mathbf{k} - \frac{\partial N_\mathbf{k}}{\partial\mathbf{k}}\boldsymbol{\nabla}\omega_\mathbf{k} = 2\gamma_\mathbf{k}N_\mathbf{k}. \tag{10}$$

The third characteristic of Eq. (10) generalizes the traditional dependence $\exp(\gamma t)$ to the case of an inhomogeneous medium:

$$N_\mathbf{k}(\mathbf{k}, \mathbf{r}) = N_\mathbf{k}(\mathbf{k}_0, \mathbf{r}_0)\exp\left[\int_{(\mathbf{k}_0, \mathbf{r}_0)}^{(\mathbf{k}, \mathbf{r})}\frac{2\gamma_\mathbf{k}}{|\partial\omega/\partial\mathbf{k}|}dl\right]. \tag{11}$$

For a given dependence $n(\mathbf{r})$, the points $(\mathbf{k}_0, \mathbf{r}_0)$ and $(\mathbf{k}, \mathbf{r})$ in phase space are connected by characteristics (8). The integral is taken along the trajectory of an ion acoustic plasmon. In one-dimensional (and, sometimes, three-dimensional) geometry, it is often convenient to write the main formulas in terms of ω rather than $\mathbf{k}$, because, in the quasi-steady-state problem, the frequency is invariant, while the wave vector $\mathbf{k}$ changes along the trajectory. In Eqs. (10) and (11), the growth rate $\gamma_\mathbf{k} = \gamma_\mathbf{k}^e + \gamma_\mathbf{k}^i$ is the sum of the electron and ion terms, which, under the condition $\omega/k \ll v_{Te}$, can be represented as

$$\gamma_\mathbf{k}^e \approx \sqrt{\frac{\pi}{8}}(\mathbf{k}\cdot\mathbf{u} - \omega)\left(\frac{\omega}{kv_{Te}}\right)^3\left(\frac{M}{m}\right),$$
$$\gamma_\mathbf{k}^i \approx -\pi^2\omega\left(\frac{\omega}{k}\right)^3 f^i\left(\frac{\omega}{k}\right), \tag{12}$$

where M/m is the ion-to-electron mass ratio and $\mathbf{u} = \mathbf{j}/ne$ is the electron current flow velocity. A slight change in this velocity (as is the case in a plasma with a fluctuating density) produces a change in the growth rate. As long as the ions are treated as a passive background, their response to the change in the phase velocity is described by the exponential function. However, in any real problem, resonant ions are always overheated because their number is small; as a result, the ion distribution function $f^i(v)$ in the resonance region is fairly smooth. That is why it is expedient to compare the quantity $j/(n(x)e)$, first of all, with the critical velocity u_{cr}. The critical velocity is usually determined from the equations

$$\gamma(\mathbf{k}, \mathbf{u}) = 0, \quad \frac{\partial\gamma(\mathbf{k}, \mathbf{u})}{\partial\mathbf{k}} = 0.$$
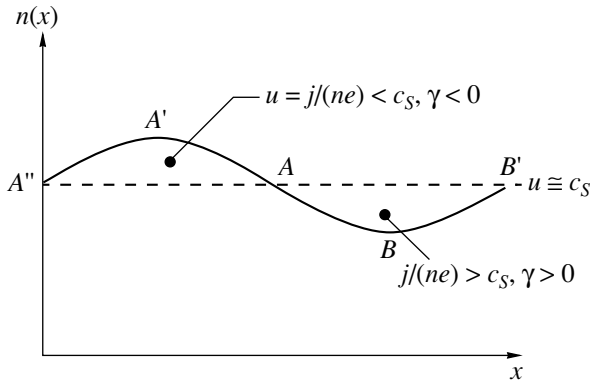
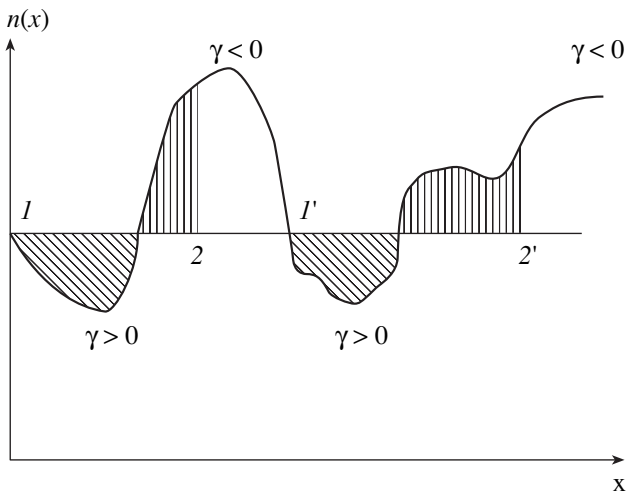**Fig. 1.** The case of a slight density modulation.

Fig. 2. A deeply modulated plasma density. The regions where the noise density is nonzero are hatched.

In the problem of the resistivity of a homogeneous plasma, it is unlikely that there exists a steady state that is governed exclusively by the balance of linear growth rates (12). The reason is that nothing can balance the momentum acquired by the majority of the ions in the electric field because there are only a few resonant ions. The limitation associated with the fact that, in the linear approximation, there are no electron and ion fluxes through the boundary of the resonance region can be overcome by taking into account quasilinear effects and modifying the dispersion relation [6], in which case, however, both plasma components tend to asymptotically go over to the free acceleration regime. This formal solution can hardly correspond to a real situation because of the influence of nonlinear effects [7]; in actual experiments, the nonlinear scenario is usually considered as the only possible one (see [8] and the references therein). As was already mentioned, accounting for the plasma inhomogeneity opens some new possi-

bilities. In order to simplify further calculations, we will use a one-dimensional model. In a sense, such a model is artificial because, strictly speaking, the anomalous resistivity cannot exist in the one-dimensional approximation. However, the purpose of the present paper is not to develop a systematic approach to a complete solution of the problem but rather to demonstrate the main effects pertaining to the subject.

3. SLIGHTLY MODULATED DENSITY APPROXIMATION

As an example, we consider a plasma whose density is modulated by a one-dimensional sinusoid (Fig. 1). Since the current I is determined by the external circuit, the current velocity satisfies the relationship $|\mathbf{u}| \propto n^{-1}$. The dashed line in Fig. 1 corresponds to the density value at which $|\mathbf{u}| = u_{cr}$. In accordance with Eq. (11), the condition for the spectrum to be quasi-steady can be represented in the form

$$\int_{k_0,\, x_0}^{k_1,\, x_1} \frac{2\gamma_k}{\partial \omega / \partial k} dl = 0, \qquad (13)$$

where the interval (x_0, x_1) is the spatial period of the density perturbation. The equation describing the momentum transfer between the waves and the plasma (and, ultimately, the ions) follows from Eqs. (6): $\partial \mathbf{k}/\partial t = -\nabla \omega \cong -(\omega_{pi}/2)(\nabla n/n_0)$. At first glance, momentum transfer is impossible because the momentum of each of the ion acoustic plasmons does not change after they pass through the modulation period. Let us, however, compare the intervals $A'A''$ and $A'A$ in Fig. 1. Over the entire interval $A''A$, the growth rate γ is negative, $\gamma < 0$; consequently, the number of quasi-particles at the descent $A'A$, where they acquire momentum, is less than that at the ascent $A''A'$, where the waves transfer their momentum to the plasma. In the interval over which the growth rate is positive, the situation is the same: the number of plasmons that lose their momentum at the ascent BB' is larger than that at the descent AB, where they take away momentum from the plasma. Hence, the waves can transfer the momentum that they take away from the electrons to the ions even when none of the nonlinear mechanisms is operating.

4. MOMENTUM BALANCE IN A PLASMA WITH A DEEPLY MODULATED DENSITY

The above model can serve merely for illustrative purposes. In a system with a prescribed current, there is no reason why the current velocity should reach a steady-state level for which condition (13) is satisfied. The situation that is depicted in Fig. 2, which refers to a sufficiently deep density modulation, is far more realistic. In this case, we are dealing with a sort of trapping of plasmons between points 1 (1'), which correspond to the instability threshold, and points 2 (2'), at which the

noises are damped to the fluctuation level (the current flows from left to right, so that the direction of the electron flow velocity coincides with the positive direction of the x-axis). Assuming that the mean plasma density gradient is zero, we can introduce the scale length L as the distance between the minima (or maxima) of the density in the trapping region:

$$J \equiv \int_L \frac{2\gamma_k}{\partial \omega / \partial k} dl \leq 0. \tag{14}$$

The spatial density of the momentum transferred between the plasma components is described by the equations

$$\frac{\partial}{\partial t}\frac{\partial \mathbf{p}_e}{\partial V} = -\frac{\partial}{\partial t}\frac{\partial \mathbf{p}_i}{\partial V} = \sum_k N_k \frac{\partial \mathbf{k}}{\partial t}$$

$$= \sum_\omega N_\omega \frac{\partial \mathbf{k}(\omega, \mathbf{r})}{\partial t} = -\sum_\omega N_\omega \nabla \omega, \tag{15}$$

where we have switched from the k representation to the ω representation. In this way, the electron momentum balance can be written in terms of the effective collision frequency:

$$\int_{x_1}^{x_2} ne\mathbf{E} dx = \mathbf{j}\frac{m}{e}\int_{x_1}^{x_2} \upsilon_{\text{eff}}(x)dx. \tag{16}$$

In deriving this formula, we took into account the fact that the electric field of the plasma current produced by an external circuit is nonzero only within the intervals (1, 2) and (1', 2'), i.e., in the regions where the density of the noise and, accordingly, the effective collision frequency υ_{eff} are nonzero. For further estimates, we introduce the integral density of the noise, $W(x) = \int \omega N_\omega d\omega$. At first glance, this parameter is far more general than the spectral density of the ion acoustic waves; however, as will be seen below, the noise spectrum in each individual instability region should be fairly narrow. As a result, the estimate of the effective collision frequency can be simplified to

$$j\frac{m}{e}\int_{x_1}^{x_2}\upsilon_{\text{eff}}(x)dx = \int_{x_1}^{x_2}dx\int d\omega N_\omega \frac{\partial \omega}{\partial x} \cong \int_{x_1}^{x_2}dx\frac{W(x)}{\omega}\frac{\partial \omega}{\partial x}. \tag{17}$$

At points 1, 1', etc., the noise level can be estimated by the level of thermal fluctuations:

$$W(x_1) \equiv W_0 \sim nT/N_D,$$

where N_D is the number of particles within a Debye sphere (taking into account the difference between T_e and T_i would lead to an excessive accuracy). From expressions (11) and (12), we readily obtain

$$W(x) = W_0 \exp \Gamma(x_1, x),$$

$$\Gamma \equiv \sqrt{\frac{\pi}{8}}\frac{\omega}{v_{Te}}\int_{x_1}^{x \leq x_2}\left(\frac{ku}{\omega} - 1\right)dx \tag{18}$$

$$= \kappa \int_{x_1}^{x \leq x_2}\left(\frac{j}{n(\xi)}\frac{k(\xi)}{e\omega} - 1\right)d\xi,$$

$$\kappa = \text{const} \sim \sqrt{\frac{m}{M}}r_{De}^{-1}\Big|_{x=0}, \quad \Gamma(x_1, x_2) = 0.$$

The dispersion relation for the ion acoustic waves yields

$$-\frac{1}{\omega}\frac{\partial \omega}{\partial x} = \frac{1}{2}\frac{\omega^2}{\omega_{pi}^2}\frac{1}{n}\frac{\partial n}{\partial x} \approx \frac{n(x_0)}{2}\frac{1}{n^2}\frac{\partial n}{\partial x} \approx \alpha\langle n\rangle \frac{\partial}{\partial x}\left(\frac{1}{n}\right), \tag{19}$$

$$\alpha \sim 1.$$

Now, we can transform formula (17) to

$$j\frac{m}{e}\int_{x_1}^{x_2}\upsilon_{\text{eff}}dx$$

$$= -\alpha\langle n\rangle \frac{\langle nT\rangle}{\langle N_D\rangle}\int_{x_1}^{x_2}\frac{\partial}{\partial x}\left(\frac{1}{n}\right)\exp[\Gamma(x_1, x)]dx. \tag{20}$$

We introduce the mean effective collision frequency υ_B in the instability region and the frequency υ_R averaged over the quasi-period L (the latter frequency determines the resistivity of the current-carrying corona):

$$\upsilon_B(x_2 - x_1) \equiv \upsilon_R L = -\beta\frac{\langle n\rangle^{5/2}e^4}{mj\sqrt{T}}I(x_1, x_2),$$

$$I(x_1, x_2) \equiv \int_{x_1}^{x_2}\frac{\partial}{\partial x}\left(\frac{1}{n}\right)\exp[\Gamma(x_1, x)]dx, \quad \beta \geq 1. \tag{21}$$

The integral on the right-hand side of formula (21) can be taken by parts with allowance for the relationships $\Gamma(x_1, x_1) = \Gamma(x_1, x_2) = 0$:

$$I(x_1, x_2) = -\left\{\frac{1}{n(x_1)} - \frac{1}{n(x_2)}\right.$$

$$\left. + \kappa\int_{x_1}^{x_2}\frac{dx}{n(x)}\left(\frac{j}{n(x)}\frac{k(x)}{e\omega} - 1\right)\exp\left[\kappa\int_{x_1}^{x}\left(\frac{j}{n(\xi)}\frac{k(\xi)}{e\omega} - 1\right)d\xi\right]\right\}. \tag{22}$$
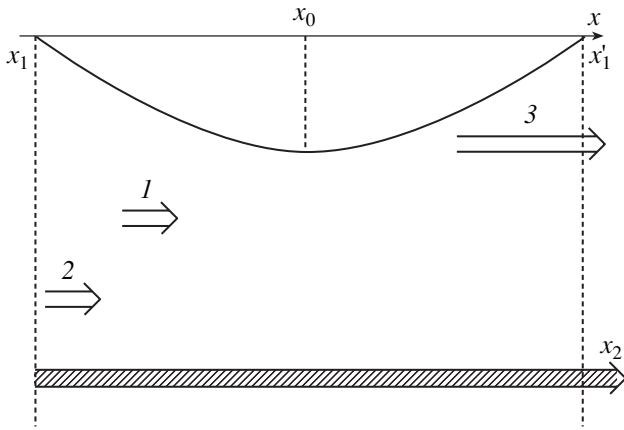
Fig. 3. Localization of plasmons in a parabolic density well.

As a result, formula (21) reduces to

$$
\upsilon_B(x_2 - x_1) = \upsilon_R L = \beta \frac{\langle n \rangle^{5/2} e^4}{m j \sqrt{T}} \left\{ \frac{1}{n(x_1)} - \frac{1}{n(x_2)} \right.
$$

$$
+ \varepsilon \frac{\omega}{v_{Te}} \int_{x_1}^{x_2} \frac{dx}{n(x)} \left(\frac{j}{n(x)} \frac{k(x)}{e\omega} - 1 \right) \tag{23}
$$

$$
\left. \times \exp\left[\kappa \int_{x_1}^{x} \left(\frac{j}{n(\xi)} \frac{k(\xi)}{e\omega} - 1 \right) d\xi \right] \right\},
$$

$$
\varepsilon \lesssim 1.
$$

We introduce the spatial scale of an individual density well, $a \lesssim L$, in such a way that the density near the bottom has the form $n = n(x_0)[1 - (x - x_0)^2/a^2]$ (see Fig. 3). All the trajectories of quasi-particles in the well should satisfy the condition $k^{-2} + r_{De}^2 = \text{inv}$. The above assumptions imply that, at a density lower than $n(x_1)$, the current velocity exceeds the critical velocity for two-stream instability. The points at which the current velocity is equal to the critical velocity are determined by the condition $j \approx n(x_1)ec_S = n(x_1')ec_S$. The growth rate is proportional to $[ku/\omega - 1]$; consequently, the higher the frequency ω (the smaller the ratio ω/k), the larger the growth rate γ. From this point of view, the anomalous resistivity is associated preferentially with the ion plasma waves. However, an ion acoustic plasmon whose invariant frequency approaches ω_{pi} at the descent of the density well (see arrows *1*, *2* in Fig. 3) will be subject to strong Landau damping (when $\omega/k \longrightarrow 0$) after passing a certain distance within the instability region. The same is true of the plasmons that originate behind the density well (arrow *3* in Fig. 3). Hence, the momentum is preferentially transported by plasmons that pass through the entire noisy region and

whose frequency is the highest, i.e., plasmons whose frequency is equal to $\omega = \omega_{pi}(x_0)$ exactly at the bottom of the well. The trajectories of such plasmons extend over the entire interval (x_1, x_2) (see the hatched arrow in Fig. 3). For these plasmons, we can use the estimates

$$
k(x_1) = k(x_1') \approx \frac{\omega_{pi}(x_0)n_1 e}{j} \approx \frac{\omega_{pi}}{c_S} \approx r_{De}^{-1}(x_0),
$$

$$
\tag{24}
$$

$$
k(x_1)r_{De}(x_1) \approx \frac{c_S n_1 e}{j} \sqrt{\frac{n_0}{n_1}} \ll 1.
$$

In the model of a quasi-parabolic plasma density profile (Fig. 3), we can derive the following relationship between the length of the "noisy" interval (x_1, x_2) and the characteristic spatial scale of the well:

$$
n_1 = j/ec_S = n_0(1 + (\Delta x)^2/a^2)
$$

$$
\Rightarrow (x_2 - x_1) \sim 2(x_1' - x_1) \sim 4\Delta x \sim 4a \sqrt{\frac{j}{n_0 ec_S} - 1}.
$$

Within the accuracy adopted for these estimates, we can neglect unity under the square root symbol. As a result, we arrive at the final estimate for the ratio of the length of the turbulent region to the characteristic scale on which the plasma density varies:

$$
\frac{(x_2 - x_1)}{a} \sim \sqrt{\frac{j}{n_{\min}ec_S}} \Rightarrow \upsilon_R \sim \upsilon_B \sqrt{\frac{j}{n_{\min}ec_S}}. \tag{25}
$$

The same (but more accurate) estimate can be obtained from the condition $\Gamma(x_1, x_2) = 0$; i.e.,

$$
\int_{x_1}^{x_2} \frac{j}{e\omega} \frac{k(\xi)}{n(\xi)} d\xi = x_2 - x_1. \tag{26}
$$

For a particular density well (Fig. 3), we can introduce the notation $x_0 = 0$, $x_1 = -\Delta$, and $x_1' = \Delta$, where $\Delta^2/a^2 = (j/n_0 ec_S) - 1$. In this notation, invariant (8) can be rewritten as

$$
k^{-2} = r_{De}^2(0)\left[1 + \delta_* + \frac{n_0}{n(\xi)} \right],
$$

where $\delta_* \ll 1$ is the factor that is used to truncate integral (26) in order to make it convergent. Thereby, the integrand in formula (26) can be transformed into

$$
\frac{k(\xi)}{n(\xi)} \frac{j}{e\omega} = \frac{n(\Delta)}{n} \frac{k}{k(\Delta)}
$$

$$
= \frac{a^2 + \Delta^2}{a^2 + \xi^2} \sqrt{\frac{1 + \delta_* - n_0/n(\Delta)}{1 + \delta_* - n_0/n(\xi)}} = \sqrt{\frac{a^2 + \Delta^2}{a^2 + \xi^2}} \sqrt{\frac{a^2\delta + \Delta^2}{a^2\delta + \xi^2}},
$$

where $\delta = \delta_*/(1 + \delta_*) \ll 1$. It is helpful to introduce the following dimensionless variables, in which a serves as a spatial scale:

$$\frac{x_2 - x_1}{a} \longrightarrow x, \quad \frac{\Delta}{a} \longrightarrow \Delta = \sqrt{(j/n_0 e c_S) - 1}.$$

In terms of these variables, Eq. (26) becomes the transcendental equation

$$x = \sqrt{1 + \Delta^2}\sqrt{\delta + \Delta^2} \int_{-\Delta}^{x - \Delta} \frac{d\xi}{\sqrt{(1 + \xi^2)(\delta + \xi^2)}}. \quad (27)$$

Estimates (23) can also be rewritten in the dimensionless form:

$$\upsilon_B x = \upsilon_R = \beta \frac{\langle n \rangle^{5/2} e^4}{mj\sqrt{T}} \left\{ \frac{x^2 - 2x\Delta}{(1 + \Delta^2)(1 + [x - \Delta]^2)} \right.$$

$$+ \varepsilon \sqrt{\frac{m}{M}} \frac{a}{r_{De}(0)} \int_{-\Delta}^{x - \Delta} \frac{dx}{1 + x^2} \left[\sqrt{\frac{1 + \Delta^2}{1 + x^2}} \sqrt{\frac{\delta + \Delta^2}{\delta + x^2}} \right]$$

$$(28)$$

$$\times \left. \exp\left[\varsigma\sqrt{\frac{m}{M}}\frac{a}{r_{De}(0)} \int_{-\Delta}^{x} d\xi \left(\sqrt{\frac{1 + \Delta^2}{1 + \xi^2}}\sqrt{\frac{\delta + \Delta^2}{\delta + \xi^2}} \right) \right] \right\},$$

$$\beta, \varepsilon, \varsigma \le 1.$$

5. CONCLUSION

In principle, formulas (27) and (28) solve the problem of the plasma resistivity. In this solution, the resistivity depends on the plasma parameters j, a, n_0, $\langle n \rangle$, and T. Let us try to determine the parameter range in which the effects under consideration dominate over the nonlinear effects. Above, we have derived the rough estimate $\Delta \approx \sqrt{(j/n_0 e c_S)}$. The restrictions imposed by the Buneman instability yield $\Delta < \sqrt{M/m}$. Although the factor that was used to truncate the integral, $\delta \approx (k(0)r_{De}(0))^{-2} \ll 1$, is small, it cannot be too small because of the Landau damping by the ions. It is natural to set $\delta \sim T_i/T_e$. In the nonlinear regime with a prescribed current, the density of the noises can be estimated as follows [9] (see also [8]):

$$(W/nT)_{nl} \sim j/ne\,\upsilon_{Te}.$$

In the case at hand, this gives

$$(W/nT)_{max} \approx (\exp\Gamma_0)/N_D,$$

$$\Gamma_0 = \sqrt{\frac{m}{M}}\frac{a}{r_{De}} \int_{-\Delta}^{\Delta} d\xi \left(\sqrt{\frac{1 + \Delta^2}{1 + \xi^2}}\sqrt{\frac{\delta + \Delta^2}{\delta + \xi^2}} - 1 \right).$$

Under the condition $(W/nT)_{max} < (W/nT)_{nl} \Rightarrow \Gamma_0 < \ln(\Delta^2 N_D)$, a more efficient mechanism for suppressing

the instability is that associated with the plasma inhomogeneity. Hence, the approximate condition for the applicability of the model developed here can be represented as

$$\sqrt{\frac{m}{M}}\frac{a}{r_{De}}\Delta\sqrt{1 + \Delta^2} \int_{-\Delta}^{\Delta} \frac{d\xi}{\sqrt{1 + \xi^2}\sqrt{\delta + \xi^2}} < \ln(\Delta^2 N_D).$$

Further progress in developing the theory and refining the boundaries of its applicability requires the use of numerical methods. However, this way seems to be unpromising because of the large number of assumptions made in finding the solution. In my opinion, the fact that it was possible to completely develop the scenario is far more important than the possibility of obtaining an exact solution. This circumstance is peculiar to the problems of the dynamics of small-scale turbulence in an inhomogeneous plasma: such studies generally yield either rough estimates [10] or exact solutions to refined model problems [11]. However, from the physical point of view, the effects of inhomogeneity that determine the deceleration of particle beams or anomalous resistivity are quite obvious and are observed experimentally (see, e.g., [12]).

The present investigation is in a sense related to the research that was carried out in the 1970s and 1980s in connection with the problem of the resistivity of randomly inhomogeneous media dominated by classical resistive effects (e.g., the so-called "Dykhne medium"), in particular, the resistivity of a weakly ionized plasma. In the present paper, however, a study has been made only of the mechanism responsible for the resistivity of a randomly inhomogeneous plasma dominated by collective effects. The construction of a three-dimensional self-consistent theory is the subject of future work.

In conclusion, I would like to say that the problem of the anomalous resistivity and turbulent heating of a weakly inhomogeneous plasma was first brought to my attention in the late 1960s, when I was a postgraduate student, by my teacher Leonid Ivanovich Rudakov and it is a pleasure to dedicate this paper to his 70th birthday.

REFERENCES

1. A. S. Kingsep and L. I. Rudakov, Fiz. Plazmy **21**, 611 (1995) [Plasma Phys. Rep. **21**, 576 (1995)].

2. A. S. Kingsep, K. V. Chukbar, and V. V. Yan'kov, in *Reviews of Plasma Physics*, Ed. by B. B. Kadomtsev (Énergoatomizdat, Moscow, 1987; Consultants Bureau, New York, 1990), Vol. 16.

3. P. V. Sasorov, Fiz. Plazmy **18**, 275 (1992) [Sov. J. Plasma Phys. **18**, 143 (1992)].

4. L. I. Rudakov and L. V. Korablev, Zh. Éksp. Teor. Fiz. **50**, 220 (1966) [Sov. Phys. JETP **23**, 145 (1966)].

5. P. Sheehey, J. E. Hammel, I. R. Lindemuth, *et al.*, Phys. Fluids B **4**, 3698 (1992); P. Sheehey and I. R. Lindemuth, Phys. Plasmas **4**, 146 (1997).

6. G. E. Vekshteĭn, D. D. Ryutov, and R. Z. Sagdeev, Zh. Éksp. Teor. Fiz. **60**, 2142 (1971) [Sov. Phys. JETP **33**, 1152 (1971)].

7. A. S. Kingsep, Zh. Éksp. Teor. Fiz. **63**, 498 (1972) [Sov. Phys. JETP **36**, 264 (1973)].

8. A. S. Kingsep, Fiz. Plazmy **17**, 582 (1991) [Sov. J. Plasma Phys. **17**, 342 (1991)].

9. B. B. Kadomtsev, in *Reviews of Plasma Physics*, Ed. by M. A. Leontovich (Atomizdat, Moscow, 1964; Consultants Bureau, New York, 1968), Vol. 4.

10. A. A. Vedenov and D. D. Ryutov, in *Reviews of Plasma Physics*, Ed. by M. A. Leontovich (Atomizdat, Moscow, 1972; Consultants Bureau, New York, 1975), Vol. 6.

11. D. D. Ryutov, Zh. Éksp. Teor. Fiz. **57**, 232 (1969) [Sov. Phys. JETP **30**, 131 (1970)].

12. Yu. P. Golovanov, N. I. Elagin, L. P. Zakatov, *et al.*, Fiz. Plazmy **3**, 619 (1977) [Sov. J. Plasma Phys. **3**, 349 (1977)].

Translated by O.E. Khadin

PLASMA
INSTABILITY

A Phenomenological Model of the Current Filamentation Instability Driven by Cathode Processes in the Livermore Spheromak[1]

D. D. Ryutov, R. H. Cohen, and D. N. Hill

Lawrence Livermore National Laboratory, Livermore, CA 94551, USA

Received December 26, 2002

Abstract—The current density on the open field lines of the Livermore spheromak (SSPX) typically exceeds the saturation current density of the bulk plasma. We assume that the mechanism that provides conditions for that is associated with the formation of a thin layer near the cathode surface, where both the plasma and the neutral density are higher than in the bulk plasma and where intense ionization occurs. The ions formed in this layer fall back onto the cathode, whereas electrons contribute to the high current density in the bulk plasma. The particle balance in the ionizing layer is determined by the recycling coefficient, which, in turn, depends on the cathode temperature and the sheath voltage. As it turns out, these dependences give rise to an instability that leads to the current filamentation and the formation of hot spots on the cathode surface. The instability can be characterized in a phenomenological manner without going into the details of the structure of the ionizing layer, whose effect on the instability shows up in the form of a couple of numerical coefficients of the order of one. We predict the characteristic size and the shape of the filaments (and the hot spots), which are in a general agreement with discoloration patterns on the surface of the cathode in the SSPX. If the magnetic field is tilted to the surface, the footpoints of the filaments move with a significant velocity, whose direction depends on the ratio of the ion gyroradius and the thickness of the ionizing layer. This instability, although primarily considered in conjunction with the SSPX experiment, may play a role in spherical tokamaks and other systems with coaxial helicity injection. © 2003 MAIK "Nauka/Interperiodica".

1. INTRODUCTION

We dedicate this paper to the 70th birthday of Leonid I. Rudakov. L.I. Rudakov was among the first plasma theorists to realize importance of the effects of the edge on the properties of high-temperature plasmas. A good example is his treatment of the role of cold near-wall plasma in stabilizing flute perturbations in a turbulently-heated mirror [1]. Our paper is also related to edge effects, although in a different setting. We present a theory of the current filamentation instability driven by the dependence of the recycling coefficient on the cathode temperature. Our work has been primarily motivated by the experimental results obtained at the SSPX spheromak at the Lawrence Livermore National Laboratory [2–4], where the characteristic patterns of cathode discoloration were found upon inspection of the cathode surface after an experimental campaign (see below). We present a theory that seems to correctly predict both the spatial scale of these patterns and their orientation.

A schematic of the SSPX experiment is shown in Fig. 1. The spheromak is formed in the following manner. First, a quasi-static poloidal magnetic field is formed by external coils. This process is slow and the field penetrates through all of the conducting shells.

(The discharge itself is, however, much shorter than the skin time for the conducting walls, and the magnetic field remains frozen into these walls for the rest of the discharge.) After that, a gas is puffed near the "knee" in the annular part of the device; the gas-puff is approximately axisymmetric. Then, a voltage is applied between the inner electrode (cathode) and the outer electrode (ground), and the gas breaks down and is expelled by the toroidal magnetic field into the confinement chamber of the device. The plasma pulls out part of the poloidal flux from the annular region, and a toroidal magnetic configuration is formed in the confinement chamber.

This paper is concerned with the processes occurring in the region of open field lines near the cathode surface (i.e., near the surface of the inner electrode in Fig. 1). The pattern that indicates the possible presence of current filamentation is shown in Fig. 2, where helical stripes ~1 cm wide are clearly visible. In this paper we explain the width and orientation of these stripes.

The current density along the field lines in the SSPX is typically a few times higher than the ion saturation current density $\sim env_{Ti}$ (see, e.g., the book [5]), which is evaluated for the parameters of the bulk plasma. The model applied to a description of the filamentation instability must take this factor into account and provide some explanations for it. We suggest that the cur-

---

[1] This article was submitted by the authors in English.
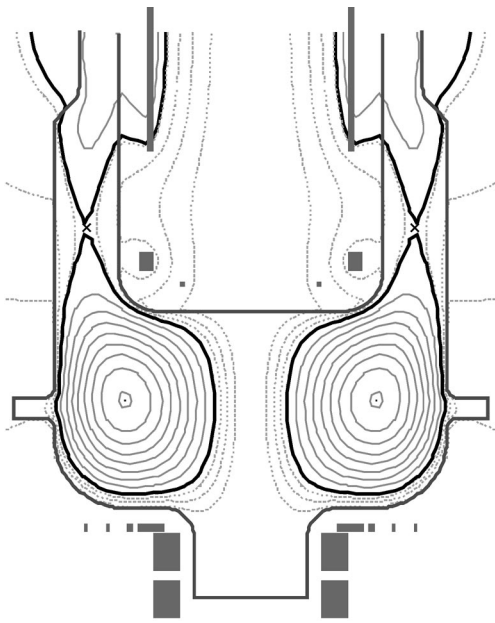
Fig. 1. Cross section of the SSPX experiment; the poloidal field coils are shown as shaded rectangles. The magnetic-flux surfaces correspond to a spheromak sitting in the flux conserver. The thick line shows the separatrix. We are concerned with the currents on the open field lines outside the separatrix. It is probable that in some regimes all of the field lines become open, though they may be quite long.

rent higher than the saturation one is attained via the formation of a centimeter-thick layer with a relatively high density of neutral atoms near the cathode; the ionization of these atoms serves as a source of electrons for

sustaining a high current density in the bulk plasma, whereas the ions fall back onto the cathode. We call this layer the ionizing layer. The idea of an increased neutral density near the material wall is by no means a new idea: it has been analyzed in great detail in conjunction with the physics of divertors in tokamaks (e.g., [6–8]). We just use this idea in a somewhat different context.

We do not present a detailed analysis of the processes occurring in the ionizing layer. As we show in Section 3, a linear dispersion relation can be obtained based on some very general considerations, in which the properties of the ionizing layers enter the problem in a compact way: via a single function μ that relates the perturbations of the ion flux to the surface and the neutral flux from the surface. This function can be considered as a phenomenological description of the ionizing layer, whence the title of our paper comes.

The spheromak external circuit contains a large inductance, $L \sim 2.5$ μH, which forces the total current through the spheromak to be essentially constant on the time scales of interest for the instability we are considering. We assume that the cathode potential drop adjusts itself in a way that maintains the total current at a constant level. On this background, however, small-scale perturbations are allowed as long as they do not cause the total current to vary. Thus, the voltage applied to the spheromak also does not change in the course of the instability development.

The instability is driven by the temperature dependence of the recycling coefficient of the cathode: if the surface temperature increases, the recycling coefficient increases, leading to an increase of the ion flux, which increases the heating and causes the instability. The sta-
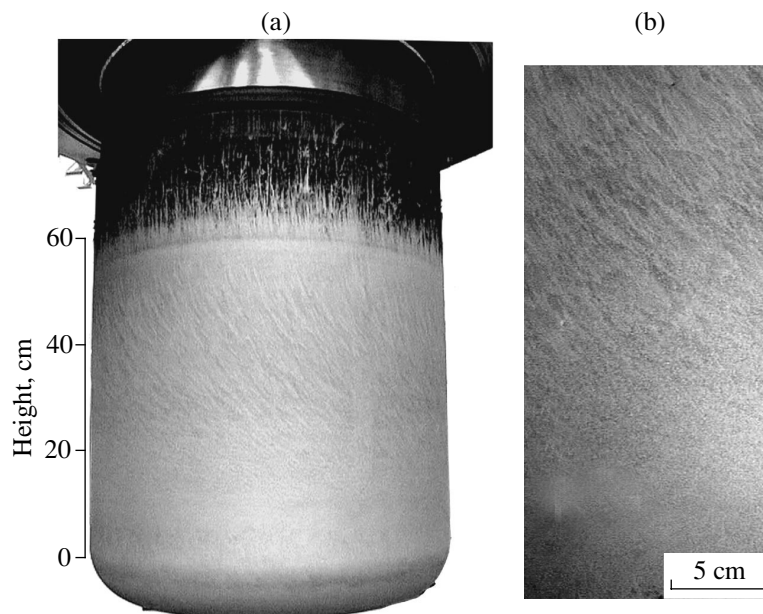
**Fig. 2.** A photograph of the SSPX cathode: (a) the whole cathode and (b) the middle part.

bilizing mechanism is related to the inductive electric field appearing in the bulk plasma in the course of the current increase in the flux tube; this inductive field leads to a decrease in the sheath voltage and a decrease in the recycling coefficient (thereby introducing a negative feedback loop).

To explain qualitatively the processes that determine the spatial scale of the filaments, we consider here the case of the normal intersection of the magnetic field with the wall (a general analysis is presented in Sections 2 and 3). The neutrals generated at the surface of the cathode have a more or less isotropic velocity distribution. Accordingly, the neutrals formed at some point on the cathode surface (Fig. 3) get ionized in a volume whose projection onto the cathode surface has a size of the order of Δ, the thickness of the ionizing layer. The ions produced by the ionization of these neutrals get accelerated towards the cathode and shower a surface element whose size is $\sim\Delta$. This consideration shows that the thermal feedback loop is inefficient for a flux tube with a transverse dimension of less than Δ; this feedback loop becomes more and more efficient as the size of the filament increases.

There exists, however, a mechanism that suppresses instability for sufficiently "thick" flux tubes. This is the inductive voltage, which is directed against the growing current and reduces the potential drop across the cathode sheath, thereby reducing the recycling coefficient. For a given current perturbation, the inductive voltage scales linearly with the transverse size of the fluxtube, thereby making positive feedback impossible for sufficiently thick flux tubes.

An optimum scale of the perturbations is established by an interplay of these two effects. It turns out to be somewhat larger than Δ (see Section 3) and, in the case of a normal intersection, does not depend on the magnetic-field strength. If the magnetic field is tilted towards the surface, the ion trajectories in the ionizing layer become sensitive to the magnetic-field strength, and the whole picture becomes more complex. In Section 4, we analyze in some detail the situation where the thickness of the ionizing layer is less than the ion gyroradius.

To put our work in the context of previous studies of the formation of hot spots, we mention an elegant analysis by Nedospasov and Petrov [9], who showed that thermal instability in a currentless plasma may occur due to the temperature dependence of electron thermoionic and secondary emission. Later, Nedospasov and Bezludny [10] considered a similar problem but including heat transport along the surface. Neither of these papers consider effects caused by high plasma currents and neutral recycling, which are crucial in our model. Cathode arcs have been surveyed by Wolff [11]. They typically have spatial scales much smaller than the 1- to 2-cm-wide helical patterns observed in the SSPX. In some areas of the SSPX cathode, chicken-track patterns are visible, whose width is less than
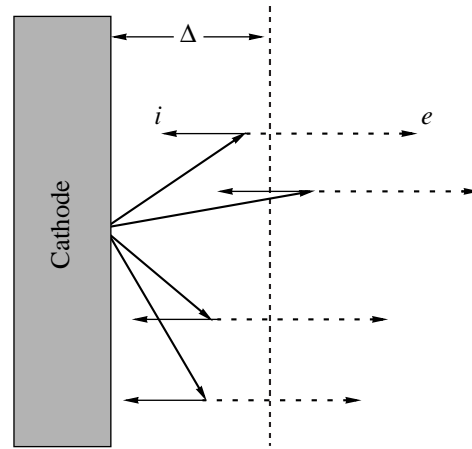
Fig. 3. The case of a normal intersection of the magnetic field with the cathode surface. Neutrals (thick arrows) originating at some point at the cathode surface propagate at various angles with respect to the magnetic field and are ionized at the tips of the arrows. The ions (solid arrows) are pulled back to the cathode by the electric field, whereas the electrons (dashed arrows) contribute to the current in the bulk plasma. Although the neutrals originated at one point, the ions cover an area comparable to the thickness of the ionizing layer Δ.

1 mm. They are probably caused by arcing. But they generally do not overlap with the zone where the aforementioned smooth helical structures with a width of 1–2 cm are observed.

In the numerical estimates, we will use the following assumptions regarding the bulk-plasma parameters:

$$n = 5 \times 10^{13} \text{ cm}^{-3}, \quad T = 100 \text{ eV}, \qquad (1)$$
$$B = 2 \text{ kG}, \quad j = 300 \text{ A/cm}^2,$$

where n and T are the density and temperature of the bulk plasma, B is the magnetic-field strength, and j is the current in the bulk plasma (which is almost parallel to the magnetic field). The sheath potential U_C can be quite high. We take as a representative value

$$U_C = 300 \text{ V}. \qquad (2)$$

A typical experimental "shot" on the SSPX device consists of a formation phase, a sustainment phase, and a decay phase. The plasma parameters may vary significantly between the phases. The set of parameters shown above corresponds to the situation of relatively long flux tubes connecting electrodes, with a connection length of $\sim$10 m or more, and high current densities. On the other hand, the general dependences found in our study may be relevant to other phases of the SSPX discharge (although we do not pretend to cover all the conceivable mechanisms of current filamentation in these other regimes). Our results may be of interest not only to gun-driven spheromaks (like the SSPX) but also to other systems with coaxial helicity injection, in particular, spherical tokamaks [12].
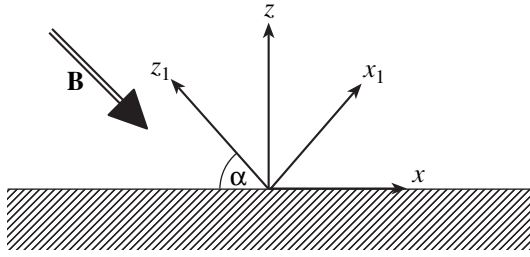
Fig. 4. The planar geometry. The *x* axis is directed along the projection of the magnetic field onto the cathode surface. The *y* axis is directed away from the viewer.

The paper is organized as follows. In Section 2, we present the physical model used in our analysis. In Section 3, which is central in our paper, we derive the linearized equations describing the instability. In Section 4, we discuss a "toy" model with specific predictions regarding the properties of the function μ and consider the role of the magnetic field. In Section 5, we relate these results to the discoloration patterns on the cathode of the SSPX. Section 6 contains a discussion of our results.

2. THE MODEL

2.1. The Recycling Coefficient

The typical spatial scale of the discoloration pattern in the SSPX is ~1 cm, which is much less than the other characteristic scales; e.g., the cathode diameter is ~80 cm, and the connection length of the magnetic-field lines (and current streamlines) between two electrodes is believed to exceed several meters. This allows us to use the planar model of the cathode surface shown in Fig. 4. The magnetic field is, generally speaking, tilted by some angle α to the cathode.

We assume that the surface of the cathode contains a significant amount of absorbed hydrogen. The number of neutral atoms *R* released from the surface when an ion hits the surface depends, generally speaking, on the surface temperature T_s and the cathode sheath voltage U_C (which determines the energy of the ions bombarding the cathode):

$$R = R(T_s, U_C). \qquad (3)$$

One can expect *R* (called the recycling coefficient, [5]) to be a growing function of both T_s and U_C in the range of parameters of interest in our problem ($T_s \sim 500$–1500 K, $U_C \sim 100$–1000 V). In principle, one might also include in the consideration the dependence of *R* on the number σ of hydrogen atoms per 1 cm^2 of the surface. This dependence is weak if this number is greater than that corresponding to one monolayer. The inclusion of this dependence does not change our results in an appreciable way. In the steady-state equilibrium, *R* is necessarily equal to one (if, as we assume, there are no

external particle sources, such as neutral beam injection or gas puff). However, in the perturbations, *R* may deviate from its equilibrium value.

Unfortunately, experimental data regarding the function *R* are essentially unavailable. On the other hand, from a general standpoint, the presence of the temperature dependence of the recycling coefficient is not surprising: One can allude here to a mechanism mentioned in [13] (although for carbon), whereby the ion bombardment creates point defects (interstitials) that diffuse to the surface and show up there as atoms very weakly bound to the surface (the binding energy is ~0.15 eV). Then, thermal activation leads to their sublimation. The same line of reasoning shows that *R* should also be a growing function of U_C. Thus, one can expect that

$$\partial R/\partial T_s > 0, \quad \partial R/\partial U_C > 0. \qquad (4)$$

The degree of the dependence of *R* on T_s and U_C at some specific value of T_s and U_C can be characterized by the dimensionless parameters

$$\xi_1 \equiv \frac{\sqrt{\pi}T_s}{2}\frac{\partial R}{\partial T_s}, \quad \xi_2 \equiv U_C\frac{\partial R}{\partial U_C}, \qquad (5)$$

which themselves depend on T_s and U_C. The numerical factor in the first one is introduced to simplify the subsequent equations (see Section 3). As the typical surface temperature is below the expected activation energy of a few tenths of an electronvolt, ξ_1 should be relatively large. In the numerical examples below, we take as a representative value $\xi_1 = 4$. With regard to ξ_2, we assume that its representative value is 2. Note that the growth rate and the characteristic spatial scale of the perturbations depends on ξ_1 and ξ_2 relatively weakly (Eq. (52) below).

We limit ourselves to these general observations. The development of a consistent theory that would describe the dependence of *R* on T_s and U_C goes beyond the scope of this paper. This is another aspect of our analysis that calls for the qualifier *phenomenological* in the title of the paper.

2.2. The Ionizing Layer

The atomic hydrogen released from the surface penetrates into the plasma to a distance Δ determined by the ionization process. A rough estimate of this distance is

$$\Delta \sim v_0/\nu, \qquad (6)$$

where v_0 is a characteristic velocity of the neutrals and

$$\nu = n\langle\sigma v\rangle_i \qquad (7)$$

is the ionization frequency, with *n* being the electron density and the averaging being performed over the electron distribution function. We assume that

$$v_0 \sim 1.5 \times 10^6 \text{ cm/s}, \quad \langle\sigma v\rangle_i \sim 2 \times 10^{-8} \text{ cm}^4/\text{s}. \qquad (8)$$

Note that in the range of electron temperatures between 10 and 100 eV, the parameter $\langle \sigma v \rangle_i$ varies only by a factor of 2 [5]. For the plasma parameters in Eq. (1), the characteristic thickness of the ionizing layer is ~1 cm and the characteristic ionization time $1/v \equiv \Delta/v_0$ is ~1 μs.

Charge exchange (e.g., [5]) also has an effect on the thickness of this layer. On the other hand, for the plasma parameters of Eq. (1) this effect is relatively modest. Note also that in the case $\alpha \sim 1$, the plasma ions in the ionizing layer move toward the absorbing cathode and fast neutrals generated by the charge exchange are directed to the wall. The same is true in the case $\alpha \ll 1$, if Δ is less than or comparable to the ion gyroradius (which it is in the SSPX).

On the other hand, when $\alpha \ll 1$ and Δ is much greater than the gyroradius, the charge-exchange process generates some number of neutrals with energies of the order of $T_i \sim 100$ eV moving away from the wall. Some of these fast neutrals would penetrate into the bulk plasma (e.g., [5]) because of their higher velocity. But under the conditions we are interested in, viz, when the current density substantially exceeds the saturation current density, the fraction of the current generated by the ionization of these neutrals is small. Accordingly, in this first rough model we assume that all the neutrals released from the cathode are ionized in the ionizing layer, even in the case of small α and a small gyroradius (Section 4.5).

A sketch of the spatial distribution of unperturbed plasma parameters is shown in Fig. 5. Note the two-scale variation of the voltage: there is a steep potential drop in the Debye sheath near the wall, followed by a more gradual variation in the layer of a thickness $\sim\Delta$ where the ionization occurs. For Maxwellian electrons, the potential difference between the plasma and the entrance to the Debye sheath will be of the order of T_e (e.g., [5]), whereas the potential drop in the Debye sheath will be on the order of a few hundred electron-volts to provide a large enough acceleration for the ions striking the cathode and thereby make the recycling coefficient R equal to 1 (we are speaking here about the quasi-steady state, not about the perturbations). If the voltage decreases, R drops, leading to a decrease in the current and restoring the voltage at the required level via the $-LdI/dt$ term. Conversely, if voltage increases, this leads to an increase in R, an increase in the current, and a return of the voltage to the level needed to keep $R = 1$. Note that here we are speaking about the uniform component of the current, which is determined by a highly inductive external circuit and essentially stays constant during the times of interest to us. Small-scale current variations (which we consider below) do not affect the global current (because their surface average is zero) and are free of these constraints (see below).

As we are interested in the situations where the current density is significantly higher than the saturation current density, the steady-state voltage U_C is high, sig-
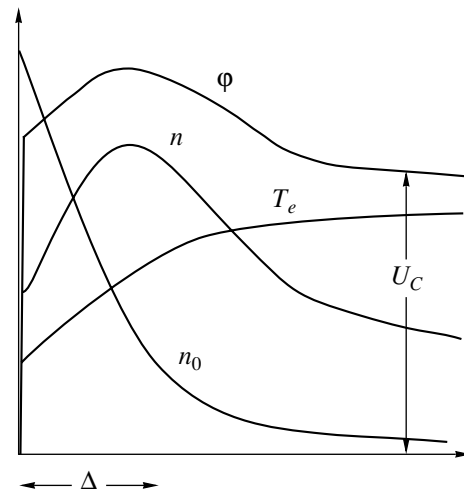

Fig. 5. A sketch depicting the spatial distribution of the plasma parameters in the ionizing layer. For simplicity, we assume that the cathode is at zero potential. Note the two-scale structure of the potential drop: a relatively smooth variation in the ionizing layer followed by a very steep drop in the Debye sheath.

nificantly higher than T_e/e in the vicinity of the cathode. The electron current to the cathode is therefore almost totally suppressed and the current to the cathode is almost entirely generated by the ions formed by the ionization of the neutrals released from the cathode. The electrons formed in the ionization events move in the opposite direction, thereby assuring a high current density in the bulk plasma.

2.3. The Surface Temperature

The energy flux to the cathode can be approximately represented as

$$P = j_i U_C, \qquad (9)$$

where j_i is the normal component of the ion current density at the cathode surface. We neglect here the thermal contribution to the energy flux. This is justified because of the inequality $U_C \gg T/e$. Note that, in the case of the tilted magnetic field $\alpha \neq \pi/2)$ j_i is related to the current density j in the bulk plasma (i.e., the current density quoted in Eq. (1)) by the following obvious relation:

$$j_i = j \sin\alpha. \qquad (10)$$

The cathode temperature gradually grows with time from its initial value (room temperature). Assuming that P in Eq. (9) is constant, one can easily obtain the following expression for the increase in the surface temperature of a semi-infinite medium:

$$T_s = P\sqrt{\frac{4\tau}{\pi \kappa C_p}}, \qquad (11)$$

where κ is thermal conductivity, C_p is heat capacity, and τ is the time elapsed since the beginning of the pulse. Black body radiation from the surface is negligible and is ignored in Eq. (11).

In the case of the SSPX, the cathode is made of copper coated by 100-μm-thick tungsten. This thickness is comparable (although somewhat less than) the heat-penetration depth for the characteristic time of the experiment, $\tau = 1$ ms. Thus, the surface temperature will lie somewhere between the value for copper and tungsten. For copper, $\kappa = 4$ W/(cm K) and $C_p = 1.9$ J/(cm^3 K), whereas for tungsten, $\kappa = 1.54$ W/(cm K) and $C_p = 2.63$ J/(cm^3 K). Taking $P = 45$ kW/cm^2 (this corresponds to $j_i = 150$ A/cm^2 and $U_C = 300$ V) and $\tau = 1$ ms, we find that $T_s = 580$ K for copper and $T_s = 800$ K for tungsten.

3. LINEAR PERTURBATIONS

3.1. Ion Current Perturbation vs. the Perturbation of the Neutral Flux

We are looking for the perturbations whose temporal dependence is $\exp(\Gamma t)$, with Γ possibly complex, and whose spatial dependence over the cathode surface is $\exp(ik_x x + ik_y y)$. For example, the perturbation of the normal component of the ion current hitting the wall is

$$\delta j_i \exp(\Gamma t + ik_x x + ik_y y), \qquad (12)$$

with δj_i being the complex amplitude. The positive real part of Γ corresponds to the instability. By using Eq. (12), we imply that the spatial scale of perturbations is much less than the "external" spatial scale of the problem (e.g., the interelectrode distance) and the growth rate is high compared to the characteristic time-constant of the discharge τ.

Denoting the complex amplitude of the perturbation of the neutral flux from the surface by δj_n (in the equivalent amperes), we have

$$\delta j_n = R\delta j_i + j_i \delta R. \qquad (13)$$

Here and below the quantities not bearing a prefix "δ" are unperturbed quantities. As in the unperturbed state $R = 1$ (see Section 2.1), Eq. (13) can be rewritten as

$$\delta j_n = \delta j_i + j_i \delta R. \qquad (14)$$

According to Eq. (3), the variation of R is caused by variations of the surface temperature and the cathode sheath voltage,

$$\delta R = \frac{\partial R}{\partial T_s}\delta T_s + \frac{\partial R}{\partial U_C}\delta U_C. \qquad (15)$$

If we want to include the dependence of R on the parameter σ introduced after Eq. (3), we have to add the term $(\partial R/\partial\sigma)\delta\sigma$ to the r.h.s., with $\delta\sigma = (\delta j_i - \delta j_n)/e\Gamma$. The addition of this term leads to some reduction of the growth rate for the slowly growing modes (small Γ) but

has little effect on the fastest growing modes. Accordingly, we will ignore this additional term.

Perturbation of the neutral flux (14) causes perturbation of the ion flux; in the linear approximation,

$$\delta j_i = \mu\delta j_n, \qquad (16)$$

where μ is a function of **k** and Γ. Its details depend on the structure of the ionizing layer, but some general properties are obvious: At large k ($k \gg \Delta^{-1}$, where Δ is the thickness of the ionizing layer), μ is much less than 1. This is because the neutrals leave the surface in a quasi-isotropic fashion, and the neutrals from the neighboring positive and negative regions of the sinusoidal perturbation mix with each other at a distance of $\sim 1/k \ll \Delta$ (Fig. 3), eliminating any neutral density perturbation over the major part of the layer. Similarly, μ is much less than 1 for large Γ, $\Gamma \gg v_0/\Delta$. Indeed, the quantity on the right-hand side of this inequality is nothing more than the inverse ionization time (see Eq. (7)). If the characteristic time of the perturbation growth is much shorter than the ionization time, the ionization lags behind the increased δj_n, and, correspondingly, μ drops. Conversely, for slow ($\Gamma \ll v_0/\Delta$) large-scale ($1/k \gg \Delta$) perturbations, all the neutrals released from the surface get ionized and return to the surface in the form of ions; accordingly, in this case μ is close to 1. (We assume here that even though k and Γ are small in the sense of inequalities $\Gamma \ll v_0/\Delta$ and $1/k \gg \Delta$, they are still compatible with our assumption that $\Gamma\tau \gg 1$ and $kL \gg 1$.) In Section 4, we present an explicit expression for μ for a particular model of the ionizing layer.

3.2. Inductive and Resistive Effects

3.2.1. Inductive effects. For perturbations of the form (12), the net current (the current integrated over the cathode surface) does not change, and these small-scale perturbations do not show themselves in the external circuit. In particular, the voltage applied to the spheromak is not affected. This is not to say that local perturbations of U_C (which affect the recycling coefficient (3)) do not exist. Indeed, as we will show in this section, the time-varying currents generate inductive electric fields and lead to variations of U_C.

In evaluating U_C, it is convenient to use a coordinate frame (marked with the subscript "1," Fig. 4) with the axis z_1 directed along the magnetic field, so that

$$x = x_1\sin\alpha - z_1\cos\alpha, \quad y = y_1,$$
$$z = x_1\cos\alpha + z_1\sin\alpha. \qquad (17)$$

We assume that the current in the bulk plasma flows along the magnetic-field lines (a good assumption for a low-beta plasma) so that only the parallel (z_1) component is present and that it is equal to $\delta j_i/\sin\alpha$, where δj_i is the current perturbation at the cathode introduced in Section 3.1. The spatial dependence of perturbations in

the frame 1 can be characterized by the wave number $\mathbf{k}_1 \equiv (k_{x1}, k_{y1}) \equiv (k_x/\sin\alpha, k_y)$. The magnetic-field perturbation can be found from equation $\nabla \times \delta\mathbf{B} = (4\pi/c)\delta\mathbf{j}$. As the current is directed along the z_1 axis and does not depend on z_1, the complex amplitude of the magnetic field perturbation is

$$\delta\mathbf{B} = -\frac{4\pi i \delta j_i}{c\sin\alpha} \cdot \frac{\mathbf{k}_1 \times \mathbf{e}_{z1}}{k_1^2}, \tag{18}$$

where $\mathbf{e}_{z1}$ is a unit vector in the z_1 direction. We neglect zones in the vicinity of the electrodes, where the surface current makes the magnetic-field perturbation tangential to the wall.

Assume first that the plasma is a perfect conductor (we consider the resistive effects later), so that the z_1 component of the electric field is absent. Then, the equation $\nabla \times \delta\mathbf{E} = -(1/c)\partial\delta\mathbf{B}/\partial t$ can be rewritten as

$$\frac{\partial}{\partial z_1}(\delta\mathbf{E} \times \mathbf{e}_{z1}) + \mathbf{e}_{z1}(k_x\delta E_y - k_y\delta E_x)$$
$$= \frac{4\pi i\Gamma\delta j_i}{c^2\sin\alpha} \cdot \frac{\mathbf{k}_1 \times \mathbf{e}_{z1}}{k_1^2}. \tag{19}$$

All the terms in this equation, except for the second term in the l.h.s., are perpendicular to $\mathbf{e}_{z1}$. Therefore, $k_x\delta E_y - k_y\delta E_x = 0$ or, in other words, the electric field in the plasma is parallel to $\mathbf{k}_1$ and varies linearly along z_1:

$$\frac{\partial\delta\mathbf{E}}{\partial z_1} = -\frac{4\pi i\Gamma\delta j_i}{c^2\sin\alpha} \cdot \frac{\mathbf{k}_1}{k_1^2}. \tag{20}$$

The integration of this equation along the field line between the cathode and the anode yields the difference of the electric field between the plasma side of the ionizing layer at the cathode and the plasma side of the sheath near the anode,

$$\delta\mathbf{E}_C - \delta\mathbf{E}_A = -\frac{4\pi i\Gamma L\delta j_i}{c^2\sin\alpha} \cdot \frac{\mathbf{k}_1}{k_1^2}, \tag{21}$$

where L is the length of the field line between the cathode and the anode. We use here separation of scales, $Lk \gg 1$, $L \gg \Delta$, and neglect contributions of the edge effects. (For distances from the conducting wall of $\sim 1/k$, the surface currents in the wall make $\delta\mathbf{B}$ parallel to the wall, so that Eq. (18) breaks down. However, as the zones where this happens are small compared to L, one can neglect their contribution to the r.h.s. of Eq. (21).)

As the tangential component of the electric field on the surface of a perfectly conducting electrode is zero, the presence of the tangential component of the electric field on the plasma side of the sheaths means that the sheath potential varies along the surface. We again use the separation of scales, $L \gg \Delta$, which allows us to clearly separate the sheath zone, where the electric field can be adequately described in terms of the electrostatic

potential, and the bulk plasma, where the electric field has an inductive component. We will denote potential variations in the cathode and anode sheaths (including the ionizing layer) by δU_C and δU_A, respectively. We define them as the potential difference between the plasma side of the sheath and the electrode (cathode or anode). Obviously, $\delta U_C = i(\delta\mathbf{E}_C \cdot \mathbf{k})/k^2$ and similarly for the anode. We then obtain from Eq. (21)

$$\delta U_A + \delta U_C$$
$$= \frac{4\pi\Gamma}{c^2}\frac{L\delta j_i}{\sin\alpha}\frac{(\mathbf{k}_1 \cdot \mathbf{k})}{k_1^2 k^2} \equiv \frac{4\pi\Gamma}{c^2}\frac{L\sin\alpha\delta j_i}{k_x^2 + k_y^2\sin^2\alpha}. \tag{22}$$

We can easily show that $e\delta U_A/T_e = \delta j/(j + j_{\text{sat}})$ (see, e.g., Appendix 2 in [14]). On the other hand, we can check that, for the most unstable modes, the r.h.s. of Eq. (22) is $U_C\delta j/j$. As in the case under consideration $U_C \gg T_e/e$, we can neglect the first term in the l.h.s. of Eq. (22) to obtain

$$\delta U_C = -\frac{4\pi\Gamma}{c^2}\frac{L\sin\alpha\delta j_i}{k_x^2 + k_y^2\sin^2\alpha}. \tag{23}$$

In principle, it is easy to retain the terms related to δU_A in the l.h.s. of (22), but this does not add any qualitatively new effects; it just makes the equations significantly longer. If the spheromak magnetic field exhibits stochastic behavior, then L should be understood as the distance at which flux tubes with a size $\sim k^{-1}$ lose their identity. In this case, L becomes less than the connection length.

3.2.2. Polarization current. The presence of the electric-field perturbation (20) causes a plasma drift in the $\mathbf{k}_1 \times \mathbf{e}_{z1}$ direction with the velocity

$$\delta\mathbf{v}_d = c\frac{\delta\mathbf{E} \times \mathbf{e}_{z1}}{B} \sim \frac{4\pi\Gamma L\delta j}{cB}\frac{\mathbf{k}_1 \times \mathbf{e}_{z1}}{k_1^2}, \tag{24}$$

which varies in time as $\exp(\Gamma t)$. Accordingly, a polarization current δj_p develops in the bulk plasma,

$$\delta\mathbf{j}_p = \frac{cMn\Gamma}{B}\delta\mathbf{v}_d \times \mathbf{e}_{z1} \sim \frac{4\pi\Gamma^2 MnL\delta j}{B^2}\frac{\mathbf{k}_1}{k_1^2}. \tag{25}$$

Because of the charge-neutrality condition, the parallel component of the current δj varies along the magnetic field according to the equation $\partial\delta j/\partial z_1 = -i\mathbf{k}_1 \cdot \delta\mathbf{j}_p$. For this variation to be small (and the analysis of the previous subsection to be correct), we have to impose the following condition (see Eq. (25)):

$$\Gamma < v_A/L, \tag{26}$$

where v_A is the Alfven velocity. For a connection length $L \sim 10$ m, a growth rate $\Gamma \sim 2 \times 10^4$ s^{-1}, and the other parameters as in Eq. (1), this inequality holds by a margin of 3–4, thereby justifying the use of Eq. (23).

In the hypothetical case where an inequality opposite to (26) holds, the instability will be accompanied

by the excitation of Alfven waves propagating into the plasma. This case can be treated in the same way as that used in [15] for the analysis of another instability driven by the boundary conditions of the wall.

3.2.3. Resistive effects. If the plasma has finite resistivity, then a parallel electric field appears in the plasma, related by the equation

$$\delta E_{z1} = \frac{\eta}{\sin\alpha}\delta j_i, \tag{27}$$

to δj_i and independent of z_1 (assuming that η and δj_i are independent of z_1). This field adds to the variation of the drop of the sheath potential and can be easily incorporated in Eq. (22) yielding

$$\delta U_A + \delta U_C$$

$$= \left(\frac{4\pi\Gamma}{c^2} + \frac{\eta(k_x^2 + k_y^2\sin^2\alpha)}{\sin^2\alpha}\right)\frac{L\sin\alpha\delta j_i}{k_x^2 + k_y^2\sin^2\alpha}. \tag{28}$$

In the case of the SSPX, the resistive term is small. Indeed, we can neglect it compared to the inductive term under the condition that $\Gamma > \eta c^2 k^2/4\pi$. For a plasma temperature of 100 eV, a wave number of ~ 0.5 cm^{-1}, $\Gamma \sim 10^5$ s^{-1}, and $\alpha \sim 0.3$, it is satisfied by a large margin. Accordingly, in what follows, we neglect this term.

3.3. Surface Temperature Variation

Variations of the current to the cathode and the sheath voltage cause variations of energy flux, δP, through the cathode surface:

$$\delta P = U_C\delta j_i + \delta U_C j_i. \tag{29}$$

This, in turn, causes variations of the cathode temperature. We use the following heat conduction equation:

$$C_p\frac{\partial\delta T}{\partial t} = \kappa\frac{\partial^2\delta T}{\partial z^2}, \tag{30}$$

where C_p is specific heat of the cathode material and κ is thermal conductivity. We neglect heat transport along the surface because the inequality $\Gamma > \kappa k^2/C_p$ holds by a very large margin. For perturbations proportional to $\exp(\Gamma t)$, this equation has the following simple solution for the perturbation of the surface temperature:

$$\delta T_s = \frac{\delta P}{\sqrt{C_p\kappa\Gamma}}. \tag{31}$$

Rapid variations in the temperature do not penetrate deeper than the tungsten coating, so the material constants in this equation should correspond to tungsten, while in the expression for T_s, some averaged constants should be used. Here we will neglect this (relatively

minor) difference; then, by combining Eqs. (11) and (31), we obtain

$$\frac{\delta T_s}{T_s} = \sqrt{\frac{\pi}{4\Gamma\tau}}\frac{\delta P}{P}. \tag{32}$$

The energy flux perturbation, according to Eqs. (23) and (29), can be presented as

$$\frac{\delta P}{P} = \frac{\delta j_i}{j_i}\left(1 - \frac{\Gamma\sin^2\alpha}{D_{\text{eff}}(k_x^2 + k_y^2\sin^2\alpha)}\right), \tag{33}$$

where

$$D_{\text{eff}} \equiv \frac{c^2 U_C}{4\pi Lj}. \tag{34}$$

Note that the parameter j that enters Eq. (34) is the bulk-plasma current density related to j_i by Eq. (10). The numerical value of D_{eff} for the set of parameters of Eqs. (1) and (2) is

$$D_{\text{eff}} = 1.06 \times 10^5 \text{ cm}^2/\text{s}. \tag{35}$$

The source of instability, as discussed in the Introduction, is related to the feedback between the temperature increase and the increase of the current in some spot. This requires δT_s be positive for positive δj_i. On the other hand, Eq. (33) shows that, for high Γ, δP and (according to Eq. (32)) δT_s become negative for positive δj_i. This obviously imposes the following constraint on the instability growth rate:

$$\Gamma < \frac{D_{\text{eff}}(k_x^2 + k_y^2\sin^2\alpha)}{\sin^2\alpha}. \tag{36}$$

For the typical parameters of the SSPX ($U_C \sim 300$ V, $j_i \sim 300$ A/cm^2, $L \sim 10$ m, and $\alpha \sim 0.3$) and perturbation wave number $k \sim 0.5$ cm^{-1}, one finds that the growth rate is limited to $\sim 6 \times 10^4$ s^{-1}—fast enough to generate instability in the SSPX (where the characteristic pulse length is 2 ms).

3.4. Dispersion Relation

Substituting into Eq. (15) the expressions for δT_s and δU_C given by Eqs. (32), (33), and (23), and using Eqs. (14) and (16), one obtains the following dispersion relation:

$$\frac{1}{\mu(\Gamma, \mathbf{k})} - 1 = \frac{\xi_1}{\sqrt{\Gamma\tau}}\left(1 - \frac{\Gamma\sin^2\alpha}{D_{\text{eff}}(k_x^2 + k_y^2\sin^2\alpha)}\right)$$

$$- \frac{\xi_2\Gamma\sin^2\alpha}{D_{\text{eff}}(k_x^2 + k_y^2\sin^2\alpha)}, \tag{37}$$

where ξ_1 and ξ_2 are positive dimensionless parameters (5). In further numerical estimates, we will assume that

$$\xi_1 = 4, \quad \xi_2 = 2. \qquad (38)$$

As has been mentioned in Section 3.1, for slow large-scale perturbations, μ becomes close to 1 and the l.h.s. of Eq. (37) vanishes, yielding a simplified dispersion relation. It is convenient to present this equation in dimensionless units,

$$\Gamma^* = \Gamma\tau, \quad k^* = k\sqrt{D_{eff}\tau}. \qquad (39)$$

It is also convenient to introduce the parameter η characterizing the direction of the wave vector $\mathbf{k}$ with respect to the tangential component of the magnetic field:

$$\eta \equiv \frac{\sin^2\alpha}{\cos^2\theta + \sin^2\theta\sin^2\alpha}, \qquad (40)$$

where θ is the angle between $\mathbf{k}$ and the tangential magnetic field. The dimensionless dispersion relation reads

$$\frac{\xi_1}{\xi_2}(k^{*2} - \eta\Gamma^*) = \eta\Gamma^{*3/2}. \qquad (41)$$

A series of plots of the dimensionless growth rate vs. the dimensionless wave vector are presented in Fig. 6 for ξ_1 and ξ_2 as in Eq. (38). As an upper limit for k^*, we take the value corresponding to the wave vector k approaching the applicability limit $\sim 1/\Delta$. To be specific, we take this limit to be $k = 0.5/\Delta$. The corresponding value of k^* is obviously

$$k^*_{max} = \frac{0.5\sqrt{D_{eff}\tau}}{\Delta} \approx 5. \qquad (42)$$

In evaluating the numerical value of k^*_{max}, we have assumed that $\tau = 1$ ms, $\Delta = 1$ cm, and D_{eff} is as in Eq. (35). This value of k^*_{max} is shown as a vertical line in Fig. 6. In dimensional numbers, $k_{max} = k^*_{max}/\sqrt{D_{eff}\tau}$ is about 0.5 cm^{-1}.

Note that, for $\theta = 0$ the perpendicular wave number in the bulk plasma is k_{max}/α (see Section 3.2.1). For the case of the SSPX, $\alpha \sim 0.3$ and so the perpendicular length scale approaches the ion gyroradius. This, however, does not necessarily mean that the current filaments get mixed with one another, because the current is carried by the electrons. It would rather mean that cross-field drifts (Eq.(24)) will be slowed down (by gyroviscous terms) and the excitation of shear Alfven waves (Section 3.2.2) will become impossible.

From Fig. 6, we see that the instability favors perturbations with wave numbers that do not deviate significantly from the direction of the tangential component of the magnetic field. This, in turn, means that cathode patterns have to be stretched in the direction perpendicular to that of the tangential magnetic field. As we dem-
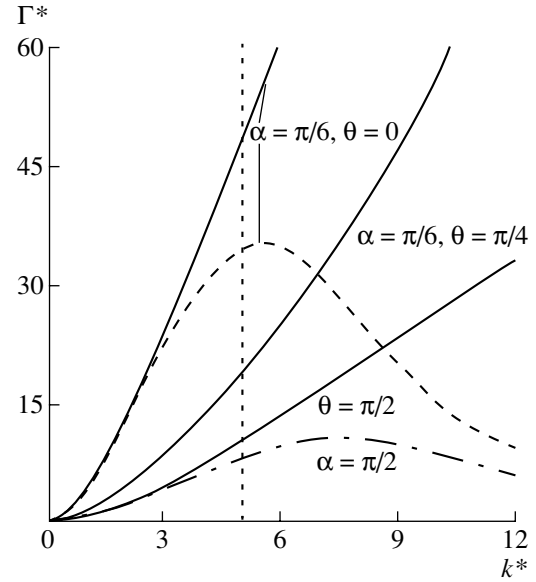
Fig. 6. The dimensionless growth rate vs. the dimensionless wave number for $\xi_1 = 4$, $\xi_2 = 2$. The solid lines represent the solution of dispersion relation (41) for various directions of the wave vector in the xy plane; $\theta = 0$ corresponds to the wave vector aligned with the magnetic-field projection onto the plane; the dotted vertical line corresponds to $k\Delta = 0.5$. The dashed line represents the dispersion curve for dispersion relation (37) with μ as in (59). The dashed-and-dotted line corresponds to dispersion relation (37) with $\alpha = \pi/2$ and μ as in (51).

onstrate in Section 5, this is in agreement with experimentally observed patterns. Maximum growth rates are much larger than $1/\tau$, meaning that the instability is fast and thereby justifying our approach to the background as being steady state.

For perturbations propagating normally to the tangential component of the magnetic field ($\theta = \pi/2$), the parameter η (Eq. (40)) and, accordingly, dispersion relation (41), do not depend on the angle α at all. In particular, the case $\theta = \pi/2$ describes the normal orientation of the magnetic field to the surface ($\alpha = \pi/2$).

Another observation that can be made from Fig. 6 is that the growth rate remains very small compared to the ionization frequency ν (Eq. (7)) even for k approaching Δ^{-1}. This means that, in the expansion of μ in the powers of small parameters, $k\Delta$ and Γ/ν,

$$\mu = 1 + Q_i k_i \Delta + Q_{ij} k_i k_j \Delta^2 + Q\Gamma/\nu + \dots, \qquad (43)$$

where Q, Q_i, Q_{ij}, etc., are some dimensionless coefficients, we can neglect the term proportional to Γ/ν and higher-order terms in Γ; i.e., we can use the expression

$$\mu \approx 1 + Q_i k_i \Delta + Q_{ij} k_i k_j \Delta^2. \qquad (44)$$

The linear term in the expansion appears only if the magnetic field is tilted with respect to the wall. One can show that this term is universally purely imaginary.

4. A SIMPLE MODEL FOR μ; MAGNETIC-FIELD EFFECTS

4.1. Main Assumptions

The growth rate in the limit of $\mu = 1$ is an increasing function of k. Therefore, we have to consider effects that turn on at large k and make μ less than 1. This will be done in this section, where we consider perturbations with arbitrary k and Γ, based on a simple model. We assume that the neutrals emerge from the cathode surface in the form of an isotropic Maxwellian distribution. In other words, the neutral distribution function at the surface of the cathode is assumed to be

$$\delta f_n\big|_{z=0} = \frac{2\delta j_n}{\pi e v_0^4}\exp\left(-\frac{v^2}{v_0^2}\right), \qquad (45)$$

where v_0 is the characteristic neutral velocity. The normalization of this distribution is taken in such a way that the neutral current from the surface is δj_n. Neutrals released from the surface travel away from it and are gradually ionized by the plasma electrons.

After an ion is formed, it is pulled towards the cathode by the electric field existing in the ionizing layer. We assume that the ion does not experience collisions on its way to the cathode. The ions reach the cathode very quickly, so we neglect temporal lags in the ions reaching the surface.

In reality, this simple picture is affected by charge-exchange processes that would change our results by an order of one. On the other hand, as will be seen from the further derivation, the most important features of our model are qualitatively quite robust.

4.2. Neutral Distribution Function

For perturbations of the form (12), the kinetic equation for the neutral distribution function reads as

$$\Gamma\delta f_n + i(k_x v_x + k_y v_y)\delta f_n + v_z\frac{\partial\delta f_n}{\partial z} = -\nu\delta f_n, \quad (46)$$

where ν is the ionization rate (6), which we assume for simplicity does not depend on the coordinates and time. As the neutrals move relatively slowly, we retain here the term $\Gamma\delta f_n$ describing the effects of temporal variation. The solution of this equation satisfying the boundary condition (45) is

$$\delta f_n = \frac{2\delta j_n}{\pi e v_0^4}\exp\left(-\frac{v^2}{v_0^2} - \frac{\Gamma + \nu + i(k_x v_x + k_y v_y)}{v_z}z\right). \ (47)$$

The neutral density perturbation is

$$\delta n_n = \int_{-\infty}^{+\infty}dv_x\int_{-\infty}^{+\infty}dv_y\int_0^{+\infty}\delta f_n dv_z. \qquad (48)$$

4.3. Ion Current to the Wall for the Normal Magnetic Field

It is instructive to find δj_i in the simplest case where the magnetic field is normal to the wall. In this case, each ion hits the wall at the point situated just "under" its point of origin. We neglect here their time-of-flight delay, because, for the ions with the energy of several tens of electronvolts it is much smaller than the neutral delay time. This means that the perturbation of the ion current to the wall is equal to

$$\delta j_i = \nu e\int_0^\infty\delta n_n dz. \qquad (49)$$

Substituting Eqs. (47) and (48) into (49) and integrating, first, over dz and, then, over dv_z, it is easy to obtain the following expression for μ:

$$\mu = \frac{\nu(\nu + \Gamma)}{\sqrt{\pi}v_0}\int_{-\infty}^{+\infty}\frac{du\exp(-u^2/v_0^2)}{(\nu + \Gamma)^2 + k^2 u^2}. \qquad (50)$$

In agreement with the preliminary discussion of Section 3.1, μ is close to unity for long-wave ($k \ll \nu/v_0 = \Delta^{-1}$) slow ($\Gamma \ll \nu$) perturbations. Also in agreement with a qualitative discussion of Section 3.1, μ becomes much less than 1 if the opposite inequalities hold. For slow long-wavelength perturbations, the following approximate (to the lowest-order corrections in Γ/ν and $k\Delta$) expression for μ holds:

$$\mu \approx 1 - \frac{\Gamma}{\nu} - k^2\Delta^2 \approx 1 - k^2\Delta^2 \qquad (51)$$

(according to the comment made at the end of Section 3.4, we have neglected the term Γ/ν). Because of the symmetry of the problem, there is no linear (over k) term in the expansion.

For the conditions of the SSPX experiment, the analysis of dispersion relation (37) with μ as in Eq. (51) is simplified because the ratio $\Delta^2/D_{eff}\tau$ in this experiment is small, $\sim 10^{-2}$. One can show that in this case the following approximate expressions for the maximum growth rate and the corresponding (optimum) wave number hold:

$$\Gamma_{max} = \frac{1}{\tau}\left(\frac{\xi_1^2 D_{eff}\tau}{4\xi_2\Delta^2}\right)^{1/2}, \quad k_{opt} = \frac{1}{\Delta}\left(\frac{\xi_2\xi_1^2\Delta^2}{4D_{eff}\tau}\right)^{1/8}. \ (52)$$

Note that indeed (as was mentioned in Section 2.1), the dependence of the growth rate and especially the characteristic wave number on the parameters ξ_1 and ξ_2 is relatively weak. Neither the growth rate nor the optimum wave number depend on the magnetic field. In particular, k_{opt} is unrelated to the ion gyroradius. The plot of Γ vs. k for the case of the magnetic field normal to the wall is shown in Fig. 6 by a dash–dotted line.

4.4. Effect of a Weak Magnetic Field

The magnetic field affects our analysis if it is tilted with respect to the surface. To get some qualitative insights into the corresponding effects, we consider here only the case where the tilt is strong, i.e., the angle α is smaller than, say, 0.5 rad (30°). By "weak" we mean such a magnetic field that the ions born in the ionizing layer reach the wall moving across the magnetic field, as illustrated by Fig. 7.

The electric field in the ionizing layer can be roughly evaluated as

$$E \sim 2T_e/e\Delta. \qquad (53)$$

For simplicity, we assume it to be uniform over the ionizing layer. It can pull the ion to the wall across the magnetic field through a gap of width Δ if

$$B < \sqrt{\frac{2EMc^2}{e\Delta}}. \qquad (54)$$

This is what we call a weak magnetic field. For an E as in Eq. (53), $\Delta \sim 1$ cm and $T_e \sim 50$ eV. Eq. (54) yields $B < 2$ kG. Such a situation can often be met in the SSPX.

In this case, the ions formed in the layer will reach the cathode not exactly under the point where they originated, but shifted along the y axis by some distance. We shall evaluate this displacement in the case where B satisfies condition (54) by some margin. Then the ion displacement with respect to its point of origin is

$$\delta y = \frac{\sqrt{2}}{3}z\left(\frac{z}{\rho*}\right)^{1/2}. \qquad (55)$$

Here, the scale length $\rho*$ (the half amplitude of the cycloidal trajectory of the ion starting at a zero velocity) is

$$\rho* = \frac{Mc^2E}{eB^2}. \qquad (56)$$

We recall that, for expression (55) to be valid, the scale length $\rho*$ must exceed Δ.

The presence of the displacement δy means that, to evaluate the contribution to the perturbation of the ion current at some point y, one would have to find the ionization rate at the point off-set by the distance δy in the y direction. In other words, instead of the integral (49), we would have now

$$\delta j_i = \nu e \int_0^\infty \delta n_n \exp\left[ik_y\frac{\sqrt{2}}{3}z\left(\frac{z}{\rho*}\right)^{1/2}\right]dz. \qquad (57)$$

As the instability is strong only for the wave numbers significantly less than the inverse thickness of the ionizing layer, the exponent is small compared to 1, and we can use the following simplified expression for δj_i:

$$\delta j_i = \nu e \int_0^\infty \delta n_n \left[1 + ik_y\frac{\sqrt{2}}{3}z\left(\frac{z}{\rho*}\right)^{1/2}\right]dz. \qquad (58)$$
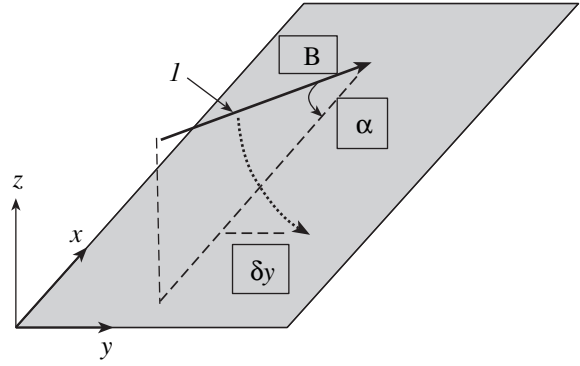
Fig. 7. Ion displacement in the case of a weak magnetic field. The dotted line shows the trajectory of an ion originating at point 1.

In the same approximation as Eq. (51) (i.e., small wave numbers and growth rates), we then obtain that

$$\mu \approx 1 - \frac{k^2 v_0^2}{v^2} + ik_y\Delta\sqrt{\frac{\Delta}{\rho*}}\frac{\sqrt{2\pi}\Gamma(7/4)}{4}. \qquad (59)$$

We will not present a detailed analysis of the dispersion relation (37) with μ as in (59). The maximum growth rate corresponds to $k_y = 0$ ($\theta = 0$) and is therefore unaffected by the presence of the last term in Eq. (59). For $k_y = 0$, the dispersion relation (37) becomes quite simple. Its solution for $\alpha = \pi/6$ is shown on Fig. 6 by a dashed line. The maximum growth rate and the corresponding wave number are described by Eq. (52), in which ξ_2 is replaced by $\xi_2 \sin^2\alpha$. The spatial scale, again, is independent of the magnetic-field strength and is unrelated to the ion gyroradius.

Although the last term in Eq. (59) does not affect the maximum growth rate or the characteristic scale of perturbations, this term brings with it a new effect, namely, that the perturbations acquire a finite phase velocity along the y axis. For the conditions of the SSPX, this phase velocity $\sim 10^6$ cm/s. Therefore, current filaments rapidly move in the direction perpendicular to the projection of the magnetic field on the cathode surface.

4.5. Effect of a Strong Magnetic Field

In the previous section, we looked into the situation where the parameter $\rho*$ (Eq. (56)) describing the extent of the ion orbit in the z direction is greater than or comparable to the width of the ionizing layer. In this section, we will very briefly consider the opposite limiting case, where the magnetic field is so strong that the ions are strongly tied to the field lines and the size of the gyroorbit is negligibly small compared to Δ.

In this case one can assume that an ion formed within the ionizing layer moves simply along the magnetic-field line. The ion that was formed at some point (x, y, z) hits the surface at the point $(x + z/\alpha, y, 0)$.

(a)   (b)

B_{azim}

B_{vert}
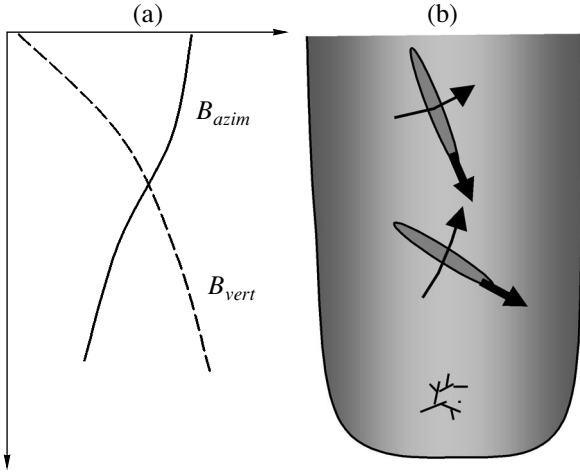
Fig. 8. Comparing theory predictions with experimentally observed patterns: (a) the dependence of the vertical and azimuthal magnetic fields on the distance from the top of the cathode; (b) the arrows show the projection of the magnetic field (near the cathode) onto the cathode surface. The shaded areas show the predicted shape of the discoloration patterns for two of the hot spots. The width of the patterns (not shown to scale) is ~ $1/k_{opt}$. The block arrows show the direction of motion of the hot spots. The overall structure shown in Fig. 2 is a superposition of a number of such patterns. In the lowest part of the cathode, such structures are replaced by chicken-track patterns produced by some other mechanism (possibly, vacuum arcs). One of them is shown near the bottom of the figure (not to scale).

Therefore, instead of expression (49) for δj_i, we now have

$$\delta j_i = \nu e \int_0^\infty \delta n_n \exp\left(\frac{ik_x z}{\alpha}\right) dz. \tag{60}$$

Assuming, as before, that $\Gamma \ll \nu$ and $k\Delta \ll 1$ (but not necessarily that $k_x\Delta/\alpha$ is small), we obtain the following expression for μ:

$$\mu = \frac{2\nu}{v_0^2}\int_0^\infty \frac{v_z\left(\nu - \frac{ik_x v_z}{\alpha}\right)}{\nu^2 + \left(\frac{k_x v_z}{\alpha}\right)^2}\exp\left(-\frac{v^2}{v_0^2}\right)dv_z. \tag{61}$$

One can show that the fastest growing perturbations are now stretched along the magnetic-field projection onto the cathode surface and the growth rate somewhat decreases compared to the case of a weak magnetic field. The perturbations are now moving in the direction parallel to the magnetic-field projection onto the cathode.

5. RELATION TO THE SSPX EXPERIMENT

A schematic of the SSPX device is shown in Fig. 1. We are concerned with the vertical part of the cathode surface, where the helical pattern is present (Fig. 2). The current flowing along the cathode surface decreases from the top to the bottom of the cathode because a substantial part of it transfers to the plasma. Accordingly, the azimuthal component of the magnetic field on the cathode surface varies with the height, decreasing toward the lower part of the electrode (the solid line in Fig. 8a). The vertical component of the magnetic field on the cathode surface, determined largely by the azimuthal currents flowing in a plasma, varies along the cathode surface as shown by the dashed line. Therefore, the projection of the field line onto the cathode surface varies from the upper to the lower part of the gun, as is shown in Fig 8b.

According to the instability analysis of Sections 3 and 4, the fastest growing perturbations in the case of the SSPX are stretched in the direction perpendicular to the magnetic-field projection onto the cathode surface. Therefore, the traces made by hot spots on the cathode surface should look like the shaded areas in Fig. 8b. This picture looks very similar to the orientation of the discoloration patterns shown in Fig. 1: the traces are oriented more or less vertically in the upper part of the gun and more or less horizontally in the lower part. The elongated spots shown in Fig. 8 move in the direction of the thick arrows, creating a characteristic helical pattern with a variable pitch as is visible in Fig. 2.

The characteristic width of the perturbations should be roughly equal to $1/k_{opt}$, where k_{opt} is the wave number corresponding to the maximum growth rate. Taking the dashed curve in Fig. 6 (it corresponds to the parameters of the SSPX) and using Eq. (39), we find that the optimum wave number (in dimensional units) is

$$k_{opt} \approx \frac{6}{\sqrt{D_{eff}\tau}}. \tag{62}$$

Taking D_{eff} as in Eq. (35) and $\tau = 1$ ms, one finds that $1/k_{opt} \sim 1$ cm, which is in reasonable agreement with the width of the discoloration patterns visible in Fig. 2. The growth rate can be evaluated (in dimensional units) as

$$\Gamma_{max} \approx 35/\tau. \tag{63}$$

It is much larger than $1/\tau$, thereby allowing the perturbations to reach large amplitude.

In the lowest part of the gun, the cathode does not display patterns of the type we have just discussed. It may mean that the current has already left the cathode surface higher up and the mechanism we discuss does not work. In this lowest part of the gun, the cathode surface displays a different type of structure, the familiar chicken-track patterns (Fig. 8b), but these certainly have a different origin and may be associated with the formation of vacuum arcs.

6. DISCUSSION

We have developed a phenomenological theory of the instability driven by the processes occurring in the

vicinity of the cathode surface, under the condition that the plasma current density is significantly greater than the saturation current density. We hypothesize that the necessary current density is provided by the ionization of neutral atoms released from the cathode surface. The layer where an elevated neutral density is present is postulated to be narrow compared to the global scale. However plausible this model is, we do not present a detailed quantitative analysis of the ionizing layer that consistently accounts for various atomic processes and the effects of a tilted magnetic field. This is deferred to a further study, based possibly on the use of codes like UEDGE [16, 17] and B2/EIRENE [18].

On the other hand, for long-wavelength modes these processes do not enter the problem at all, whereas for the modes that determine the maximum growth rate they enter the problem via numerical coefficients of the order of one (Q_i and Q_{ij} in Eq. (44)). This makes our results quite robust.

We have not touched upon the important issue of the nonlinear behavior of the perturbations. One can imagine that flux tubes with a higher current density would gradually starve the rest of the flux tubes of the current, thereby leading to a significant nonuniformity of the current density inside the plasma. The natural limit of the current concentration would be set by reaching surface temperatures close to the activation energy, thereby terminating the further variation of the recycling coefficient with the temperature. Another limitation may be set by the total current in the high-current density flux tubes reaching the current set by the external circuit. The analysis of these and other possibilities is a topic for future work.

In the context of spheromak experiments, an interesting question is the possible relation of the current filamentation to the problem of the helicity injection [19] and plasma rotation: note that, for the fastest growing perturbations, the flux tubes slide over the surface of the electrodes (Section 4.4). We can speculate that this may cause plasma entrainment and give rise to macroscopic plasma rotation. These issues are also left for future studies.

ACKNOWLEDGMENTS

REFERENCES

1. M. V. Babykin, P. P. Gavrin, E. K. Zavoiskiĭ, L. I. Rudakov, and V. A. Skoryupin, Zh. Éksp. Teor. Fiz. **47**, 1631 (1964) [Sov. Phys. JETP **20**, 1096 (1964)].
2. E. B. Hooper, L. D. Pearlstein, and R. H. Bulmer, Nucl. Fusion **39**, 863 (1999).
3. D. N. Hill, R. H. Bulmer, B. I. Cohen, *et al.*, in *Proceedings of the 18th IAEA Conference on Fusion Energy, Sorrento, 2000*, paper ICP/09.
4. H. S. McLean, S. Woodruff, E. B. Hooper, *et al.*, Phys. Rev. Lett. **88**, 125004 (2002).
5. P. Stangeby, *The Plasma Boundary of Magnetic Fusion Devices* (IOP, Bristol, 2000).
6. M. Ali Mahdavi, J. C. DeBoo, C. L. Hsieh, *et al.*, Phys. Rev. Lett. **47**, 1602 (1981).
7. D. Buchenauer, J. W. Cutberson, D. N. Hill, *et al.*, J. Nucl. Mater. **196–198**, 133 (1992).
8. A. Loarte, J. Nucl. Mater. **290–293**, 137 (1999).
9. A. V. Nedospasov and V. G. Petrov, Dokl. Akad. Nauk SSSR **269**, 603 (1983) [Sov. Phys. Dokl. **28**, 293 (1983)].
10. A. V. Nedospasov and I. V. Bezludny, Contrib. Plasma Phys. **38**, 337 (1998).
11. H. Wolff, in *Atomic and Plasma–Material Interaction Data for Fusion* (IAEA, Vienna, 1991), Nucl. Fusion Suppl. **1**, 79 (1991).
12. S. M. Kaye, M. G. Bell, R. E. Bell, *et al.*, Phys. Plasmas **8**, 1977 (2001).
13. J. Roth, E. Vietzke, and A. A. Haas, in *Atomic and Plasma–Material Interaction Data for Fusion* (IAEA, Vienna, 1991), Nucl. Fusion Suppl. **1**, 63 (1991).
14. D. D. Ryutov, P. Helander, and R. H. Cohen, Plasma Phys. Controlled Fusion **43**, 1399 (2001).
15. H. Berk, D. D. Ryutov, and Yu. A. Tsidulko, Pis'ma Zh. Éksp. Teor. Fiz. **52**, 674 (1990) [JETP Lett. **52**, 23 (1990)].
16. T. D. Rognlien, D. D. Ryutov, N. Mattor, and G. D. Porter, Phys. Plasmas **6**, 1851 (1999).
17. F. Wising, D. A. Knoll, S. Krasheninnikov, *et al.*, Contrib. Plasma Phys. **36**, 1996 (1996).
18. R. Schneider, D. Reiter, H. P. Zehrfeld, *et al.*, J. Nucl. Mater. **196–198**, 810 (1992).
19. T. R. Jarboe, Plasma Phys. Controlled Fusion **36**, 945 (1994).

Obtaining High Pressures and Metastable States in Condensed Media by Using High-Current Relativistic Electron Beams

B. A. Demidov

Russian Research Centre Kurchatov Institute, pl. Kurchatova 1, Moscow, 123182 Russia
Received October 24, 2002

Abstract—Experimental studies performed at the Russian Research Centre Kurchatov Institute on the interaction of high-current relativistic electron beams with various condensed media, including highly porous materials, are reviewed. The experiments on obtaining high pressures and accomplishing the structural and chemical conversions in the focal spot of a high-current beam are described. The principles of imitating an ultra-high-speed impact and other energetic actions on an obstacle with the help of high-current relativistic beams are discussed. The possibility of using such beams for surface modification is considered. Experimental data on the induced electric conductivity in highly porous SiO_2 aerogels in the region of the beam energy deposition are presented. © *2003 MAIK "Nauka/Interperiodica".*

1. INTRODUCTION

Inertial confinement fusion (ICF) research, computer simulations of explosions and high-speed impacts, and the physics of shocks in condensed media require information about the physical properties of matter within a wide region of the phase diagram, including the region of very high pressures and temperatures. This calls for the broadening of the pressure range attainable under laboratory conditions.

A great body of experimental data on the thermophysical properties of matter in the megabar pressure range has been obtained by using the dynamic methods employing intense shocks excited by chemical explosives for compressing and irreversibly heating substances. However, a further increase in pulsed pressures under laboratory conditions is limited by the relatively low power flux and volume energy density of chemical explosions, which do not exceed 10^{10} W/cm^2 and 10^4 J/cm^3, respectively. In this context, it is very important to search for methods of further increasing the pulsed pressure under laboratory conditions. High-current relativistic electron beams (REBs) have certain advantages in comparison with other sources of intense shocks (such as lasers, electric explosions, and electrodynamic devices) and allow one to attain power densities much higher than those obtained with chemical explosives.

During the interaction of a high-current REB with a target, the volume energy density that is released within a thin target layer is very high. This leads to the explosion of the target surface and the formation of a plasma corona, which expands toward the electron beam. The recoil momentum arising due to the expansion of the corona induces a shock wave, which propagates into the target and compresses and irreversibly heats the target substance. Note that laser beams surpass high-current REBs in the energy density and power fluxes and allow one to attain even higher pulsed pressures. However, because the total energy of an REB is typically much higher than the laser pulse energy, high-current REBs enable the irradiation of significantly larger volumes of condensed matter, which facilitates the diagnostics of such interaction.

## 2. OBTAINING HIGH PRESSURES IN THE FOCAL SPOT OF A HIGH-CURRENT REB

Experiments on the interaction of high-current REBs with condensed media were begun in the Department of Relativistic Beams (headed by L.I. Rudakov) of the Kurchatov Atomic Energy Institute in the late 1970s. The experiments were carried out in the Kalmar high-current accelerator [1, 2] in cooperation with the Institute of High Temperatures of the USSR Academy of Sciences, the Research Institute of Physicotechnical and Radio Engineering Measurements, the Moscow Institute of Steel and Alloys, the Institute of Mechanics of the Moscow State University, and the Karpov Research Institute of Physical Chemistry. An external view of the Kalmar accelerator is shown in Fig. 1.

The first experiments were devoted to the interaction of an electron beam with metals; then, other materials were subject to irradiation. The effect of a pulsed electron beam on different materials is illustrated in Fig. 2.

At the maximum output parameters of the Kalmar accelerator ($J = 200$ kA, $\varepsilon = 0.5$ MeV, and $\tau \approx 10^{-7}$ s), a single-pulse focused REB interacting with an Al anode produced, besides backside spalls at the anode, a hemi-
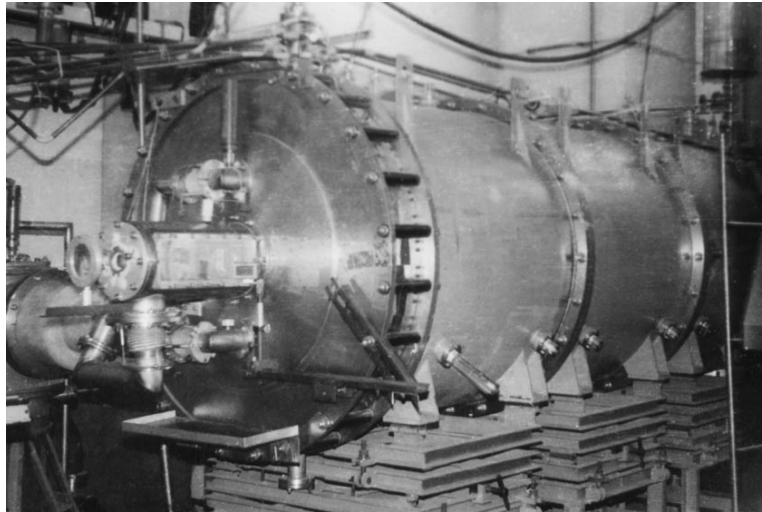
Fig. 1. External view of the Kalmar accelerator (the accelerator diameter is 1 m).

(a)   (b)   (c)
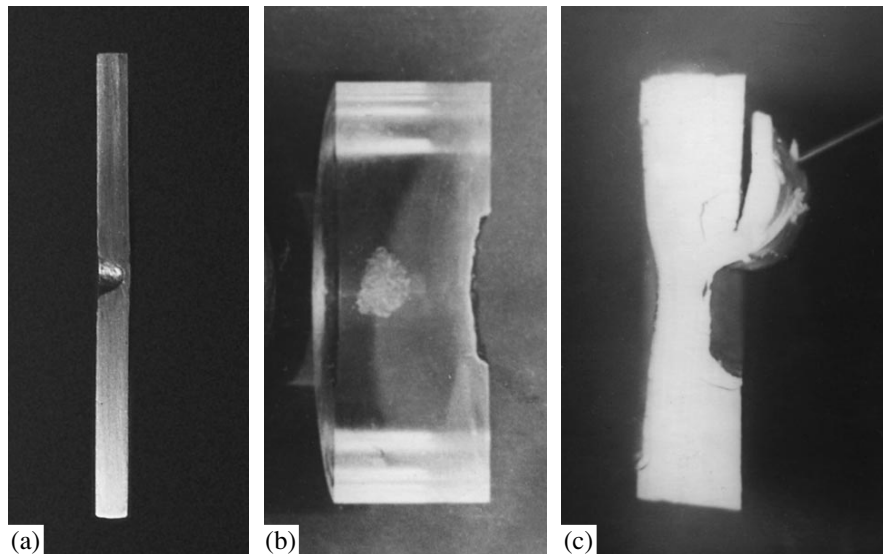
Fig. 2. Effect of an electron beam on different materials: (a) aluminum, (b) organic glass, and (c) vacuum rubber.

spherical crater with a depth of 5.0–5.5 mm on the front surface (Fig. 2a). Occasionally, the beam broke through the 6-mm-thick Al anode. An unfocused electron beam produced front- and backside spalls at plates made of PMMA organic glass, whereas lateral unloading waves resulted in irreversible changes inside the target (Fig. 2b).

The phenomenon of backside spalls at a vacuum-rubber target (Fig. 2c), which is rather difficult to observe in explosion experiments, is of especial interest because spalls in rubber usually occur at specific elongations exceeding 600% [3, 4].

In the first experiments, an attempt was made to estimate the pressure in the focal spot of a high-current REB interacting with a metal anode. In [5], the recoil momentum caused by the reactive force that arose due to the expansion of the material evaporated from the REB focal spot was measured for the first time. By using a calibrated spring gauge, it was shown that an REB with a current of 180 kA, an electron energy of 0.5 MeV, a current pulse duration of 10^{-7} s, and a power flux of 10^{12} W/cm^2 produced a recoil momentum of 0.15 N s at an Al anode. In subsequent experiments [6], the dependence of the recoil momentum on the REB

parameters was determined. Based on the results of the momentum measurements, the pressure was roughly estimated as $P \leq 7.5 \times 10^{11}$ Pa.

Obviously, this pressure is somewhat overestimated because the contribution to the recoil momentum from the cold components of the plasma and vapor expanding with a characteristic time longer than 10^{-7} s was not taken into account. The pressure in the REB focal spot was estimated more precisely by means of a metallographic analysis of Cu samples irradiated with REBs [5]. Since multiple-slip bands and copper hardening, which arise at pressures of $P \geq 2 \times 10^{10}$ Pa, were recorded at depths of ≤ 4.5 mm from the anode front surface, we may conclude that the pressure in the focal spot area amounts to $\sim 3 \times 10^{11}$ Pa.

In [7], a detailed study of changes in the microstructure and mechanical properties of various metals and alloys irradiated with REBs demonstrated irreversible phenomena in steel at depths of up to 25 mm.

In subsequent experiments [8], it was shown that the time-of-flight technique and high-speed photography can be successfully applied to determine the velocity of the rear side of the anode plate.

The most comprehensive measurements of the characteristics of shock waves excited by high-current REBs in metals were carried out in [9, 10]. In those studies, various techniques that employed long flexible single-channel fibers, two-stage targets, and targets of complex configuration were used to determine the mass velocity and the shock-wave speed. The diagnostics employed are characterized by a high interference immunity and high sensitivity and, thus, can be used to study the equations of state of various materials in the pressure range $(1-2) \times 10^{12}$ Pa. The measured attenuation of a shock wave during its propagation into metal agrees well with the results of computer simulations performed by Akkerman *et al.* [9–11]. The results of experiments and numerical simulations show that the pressure in the REB focal spot at the Kalmar accelerator reaches 2×10^{11} Pa.

Assuming that the heating is isochoric, the pressure in the REB focal spot can be roughly estimated as

$$P = \Gamma \omega, \qquad (1)$$

where Γ is the Gruneisen factor ($\Gamma \approx 1$) and ω is the volume energy density in the energy deposition region.

In fact, the pressure is lower because of the expansion of the heated substance. Taking into account this feature and the available experimental data, the following scaling for the pressure in the REB focal spot in terms of the electron beam and target parameters was proposed in [6, 12]:

$$P = 0.3 q_0^{2/3} \rho_0^{1/3} \qquad (2)$$

for a rectangle REB pulse and

$$P = 0.3 \left(\frac{q_0}{\tau_0} h \rho_0 \right)^{1/2} \qquad (3)$$

for a triangular REB pulse. Here, the maximum power flux density q_0, the initial substance mass density ρ_0, the average depth of the energy deposition region h, and the REB pulse duration τ_0 are in SI units.

The high values of the thermodynamic parameters attained in the REB focal spot offer wide opportunities for studying the behavior of the material under extreme conditions and allow one to perform structural and chemical transformations. X-ray structure analysis and the measurements of IR absorption spectra [13, 14] show that the irradiation of a target containing boron nitride or graphite with a high-current REB at a power flux density of $q_0 = 10^{12}$ W/cm^2 leads to the formation of denser diamondlike phases of the initial substance. The joint action of high pressures and temperatures in the REB focal spot is of especial interest for chemical synthesis. Thus, under these conditions, the yield of the reaction $CuBr_2 + Cu \longrightarrow 2CuBr$ is 100%. Copper and iron carbides, which, commonly, require prolonged heating, are also easily produced. This method seems to be the most promising for the initiation of chemical interactions with high activation energies.

3. MODELING OF THE EFFECT OF AN ULTRA-HIGH-SPEED IMPACT AND HIGH-POWER IRRADIATION ON AN OBSTACLE

In [15], it was shown that high-current REBs can be used to model many phenomena occurring during an ultra-high-speed impact or near-surface explosion. It was noted that the experimental data on ultra-high-speed impacts are in good agreement with those on the interaction of REB with matter. In particular, the following estimate for the anode crater depth in the REB experiments was proposed:

$$H = 4.5 L^{1/3} (u_0/C_s)^{2/3} + h, \qquad (4)$$

where H is the crater depth; C_s is the sound speed in the metal under study; u_0 is the mass velocity in the REB focal spot region; and h and L are the depth and volume of the REB energy deposition region, respectively. This expression was obtained by modifying the known empirical formula for the crater depth in shock experiments. Increasing interest in these phenomena is caused by the need to protect space vehicles from meteor showers. The modeling of impacts was carried out under the program of developing the shields for the protection of the *Vega* space vehicle from destruction by micrometeors [16]. Experiments on the REB interaction with the protective shields and the numerical simulations of this effect allow one to improve the physical model of high-speed breakthrough [17] and give rec-

ommendations of how to increase the reliability of the protection system as a whole. In particular, the role of the particles that are produced due to the scabbing of the first protective shield and can damage the second shield was investigated.

High-current REBs allow one to model the effects of other intense radiation fluxes incident on protective shields [18]. The modeling is based on the similarity between the destructions that are produced far from the energy deposition region by pressure pulses caused by different sources. In practice, the shield thickness is larger than the depth of the energy deposition region; hence, unloading from the back is completely determined by the pressure pulse. In this case, the coincidence between the spatial and temporal characteristics of the energy deposition process is of minor importance and the relation between the destruction effects can be found by numerical simulations with allowance for the data obtained in the model experiments. Such an approach is most advantageous when modeling the effect of pulsed irradiation on heterogeneous materials. The modeling consists in fitting the electron beam parameters in such a way that, for a given sample, the values of the mass removal and mechanical momentum coincide with those occurring under actual irradiation conditions. The validity of the results of numerical simulations is tested in a modeling facility.

4. TECHNOLOGICAL APPLICATIONS OF HIGH-CURRENT REBS

High-current REBs are promising energy sources for the modification and thermochemical treatment of surfaces; they also can be used to develop new methods for film deposition. The power flux density q_0 can be varied in a wide range by varying the diameter and shape of the cathode and the distance between the cathode and anode. At moderate power flux densities ($q_0 = 10^8–10^9$ W/cm^2), the accelerator anode surface is not melted and only a thin surface layer is instantly heated and then cooled, which results in the hardening of the steel surface. When 40-mm-diameter samples of St45 and St40Kh commercial grade steels are exposed to an electron beam, a fine-grained layer with a thickness of ~30 μm and microhardness exceeding the initial one by a factor of 4–5 forms on the surface [19]. The increase in the power flux density to $q_0 = (1–5) \times 10^9$ W/cm^2 leads to the melting and subsequent solidification of a thin surface layer. The irradiation of easy-to-amorphize alloys in such a regime results in the formation of an amorphous layer on the alloy surface. Based on the results of metallographic, X-ray structural, and electrochemical studies, it was shown that the thickness of the amorphous layer produced on the surface of a 20-mm-diameter discs made of FeCr$_{8–13}$P$_{13}$C$_7$, Ni$_{42}$Nb$_{58}$, or Ni$_{58}$Ta$_{42}$ alloy reaches 40–50 μm [20, 21].

At high power flux densities ($q_0 \geq 10^{10}$ W/cm^2), the anode material is evaporated and, then, deposited onto the different parts of the cathode unit in the form of melted droplets and ionized atoms, thus forming a coating.

Cu, Al, and St45 coatings were obtained on various metals placed in the cathode region. The high cooling rate caused by heat conduction into the target (up to 10^7 K/s) leads to the formation of metastable phases, including amorphous ones. In [21–23], amorphous FeCr$_{12}$P$_{13}$C$_7$ and Ni$_{58}$Ta$_{42}$ coatings with thicknesses of about 10 μm were obtained. The possibility of employing pulsed electron beams for depositing corrosion-proof coatings consisting of Fe–Si alloys (with a Si atomic content of $\geq 25\%$) onto substrates made of iron and St3 grade steel was studied in [24]. In particular, a coating with an elevated corrosion resistance was obtained and the possibility of producing multilayer Fe–Si protective coatings with intermediate layers made of corrosion-proof ductile metals (such as Pb) and alloys was demonstrated.

5. INTERACTION OF REBS WITH POROUS MATERIALS

Recently, much attention has been paid to studying the behavior of materials under the conditions of rapid isochoric heating. Interest in these studies is related to the problem of creating new types of complex targets for ICF research. A necessary element of such targets is porous material.

Fig. 3. SiO$_2$ aerogel with the mass density $\rho = 0.15$ g/cm^3. The balance weight is 0.5 kg.
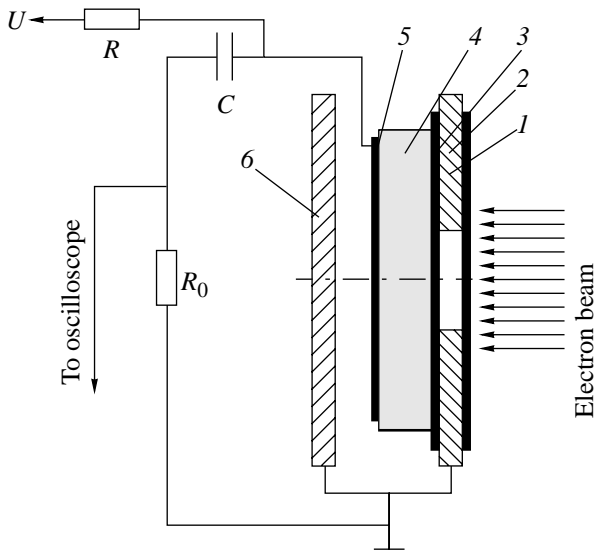
Fig. 4. Schematic of the experiment: (*1*) Ti foil, (*2*) anode, (*3*) Al foil, (*4*) aerogel, (*5*) Al foil, and (*6*) receiving plate.
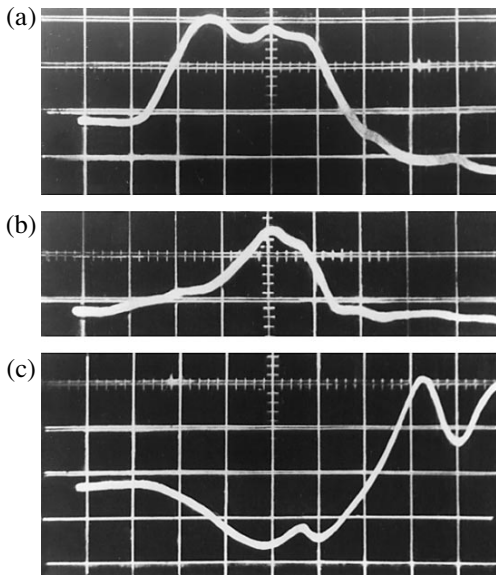
Fig. 5. Waveforms of (a) the accelerating voltage (the amplitude is 300 kV), (b) the irradiating bean current (the amplitude is 2.5 kA), and (c) the total accelerator current (the amplitude is 10 kA). The time scale is 50 ns/div.

On the initiative of V.E. Fortov, a series of experiments on the behavior of SiO_2 aerogels under the action of pulsed energy sources was carried out in the Kalmar accelerator.

SiO_2 aerogels are porous dielectric materials that possess unique properties. They have a low mass density ($\rho = 0.05$–0.36 g/cm^3) and a relatively high mechanical strength (see Fig. 3) and, due to their transparency, allow one to study the interaction of an electron beam with a porous medium by optical methods.

In our experiments, targets made of SiO_2 aerogel were irradiated with a 10-mm-diameter pulsed electron beam with a current $J = 10$–20 kA, electron energy $\varepsilon = 0.3$ MeV, and pulse duration $\tau \approx 10^{-7}$ s.

By using optical and interferometric measurements, the excitation of shock waves in aerogels of different mass densities was investigated and the profiles of the electron beam energy deposition, the velocity of aerogel expansion toward the electron beam, the expansion velocity of scabbing fragments, and the propagation velocity of perturbations in aerogels were measured.

It was found that, at aerogel mass densities $\rho \leq 0.2$ g/cm^3, the dimensions of the energy deposition region are greatly affected by the arising space charge. In this case, the depth of the energy deposition region is significantly less than that calculated without allowance for the space charge [25, 26]. To interpret the experimental data, I.A. Ivonin proposed a model equation of state for microporous materials. This equation self-consistently takes into account the change in the porosity during compression, reflects the fractal properties of aerogels, and enables the determination of their thermodynamic characteristics. In this model, the elastic and shear moduli and the Gruneisen factor depend on the porosity in a power-law manner, which is a consequence of the cluster structure of a porous substance. The calculations by this model show that, in the absence of shear stresses, the percolation coefficient (the power index in the dependence of the elastic modulus on the porosity) agrees with its theoretical value $\gamma = 1.7$. For an unheated aerogel, calculations give $\gamma = 3.2$ [27]. Direct experiments confirm the power-law dependence of the speed of sound in aerogel on its mass density. The measured percolation coefficient ($\gamma = 3.0$) agrees with that used in earlier calculations ($\gamma = 3.2$).

When studying the time evolution of the volume glow from an aerogel exposed to a pulsed high-power electron beam, it was found that, together with the conventional glow of a transparent dielectric material under the action of an electron beam, the glow also had a slow component ($\tau \approx 2 \times 10^{-5}$ s), whose time behavior coincides with the dynamics of the unloading wave propagating into the aerogel. It seems that, this slow component can be attributed to the volume electrization of the highly-porous aerogel exposed to an electron beam [28].

The electric conductivity in the beam energy deposition region is nonzero, because the electrons lying below the forbidden zone pass to the conduction zone. To adequately describe the process of electron absorption in an aerogel, it is necessary to measure the aerogel conductivity as a function of the irradiation power and the aerogel mass density. Such experiments were carried out at the Kalmar facility. The measurement tech-
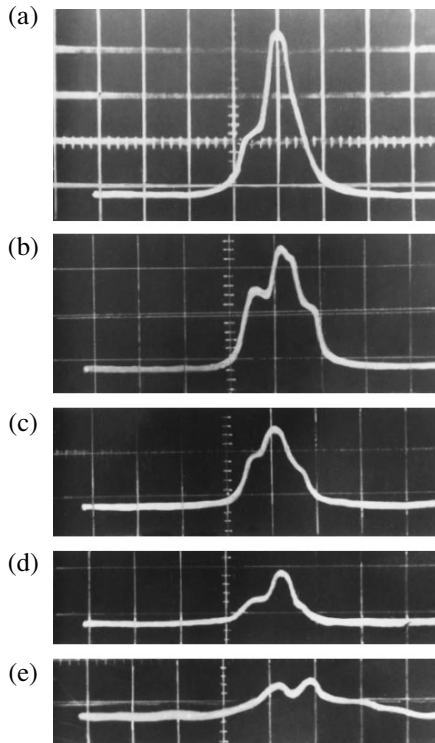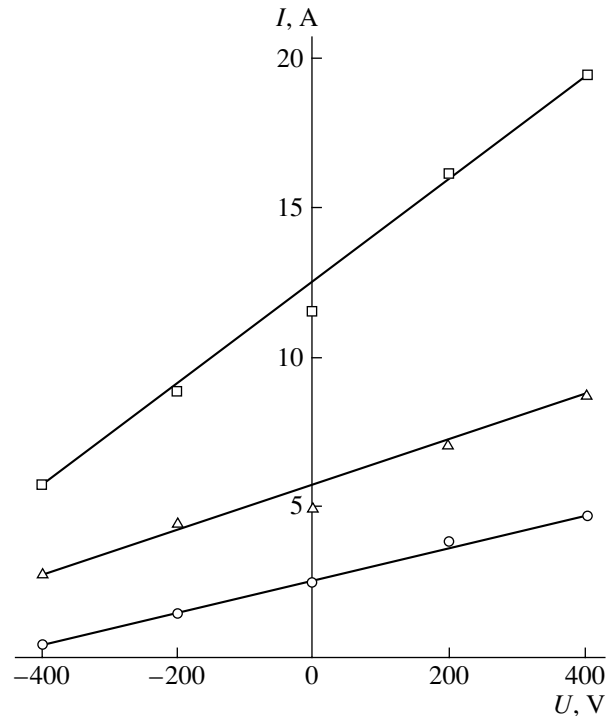
Fig. 6. Waveforms of the currents through the resistor R_0 for different bias voltages: V = (a) +400, (b) +200, (c) 0, (d) –200, and (e) –400 V. The time scale is 50 ns/div, and the current scale is 1.5 A/div.

Fig. 7. Current–voltage characteristics of aerogels irradiated with an electron beam with a current density of 200 A/cm^2 for different aerogel mass densities: ρ = 0.08 (circles), 0.15 (triangles), and 0.26 g/cm^3 (squares).

nique was the same as that previously used in [29] to measure the conductivity induced in various crystals under the action of an electron beam. A schematic of the experiment is shown in Fig. 4.

A 0.3-MeV electron beam, which is separated with the help of diaphragms from the total accelerator current, passes through an 80-µm-thick Ti foil *1* and a 10-mm-diameter opening in the anode *2* and then hits an aerogel sample *4* with transverse dimensions 25 × 25 mm. The front and rear sides of the sample are covered with 10-µm-thick Al foils *3* and *5*. After passing through the aerogel, the beam arrives at a receiving plate *6*, which is a part of the anode unit. An Al foil *5* is connected to a low-inductive capacitor C (C = 0.4 µF), which is charged through a high-ohmic resistor R up to ±400 V. When the aerogel conductivity becomes nonzero, the capacitor C discharges through the load resistor R_0, the signal from which is fed to the input of a C8-14 oscilloscope. The R_0 value is chosen such as to meet three contradicting requirements, namely, $R_0 < R_a$, $R_0C > 1$ µs, and $L/R_0 < 10$ ns, where R_a is the aerogel resistance and L is the inductance of the measurement system.

The induced conductivity in aerogel samples with mass densities ρ_1 = 0.08 g/cm^3, ρ_2 = 0.15 g/cm^3, and ρ_3 = 0.26 g/cm^3 and thicknesses l_1 = 7 mm, l_2 = 4 mm,

and l_3 = 2.2 mm, respectively, was investigated. The target thicknesses were approximately equal to one-half of the depth of the beam energy deposition region in these samples.
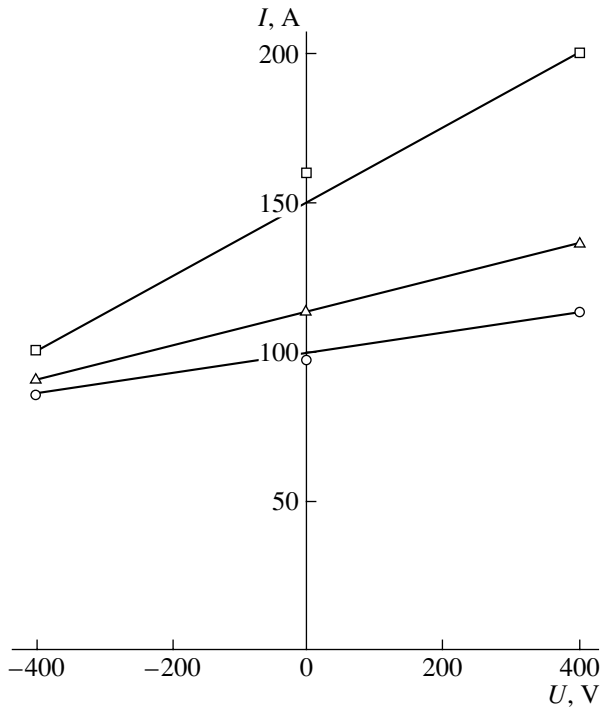
Figure 5 shows the waveforms of the accelerating voltage, irradiating beam current, and total accelerator current. It is seen that the duration of the irradiating beam current pulse is 50 ns, which is shorter than the duration of the total current pulse. The experiments were performed for two irradiation regimes with current densities j_1 = 200 A/cm^2 and j_2 = 2.5 kA/cm^2.

The waveforms of the current through the R_0 resistor are shown in Fig. 6 for j_1 = 200 A/cm^2, aerogel mass density ρ_1 = 0.08 g/cm^3, and different bias voltages. It can be seen that the current decreases with increasing magnitude of the negative bias voltage. However, even

Table 1. Experimental data on the induced conductivity of aerogels at a beam current of 200 A/cm^2

ρ, g/cm^3	0.08	0.15	0.26
l, mm	7	4	2.2
R_0, Ω	19	19	9
R_a, Ω	175	114	49
σ_{exp}, Ω^{-1} cm^{-1}	5×10^{-3}	4.5×10^{-3}	5.6×10^{-3}

Fig. 8. Current–voltage characteristics of aerogels irradiated with an electron beam with a current density of 2.5 kA/cm^2 for different aerogel mass densities: ρ = 0.08 (circles), 0.15 (triangles), and 0.26 g/cm^3 (squares).

at the highest negative bias voltage of –400 V, the current does not change its sign, which is due to the influence of the positive ac component of the beam current.

Figures 7 and 8 show the current–voltage characteristics of aerogels of various mass densities for different irradiation regimes. From the slopes of the characteristics, the total resistance $(R_0 + R_a)$ of the circuit and the aerogel conductivity were calculated. The results of experiments are presented in Tables 1 and 2, where σ_{exp} and σ_{th} are the measured and theoretical conductivities, respectively.

The theoretical values of the induced conductivity in aerogels at j = 2.5 kA/cm^2 were calculated by I.A. Ivonin based on the theory of ultra-high-energy conductivity [29].

Table 2. Experimental and theoretical data on the induced conductivity of aerogels at a beam current of 2.5 kA/cm^2

ρ, g/cm^3	0.08	0.15	0.26
l, mm	7	4	2.2
R_0, Ω	7	7	4
R_a, Ω	21.5	10.5	4
σ_{exp}, Ω^{-1} cm^{-1}	4×10^{-2}	4.8×10^{-2}	6.8×10^{-2}
σ_{th}, Ω^{-1} cm^{-1}	0.1	0.2	0.3

It can seen from Table 2 that the measured and theoretical conductivities differ by a factor of more than 2. The reason for this discrepancy is still unclear. In particular, it can be caused by an error in measuring the aerogel current–voltage characteristics at a current density of 2.5 kA/cm^2; such an error may appear, e.g., due to the presence of a large ac component of the irradiating beam current.

6. CONCLUSIONS

The possibility of obtaining and recording ultrahigh pressures in the focal spot of a high-current REB has been demonstrated. Regardless of the moderate parameters of the Kalmar accelerator with an REB power flux density of 10^{12} W/cm^2, a pressure of 2×10^{11} Pa has been experimentally recorded in metallic anodes. It can be expected that modern larger-scale relativistic electron accelerators with a power flux density of 5×10^{13} W/cm^2 will allow one to attain pressures higher than 10^{12} Pa.

This opens new opportunities for the direct study of the equations of state in this pressure range under laboratory conditions, as well as for modeling ultra-high-speed impacts in a speed range that is unattainable with other techniques. At a power flux density of $\approx 10^{14}$ W/cm^2 and an REB energy of ≈ 100 kJ, it is possible to simulate experiments on aluminum-against-aluminum ultrahigh-speed impacts with speeds of up to ≈ 50 km/s.

The joint action of the high pressure and temperature in the REB focal spot is promising for accomplishing structural changes in a substance and initiating chemical reactions with a high activation energy.

High-current relativistic electron accelerators can also be used to study new methods of surface modification (including steel hardening), surface amorphization, and the deposition of protective coatings by means of melting and sputtering the anode material.

Based on the data obtained in experiments on the interaction of REBs with SiO$_2$ aerogels (in particular, the data on the energy deposition profile, the velocity of aerogel expansion toward the electron beam, and the propagation velocity of perturbations in aerogels with different mass densities), a model has been developed that is capable of describing highly porous materials. In particular, this model enables one to study the fractal properties of aerogels and determine their thermodynamic parameters for a porosity varying by several tens of times.

Measurements of the induced pulsed conductivity of SiO$_2$ aerogels irradiated with an REB have shown that, at a low irradiation power (j = 200 A/cm^2), the conductivity is about 5×10^{-2} Ω^{-1} cm^{-1} and is almost independent of the aerogel mass density. At a high irradiation power (j = 2.5 kA/cm^2), the conductivity is higher by one order of magnitude and slightly increases with the aerogel mass density. To explain a certain discrepancy

between the experimental and theoretical data, more detailed investigations are required.

REFERENCES

1. B. A. Demidov, M. V. Ivkin, V. A. Petrov, *et al.*, At. Énerg. **46**, 100 (1979).

2. B. A. Demidov, M. V. Ivkin, V. A. Petrov, *et al.*, Zh. Tekh. Fiz. **48**, 2528 (1978) [Sov. Phys. Tech. Phys. **23**, 1445 (1978)].

3. G. I. Kanel', S. V. Razorenov, A. V. Utkin, and V. E. Fortov, *Shock Wave Phenomena in Condensed Media* (Yanus-K, Moscow, 1996).

4. Yu. B. Kalmykov, G. I. Kanel', A. V. Utkin, and V. E. Fortov, Prikl. Mekh. Tekh. Fiz., No. 1, 126 (1990).

5. B. A. Demidov, M. V. Ivkin, V. A. Petrov, *et al.*, Zh. Tekh. Fiz. **50**, 2205 (1980) [Sov. Phys. Tech. Phys. **25**, 1285 (1980)].

6. B. A. Demidov, M. V. Ivkin, V. V. Obukhov, *et al.*, Zh. Tekh. Fiz. **50**, 2209 (1980) [Sov. Phys. Tech. Phys. **25**, 1288 (1980)].

7. B. A. Demidov, G. S. Knizhnik, and Yu. F. Tomashchuk, Fiz. Khim. Obrab. Mater., No. 5, 5 (1982).

8. B. A. Demidov, M. V. Ivkin, V. A. Petrov, *et al.*, Zh. Tekh. Fiz. **54**, 155 (1984) [Sov. Phys. Tech. Phys. **29**, 86 (1984)].

9. A. F. Akkerman, A. V. Bushman, B. A. Demidov, *et al.*, Zh. Éksp. Teor. Fiz. **89**, 852 (1985) [Sov. Phys. JETP **62**, 489 (1985)].

10. A. F. Akkerman, A. V. Bushman, B. A. Demidov, *et al.*, Zh. Éksp. Teor. Fiz. **91**, 1762 (1986) [Sov. Phys. JETP **64**, 1043 (1986)].

11. A. F. Akkerman, B. A. Demidov, A. L. Ni, L. I. Rudakov, and V. E. Fortov, *Application of High-Current Relativistic Beams to the Physics of High-Temperature and High-Pressure Dynamics* (Inst. for High Temperatures, USSR Acad. Sci., Chernogolovka, 1989).

12. B. A. Demidov, *4th All-Russian Symposium on High-Current Electronics, Tomsk, 1982*, Abstracts of Papers, Vol. 2, p. 264.

13. S. S. Batsanov, B. A. Demidov, and L. I. Rudakov, Pis'ma Zh. Éksp. Teor. Fiz. **30**, 611 (1979) [JETP Lett. **30**, 575 (1979)].

14. S. S. Batsanov, B. A. Demidov, M. V. Ivkin, *et al.*, Neorg. Mater. **26**, 2100 (1990).

15. B. A. Demidov and A. I. Martynov, Zh. Éksp. Teor. Fiz. **80**, 738 (1981) [Sov. Phys. JETP **53**, 374 (1981)].

16. S. I. Anisimov, B. A. Demidov, L. I. Rudakov, *et al.*, Pis'ma Zh. Éksp. Teor. Fiz. **41**, 455 (1985) [JETP Lett. **41**, 554 (1985)].

17. S. I. Anisimov, A. V. Bushman, G. I. Kanel', *et al.*, Pis'ma Zh. Éksp. Teor. Fiz. **39**, 9 (1984) [JETP Lett. **39**, 8 (1984)].

18. V. P. Efremov, B. A. Demidov, A. I. Potapenko, *et al.*, *9th International Conference on Computational Mechanics and Modern Applied Software Systems, Moscow, 2001*, Abstracts of Papers, p. 186.

19. B. A. Demidov, M. V. Ivkin, V. A. Petrov, *et al.*, Poverkhnost, No. 12, 87 (1985).

20. V. Yu. Vasil'ev, B. A. Demidov, T. G. Kuz'menko, and L. I. Rudakov, Dokl. Akad. Nauk SSSR **268**, 605 (1983) [Sov. Phys. Dokl. **28**, 70 (1983)].

21. G. N. Andreeva, B. A. Demidov, N. V. Edneral, *et al.*, Poverkhnost, No. 8, 137 (1989).

22. L. I. Rudakov, B. A. Demidov, and V. S. Uglov, Fiz. Khim. Obrab. Mater., No. 5, 11 (1989).

23. B. A. Demidov, M. V. Ivkin, L. L. Krapivina, *et al.*, Fiz. Khim. Obrab. Mater., No. 3, 74 (1991).

24. V. I. Kolotyrkin, V. A. Tomashpol'skiĭ, V. M. Knyazheva, *et al.*, Zashch. Met. **28**, 287 (1992).

25. B. A. Demidov, V. P. Efremov, I. A. Ivonin, *et al.*, Zh. Tekh. Fiz. **67** (11), 26 (1997) [Tech. Phys. **42**, 1264 (1997)].

26. B. A. Demidov, V. P. Efremov, I. A. Ivonin, *et al.*, Zh. Tekh. Fiz. **68** (10), 112 (1998) [Tech. Phys. **43**, 1239 (1998)].

27. B. A. Demidov, V. P. Efremov, I. A. Ivonin, *et al.*, Zh. Tekh. Fiz. **69** (12), 18 (1999) [Tech. Phys. **44**, 1413 (1999)].

28. B. A. Demidov, V. P. Efremov, I. A. Ivonin, *et al.*, Zh. Tekh. Fiz. **70** (7), 57 (2000) [Tech. Phys. **45**, 870 (2000)].

29. D. I. Vaĭsburd, *High-Energy Solid-State Electronics* (Novosibirsk, 1982).

Translated by N.N. Ustinovskiĭ

Classical Transport in a Field Reversed Configuration[1]

N. Rostoker and A. Qerushi

University of California at Irvine, Irvine, CA 92697–0001, USA

Received October 26, 2002

Abstract—The transport of charged particles in a field reversed configuration (FRC) was previously considered to be turbulent because it is much faster than classical predictions. Classical transport has mainly been developed for plasmas in which the gyroradii of particles are small compared to the scale lengths of the variation of the density and magnetic field. This assumption is quite inappropriate for an FRC where the magnetic field vanishes on a surface within the plasma. Classical theory has been extended to include large ion gyroradii. A classical loss-cone process is revealed that is consistent with the transport experiments in which the ion gyroradii were comparable in size to the plasma radius. © *2003 MAIK "Nauka/Interperiodica"*.

1. INTRODUCTION

Field reversed configurations (FRCs) have been studied for more than 40 years, mainly in the USA and Japan. There is a considerable amount of literature on the subject. The 1988 review paper [1] by Tuszewski contains 416 references. Almost all previous research employs the Θ-pinch method that was developed by A.C. Kolb [2] in 1959. The experimental results fall into two different classes, distinguished by the dominance of drift orbits or betatron orbits, which are illustrated in Fig. 1. When the particles move in the diamagnetic direction, as in Fig. 1a, they always bend towards the null circle, resulting in a betatron orbit. When they move in the opposite direction as in Fig. 1b, they always bend away from the null circle and are in a drift orbit. The parameter that determines which type of orbit dominates is the ratio of the size of the plasma to the average gyroradius of the ions. This parameter is $s \cong L_n/\bar{a}_i$, where L_n is the length that characterizes the density gradient. For most of the experiments [1] at the Los Alamos National Laboratory, $1 \le s \le 2$. For the majority of experiments at the University of Washington [3], $s \gg 1$.

Transport has been studied in both cases. It involves the loss rates of ions, electrons, trapped magnetic flux, and energy. We mainly consider the loss rate for ions. The measurements involving time-dependent density were conducted with a microwave interferometer. In almost all of the measurements, the confinement time for ions is lower than the expectations based on classical-transport theory by an order of magnitude.

For the case when $s \gg 1$, there is a well-established classical theory with which to make comparisons. Anomalous transport is attributed to turbulence. There are detailed calculations that are in agreement with experimental measurements based on turbulence from low-frequency drift waves [4]. The case when $1 \le s \le 2$ is the main emphasis of this paper. In this case, the beta-

tron orbits dominate; the usual classical theory of transport for this case is inapplicable because it was developed only for small gyroradii. The turbulence calculation [4] is based on low-frequency drift waves and depends on similar approximations. This paper contains a purely classical investigation that does not assume a small ion gyroradius. It leads to a loss-cone process that accounts for the observed confinement times in small-s experiments.

2. MOTIVATION FOR LARGE ORBIT IONS

Recent experiments with large tokamaks [5] in the USA, England, and Japan involved heating plasma with high-energy neutral beams that were injected and trapped in the plasma. Detailed measurements revealed that the transport of the high-energy ions (of the order of 100 keV) was classical, while the high-density low-energy plasma (tens of keV) had the usual anomalous transport.

Transport is caused by fluctuations in electric fields. There are fluctuations just because particles are discrete, which is the cause for the irreducible Coulomb scattering of charged particles. There are collective motions in plasmas that involve waves characterized by a certain wavelength. For some wavelengths there can be an instability, which produces a large fluctuation level. It is essential that there be no long wavelength instabilities, because they would disrupt magnetic confinement on a very short timescale. The fusion effort to date has been successful in stabilizing long-wavelength instabilities in many configurations, but some short-wavelength instabilities, which are believed to be responsible for anomalous transport, remain in all devices to date. Wavelengths that are short compared to the gyro-radius should not cause transport because the particles average the electric fields. Only wavelengths of the order of the gyroradius or longer cause transport. For particles with a very small gyroradius, almost all of

---

[1] This article was submitted by the authors in English.
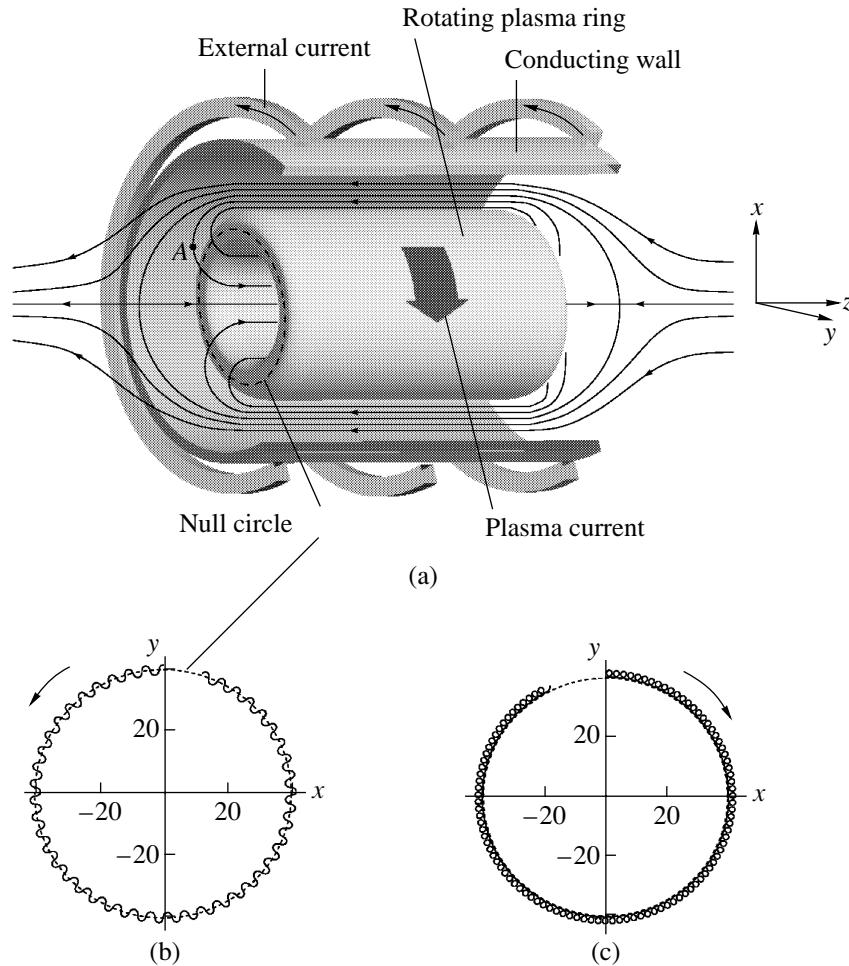
Fig. 1. Illustration of an FRC (a) and its main particle orbits: a betatron orbit (b) and a drift orbit (c). In plots (b) and (c), the arrows indicate the direction of rotation of the orbits when seen from the tip of the z axis.

the spectrum of fluctuations can cause transport; for particles with a large gyro-radius, only long wavelength fluctuations can cause transport. Long wavelengths must be stable, and the corresponding fluctuations, minimal. This intuitive explanation of classical transport for large-orbit particles has been verified by computer simulation [6, 7]. Based on this explanation, we conjecture that the anomalous transport of ions can be avoided for a plasma with a high density of large-gyro-radius ions.

A device with a high density of large-gyroradius ions is the FRC. Experiments with FRCs were carried out at the Los Alamos National Laboratory for at least ten years. There exists a considerable amount of experimental data [1] for FRCs with $1 \leq s \leq 2$. The confinement time for ions was usually about a factor of ten shorter than the classical one, which was attributed to turbulence. The purpose of this paper is to reconsider what is meant by *classical* when the average ion gyro-radius is not small.

3. ION DYNAMICS IN A SMALL-*s* FRC

The typical particle orbits in a FRC are illustrated in Fig. 1. The diamagnetic direction of rotation is counter-clockwise. Ions that rotate in this direction will always bend towards the null circle and are in betatron orbits. At the ends of the FRC plasma, the field lines are closed and there must be a radial magnetic field in the directions indicated in Fig. 1. In addition to their rotational motion, ions have a finite value of v_z; after a transit time they reach the ends of the FRC, where they experience a Lorentz force $F_z = -v_\theta B_r/c$. For example, at point A in Fig. 1a, $B_r < 0$, and for $v_\theta > 0$, one has $F_z > 0$, which is a focusing force. Similar reasoning applies to the other end of the FRC; i.e., the ions in a betatron orbit will be reflected at both ends of the plasma.

The drift orbit has a drift velocity

$$\mathbf{v}_D = \frac{c}{qB^2}\mu(\nabla B \times \mathbf{B}), \qquad (1)$$

Drift orbit

Null circle
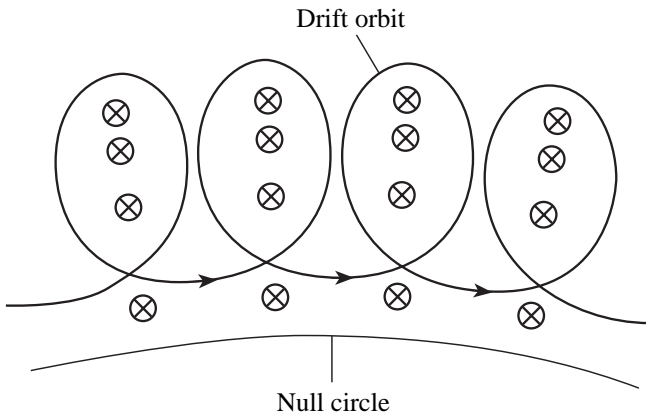
Fig. 2. Direction of the drift orbit of the ions. The crosses indicate a magnetic field pointing into the paper. The magnetic field has a gradient as indicated by the density of the crosses. The average drift velocity is in the counterdiamagnetic direction, i.e., clockwise when seen from the tip of the z axis (see Fig. 1a).

$$v_\theta = -\frac{c}{qB^2}\mu B_z \frac{\partial B}{\partial r}, \qquad (2)$$

Here, q is the ion charge; $\mathbf{B}$ is the magnetic field; and $\mu = \frac{1}{2}m_i v_\perp^2/B$ is the magnetic moment, where $\frac{1}{2}m_i v_\perp^2$ is the perpendicular energy. Outside the null circle, $B_z < 0$, $\frac{\partial B}{\partial r} > 0$, so v_θ is positive, which is in the clockwise or antidiamagnetic direction. Equations (1) and (2) are appropriate for small gyroradius particles. The drift velocity must be small compared to the perpendicular velocity; i.e., $\frac{v_\theta}{v_\perp} = \frac{1}{2}\frac{a_i}{L_n}$, where a_i is the ion gyroradius

and $L_n = B/|\partial B/\partial r|$. Although the Lorentz force would be defocusing at the ends, it would be insufficient to cause significant particle losses because the particles follow the field lines with a velocity $v_p \gg v_\theta$. Most of the ions would not spend enough time at the ends to be ejected. For large-orbit ions, the drift orbit is illustrated in Fig. 2. In this case, $v_\theta \approx v_\perp$ and most of the ions in such orbits would be expelled at the ends in the transit time, which would be a few microseconds.

4. TRANSPORT IN A SMALL-s FRC

Because of the long range of Coulomb forces, collisions with distant particles are more important than collisions with near neighbors. This distinguishes a plasma from any other state of matter. For fusion plasma, the cumulative effect of many small deflections from collisions with distant particles is more important than infrequent large-angle deflections from collisions with near neighbors by a factor of about twenty. This is the basis for the theoretical treatment of plasmas. The cumulative effect of small deflections from collisions with distant particles on a betatron orbit is illustrated in Fig. 3a. The orbit expands without changing its topology. The net result for a magnetically confined plasma is diffusion. The particle orbits change slowly but remain confined for a time determined by the boundary conditions. The plasma density decays on a time scale determined by the effective collision frequency, which may be classical or anomalous. Figure 3b illustrates how a single large-angle collision can change the orbit topology from a betatron to a drift orbit. The drift orbit would not be contained because the Lorentz force at the ends is defocusing, as was discussed in the previous paragraph. This is a loss process that may have a shorter time scale than diffusion. It is similar to the loss-cone

      (a)   (b)
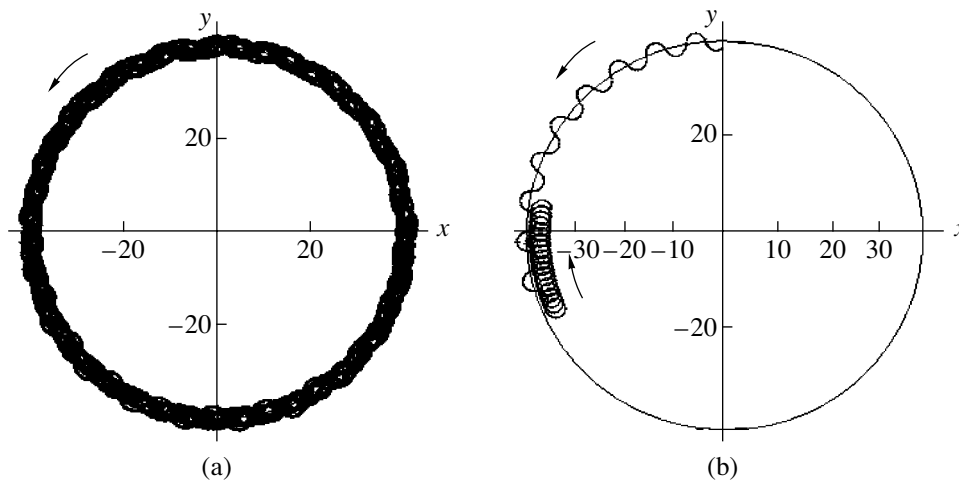
Fig. 3. (a) Cumulative small-angle deflections from distant particle collisions do not change the topology of a betatron orbit. This leads to conventional diffusion. (b) A large-angle deflection from a near-neighbor collision may change the betatron orbit into a drift orbit, which is not contained. Such collisions lead to a particle loss channel, which is more rapid than diffusion.

process [8] that dominates the confinement time of mirror machines.

In order to evaluate the loss-cone theory, we consider typical data from Los Alamos experiments [1] for an FRC:

(i) Temperature: $T_i \simeq T_e = 100$ eV.

(ii) Ion rotational energy: $\frac{1}{2} m_i v_\theta^2 = 1$ keV.

(iii) Dimensions:

radius of the null surface, $r_0 = 10$ cm;

gradient length, $L_n = 2.5$ cm;

distance from the null surface to the separatrix, $\Delta r = 4.14$ cm.

(iv) Gyroradii of ions:

average gyroradius for betatron orbits, $\bar{R}_i = 10$ cm;

average gyroradius for drift orbits, $\bar{r}_i = \dfrac{v_i}{\Omega_i} = 0.14$ cm;

where

$$v_i^2 = \frac{T_i}{m_i}, \quad \Omega_i = \frac{eB}{m_i c}.$$

(v) Magnetic fields:

applied field, $B_0 = 2.5$ kG;

maximum field due to plasma current, $B_m = 7.5$ kG;

$\Omega_i = \dfrac{e}{m_i c}(B_0 + B_m)$ (in the expression for $\bar{r}_i$).

The ion gyroradius varies from 0.14 to 10 cm. However, the density also varies from a peak of $n_0 = 10^{15}$ cm^{-3} to a very low value. The highest density is near the null surface, where the magnetic field is very small, and the lowest density is where the magnetic field achieves its largest value $B_0 + B_m$. The average gyroradius of the ions $\bar{a}_i$ involves a density-weighted average, $s = L_n/\bar{a}_i$, with $1 \leq s \leq 2$ [1].

The diffusion time can be estimated as

$$\tau_i \cong \left(\frac{L_n}{\bar{r}_i}\right)^2 t_{ie},$$

where t_{ie} is the momentum transfer time due to the Coulomb collisions of ions with electrons. The relevant numbers are

$$t_{ie} = \frac{3}{4}\sqrt{\frac{\pi}{2}} \frac{T_e^{3/2}}{4\pi n_0 e^4 \ln\Lambda}\left(\frac{m_i}{\sqrt{m}}\right) = 61.6 \ \mu s,$$

$$\tau_i = 19.6 \ ms.$$

The density and gyroradius change rapidly, so that averaging is required to obtain a meaningful result for the classical confinement time. The above value is a lower bound for the high field region. Where the density is low and the field is high, adiabatic dynamics would prevail and there would be no losses of the drift orbit particles at the ends. The classical containment time is, of course, much longer than the observed time of a few hundred microseconds. This could be explained by turbulence, as small orbit particles are sensitive to turbulence. However, for a small-s FRC, this would only apply to a small percentage of the particles.

In the low field region, where the density is high and the gyroradius is large, we expect an insensitivity to turbulence, as we have learned from experiments with tokamaks [5]. There would be ions with betatron orbits and drift orbits involving large orbit radii. The betatron orbits would be contained. The drift orbits would not be contained due to defocusing at the ends. A topological change from a betatron to a drift orbit can take place due to large-angle scattering from Coulomb collisions with neighboring particles. The confinement time can be estimated from this process. Whereas only ion–electron collisions are important for diffusion, ion–ion collisions would be dominant for this loss process.

The lifetime of an ion in a betatron orbit would be

$$\tau_i = \frac{1}{n_i^* \langle \sigma \rangle v_i}.$$

Here,

$$\frac{d\sigma}{d\Omega} = \frac{b^2}{4\sin^4\left(\frac{\theta}{2}\right)},$$

$$b = \frac{e^2}{\mu v_i^2}, \quad \mu = \frac{m_i}{2} \ \text{(for ion–ion scattering)},$$

$$\langle \sigma \rangle = 2\pi \int_{\pi/2}^{2\pi} \sin\theta \, d\theta \left(\frac{d\sigma}{d\Omega}\right) \simeq 1.6\pi b^2.$$

Scattering from ions moving at the same azimuthal velocity would not produce a large-angle scattering in the laboratory frame. If the ion distribution is of the form

$$f_i(v_\theta) = \frac{1}{\sqrt{2\pi} v_i} e^{-\frac{(v_\theta - V_i)^2}{2 v_i^2}},$$

then the target ions require $v_\theta < v_i/2$ for an ion at the average speed to be deflected at a large angle in the laboratory frame. The number of such ions is

$$n_i^* = \frac{n_i}{2} \text{erfc}\left(\frac{V_i}{2\sqrt{2} v_i}\right) \simeq \frac{n_i}{6.8}.$$

The result is that the lifetime of an ion in a betatron orbit $\tau \approx 185 \ \mu s$.

5. CONCLUSION

Considering the experience with large-orbit particles in tokamaks, the above explanation of the lifetime of small-s FRCs seems more likely than the conventional explanations based on turbulence.

REFERENCES

1. M. Tuszewski, Nucl. Fusion **28**, 2033 (1988).
2. A. C. Kolb, C. B. Dobbie, and H. R. Griem, Phys. Rev. Lett. **3**, 5 (1959).
3. J. T. Slough, A. L. Hoffman, R. D. Milroy, *et al.*, Phys. Plasmas **2**, 2286 (1995).
4. N. A. Krall, Phys. Fluids B **1**, 1811 (1989).
5. W. Heidbrink and G. L. Sadler, Nucl. Fusion **34**, 535 (1994).
6. H. Naitou, T. Kamimura, and J. M. Dawson, J. Phys. Soc. Jpn. **46**, 258 (1979).
7. G. Manfredi and R. O. Dendy, Phys. Rev. Lett. **76**, 4360 (1996).
8. K. Miyamoto, *Plasma Physics for Nuclear Fusion* (MIT Press, Cambridge, MA, 1989), p. 62.

BRIEF
COMMUNICATIONS

Concerning Arc Discharge in a Transverse Magnetic Field

A. V. Zharinov

Lenin All-Russia Electrotechnical Institute, Krasnokazarmennaya ul. 12, Moscow, 111250 Russia
Received December 26, 2002

Abstract—The retrograde motion of an arc in a transverse magnetic field is attributed to the onset of a tangential flow of gas or vapor. The physics of a polarized plasma jet conducting the current between the cathode and anode is discussed. © *2003 MAIK "Nauka/Interperiodica"*.

1. INTRODUCTION

A vacuum arc discharge with a mercury cathode operates in transverse magnetic fields of up to 2×10^4 Oe. The arc, together with the cathode spot and plasma jet conducting the current, moves with a velocity of $\sim 10^4$ cm/s in a direction opposite to the magnetic force acting on the current-carrying wire [1–3]. Such motion is referred to as "retrograde"; accordingly, we will use the term "retrograde arc." Retrograde motion is evidently caused by a nonmagnetic force. Hence, the retrograde arc somewhat resembles an electric generator and behaves like a conductor entrained by a vapor stream. A tangentially propagating vapor flow arises at the cathode spot and in the plasma train behind the spot.

The motion of a body entrained by a vapor flow is one of the most important issues of gasdynamics. However, the retrograde arc is much more complicated than typical gas-dynamic objects (such as a steam turbine). The retrograde arc involves a lot of fundamental physical processes. Therefore, studying this discharge can reveal some unknown phenomena that may be even more important than the retrograde arc itself.

The present study is aimed at investigating the most interesting and important features of the retrograde arc. Perhaps, it will inspire more comprehensive studies of this phenomenon.

2. RETROGRADE MOTION

An intense discharge is feasible only if there is a positive feedback between the electron current from the cathode and the ion current to the cathode. In this case, a very rigid requirement is the quasineutrality condition, which implies that the local ion and electron densities are equal to each other and the counterpropagating ion and electron flows overlap with an accuracy of up to the Debye radius. Thus, if the gas flows with a certain velocity along the cathode surface, then the arc, together with the cathode spot emitting electrons, should follow the gas flow with approximately the same velocity; otherwise, the arc goes out.

Figure 1 illustrates the effect of the relative motion of the gas and the cathode spot. Rectangle *2* shows an active plasma layer (APL) in an immobile gas; the APL with the height L_0 resides on cathode spot *1*. All of the ions from the volume with the height L_0 reach the cathode spot. Shaded triangle *3* with the height $L_V < L_0$ shows the APL region in the gas flowing with a velocity V along the y-axis. In the gas flow, the APL volume decreases by a factor of $2L_0/L_V$. The discharge current decreases either by the same factor or even to zero in the case of arc extinction. Hence, the arc should be entrained by the gas flow like a turbine blade. Since retrograde motion occurs in a transverse magnetic field, it is obviously the magnetic field that is responsible for the production of the tangential flow of a gas or cathode vapor.

The mechanism for the production of such a flow can be outlined as follows. Let a discharge with the electron current density $j = j_i \sqrt{M/m}$ (where j_i is the ion current density at the cathode and M/m is the ion-to-electron mass ratio) operate in an immobile gas. The neutralization of ions at the cathode results in the generation of an atomic flow from the cathode. Then, these atoms get ionized again and return to the cathode. Hence, under steady-state conditions, the atomic density near the cathode increases to a value of Jn_0, where
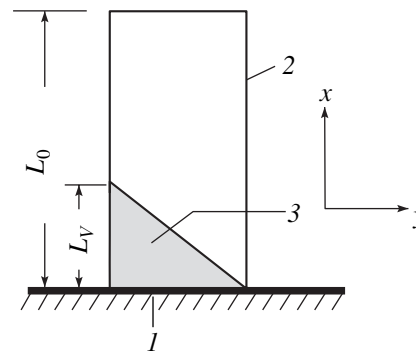
Fig. 1. Schematic of an active plasma layer.

n_0 is the initial gas density and J is the gas compression ratio [4].

The compression ratio is described by the formula

$$J = \exp\left[\frac{\sigma_i v_e}{v_g}\int_0^L n_e(x)dx\right],$$

where σ_i is the electron ionization cross section, v_e is the electron velocity, $n_e(x)$ is the electron density, v_g is the mean atom velocity along the x-axis, and L is the APL height.

In a transverse magnetic field, the APL height grows along the y direction due to the magnetic deflection of fast cathode electrons. If $y \gg \rho$, then the electrons move diffusely, and we have $L(y) \approx y\rho/\lambda$, where λ is the electron mean free path and ρ is the electron Larmor radius.

If $y \le \rho \ll \lambda$, then $L(y) = \rho\sqrt{1-\left(1-\frac{y}{\rho}\right)^2}$.

In both cases, $\int_0^{L(y)}n_e(x)dx$ increases with y, hence, the compression ratio increases in the direction in which Ampère force acts.

For a collisionless APL ($y \le \rho \ll \lambda$) at $j \gg j_i$, we have

$$J = \exp\left[\chi\arcsin\sqrt{1-\left(1-\frac{y}{\rho}\right)^2}\right], \qquad (1)$$

where

$$\chi = \frac{\sigma_i j\rho}{e v_g} \approx \frac{0.33 j}{H}. \qquad (2)$$

At $\chi = 4$, the compression ratio increases from 1 to 535 over the interval $0 \le y/\rho \le 1$. The gas pressure P and the tangential pressure derivative dP/dy change accordingly; as a result, a retrograde atomic flow with a velocity on the order of the thermal velocity arises. There is also a gas flow moving in the opposite direction; however, this flow rapidly leaves the APL and irreversibly escapes into a vacuum.

The ions arriving at the cathode give rise to a tangential force applied to the surface. Hence, if there is a liquid (melted) film on the surface, then it can be entrained in retrograde motion not only by the thermocapillary force but also the ion flow.

Note that the above mechanism for the generation of a tangential atomic flow occurs also in a non-self-sustained discharge with a heated cathode in the presence of a transverse magnetic field. If such a cathode is allowed to move freely, then it will be dragged in the retrograde direction under the action of ion bombardment.

One can easily imagine a "carousel" of circumferentially spaced identical cathodes in a radial magnetic field. In this case, each cathode will be blown around by two oppositely directed gas flows, namely, its own retrograde cathode flow and the flow produced by the preceding discharge.

Obviously, the rotation velocity of the carousel decreases (to a full stop) as the number of cathodes (i.e., the total current) increases.

Apparently, intense ion bombardment results in the positive gradients of the temperature (dT/dy), current density (dj/dy), and evaporation rate (dq/dy). This process is nonlinear and leads to the onset of thermal instability of the cathode spot surface near the edge toward which the Ampère force is directed. However, until the onset of instability, the motion can remain continuous and steady-state [3].

In general, the calculation of the retrograde motion velocity is an extremely difficult problem. Similar (but simpler) problems of gas-dynamics are usually solved by testing various profiles in a wind tunnel. However, it is obvious that the maximum velocity of the retrograde motion does not exceed the atomic thermal velocity.

Instead of measuring the retrograde velocity, it may be more important to perform certain control experiments. For example, let us consider a retrograde arc moving circumferentially in a radial magnetic field. In this case, the following results can be expected:

(i) If the magnetic field is too strong in some sector, then, at $\chi \ll 1$ [see (2)], the arc should go out inside this sector.

(ii) If the disc cathode is rotated in an axisymmetric magnetic field in the direction in which the Ampère force acts, then the arc can be brought to a stop.

(iii) If the disc cathode can rotate freely without friction, then the retrograde arc is able to spin up the disc until it becomes destroyed by the centrifugal force.

3. CURRENT-CARRYING PLASMA JET IN A TRANSVERSE MAGNETIC FIELD

Far from the cathode spot, the gas or vapor density decreases inversely proportional to the distance squared; hence, electron collisions can be ignored. A long quasineutral plasma jet in a transverse magnetic field is always polarized. Thus, there can exist an electron beam with the radius of curvature

$$R = \frac{\rho}{\left(1 \pm \frac{v_d}{v}\right)},$$

where v is the tangential velocity, $v_d = \left|\frac{cE_r}{H}\right|$ is the drift velocity, and E_r is the radial electric field. The case $R < \rho$ is of no interest. If there is the minus sign in the denominator, then, at $\frac{v_d}{v} < 1$, we have $R > 0$, which corresponds to rotation in the direction of the electron

gyration, and at $\frac{v_d}{v} > 1$, we have $R < 0$, which corresponds to rotation in the direction of the ion gyration. At $\frac{v_d}{v} \longrightarrow 1$, we have $R \longrightarrow \infty$; i.e., the trajectory becomes straight.

In the general case, a plasma jet can have a complex configuration, as is shown in Fig. 2.

Since the cathode electrons move toward the anode along the x-axis, the transverse component of the electric field is positive ($E_y > 0$) over the entire plasma jet. After entering the jet, the gas atoms can turn into ions via ionization or resonant charge exchange. The acceleration of the ions by the jet's electric field gives rise to the reactive force, which balances both the magnetic force and the inertial forces (including the centrifugal one). Thus, the plasma jet interacts with the gas flow like a very light and perfectly flexible metal conductor. If the gas flow varies in space and time, then the plasma jet twists like a water hose.

At $R = \infty$, the equilibrium state of the plasma jet corresponds to the balance between the transverse magnetic force and the reactive force (per square centimeter):

$$\frac{I_n H}{c} \cong \frac{j_i}{e} M \Delta V_i, \qquad (3)$$

where I_n is the Hall current (in A/cm) along the jet (this current is equal to the arc current divided by the jet width along the magnetic field), j_i is the density of the transverse ion current ejected from the jet, and ΔV_i is the averaged variation in the particle velocity due to the interaction with the jet.

If the jet is parallel to the x-axis, then we have $v_{ex} = cE_y/H \cong \sqrt{2e\varphi/m}$; i.e., the current is carried by the electrons accelerated in the cathode sheath with the cathode fall voltage φ. The electric field E_y is fairly high, $E_y \sim 2.5H$ V/cm (where H is in units of Oe). At the jet width on the order of ρ, this value does not contradict the quasineutrality condition, provided that the electron current density is sufficiently high:

$$j \gg j_B = 10^{-6} H^2 \sqrt{\varphi},$$

where $j_B = en_B\sqrt{2e\varphi/m}$ is the current density at the Brillouin electron density ($n_e = n_B = \dfrac{H^2}{4\pi mc^2}$). At $H = 10^4$ Oe and $\varphi = 16$ V, it should be $j \gg 400$ A/cm^2, which, apparently, is always satisfied in a retrograde arc.

The limitation on the transverse potential drop, namely, $E_y b < \varphi$, is quite natural and leads to the constraint $b < \rho/2$. However, one should take into account the jet diamagnetism, which, at $4\pi I_n/c \sim H$, significantly softens the limitation on b. Equilibrium condition (3) is not explicitly dependent on the retrograde
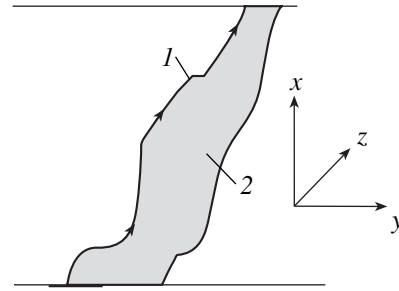
Fig. 2. Schematic of a plasma jet: (*1*) plasma jet and (*2*) plasma train.

velocity. Hence, the plasma jet merely follows the motion of the APL and cathode spot. At the same time, the retrograde direction of motion is the most favorable from the standpoint of neutralizing the volume charge of the ion flow ejected from the plasma jet into the nearly current-free plasma train (in Fig. 2, the plasma train is shaded). Because of both the resonant charge exchange and the ambipolar motion of ions along the magnetic field, the thickness of the plasma train is less than the ion Larmor radius $\rho_i = \rho \sqrt{M/m}$.

The plasma-jet problems sketched in this paper have a long history. For at least 50 years, the problems of the transverse motion of current-carrying and current-free plasmas have attracted the attention of researchers in the fields of controlled nuclear fusion, plasma accelerators, magnetosphere physics, and space electrodynamics [5–7].

Thus, plasma-jet physics is one of the important areas of plasma physics, rather than merely an issue of a retrograde arc. The experimental studies of the plasma jet in a retrograde arc are extremely difficult. Hence, it is reasonable to model this phenomenon using special experimental facilities.

4. CONCLUSIONS

The retrograde motion of an arc can be explained by its entrainment by a vapor flow. Such motion is caused by a tangentially nonuniform gas compression in the APL of an intense discharge in a transverse magnetic field. A detailed experimental study of this phenomenon is much easier to perform in a non-self-sustained discharge with a heated cathode; the same is true of a polarized plasma jet.

ACKNOWLEDGMENTS

REFERENCES

1. V. A. Granovskiĭ, *Electric Current in Gases* (Nauka, Moscow, 1971), p. 362.

2. R. M. St.-John and J. G. Winaus, Phys. Rev. **94**, 1094 (1954).

3. B. Juttner and I. Kleterg, J. Phys. D: Appl. Phys. **33**, 2025 (2000).

4. A. V. Zharinov, in *Proceedings of XXV International Conference on Phenomena in Ionized Gases, Nagoya, 2001*, Ed. by T. Goto (Nagoya Univ., Nagoya, 2001), Vol. 3, p. 335.

5. L. A. Artsimovich, *Controlled Thermonuclear Reactions* (Fizmatgiz, Moscow, 1961).

6. H. Alfvén, *Space Electrodynamics* (Clarendon Press, Oxford, 1950; Inostrannaya Literatura, Moscow, 1952).

7. S. B. Pikel'ner, *Principles of Space Electrodynamics* (Fizmatgiz, Moscow, 1961).

Translated by N.N. Ustinovskiĭ